Study of 2D/3D perovskites heterostructures for solar cells

Thomas Campos

université
PARIS-SACLAY

Étude d'hétérostructures de pérovskites 2D/3D pour cellules photovoltaïques

Study of 2D/3D perovskites heterostructures for solar cells

Thèse de doctorat de l'Université Paris-Saclay

École doctorale n° 572, Ondes et Matière (EDOM)
Spécialité de doctorat: Physique
Graduate School : Physique. Référent : ENS Paris-Saclay

Thèse préparée dans les unités de recherche **LuMIn** (Université Paris-Saclay, ENS Paris-Saclay, CNRS, CentraleSupélec) et **IPVF**, sous la direction d'**Emmanuelle DELEPORTE**, Professeure, et le co-encadrement de **Damien GARROT**, maître de conférence, **Aurélien DUCHATELET** et **Jean ROUSSET**, ingénieurs R&D.

Thèse soutenue à Paris-Saclay, le 16 mai 2023, par

Thomas CAMPOS

Composition du jury

Membres du jury avec voix délibérative

Nadine WITKOWSKI Professeure, Sorbonne Université (INSP)	Présidente du jury
Lionel HIRSCH Directeur de recherche CNRS, Université de Bordeaux (IMS)	Rapporteur & Examinateur
Johann BOUCLÉ Maître de conférence, HdR, Université de Limoges (XLIM)	Rapporteur & Examinateur
Olivier PLANTEVIN Maître de conférence, HdR, Université Paris-Saclay (LPS)	Examinateur
Philip SCHULZ Directeur de recherche, CNRS (IPVF)	Examinateur

THESE DE DOCTORAT
NNT : 2023UPASP046

Acknowledgements

Une thèse, bien qu'elle soit rarement dissociable de son doctorant, est rarement réalisée en autarcie. Il semble donc logique que ce manuscrit de thèse, comme tant d'autres, commence par la traditionnelle étape des remerciements, afin de pouvoir exprimer ma reconnaissance envers toutes les personnes qui ont contribué à l'existence de cette trace de mon passage dans le monde de la recherche. Ce manuscrit conclut plus de trois ans passés entre le laboratoire Lumière, Matière, et Interfaces (LuMIn) et l'Institut Photovoltaïque d'Ile-de-France (IPVF). Je remercie donc en premier lieu le LabEx CHARMMMAT ainsi que l'IPVF pour avoir financé la réalisation de ces travaux.

Je tiens également à remercier les membres de mon jury de thèse, qui, en acceptant d'évaluer mes travaux, m'ont permis d'y apporter une fin : Nadine Witkowski qui l'aura présidé, Lionel Hirsch et Johann Bouclé pour en avoir été les rapporteurs, ainsi que Philip Schulz et Olivier Plantevin.

Il convient ensuite de remercier les personnes responsables de mon encadrement. Pour avoir initialement cru en moi pour réaliser cette thèse, ainsi que pour toutes les discussions que l'on a pu avoir, pour sa bienveillance, son implication, et pour avoir été présente à chaque fois que j'en avais besoin malgré un emploi du temps de ministre (je sais qu'il est bien plus chargé que ça en réalité), je suis infiniment reconnaissant envers ma directrice de thèse Emmanuelle Deleporte. J'aurais difficilement pu rêver d'une meilleure directrice de thèse que toi, et je souhaite cette chance à tous les doctorants. Merci ensuite à Jean Rousset d'avoir accepté de rejoindre ce bateau en cours de route malgré beaucoup d'autres responsabilité à gérer, apportant avec lui son humour et sa pertinence (ainsi que son petit accent mythique). Merci ensuite à Aurélien Duchatelet de m'avoir accompagné pendant la première moitié de ma thèse et de m'avoir poussé lorsque j'étais un jeune thésard pas très rigoureux. J'espère que tu te plais là où tu es aujourd'hui. Merci enfin à Damien Garrot qui posait les bonnes questions et qui, par son entêtement sur la position des pics de PL, nous a permis de dérouler un fil d'étude très intéressant.

Mes caractérisations optiques étaient réalisées au laboratoire LuMIn, d'abord dans les locaux de l'ISMO que je remercie pour l'accueil, puis de retour dans notre cher bâtiment 505. Merci à Céline, Edith et Isabelle, qui m'ont aidé à résoudre toutes mes galères administratives, ainsi que Fabien Bretenaker à la direction du laboratoire. Plus spécifiquement, je remercie l'équipe Noos pour la super ambiance, que ce soit avec les discussions autour de repas mangés beaucoup trop rapidement au CESFO ou avec les pauses cafés difficiles à conclure pour "retourner faire avancer la science". L'ambiance était aussi assurée par les anciens de l'époque du Basket-bullet : Paul, François, Gabriel, et Timothée, ainsi que par les un peu moins anciens Joanna, Thomas 1, Christine, Hugo (que je remercie toutes les fois où je venais maniper), Damien (et ses filtres auxquels je ne comprenais pas grand-chose), Ines, et Trung, qui ont vu la création des soirées resto découverte. Un grand merci aussi à Gaëlle, ma dealeuse officielle de molécules.

Je remercie toutes les personnes avec qui j'ai collaboré en dehors de mes laboratoires de rattachement, et tout particulièrement l'équipe de l'Institut Lavoisier de Versailles (ILV) composée de Muriel Bouttemy, Pia Dally, et Mirella Al Katrib, pour l'ensemble des résultats XPS qui se sont révélés très précieux pour cette thèse, et avec qui j'ai beaucoup apprécié échanger.

Du côté de l'IPVF, la synthèse et la caractérisation d'échantillons reposait sur le bon fonctionnement des labos, assurés par les chefs de pôle Julie, Frédérique, Nicolas L. et Nicolas V. Je remercie également tous les responsables d'équipements et de postes clés, tels que Régis aux simulateurs solaires, Sam puis Valérie à l'évaporateur, l'équipe ALD, Stéphanie et Marion pour les stocks d'échantillons, ou encore Sophie G., toujours prête à aider n'importe qui. Merci également à Thomas G. pour les modules, Karim pour l'encapsulation et le vieillissement d'échantillons, ainsi qu'à Alexandre B. le photographe officiel MEB et AFM du labo. Merci aussi à la légende Armelle, qui m'a appris (presque) tout ce que je sais et qui me pardonnait même quand je lui piquais ses affaires dans son dos. Merci à mes voisins de bureau : Daniel et sa bonne humeur (et son code pour la biblio LaTeX), Jorge et sa nostalgie touchante de l'IRDEP, Aleksandra et sa gentillesse. Merci et bon courage aux docteurs et doctorants qui participent toujours à la vie de l'IPVF : Javide, Marie, Alexandre Py, Jean C. (il craquera sur la thèse un jour), Nao, Vincent, Célia, Arthur, Thomas V., et Lauriane. Merci aussi à tous ceux avec qui j'ai pu aller partager des sessions d'escalade à Arkose : Anatole (SIUUUUU !), Olivier (M. Technique et gaufrier en chef), "Aaaaaaarpit Mishra", Alexandre Py (le gecko), Géraud, Alexandre C., Marie, et Arthur. Un grand merci et salutations aux gentils anciens qui m'ont aussi bien inspiré dans la rédaction de ce manuscrit : Salim (le parisien originel), Emilie (la reine des meringues), Olivier et son style vestimentaire controversé, Anatole et son "Chapitre 5", et Margot, autoproclamée "personne la plus importante dans l'aboutissement de cette thèse". Enfin, je remercie sincèrement "le S", dite "Alice", pour cette dernière année. Merci pour ton humour incroyable et ta patience légendaire. Merci de m'avoir supporté pendant la rédaction, et merci pour tous les autres (meilleurs) moments passés ensemble.

Comme il est admis de garder le meilleur pour la fin, je remercie profondément mes amis et mes proches. En particulier, je remercie du fond du cœur ma famille pour tout ce qu'ils ont fait pour moi et de m'avoir toujours supporté, me permettant d'être la personne que je suis aujourd'hui. Je vous suis infiniment reconnaissant de m'avoir donné l'occasion de faire les études qui m'ont amené à écrire ces remerciements, et j'espère pouvoir un jour vous rendre tout ce que vous m'avez apporté.

Enfin, je vous remercie, vous qui lirez ce manuscrit, en espérant qu'il vous plaira !

Résumé en français

Cette thèse est le fruit d'une collaboration entre le groupe de recherche dirigé par E. Deleporte au laboratoire LuMIn, qui étudie les propriétés optiques des pérovskites 2D, et le programme de l'IPVF spécialisé dans les cellules solaires tandem pérovskite-silicium.

Les cellules solaires à base de pérovskite ont atteint en seulement une décennie des rendements similaires à la technologie silicium. Cependant, plusieurs défis doivent être résolus pour que les pérovskites puissent intégrer le marché photovoltaïque, dont une amélioration de la stabilité des dispositifs. A cet égard, les hétérostructures de pérovskites 2D/3D, combinant les pérovskites 2D et 3D afin d'allier la meilleure stabilité des pérovskites 2D aux rendements élevés des pérovskites 3D, se sont distinguées.

L'objectif de ce travail était l'étude des hétérostructures 2D/3D, afin de les intégrer dans des cellules solaires à base de pérovskite. Dans ce but, une structure 2D/3D en traitement de surface, la plus prometteuse dans la littérature, a été choisie, en combinaison avec l'iodure de phenylethylammonium fluoré (4-FPEAI) comme cation espaceur. Cette thèse s'est attelée à caractériser l'effet de la structure 2D/3D sur l'efficacité et la stabilité de cellules solaires, ainsi que sur les propriétés du matériau pérovskite. Pour cela, différentes techniques ont été utilisées, telles que la photoluminescence, la diffraction des rayons X, ou encore la spectrométrie photoélectronique X

La formation d'une couche de pérovskite 2D de seulement quelques nanomètres d'épaisseur sur la pérovskite 3D via une réaction du cation espaceur avec l'excès d'iodure plomb présent dans la pérovskite 3D a été établie. La concentration de la solution du précurseur 4-FPEAI s'est révélée cruciale pour modifier l'épaisseur de la couche 2D formée. Le traitement au 4-FPEAI a significativement amélioré la stabilité des dispositifs, tout en améliorant leur efficacité, permettant l'obtention d'une efficacité prometteuse de 20,48% sur des cellules de taille standard (0,09 cm^2). Des dispositifs de 4 cm^2 ont également été réalisés, et ont atteint une excellente efficacité proche de 18%, confirmant la pertinence des hétérostructures 2D/3D dans les cellules solaires.

En raison d'un décalage vers le bleu des propriétés optiques de la couche 2D, la présence de brome dans celle-ci a été révélée. Le mécanisme de formation le plus commun ne pouvant pas expliquer la présence de brome au sein du matériau 2D, l'hypothèse que le 4-FPEAI réagit avec la pérovskite 3D et substitue ses cations du site A pour former une couche 2D contenant du brome a été émise. Ainsi, une compréhension plus approfondie des mécanismes de formation des hétérostructures 2D/3D a été apportée, et deux mécanismes se produiraient simultanément pour former la couche 2D.

Ces connaissances ont été utilisées pour étudier la formation d'une structure 2D/3D via un autre cation espaceur, le n-octylammonium (OAI). Cette étude a révélé que les cellules solaires utilisant l'OAI avaient des propriétés similaires à celles utilisant du 4-FPEAI, bien que la couche 2D formée soit constituée de phases différentes. Malgré la détection de brome dans ces phases, une étude plus approfondie est nécessaire afin de confirmer les mécanismes impliqués pour ce cation espaceur.

Table of Contents

Acronyms and Symbols

4-FPEAI para-fluorophenylethylammonium iodide.

AFM Atomic Force Microscopy.

ALD Atomic Layer Deposition.

CB Conduction Band.

DMF N,N-Dimethylformamide.

DMSO Dimethylsulfoxide.

$\mathbf{E}_b$ Binding Energy.

$\mathbf{E}_g$ Bangap Energy.

EQE External Quantum Efficiency.

ETL Electron Transport Layer.

$\mathbf{FA}^+$ Formamidinium.

FAPI Formamidinium Lead Iodide.

FF Fill Factor.

FTO Fluorine-doped Tin Oxide.

FW Forward.

GIXRD Grazing-Incidence X-Ray Diffraction.

HTL Hole Transport Layer.

$\mathbf{I}_{SC}$ Short-Circuit Current.

IPA Isopropanol.

IV Current-Voltage.

$\mathbf{J}_{SC}$ Short-Circuit Current Density.

$\mathbf{MA}^+$ Methylammonium.

MAPI Methylammonium Lead Iodide.

MPPT Maximum Power Point Tracking.

n-OAI n-octylammonium iodide.

PCE Power Conversion Efficiency.

PEAI Phenylethylammonium iodide.

PL Photoluminescence.

PSC Perovskite Solar Cell.

PTAA poly[bis(4-phenyl)(2,4,6-trimethylphenyl)amine].

PV Photovoltaic.

RP Ruddlesden-Popper.

RV Reverse.

$\mathbf{S}_a$ Arithmetic Mean.

$\mathbf{S}_q$ Root Mean Square.

SEM Scanning Electron Microscopy.

$\mathbf{V}_{OC}$ Open-Circuit Voltage.

VB Valence Band.

XPS X-Ray Photoelectron Spectroscopy.

XRD X-Ray Diffraction.

List of Figures

List of Tables

Introduction

Over the last few decades, the perception of human society impact on the environment and climate change has evolved drastically. After being raised for the first time in 1972 by the Club of Rome in the report "The Limits to Growth" [Meadows *et al.* 1972], a growing number of links have been established between human activity and climate change. Nowadays, human activity is almost universally recognized within the scientific community [Lynas *et al.* 2021], and the subject of climate change has become a major societal and political concern.

One major highlight of this evolution was set in 2015 by the adoption of the Paris Agreement. With this agreement, most countries are committed to "substantially reduce global greenhouse gas emissions to limit the global temperature increase in this century to 2°C, while pursuing efforts to limit the increase even further to 1.5°C" in comparison with pre-industrial levels. In 2018, the Intergovernmental Panel on Climate Change (IPCC) released a special report titled "Global Warming of 1.5°C", focusing on several key points related to the Paris Agreement, such as predicting the consequences of 1.5 and 2°C global warming. This report estimated that global CO_2 emissions should decline by 45% in 2030 (in comparison with 2010 levels) and reach net zero around 2050 to limit global warming to less than 1.5°C. To limit global warming below 2°C, a decrease of 25% of emissions by 2030 was predicted, and a net zero reached around 2070 [IPCC 2018].

In this regard, the energy sector plays the leading role. In fact, since the beginning of the industrial era, energy has become essential to almost every sector of our society, from industry to transport, and energy consumption has been continuously increasing, to reach 606 EJ (10^{18} J) in 2019, as illustrated in Figure 1.

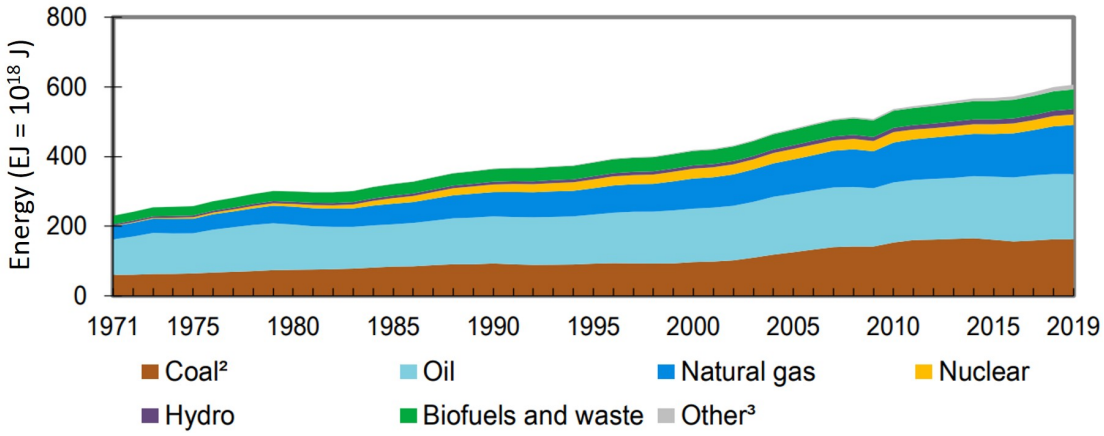

Figure 1: World total energy supply by source. Reproduced from [IEA 2021b]

Until now, this growth was allowed by the ever-increasing use of fossil fuels (oil, coal, and gas), which accounted in 2019 for more than 80% of the total energy supply (see Figure 2a). Fossil fuels are responsible for most of worldwide greenhouse gas emissions. As a result, these emissions have been in constant growth, and each new year comes with a new record, except for 2020, due to the COVID-19 pandemic. In 2021, the emissions reached 36.3 Gt of CO_2e, as seen in Figure 2b.

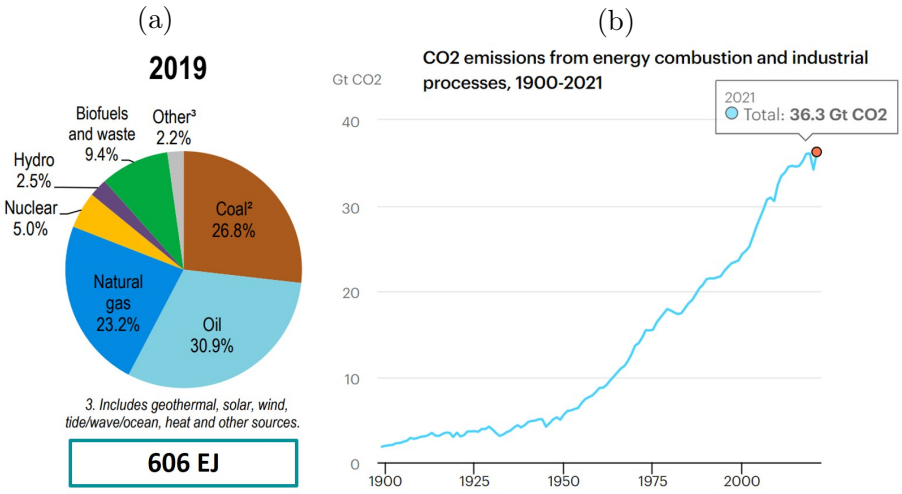

Figure 2: (a) Share of world total energy supply by sources. Reproduced from [IEA 2021b]. (b) Evolution of global CO_2e emissions. Reproduced from [IEA 2021a].

Thus, reaching the Paris Agreement objectives requires an extensive overhaul of our society and its energy model. In 2021, the International Energy Agency (IEA) published a roadmap for the global energy sector to match net zero emissions by 2050 [IEA 2021c], which was further developed in 2022 [IEA 2022b]. In this plan, final energy consumption drops from 435 to 340 EJ, and the energy sector undergoes massive electrification, with the share of electricity in this final energy rising from 20% in 2020 to 50% in 2050. Figure 3 shows that wind and solar photovoltaic (PV) power mainly ensures this electricity production.

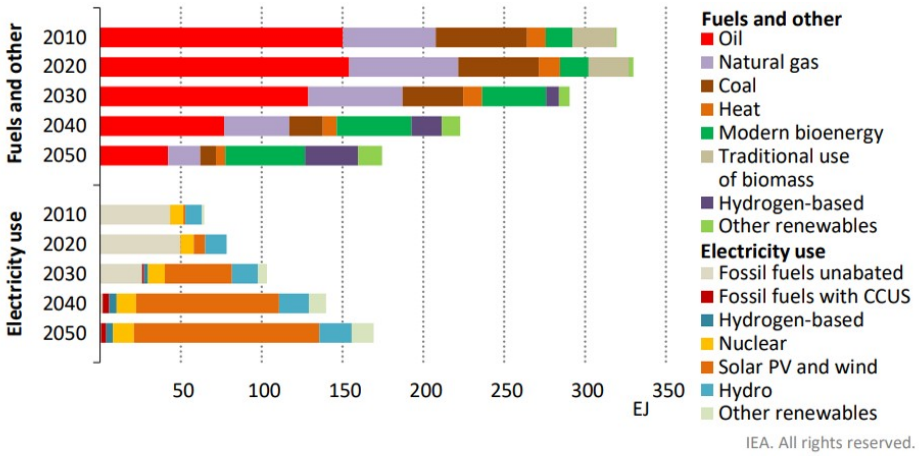

Figure 3: Global total final consumption by fuel in the net zero emission scenario. Reproduced from [IEA 2021c].

In a net zero scenario, solar PV is an interesting energy source. This technology directly converts sunlight into electricity, leading to a much lower carbon footprint than fossil fuels. In 2021, the National Renewable Energy Laboratory (NREL) estimated the emissions of greenhouse gas per kWh of produced electricity at 43 gCO_2e/kWh for solar PV, versus 486 gCO_2e/kWh for natural gas and 1001 gCO_2e/kWh for coal [NREL 2021]. Thus, its interest becomes obvious to limit the greenhouse gas emissions of electricity production.

Economic competitiveness is also essential to consider any energy production system as relevant. Silicon solar cells currently dominate the solar PV market, with more than 95% of the 2021 electricity production ensured by this technology. As a result, it has reached a high level of maturity, and the production cost of solar PV electricity has dropped drastically over the last decades. From 1976 to 2021, the price of solar PV electricity went down by 24.1% each time its cumulative capacity doubled, which is called the learning rate and is illustrated in Figure 4a [VDMA 2022]. Many factors can explain this decrease, such as the silicon-wafer industry's development reducing the cost of PV module manufacturing, scale economic factors decreasing the cost of hardware and inverters, and the increase of module efficiency. With the boom in global installed capacity during the 2010s that saw the installed capacity increase from less than 50 GW to more than 1 TW in 2022 [BP 2022] (see Figure 4b), the cost of solar PV electricity was almost divided by 10 in only a decade.

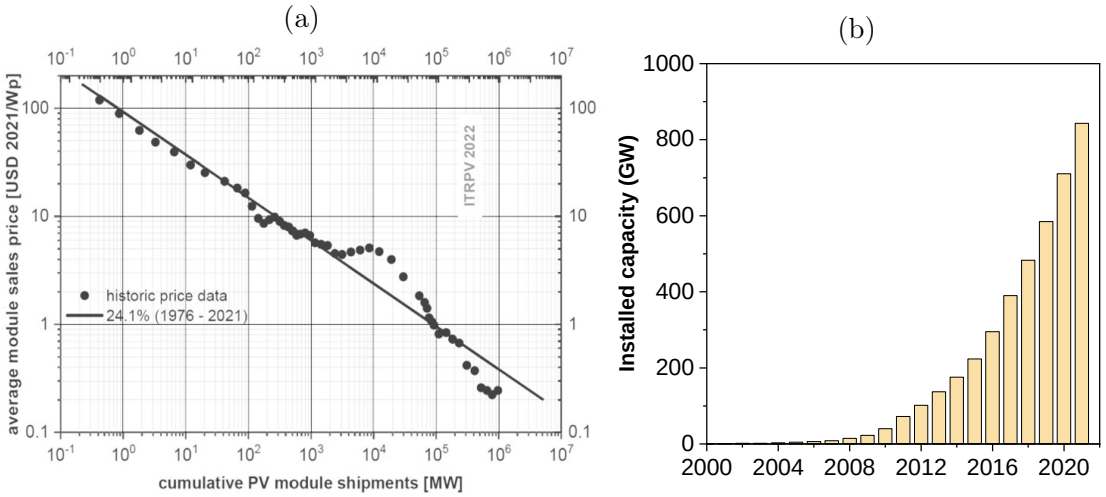

Figure 4: (a) Learning curve of the module spot market prices as a function of the cumulative PV module shipments. Reproduced from [VDMA 2022]. (b) Global cumulative capacity of solar PV from 2000 to 2021. Reproduced from [BP 2022].

Hence, the levelized cost of electricity (LCOE), which corresponds to the cost of one kWh of electricity produced by a system over its entire lifetime (including manufacturing, operation, and disposal) of solar PV has become very competitive. As of 2021, the LCOE of large-scale PV installations was estimated as lower than most energy sources in Germany, including fossil fuels, as shown in Figure 5 [Kost *et al.* 2021].

Increasing the efficiency of solar modules, and so the power output per surface unit, also reduces the cost of solar PV electricity. However, the current technology of solar modules, based on single-junction silicon cells, is limited to a theoretical maximum efficiency of 29.4% [Richter *et al.* 2013]. In this regard, the development of tandem technology, made of two solar cells stacked on top of each other to capture solar radiation

more efficiently, is a promising path. Such technology benefits from the use of silicon cells as the bottom-cell and has a higher theoretical efficiency of 47% [Wali *et al.* 2018].

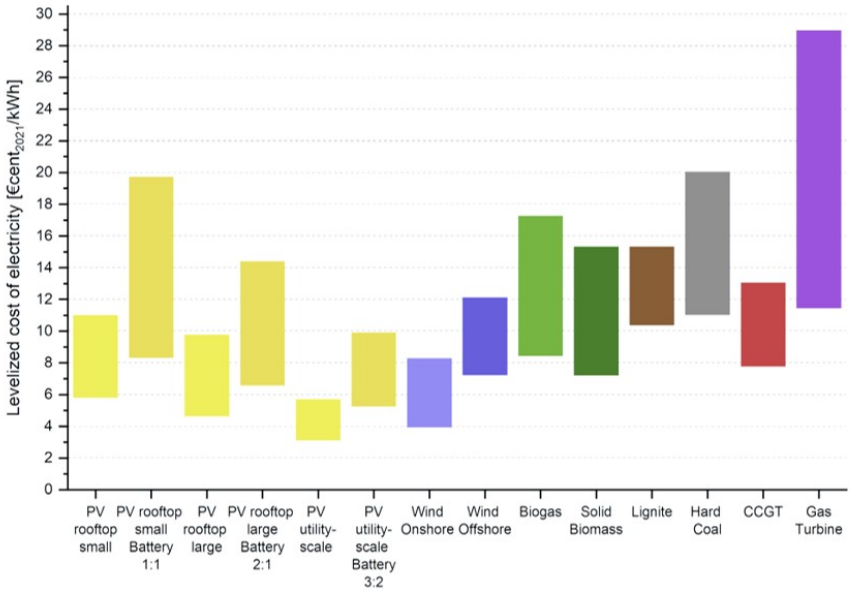

Figure 5: LCOE of renewable energy technologies and conventional power plants in Germany in 2021. (*the ratio for PV battery systems expresses PV power output (kWp) over usable battery capacity (kWh)).* Reproduced from [IEA 2021c].

The most promising top-cell technology is perovskite solar cells, based on 3D perovskites, a class of materials with ABX_3 structure. These materials possess many favorable properties for solar cells. They have a direct band gap that can be tuned by changing the elements in A, B, or X-sites, allowing their use in single-junction and tandem cells. They also have a high absorption coefficient, good diffusion lengths, and are defect tolerant. Therefore, they are used in thin films and can be synthesized with many different techniques, from low-temperature solution processing to vapor deposition. As a result, they experienced rapid development, with lab-scale device efficiency rising from 3.8% in 2009 [Kojima *et al.* 2009] to 25.7% in 2022 [Green *et al.* 2022].

Several challenges must be tackled to bring perovskite technology to the photovoltaic market. Among them, improving the stability of perovskite solar cells is crucial. For this purpose, layered 2D perovskites stood out thanks to better intrinsic and extrinsic stability than their 3D counterpart. Their main application involves coupling them with 3D perovskites to form 2D/3D perovskite heterostructures. These structures are expected to combine the better stability of 2D perovskites with the good efficiency of 3D perovskites to create a stable and efficient material. This thesis focuses on synthesizing and characterizing such 2D/3D structures, aiming to integrate them in solar cell devices. It is a joint work between the *Laboratoire Lumière, Matière, et Interfaces* (LuMIn, Université Paris-Saclay, France) and the *Institut Photovoltaïque d'Ile-de-France* (IPVF, France). The current manuscript presenting this work is divided into five main chapters:

- The background of this dissertation is set in Chapter 1. It introduces the working principle of solar cells and focuses on the state of the art of perovskite solar cell technology. The properties of 2D perovskites are detailed, and their application in 2D/3D perovskite heterostructures is presented to contextualize this work.

- Chapter 2 describes the fabrication of perovskite solar cells, synthesizing each layer constituting these devices. Particular attention is given to integrating 2D/3D perovskite materials in this fabrication process. All the techniques applied to characterize the materials and devices developed in this work are also presented.

- Understanding the 2D/3D structure is the main objective of Chapter 3. Through the modification of two main synthesis parameters (the concentration of the 2D perovskite solution and the static deposition of this solution), the characteristics of the 2D/3D material are investigated. The benefits obtained from its application in solar cell devices are also evaluated.

- Chapter 4 focuses on the formation mechanisms behind 2D/3D perovskites. It reveals the unexpected chemical composition of the 2D phase. This finding is used to propose a second mechanism to the one commonly accepted in the literature for the formation of the 2D material, providing a better understanding of the synthesis of 3D/2D structures.

- Chapter 5 explores the formation of a 2D/3D structure with a new spacer cation. It reveals the formation of different phases induced by this new treatment. It also suggests that these phases do not impact significantly the properties of the perovskite material and the resulting solar cell devices.

Chapter 1

Context and state of the art

This first chapter introduces the general background behind this thesis work. This introduction starts with solar cells, and how they convert sunlight into electricity. Then, we present hybrid halide perovskites, their application in solar cells, and the challenges required for this technology's future development. One of these challenges is the stability of perovskite solar cells, which leads us to deal with 2D hybrid halide perovskites and their unique properties. Finally, we describe how 2D and 3D perovskites were combined into 2D/3D heterostructures to improve perovskite solar cells.

Contents

1.1 General background of solar cells

The whole purpose of this work relies on the photovoltaic effect, which was discovered by E. Becquerel in 1839 when he observed the production of an electric current between two metal plates immersed in a solution and exposed asymmetrically to solar radiations [Becquerel 1839]. This discovery led to the creation of the photovoltaic (PV) technology. After more than a century of development, it generated more than 1000 TWh of electricity in 2021, around 3% of the global electricity production [IEA 2022a]. Here, we start by presenting the theoretical background behind the production of PV solar energy.

1.1.1 From the Sun to electrons

Solar irradiance

Explaining the physics behind solar cells requires to look at the Sun (metaphorically), a star that emits light continuously. From a thermodynamic point of view, it is approximated as a black body with a temperature T = 5800 K. Therefore, the spectral density of its radiation can be calculated using Planck's law:

$$B(\lambda, T) = \frac{2hc^2}{\lambda^5} \frac{1}{exp\left(\frac{hc}{\lambda k_B T}\right) - 1} \tag{1.1}$$

where B(λ, T) is the black body spectral radiance with wavelength dependency in W.m^{-2}.nm^{-1}.sr^{-1}, λ is the radiation wavelength, T the black body's temperature, h the Planck constant, c the speed of light in vacuum, and k$_B$ the Boltzmann constant. Approximating the black body as a Lambertian emitter allows the estimation of the total black body irradiance received outside of Earth atmosphere with the following equation:

$$I_0(\lambda, T) = \pi . \left(\frac{r_{Sun}}{d_{S-E}} \right)^2 . B(\lambda, T) \tag{1.2}$$

where I$_0$(λ, T) is the black body irradiance spectrum received outside of the atmosphere, r$_{Sun}$ is the radius of the Sun, and d$_{S-E}$ is the Sun-Earth distance. Figure 1.1 shows that this theoretical spectrum is close to the reference solar irradiance spectrum outside the atmosphere, called AM0.

AM stands for Air-Mass and indicates the optical path of solar radiation through Earth's atmosphere, which acts as a filter for sunlight. For example, a zenithal illumination corresponds to AM1.0, while AM2.0 is an illumination with a Sun angle to the zenith z = 60°. AM0 is a special case, representing the solar spectrum outside the atmosphere.

In the PV industry, the performance of every device is assessed under the standard illumination spectrum AM1.5G (considering direct and diffuse sunlight, G stands for Global), illustrated in Figure 1.1. AM1.5G is the average illumination in middle latitudes with a Sun position of z = 48.2°. It has a reference irradiance of 1000 W.m^{-2} while AM0 spectrum has a total irradiance of around 1366 W.m^{-2}, revealing the amount of sunlight that is filtered by the atmosphere.

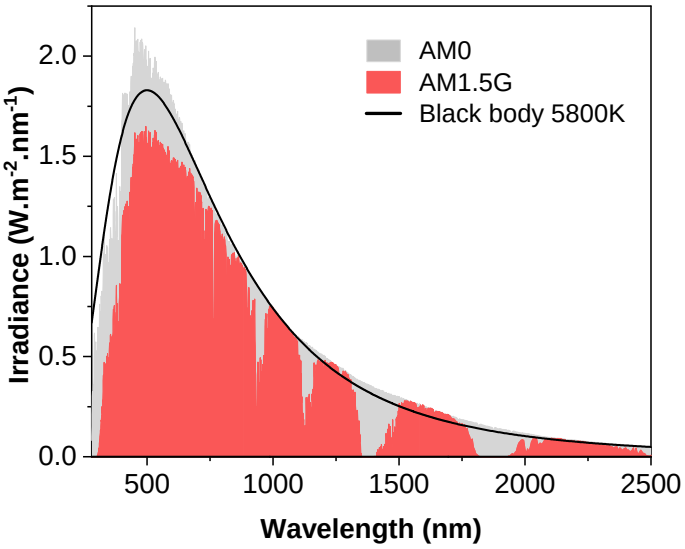

Figure 1.1: Extraterrestrial 5800K back body irradiance spectrum, compared to AM0 and standard AM1.5G solar irradiance spectra references [NREL].

Semiconductors and electron-hole pair

Solar cells use semiconductor materials to convert solar radiation into electricity. Due to their electronic band structure, semiconductors have an intermediate electrical conductivity between a conductor and an insulator, which increases along with temperature.

Bringing several atoms together leads to hybridizing their discrete energy orbitals, which start to overlap. In a macroscopic crystal, the number of atoms is so important that the combination of their energy levels provides a band structure, with allowed and forbidden bands [Ashcroft and Mermin 1976]. The distribution of electrons in a semiconductor for a specific temperature T follows the latter Fermi-Dirac distribution:

$$f_e(E_e) = \frac{1}{exp\left(\frac{E_e - E_F}{k_B T}\right) + 1} \tag{1.3}$$

where $f_e(E_e)$ is the probability of an energy level E_e to be occupied by an electron, and E_F is the chemical potential. In a semiconductor, at T = 0 K, the chemical potential, named the Fermi level, is located between two energy bands. Therefore, at a temperature T = 0 K, all bands below the Fermi level are fully occupied by electrons. The occupied band with the highest energy is called the valence band (VB), and the unoccupied band with the lowest energy is called the conduction band (CB). The energy difference between the CB minimum, designated as E_C, and the VB maximum, designated as E_V, is called the bandgap energy (E_g) and is a paramount property of a semiconductor. Figure 1.2a illustrates this electronic band structure.

Providing energy to the semiconductor with a photon of energy $h\nu$ higher than its bandgap leads to the photon absorption by the semiconductor. The photon's energy is transmitted to an electron in the valence band, which gets promoted to an available free energy level in the conduction band, leaving an electron absence in the valence band assimilated to a quasi-particle named hole. The combination of electron and hole is called an electron-hole pair. Electrons and holes are designated as charge carriers, as they can both move within the material and are electrically charged (elementary negative charge -q for electrons and positive charge +q for holes).

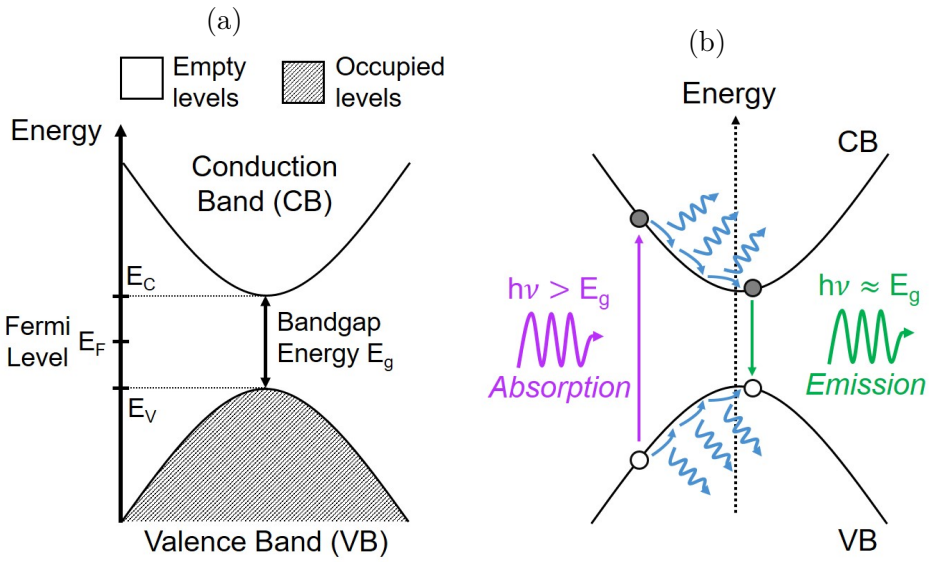

Figure 1.2: (a) Representation of a semiconductor band structure. (b) Electron-hole pair creation in a semiconductor by electron excitation through absorption of a photon $E > E_g$, electron relaxation through emission of phonons, and electron-hole recombination with photon $E \approx E_g$ emission.

Rapidly after being generated (in the order of picoseconds), the electron-hole pair loses its energy by emitting phonons (vibration modes within the material's lattice). The electron will go back to the bottom of the conduction band. In contrast, the hole will go at the top of the valence band. Then, only a few nanoseconds after the electron-hole pair was generated, the electron recombines with the hole in the valence band by emitting a photon close to the semiconductor bandgap. This phenomenon, called photoluminescence, is illustrated in Figure 1.2b, and Section 2.2.2 will present how it was used in this work. Therefore, to generate electricity from this semiconductor, the role of the solar cell is to separate the electron-hole pair.

1.1.2 Homojunction and solar cell characteristics

p-n junction in first generation solar cells

In solar cells, p-n junctions are commonly used to separate electron-hole pairs. Introducing a controlled amount of impurities into a semiconductor material is called doping. With n-type doping, electron donor impurities bring electrons to the conduction band and become majority carriers, while holes become minority carriers. With p-type doping, electron acceptor impurities bring holes to the valence band, which become majority carriers, while electrons become minority carriers. A p-n junction is an heterostructure made with a p-doped and an n-doped semiconductors, separated by an interface. The first generation and most mature solar cell technology is silicon p-n homojunction, which uses p-type and n-type layers of the same semiconductor material: silicon.

In the p-n junction, electrons from the n-type region diffuse to the p-type, and holes diffuse from the p-type to the n-type region. By diffusing, electrons leave positively charged donor ions on the n-type side, while holes leave negatively charged acceptor atoms on the p-type side. These ions are embedded into the crystal structure and cannot

move. Hence, close to the interface, the n-type region becomes positively charged, and the p-type region gets negatively charged, forming an electric field between them. This field drifts holes to the p-type region and electrons to the n-type region, resulting in a region without charge carriers called the depletion region (see Figure 1.3a).

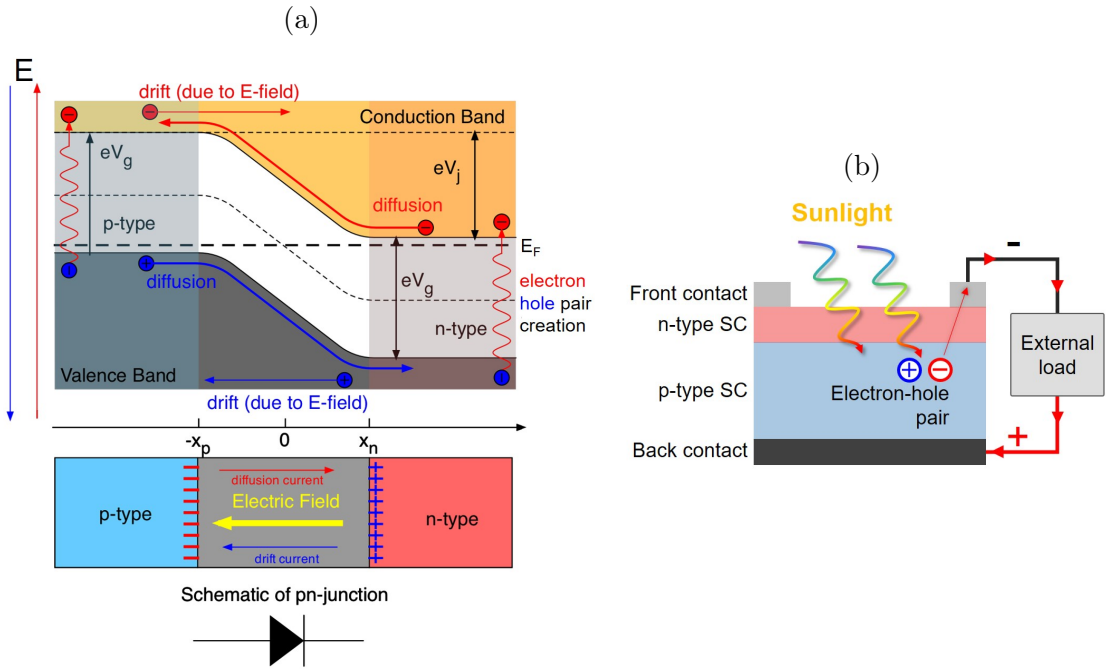

Figure 1.3: (a) Diagram of a p-n junction with charge carriers currents. Reproduced from [Boeglin 2022]. (b) Solar cell operation with charge carriers movement.

Adding electrical contacts to the p-n junction completes the solar cell. Once exposed to light, electron-hole pairs are created. The ones generated near the depletion region are separated and sent to the electrodes by the junction's electric field. There, the current of photo-generated charges (i.e., photocurrent) can be sent in a circuit to supply electric systems before returning to the solar cell, as pictured in Figure 1.3b. The cell's electrical power output depends on the number of collected charge carriers (current) and how much energy they carry (voltage).

Solar cell characteristics

From an electric device point of view, without illumination, the behavior of a solar cell is comparable to a diode, while under illumination, it also generates a photocurrent. This current generation comes with electrical losses, represented as resistances. Hence, the electrical behavior of a solar cell can be assimilated to the one-diode equivalent circuit shown in Figure 1.4a. The relation between the output current of the cell and its corresponding voltage, or IV characteristics, can be fitted by the following equation (expressed with the generator convention):

$$I(V) = I_{ph} - I_0 \left[exp\left(\frac{q(V + IR_s)}{nk_BT} \right) - 1 \right] - \frac{V + IR_s}{R_p} \tag{1.4}$$

where I_{ph} is the photocurrent, I_0 the saturation current, q the elementary charge, n the ideality factor (usually between 1 and 2), R_s the series resistance (related to the electrodes' resistance, the resistance of the contact absorber/electrodes, and to the conductivity of the absorber), and R_{sh} the shunt (or parallel) resistance (related to leakage currents and defects in the absorber layer). R_s has to be minimized for efficient devices, while R_{sh} has to be maximized.

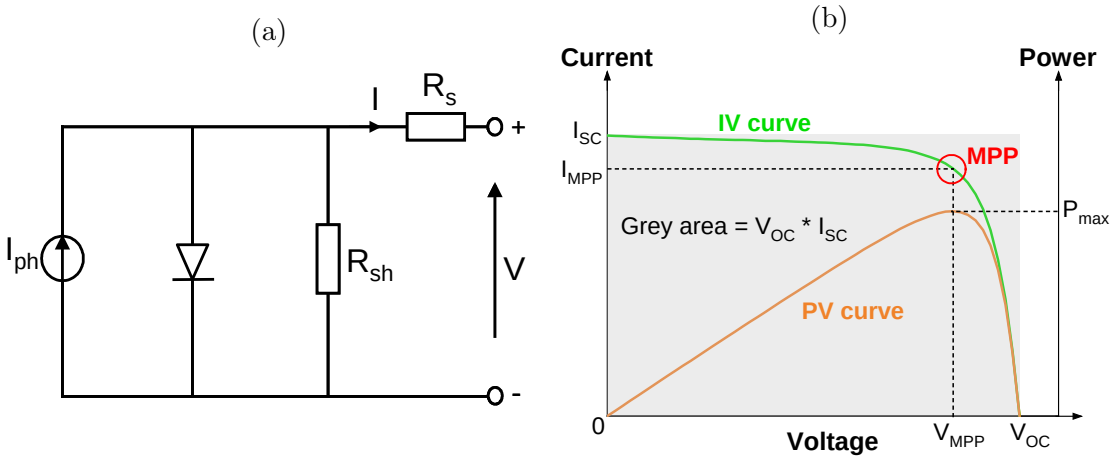

Figure 1.4: (a) One-diode model equivalent circuit of a solar cell. (b) Current-voltage (IV) characteristic of a solar cell.

From the IV characteristic of a solar cell visible in Figure 1.4b, its characteristic photovoltaic parameters can be extracted, such as its maximum power point (which corresponds to the maximum power output P_{MPP} of the cell, associated to a voltage V_{MPP} and a current I_{MPP}), its open-circuit voltage (V_{OC}, for which I = 0), its short-circuit current (I_{SC}, for which V = 0), and its Fill Factor (FF), defined as the ratio from the measured IV curve of the cell to its ideal one, and calculated as:

$$FF = \frac{P_{MPP}}{V_{OC} * I_{SC}} \tag{1.5}$$

Finally, power conversion efficiency (PCE) is the most important characteristic of a solar cell and quantifies how much of the incident radiation P_{inc} is converted into electricity, calculated as:

$$PCE = \frac{P_{MPP}}{P_{inc}} = \frac{FF * V_{OC} * I_{SC}}{P_{inc}} \tag{1.6}$$

1.1.3 Tandem solar cells

Limits of single-junction cells

Improving PCE is central to reduce the cost of PV electricity production and increase its attractiveness. However, the PCE of single-junction solar cells, using only one absorber

material, cannot exceed the Shockley-Queisser (SQ) theoretical limit of 33% established in 1961 by W. Shockley and H. J. Queisser [Shockley and Queisser 1961]. This limit is caused by several phenomena, illustrated in Figure 1.5, such as photons not absorbed due to energy below the absorber's bandgap or thermalization losses due to charge carriers relaxation to the bandgap edges (see [Hirst and Ekins-Daukes 2011] for details).

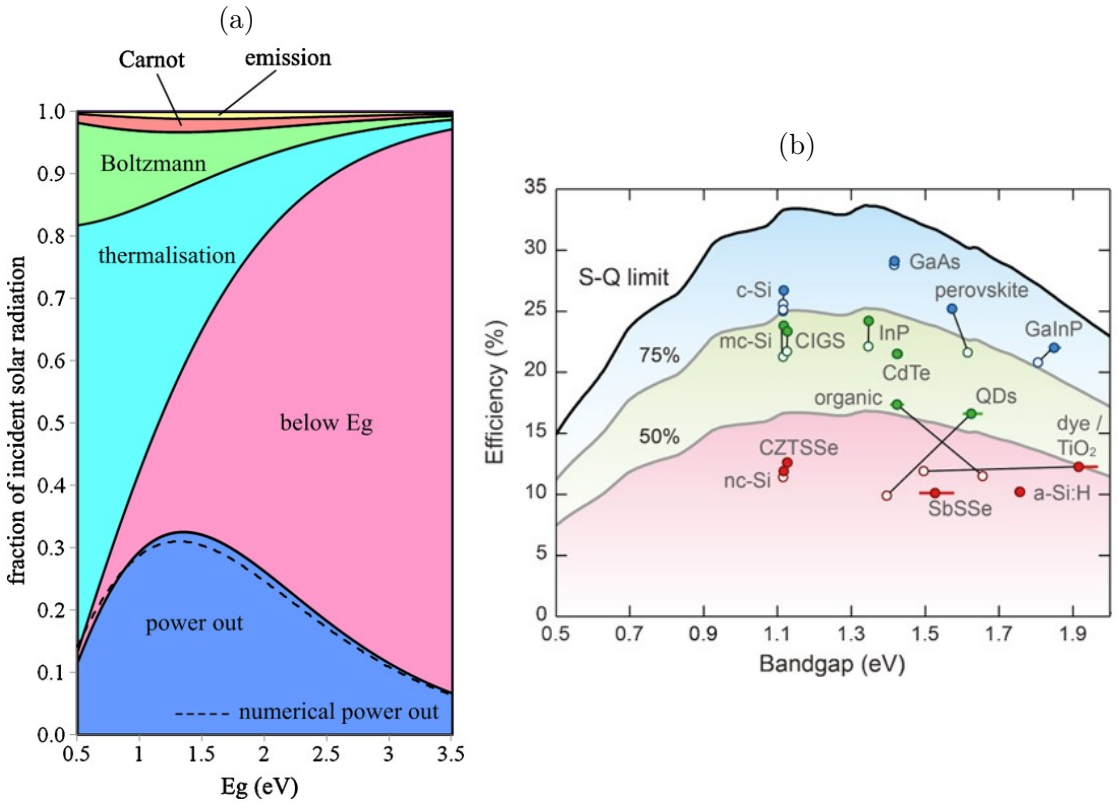

Figure 1.5: (a) SQ limit and intrinsic losses in solar cells regarding their bandgap. Reproduced from [Hirst and Ekins-Daukes 2011]. (b) Record PCE of solar cell technologies compared to the SQ limit for corresponding bandgaps (*open symbol: 2016 records, solid symbol: 2020 records*). Reproduced from [Ehrler *et al.* 2020].

Hence, the PCE of single junction solar cells is limited and cannot be optimized up to 100%. The most efficient PV technologies are already close to the SQ limit, as illustrated in Figure 1.5b. Furthermore, other theoretical and practical constraints hinder the maximum potential efficiency of solar cells. As an example, the theoretical SQ limit of the mature silicon technology was reduced from 32% to 29.4% by more recent calculations (taking into accounts intrinsic recombination effects), and other works estimated a maximum practical efficiency of 27.1%, very close to the 26.7% current record [Richter *et al.* 2013, Yoshikawa *et al.* 2017].

One is not enough? Add more!

Among existing techniques to overcome the SQ limit (hot-carriers [Ross and Nozik 1982], down or up-conversion [Klampaftis *et al.* 2009, Boriskina and Chen 2014]), multi-junction solar cells are a promising solution. A multi-junction solar cell combines multiple absorbers of different bandgaps, each one optimized for a specific part of the solar spectrum.

The theoretical limit of multi-junction solar cells increases with the number of junctions, up to 68% with an infinite number of junctions (under 1-sun) [Vos 1980, Meillaud *et al.* 2006]. However, multi-junction cells with numerous junctions are expensive and more suited for specific purposes, such as spatial applications [Geisz *et al.* 2020].

For large-scale development, the focus is on cheaper two-junction cells, named tandem cells, using a high bandgap top-cell to absorb short wavelengths and a low bandgap bottom-cell for higher wavelengths. Silicon technology is the ideal bottom-cell candidate, with a low 1.1 eV bandgap and important technological maturity. The emerging perovskite technology has proven to be a promising top-cell thanks to a highly tunable bandgap combined with easy and low-cost manufacturing. With a theoretical efficiency limit close to 45.7% while current PCE records have already bypassed the 30% threshold, perovskite/silicon tandems attract significant attention and have much room for development [Wali *et al.* 2018, Akhil *et al.* 2021, Cheng and Ding 2021].

The main architectures are four-terminal (4T) and two-terminal (2T), schematized in Figure 1.6a. 4T consists of autonomous top and bottom cells, fabricated independently and interconnected externally, for a total PCE equal to the PCE sum of each sub-cell. This simple structure comes with higher processing costs due to the duplication of all electrical connections, which can be mitigated with voltage-matched configuration, where both sub-cells are connected in parallel. Reducing absorption losses from the intermediate transparent electrodes is also necessary for optimal performances of a 4T cell. In 2T tandems, top and bottom cells are connected in series via a recombination layer. Only two electrodes are required, resulting in lower costs. This structure has drawbacks, as the top-cell deposition process must not damage the bottom-cell, and the bottom-cell needs a suitable texture to grow a quality top-cell. Furthermore, the lowest current between the two sub-cells limits the total current due to their series connection, making this configuration more sensitive to bandgap optimization, as shown in Figure 1.6b.

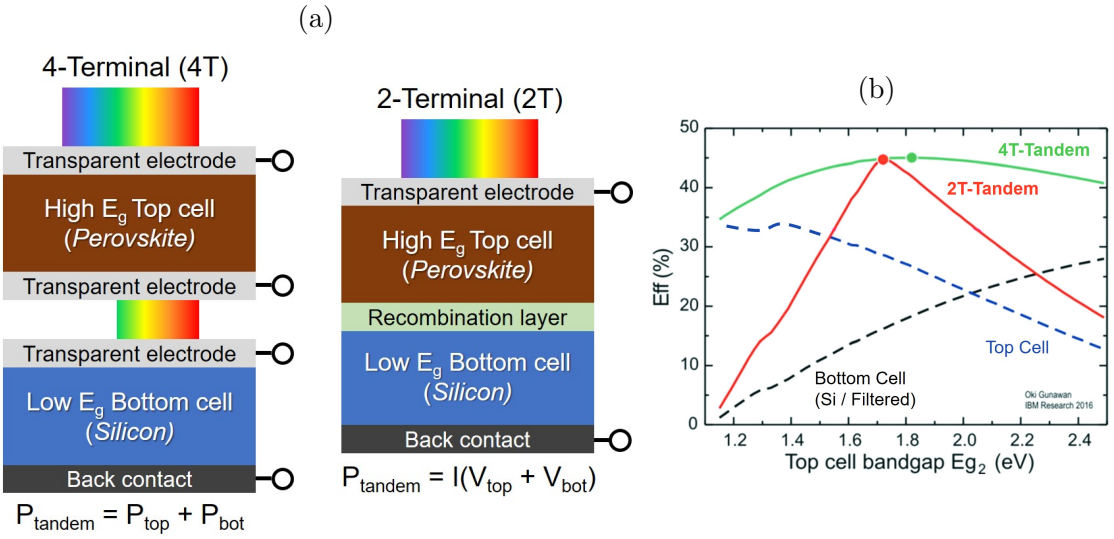

Figure 1.6: (a) 4T and 2T tandem solar cell architectures. Adapted from [Lal *et al.* 2017]. (b) Maximum theoretical efficiency of 4T and 2T tandem cells and their sub-cells regarding the top-cell bandgap E_{g2} (silicon 1.1 eV bottom-cell). Reproduced from [Todorov *et al.* 2016].

1.2 Perovskite solar cells

1.2.1 Hybrid halide perovskites

Structure

The term perovskite initially designated calcium titanate $CaTiO_3$, discovered in 1839 by G. Rose and named after the Russian mineralogist L. A. Perovski [Rose 1840]. Nowadays, this name describes every material with a similar ABX_3 crystal structure. Each A, B, and X-sites can be tuned with different elements, resulting in myriad combinations with specific properties and applications. Organic-inorganic hybrid halide perovskites (shortened as hybrid halide perovskites) are a specific class of ABX_3 perovskites. In this class, the A-site species is an organic monovalent cation, often methylammonium $CH_3NH_3^+$ (MA^+), or formamidinium $CH_2(NH_2)_2^+$ (FA^+), the B-site species is a divalent metallic cation, usually lead Pb^{2+}, or tin Sn^{2+}, and the X-site species is a monovalent halide anion, such as iodide I^-, bromide Br^-, or chloride Cl^-. The small inorganic cesium cation (Cs^+) is also common in A-site, forming an inorganic halide perovkite.

They ideally have a cubic Pm3m structure, illustrated in Figure 1.7a. The B-site cation is six times coordinated and surrounded by an octahedron with halide anions in its corners, forming BX_6 inorganic octahedra. Meanwhile, the A-site cation is twelve times coordinated and is located between BX_6 octahedra. The cohesion of the structure is held by ionic bonding, along with hydrogen bonding and van der Walls interactions to a lesser extent [Wang *et al.* 2013, Menéndez-Proupin *et al.* 2014, Egger *et al.* 2016]. The Goldschmidt tolerance factor (t), from V. Goldschmidt [Goldschmidt 1926], and the octahedral factor (μ), proposed by Li *et al.* [Li *et al.* 2004, Li *et al.* 2008], are tools to predict the stability of a perovskite structure, based on the following equations:

$$t = \frac{r_A + r_X}{\sqrt{2}(r_B + r_X)} \qquad \mu = \frac{r_B}{r_X} \tag{1.7}$$

where r_A, r_B, and r_X are the atomic radius of the A, B, and X-sites species. To obtain stable ABX_3 perovskite structures, $0.813 < t < 1.107$ and $0.442 < \mu < 0.895$ are required, and tolerance factors outside these limits lead to non-perovskite structures. Ideal t values in the 0.9 - 1.0 range form cubic structures [Kieslich *et al.* 2014, Kim *et al.* 2016, Sun and Yin 2017], while $t < 0.89$ and $t > 1.0$ lead to more distorted tetragonal, hexagonal, or orthorhombic structures, visible in Figures 1.7b, 1.7c, and 1.7d.

The structure of hybrid halide perovskites is not determined only by their composition. Most of them undergo phase transitions regarding their temperature, as illustrated in Figure 1.7e for the common $MAPbI_3$ and $FAPbI_3$ (or MAPI/FAPI) perovskites [Stoumpos *et al.* 2013, Kim *et al.* 2020a]. They are both found in stable cubic α-phase at high temperatures. Decreasing their temperature, MAPI transitions into a tetragonal β-phase, while FAPI does so into a hexagonal δ-phase. Another phase transition exist around cryogenic temperatures. FAPI stabilizes into the tetragonal β-phase and MAPI abandons it and forms an orthorhombic γ-phase. Even though cryogenic phases are not relevant for solar cell purposes, phase transitions remain a significant topic. For example, FAPI's stable phase at room temperature is the non photo-active δ-phase (δ-FAPI), while the α-phase (α-FAPI) has very interesting properties for PV, and several ways to stabilize it have been studied (see Section 1.2.2) [Ma *et al.* 2017].

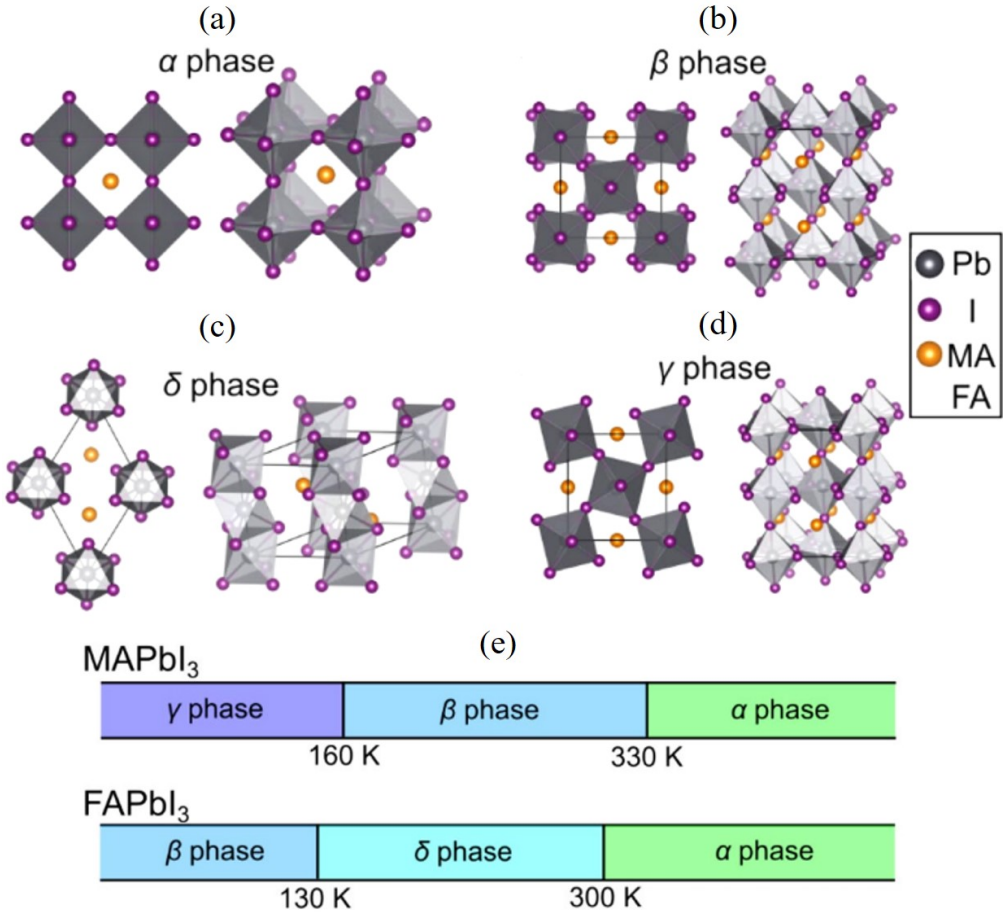

Figure 1.7: (a) Cubic α-phase, (b) tetragonal β-phase, (c) hexagonal δ-phase, and (d) orthorhombic γ-phase of MAPI and FAPI perovskites. (e) Temperature-related phase transitions of these perovskites. Reproduced from [Kim *et al.* 2020a].

Opto-electronic properties

The spectacular success of perovskites for solar cells is explained by their favorable opto-electronic properties, illustrated through the example of MAPI, the first composition used in a PV device. First, it has a direct bandgap around 1.55 eV [Lee *et al.* 2012, Motta *et al.* 2015], as shown in Figure 1.8a. This direct bandgap leads to an absorption coefficient close to 10^5 cm^{-1} over the visible part of the solar spectrum, the most important to absorb [De Wolf *et al.* 2014]. This absorption coefficient is between one and two orders of magnitude higher than silicon, which is an indirect bandgap semiconductor, as seen in Figure 1.8b. This allows the application of MAPI as thin films of only a few hundred nanometers thick. At the same time, typical commercial silicon solar cells use silicon layers with thicknesses of hundreds of micrometers [Andreani *et al.* 2019].

In addition, MAPI possesses very good charge transport properties. The diffusion lengths in the material have been estimated from 100 to 1000 nm [Stranks *et al.* 2013, Xing *et al.* 2013, Bercegol *et al.* 2018], with carrier lifetime close to 1 μs [Zhou *et al.* 2014, de Quilettes *et al.* 2015]. Such diffusion lengths are in the same order of magnitude as the thickness of the perovskite film itself. Hence, photogenerated carriers can be extracted without noticeable difficulty from the absorber, no matter where they were

generated in the layer. In ambient conditions, MAPI has low exciton binding energy (see Section 1.3.2), facilitating even further charge extraction from the material [Miyata *et al.* 2015, Baranowski and Plochocka 2020]. Hybrid halide perovskites also have high defect tolerance, allowing the use of solution-processing deposition techniques, while silicon used in PV requires solar grade purity (> 99.999%) to produce efficient devices [Yin *et al.* 2014, Kim *et al.* 2014, Gribov and Zinov'ev 2003].

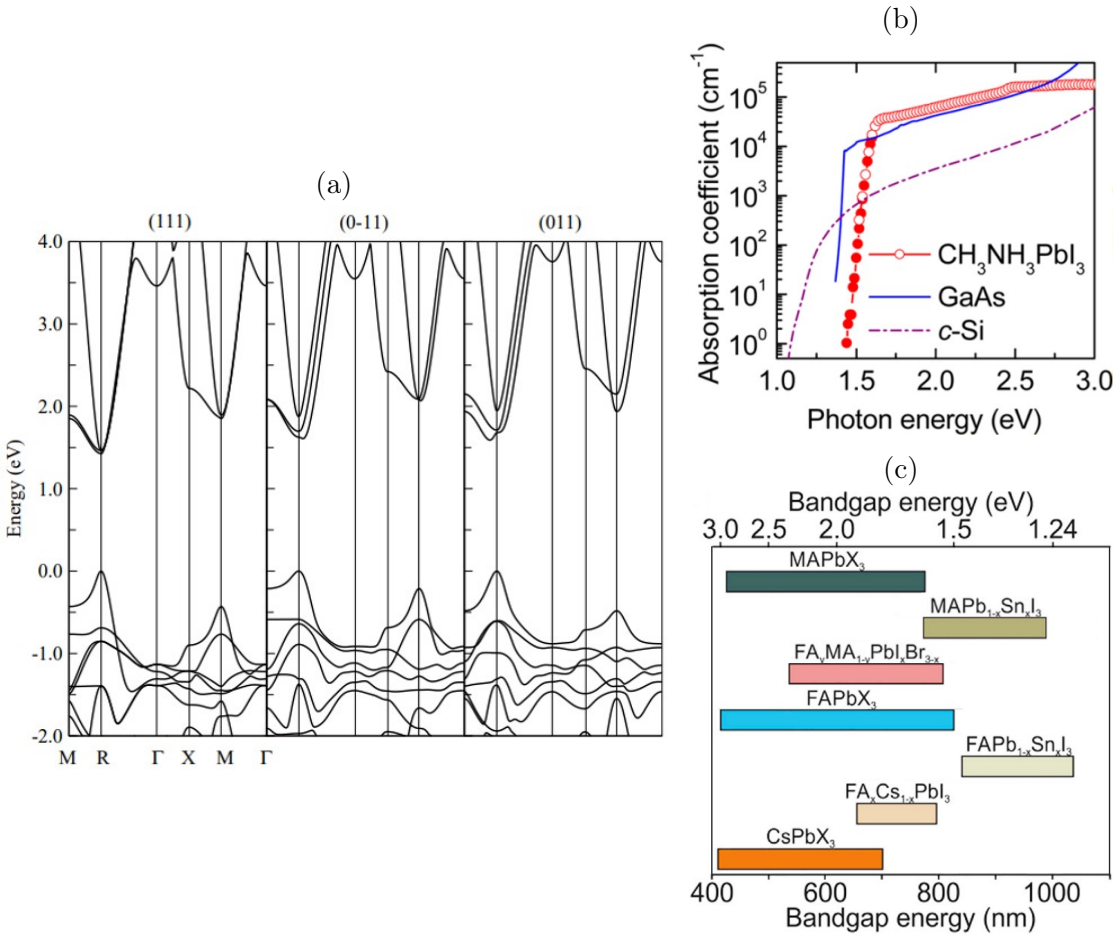

Figure 1.8: (a) Band structure of a MAPI crystal for (111), (0-11), and (011) orientations of the organic molecule. Reproduced from [Motta *et al.* 2015]. (b) Absorption coefficient of MAPI compared with other PV materials *(Gallium Arsenide GaAs, and crystalline silicon c-Si)*. Reproduced from [De Wolf *et al.* 2014]. (c) Bandgap energy range of various ABX_3 perovskites compositions. Reproduced from [Anaya *et al.* 2017].

Another crucial opto-electronic property of hybrid halide perovskites, especially for tandem cells, is the possibility to tailor their bandgap by changing the nature of A, B, and X elements. Replacing the X-site anion leads to the biggest change, as using a smaller halide (I > Br > Cl) widens the perovskite bandgap. Taking $MAPbX_3$ compositions as an example: E_g = 1.55 eV for $MAPbI_3$, 2.3 eV for $MAPbBr_3$, and 3.1 eV for $MAPbCl_3$ [Jang *et al.* 2015]. On the other hand, switching lead for the smaller tin metal cation narrows the bandgap of the $MASnI_3$ perovskite to E_g = 1.25 eV. [Ke *et al.* 2017]. The A-site cation has the least impact, with $FAPbI_3$: 1.50 eV, $MAPbI_3$: 1.55 eV, and $CsPbI_3$:

1.73 eV. Furthermore, A, B, and X-sites can be occupied by a mix of species to tune the perovskite properties finely. For example, $MAPbI_{3-x}Br_x$ stoichiometry, with gradual substitution of I by Br, has a bandgap that can be tuned between 1.55 and 2.3 eV. Hence, the bandgap of a specific perovskite can be optimized for dedicated purposes, such as single-junction cell or tandem integration. Figure 1.8c illustrates the bandgap range of various perovskite compositions.

1.2.2 Application in solar cells

The first application of perovskites in photovoltaics dates back to 2009 when the group of T. Miyasaka reported a PCE of 3.81% using MAPI as the absorber material in dye-sensitized solar cells (DSSCs) [Kojima *et al.* 2009]. However, those cells only functioned for a few minutes, as the corrosive liquid electrolyte quickly degraded the perovskite material. A breakthrough occurred in 2012 when groups of N-G. Park *et al.* and H. Snaith *et al.* applied hybrid halide perovskites in solid-state sensitized solar cells, replacing the electrolyte with a solid-state Spiro-OMeTAD hole transport layer, reaching respectively 9.7 and 10.9% PCEs [Kim *et al.* 2012, Lee *et al.* 2012].

These works showed the potential of perovskite solar cells (PSCs) in thin-film architectures, thanks to their ideal opto-electronic properties. It marked a breaking point in the literature, with increased interest in perovskites and their PV application. In 2015, after only three more years, the 20% PCE threshold was surpassed by researchers from the Korea Research Institute of Chemical Technology (KRICT), who certified a record PCE of 20.2% [Yang *et al.* 2015]. PCE growth began to slow down as the SQ limit for such materials was getting closer. Finally, after less than a decade of development of this technology, a PSC record efficiency of 25.7% was achieved in 2022 at Ulsan National Institute of Science and Technology (UNIST), close to the 26.7% record for the mature silicon technology [Green *et al.* 2022, NREL 2022].

Synthesis of the perovskite absorber

Various techniques exist to form perovskite thin films for PV devices. Among them, spin-coating deposition is the most popular in the literature for lab-scale devices, allowing the quick deposition of uniform films under an ambient or controlled atmosphere. It was was also applied in this work. Here, we propose a rapid summary of the processes used for perovskite film synthesis, found in more detail in the following works [Pascoe *et al.* 2017, Jung *et al.* 2019].

A precursor solution is prepared with the stoichiometric dissolution of organic halide salts with metal halides (e.g., formamidinium iodide (FAI) with lead iodide (PbI_2) for FAPI perovskite). Solvent engineering introduced the solvent's importance on the perovskite layer formation and the performance of resulting PSCs. In this regard, the mixture of N,N-dimethylformamide (DMF) and dimethylsulfoxide (DMSO) provides great control over the crystallization of the perovskite films due to the coordination of DMSO with PbI_2, and leads to high PCEs [Ahn *et al.* 2015, Seo *et al.* 2017].

The formation of the perovskite layer is then ensured by the anti-solvent method developed in 2014 by Xiao *et al.* [Xiao *et al.* 2014, Jeon *et al.* 2014]. After the spin-coating deposition of the precursor solution and the formation of a homogeneous precursor film, an anti-solvent is poured on this film, such as chlorobenzene, toluene, or ethyl acetate. This anti-solvent must be miscible with the solvent of the precursor solution without dissolving the precursor film. Adding the anti-solvent removes the excess uncoordinated

solvent from the film, forming an intermediate film of FAI·PbI_2·DMSO complex through several nucleation sites. Finally, thermal annealing evaporates the remaining DMSO and leads to the phase transition of the intermediate film into a perovskite film. This process is illustrated in Figure 1.9.

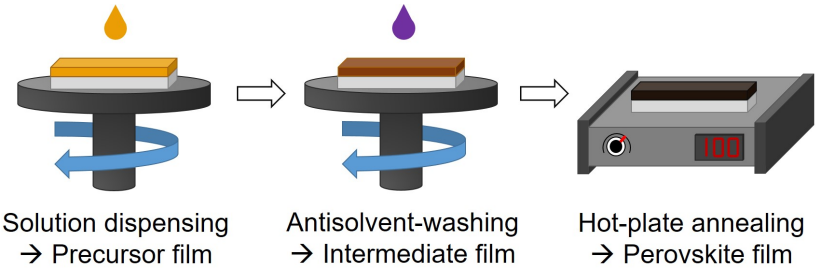

Figure 1.9: Illustration of the synthesis steps of a perovskite thin film with a spin-coating anti-solvent method.

Vapor-phase deposition techniques, including single-source, sequential, or multi-source evaporation [Zheng *et al.* 2019, Xiang *et al.* 2021], have attracted less attention in the literature so far, despite good results [Pérez-del-Rey *et al.* 2018]. The most common processes are based on one-step co-evaporation of organic halide (MAI, FAI...) and lead halide (PbI_2, $PbBr_2$) vapors to form the perovskite film [Borchert *et al.* 2017].

Perovskite solar cell architectures

In a perovskite solar cell (PSC), the perovskite absorber is not doped and is designated as an intrinsic semiconductor. It is placed between p-type and n-type layers (respectively HTL for hole transport layer and ETL for electron transport layer). This structure is labeled as a p-i-n junction and operates differently than classic p-n junctions used in silicon technology, as illustrated in Figure 1.10a.

The HTL has conduction and valence bands of higher energies than the ones of the perovskite, while the conduction and valence bands of the ETL are at lower energies than the ones of the perovskite. As a result, when photons are absorbed and electron-hole pairs are created in the perovskite material, the holes go to higher energy levels. In contrast, the electrons go to lower energy levels. Hence, the HTL extracts holes from the perovskite layer and blocks the electrons, while the ETL extracts the photogenerated electrons and blocks the holes.

Finally, two electrodes connect the HTL and ETL to an external circuit. On the cell's front side, transparent conducting oxides (TCO) are used, such as fluorine-doped tin oxide (FTO) or indium-doped tin oxide (ITO). The back electrode is usually a conductive metal, like gold or silver, but TCOs are also used in tandem applications.

According to the order in which the layers are illuminated, the structure is named p-i-n (HTL enlightened first) or n-i-p (ETL enlightened first). Another distinction is made between mesoscopic (or mesoporous) and planar structures. In mesoscopic structures, the transport layer on which the perovskite is deposited is made with a mesoporous material. This structure is inherited from DSSCs, which used mesoporous materials to increase the contact surface between the extracting layer and the absorber dye to compensate for small diffusion lenghts in the dye. Thanks to the better charge transport properties of perovskites, this architecture is not mandatory anymore, and planar architectures appeared in PSCs. These structures are summarized in Figure 1.10b.

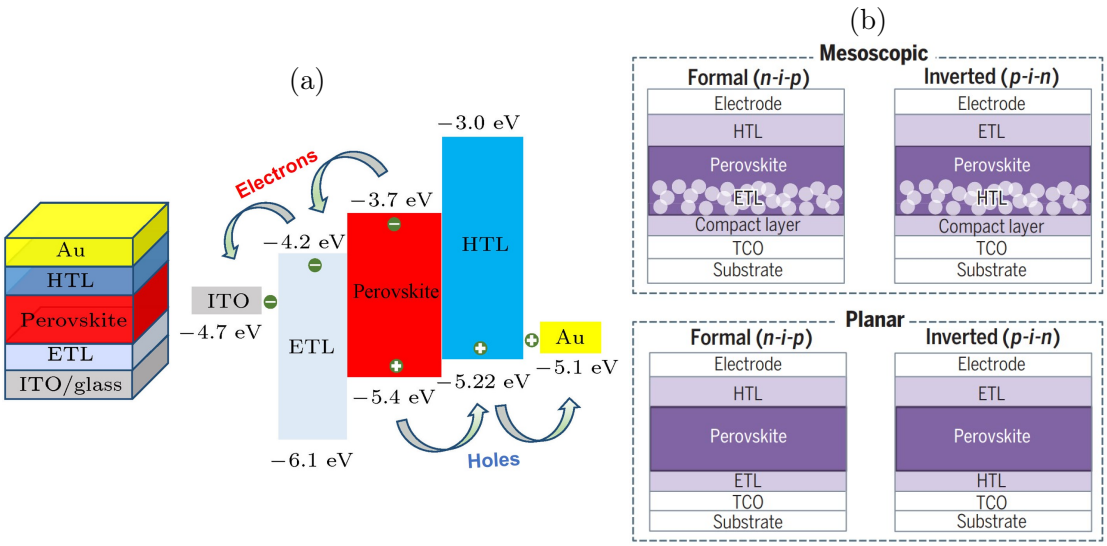

Figure 1.10: (a) Energy level diagram of a typical perovskite solar cell. Reproduced from [Yong-Liang *et al.* 2020]. (b) Representation of common perovskite solar cell architectures. Reproduced from [Rong *et al.* 2018].

In n-i-p architectures, typical mesoscopic ETL use a bi-layer of compact and mesoporous titanium oxide (TiO_2), while planar ETL can use inorganic tin(IV) oxide (SnO_2) or zinc oxide (ZnO) materials [Xiong *et al.* 2018, Zhang *et al.* 2018, Min *et al.* 2021]. Spiro-OMeTAD is the most used HTL, but other materials started to gain popularity, such as PTAA or CuSCN (more details in Section 2.1.5). In p-i-n architectures, the most common ETL are made with organic fullerenes layers, such as C_{60} or PCBM, usually combined with bathocuprione (BCP) [Gatti *et al.* 2017, Zhang *et al.* 2019, Jiang *et al.* 2020]. For the HTL, mesoporous structures often use inorganic nickel oxide NiO_x [Liu *et al.* 2017c], which is also found in planar architectures, along with PEDOT:PSS polymer [Hu *et al.* 2018] or self-assembled molecules (SAM) [Al-Ashouri *et al.* 2019].

Evolution of the perovskite composition

In their early part, PSCs mostly used MAPI as perovskite absorber due to its good optoelectronic properties and historical reasons. However, the growing number of works on this material highlighted important weaknesses. The high volatility of the MA cation, its hygroscopic nature, and MAPI crystal softness cause poor thermal and moisture stability [Conings *et al.* 2015, Song *et al.* 2016]. The degradation of MAPI films when exposed to ambient conditions or temperatures above 85 °C under an inert atmosphere was observed, eventually decomposing into PbI_2. Hence, the literature gradually shifted towards less MA-based perovskites and even MA-free compositions to avoid stability issues caused by MAPI [Turren-Cruz *et al.* 2018, Gao *et al.* 2020].

In this regard, FAPI perovskite seemed a promising candidate, with similar optoelectronic (absorption, transport...) properties than MAPI, with a slightly smaller 1.50 eV bandgap, better for single-junction, but worse for silicon-tandems [Eperon *et al.* 2014, Lee *et al.* 2014]. This perovskite has better thermal stability than MAPI, thanks to the higher chemical stability of the FA cation and higher thermal activation energies for the FAPI structure [Juarez-Perez *et al.* 2019]. Although the photoactive α-FAPI can be obtained at room temperature, because of lattice distortion induced by the larger FA cation, it is

not thermodynamically stable and rapidly turns into the non-photoactive δ-FAPI [Weller *et al.* 2015, Li *et al.* 2016, Ma *et al.* 2017]. At first, this intrinsic instability limited the use of FAPI in PSCs. A major solution to this problem was the inclusion of smaller A-site cations (Cs, or even the smaller Rb) in the FAPI structure, through solid-state alloys, to optimize its tolerance factor (see Figure 1.11a). The inclusion of MA cations or Br halides also helped to stabilize the photoactive α-FAPI at room temperature [Li *et al.* 2016, Saliba *et al.* 2016, Park *et al.* 2017, Rehman *et al.* 2017].

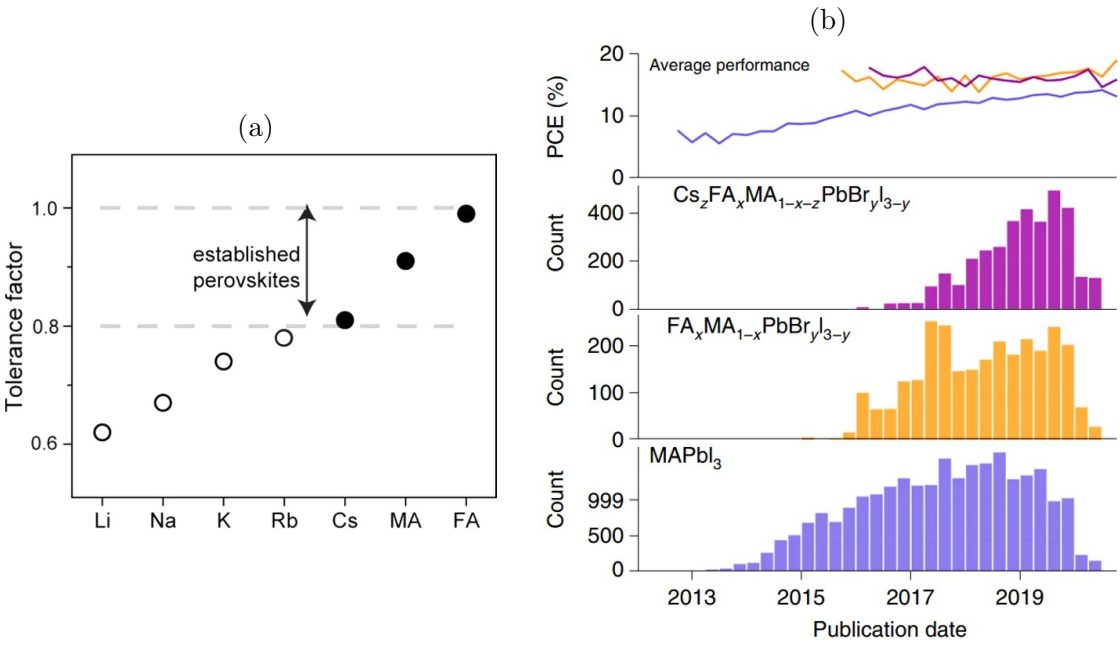

Figure 1.11: (a) Tolerance factor of $APbI_3$ perovskite for various A-site cations. *(Solid circles: photoactive black phase; open circles: non-photoactive phases).* Reproduced from [Saliba *et al.* 2016]. (b) Average PCE and popularity of various perovskite compositions along time. Reproduced from [Jacobsson *et al.* 2022].

As shown in Figure 1.11b, the literature has progressively moved away from single-cation MAPI compositions towards double-cation $FA_xMA_{1-x}PbBr_yI_{3-y}$, and then triple-cation $Cs_zFA_xMA_{1-x-z}PbBr_yI_{3-y}$ stoichiometries, stabilizing a FAPI base with the successive addition of MA and Cs cations, and controlling its bandgap via a halide mixture of I, Br, or even Cl. Quadruple-cation compositions, adding Rb or K cations to FA, MA, and Cs, also exist in the literature but remain marginal [Duong *et al.* 2017, Bu *et al.* 2017]. Nowadays, for stability purposes, the literature focuses more on removing MA or full inorganic $CsPbI_3$ compositions [Xiang and Tress 2019, Ouedraogo *et al.* 2020]. In addition, the pure FAPI composition is still very common, as the use of additives has proven to be another effective way to stabilize it [Zheng *et al.* 2022].

1.2.3 Development towards industrialization

Thanks to rapid growth over the past decade, the current PCE record held by the perovskite technology (25.7%) competes with silicon technology (26.7%). However, several key areas are to be improved for perovskites to match silicon in the photovoltaic market [Green *et al.* 2022, NREL 2022].

Upscale to larger areas

One of the first problematic aspect of the PSC technology is the active device area. Among the PCE records presented above, the 26.7% silicon technology record was obtained by Kaneka Corporation for a 79.0 cm^2 active area [Yoshikawa *et al.* 2017]. Meanwhile, the 25.7% perovskite record cell developed at UNIST had an active area of only 0.096 cm^2 [Min *et al.* 2021].

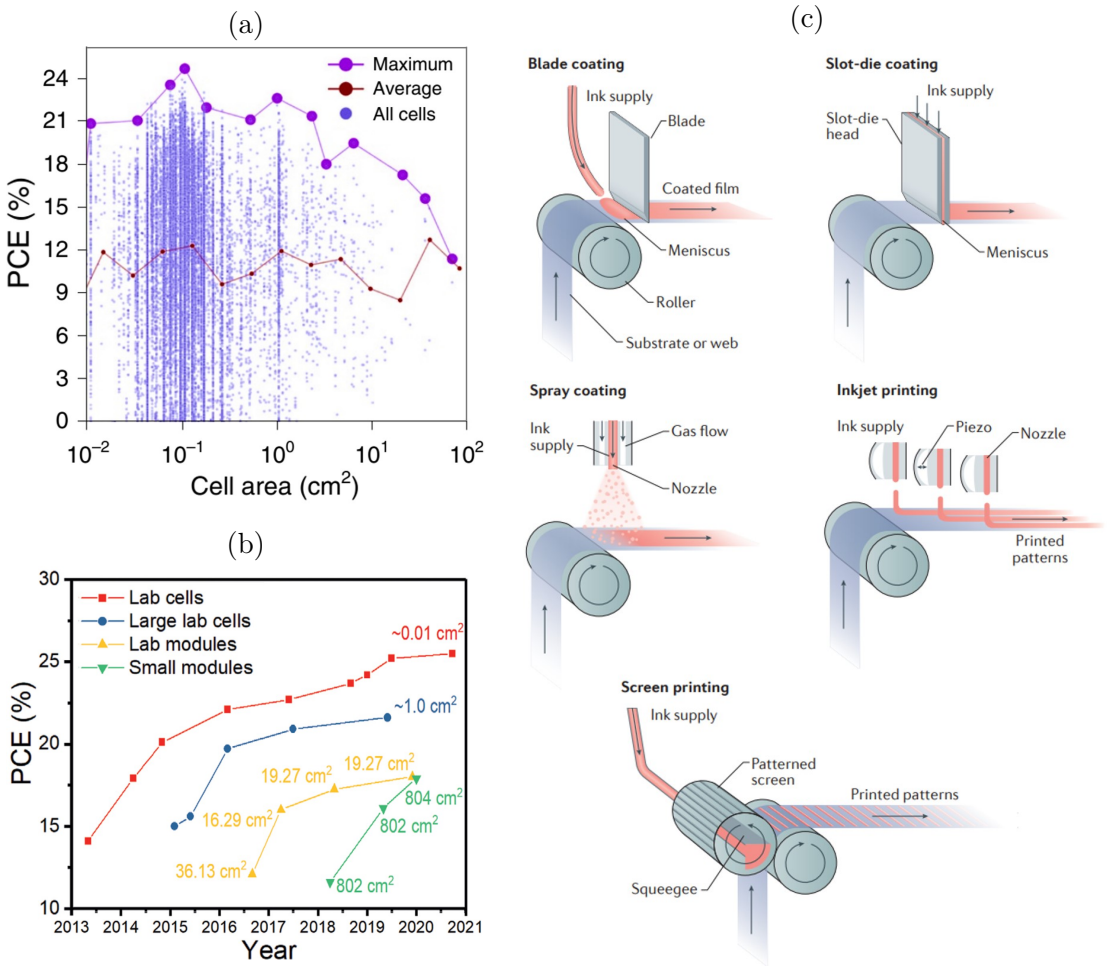

Figure 1.12: (a) Reported device PCE of perovskite-based PV devices regarding their area. Reproduced from [Jacobsson *et al.* 2022]. (b) Record PCE evolution for various scale categories of perovskite-based PV devices. Reproduced from [Li *et al.* 2021a].(c) Solution-based deposition methods for large-scale fabrication of PSCs. Reproduced from [Li *et al.* 2018].

The widespread spin-coating deposition partially explains this difference. Despite many advantages, it is not suitable for industrialized large-scale deposition. First of all, over large substrates with typical silicon solar cells area (> 100 cm^2), the uniformity of a spin-coated film is not insured, which is detrimental to device performances. Furthermore, most of the deposited solution is evacuated as waste during the rotation, leading to higher processing costs. Figure 1.12a illustrates how most devices in the perovskite literature are small-scale (< 0.01 cm^2) and how the PCE records fall off as the active area increases past this threshold.

For the industrialized synthesis of large-scale perovskite films, solution-processing techniques have proven to be interesting candidates, such as meniscus techniques (blade coating and slot-die coating) [Dai *et al.* 2019, Ding *et al.* 2016], spray coating [Heo *et al.* 2016], inkjet printing [Karunakaran *et al.* 2019], or the less popular screen printing [Mei *et al.* 2014]. These techniques are illustrated in Figure 1.12c. Like in small-scale devices, vapor-phase deposition also exists.

The development of large-scale area devices comes with many challenges, such as the deposition of uniform films, or the proper control of solvent evaporation and perovskite crystallization without the antisolvent method, incompatible with large scales [Baker *et al.* 2017]. Nevertheless, the interest for larger perovskite modules is in constant growth, and promising results were already obtained, as seen in Figure 1.12b. Notably, lab module from Microquanta Semiconductor with 18.0% PCE for an active area of 19.276 cm^2 was certified in 2019, and a record PCE of 17.9% was obtained in 2020 by Panasonic Corporation for a large-scale perovskite module of 804 cm^2 made of 55 cells [Li *et al.* 2021a, Green *et al.* 2022].

Stability

Nowadays, silicon solar modules in the market are guaranteed to keep 80% of their initial PCE after 25 years of lifetime [Jordan *et al.* 2016]. The commercial viability and the relevance of PSCs for tandem applications are bound to their stability. Hence, important attention has been paid to identify and solve instability sources [Wang *et al.* 2019], and a consensus was proposed in the literature to assess the stability of PSCs through standardized procedures [Khenkin *et al.* 2020].

Intrinsic instability sources have been identified in perovskites, such as ionic migration, or phase segregation in perovskite mixtures [Lee *et al.* 2019, Liu *et al.* 2021a]. Extrinsic sources also play a critical role in the degradation of perovskites, with variable criticality regarding their composition. For example, thermal stress, on top of promoting ionic migration, is more detrimental in MA-based perovskites due to the volatility of this cation mentioned in Section 1.2.2. Mixed-halide compositions suffer from UV light-induced halide phase segregation, also known as the Hoke effect [T. Hoke *et al.* 2015, Slotcavage *et al.* 2016]. Due to hygroscopic organic A-site cations, oxygen and moisture are major factors in the decomposition of perovskites into lead halide (usually PbI_2) [Kwon *et al.* 2014, Philippe *et al.* 2015].

Integrating the perovskite layer into solar cell architectures comes with new degradation sources. Degradation-induced phenomena, such as ionic migration from the perovskite absorber, can deteriorate other layers of the structure. The interfaces between the perovskite and its neighboring layers have also been identified as critical aspects of PSCs stability [Schulz *et al.* 2019]. Nevertheless, other layers of the stack can also be sources of instability in PSCs, with the example of the organic HTL Spiro-OMeTAD and its additives discussed later in Section 2.1.5, or ionic diffusion from gold metal electrode towards the perovskite layer [Domanski *et al.* 2016].

In the literature, composition engineering was cited earlier as an efficient way to solve the thermodynamic instability of the material, e.g., with the addition of smaller A-site cations to stabilize α-FAPI. This answer can also solve extrinsic sources of instability, such as the already mentioned MA cation removal or full-inorganic $CsPbI_3$ compositions to increase the stability towards heat and moisture. Many solutions have been explored to solve stability issues. Some of these solutions focus on the perovskite layer itself, with the introduction of chloride additives, organic molecules, polymers, or Lewis base compounds

[Kim *et al.* 2019c, Tavakoli *et al.* 2019, Liu *et al.* 2017a, Li *et al.* 2015, Yang *et al.* 2020b]. On the other hand, other strategies focus on improving the interfaces, including organic and inorganic molecules or polymers [Azmi *et al.* 2018, Qi *et al.* 2020, Jiang *et al.* 2019b]. Using 2D perovskites through 2D/3D heterostructures is another technique to improve the stability of PSCs, either as an additive in the perovskite layer or as an interfacial layer agent, and was the focus of this work.

Finally, the encapsulation of PSCs is also an effective method to prevent moisture and oxygen diffusion, filter UV light, and partially insulate them from thermal variations [Li *et al.* 2021b]. Glass-glass is the most common approach, inspired by silicon solar modules, and consists in sealing the device between two glass sheets using thermoplastic polymers such as ethylene vinyl acetate (EVA) or polyolefin (POE) [Cheacharoen *et al.* 2018, Fu *et al.* 2019].

Toxicity

Another barrier to the development of PSCs is the use of lead in the B-site. While PSCs only contain limited amounts of lead, this heavy metal is very toxic for living organisms and can spread easily and contanimate media such as air or water [Babayigit *et al.* 2016].

To solve this toxicity issue, the most obvious solution is to replace lead with less toxic elements. In this regard, tin has shown the most promising properties. However, the poor stability of Sn-based compared to Pb-based perovskites, due to the rapid oxidation of tin from Sn^{2+} to Sn^{4+} under air exposure, is a major obstacle to their development [Ding *et al.* 2022]. Hence, the main solution to solve the toxicity issue matches with the stability issue, and lies in the development of efficient encapsulation methods. Such encapsulation will have the dual function of insulating devices from external instability sources and preventing lead leakage from the PSCs to their environment [Ravi *et al.* 2020].

1.3 2D hybrid halide perovskites

Even though the perovskite name is associated with ABX_3 structures, nowadays, it also designates a myriad of configurations related to the original material. This work is interested in layered perovskites, also named two-dimensional (2D) perovskites, in opposition with classic ABX_3 three-dimensional (3D) perovskites. Before the rise of interest in 3D perovskite in the early 2010s, 2D perovskites attracted more attention. Various works were already investigating their structural, dielectric, magnetic, or optical properties during the 1980s [Nakajima *et al.* 1983, Dolzhenko *et al.* 1986, Ishihara *et al.* 1989], and the group led by E. Deleporte started to study their integration in optical cavities in 2005 [Brehier *et al.* 2006]. Here, similarly to 3D perovskites, a focus will be done on organic-inorganic hybrid halide 2D perovskites.

1.3.1 Structure

A hybrid halide 2D perovskite structure consists of alternated inorganic and organic layers. It is formed by using bulky organic cations $(A')^+$, (or spacer cations) that have to possess specific features [Mitzi *et al.* 1999, Mao *et al.* 2019]:

- An anchoring group with a positive charge that binds with the inorganic layer. The most common in hybrid halide 2D perovskites is the ammonium NH_3^+ group.

- A good stereochemical configuration to fit between two inorganic layers.
- A limited space-filling ability to prevent interaction between neighboring spacers.

If a bulky organic cation fits these conditions, it can be considered a possible spacer cation, such as the most popular n-butylammonium ($C_4H_9NH_3^+$, BA^+) alkyl chain, and phenylethylammonium ($C_6H_5C_2H_4NH_3^+$, PEA^+) aromatic cycle. Adding it to a 3D perovskite leads to a "cutting" of the 3D structure along either <100>, <110>, or <111> crystallographic planes, based on the spacer cation used [Mitzi 2001, Lee *et al.* 2021]. With the <100> orientation - the most frequent in the literature and the one studied in this work - the cutting forms inorganic PbI_4^{2-} octahedra monolayers bound by their corners. Thanks to hydrogen bonding, the anchoring group of the organic spacer attaches to the inorganic layers, forming an alternation of inorganic octahedra layers separated by organic layers of spacer cation $(A')^+$. All orientations are illustrated in Figure 1.13, along with the <100> resulting 2D perovskite.

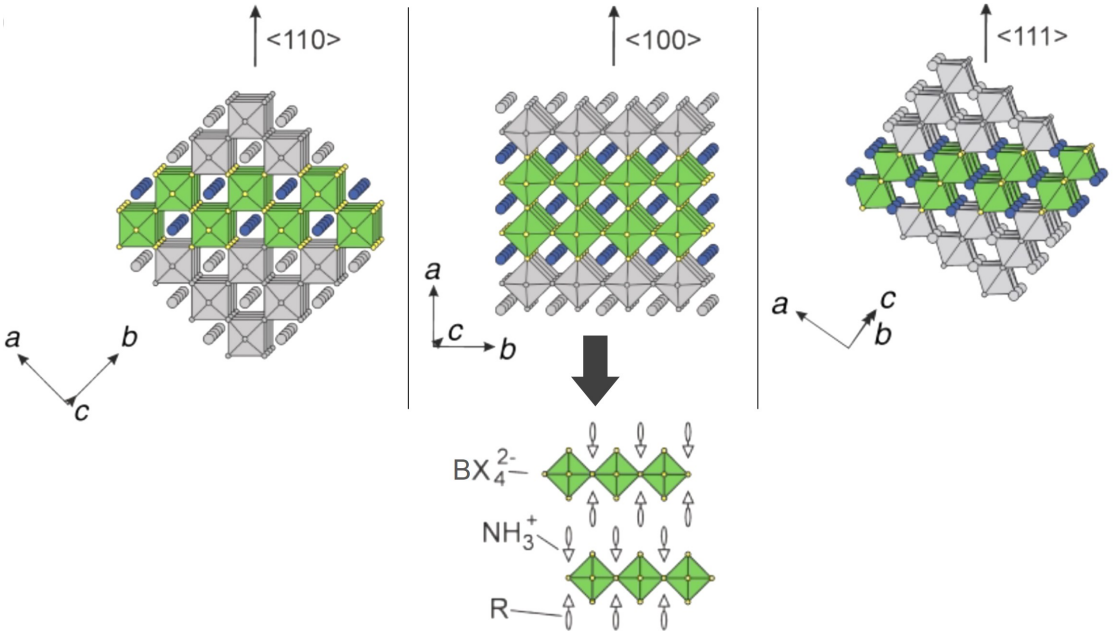

Figure 1.13: Formation of a 2D perovskite structure by "cutting" of the 3D perovskite along <100>, <110>, or <111> planes, and resulting <100> oriented 2D perovskite. Reproduced from [Mitzi 2001].

Cutting the 3D perovskite structure does not necessarily form octahedra monolayers, which is described by the n-factor in the chemical formula of RP 2D perovskites. This factor corresponds to the number of consecutive inorganic layers separated by the spacer layer(s), and is paramount to characterize 2D perovskites, as it significantly modifies their opto-electronic properties. With $n = 1$, the structure is designated as a purely 2D perovskite, with the chemical formula $(A')_2BX_4$. Oppositely, a value $n = \infty$ describes an infinite number of consecutive inorganic octahedra layers, corresponding to a purely ABX_3 3D perovskite. All values $1 < n < \infty$ are considered as intermediate structures between 2D and 3D perovskites and can be separated into three main categories, shown in Figure 1.14, based on the nature of the organic spacer used [Mitzi *et al.* 1999, Mao *et al.* 2019, Blancon *et al.* 2020]:

- Ruddlesden-Popper (RP) 2D perovskites, of chemical formula $(A')_2A_{n-1}B_nX_{3n+1}$, use a monoammonium R-NH_3^+ molecule as organic spacer A'. In this case, to obtain an electrically neutral structure, octahedra layers are separated by two spacer monolayers bound to each other with van der Walls interactions, or π-π in the case of aromatic spacers. See Figure 1.14a.

- Dion-Jacobson (DJ) 2D perovskites, of chemical formula $A'A_{n-1}B_nX_{3n+1}$, use a diammonium NH_3^+-R-NH_3^+ molecule as A' spacer. Therefore, only one spacer monolayer is necessary to obtain the electrical neutrality of the structure, and only hydrogen bonding is involved between each layer of the stack. See Figure 1.14b.

- Alternating Cation in the Interlayer space (ACI) 2D perovskites, of chemical formula $A'A_nB_nX_{3n+1}$. The octahedra layers are separated in the ACI structure by alternating the A' spacer cation and the A-site "perovskite" cation. This structure has yet only be reported with guanidinium ($C(NH_2^+)_3$, GA^+) as the spacer cation, combined with MA^+ A-site cation. See Figure 1.14c.

Figure 1.14d illustrates an example of DJ 2D perovskite with n=1, 2, and 3. This work was focused on RP perovskites. Therefore, we will only detail the properties of these specific RP 2D perovskites.

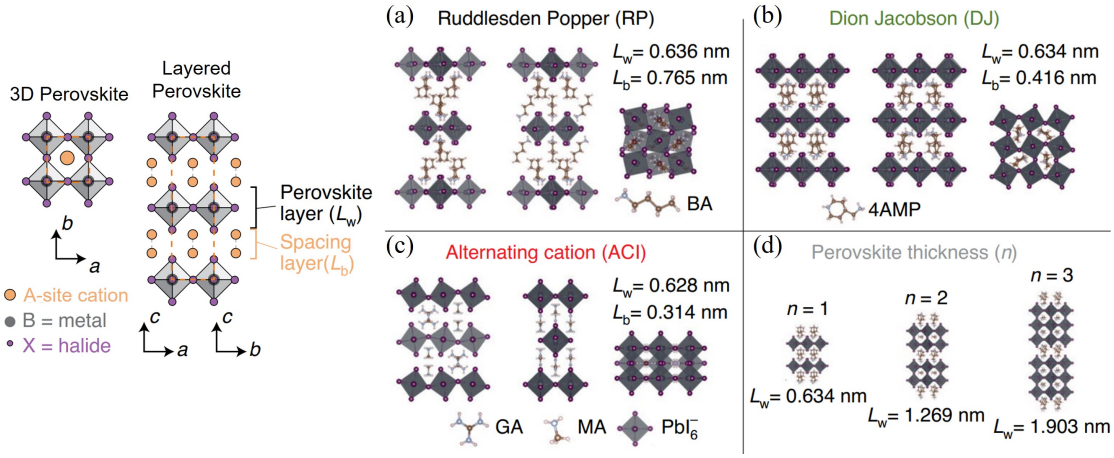

Figure 1.14: Comparison between RP, DJ, and ACI 2D perovskite phases. (*4-AMP : 4-(aminomethyl)piperidinium*) Reproduced from [Blancon *et al.* 2020].

Since 2D perovskites do not need to fit the Goldschmidt factor, a larger number of spacer cations can be used compared to the A-site cations of 3D perovskites [Zhang *et al.* 2009]. Hence, 2D perovskites have more chemical versatility than 3D perovskites. Furthermore, the n-factor value offers an additional degree of customization to this material [Jemli *et al.* 2015].

Another significant advantage provided by this unique structure is the increased stability of 2D perovskites in comparison with 3D perovskites [Fu *et al.* 2021]. Higher formation energy of the 2D stack, combined with Van der Waals interactions between spacer and inorganic layers leads to better chemical intrinsic stability [Quan *et al.* 2016]. Moreover, the hydrophobic nature of bulky spacer cations can block moisture infiltration, increasing extrinsic stability towards environmental conditions, and especially against moisture [Zheng *et al.* 2018, Zhao *et al.* 2022].

1.3.2 Opto-electronic properties

Excitons

In Section 1.1.1, we discussed how solar cells use the properties of semiconductor materials to convert sunlight into electricity. In this discussion, we did not mention an element that is central to explain the properties of 2D perovskites: excitons.

We established that when a semiconductor absorbs a photon with an energy $h\nu$ superior to its bandgap energy, an electron is promoted in the CB, and a hole is generated in the VB, creating an electron-hole pair. This electron-hole pair interacts via attractive Coulomb force, stabilizing it. The resulting state is a quasi-particle named exciton, described by its binding energy E_b, which is the energy required to dissociate the electron-hole pair, and its exciton Bohr radius a_B, which is the average distance between the electron and the hole. Based on these criteria, two types of excitons are described in the literature and illustrated in Figure 1.15: Wannier-Mott and Frenkel excitons (from [Frenkel 1931], and [Wannier 1937]).

- Wannier-Mott excitons are typically found within inorganic semiconductors with large dielectric constant. Weak binding energies characterize them ($E_b \approx$ 1-10 meV), and large exciton Bohr radius ($a_B \approx$ few nm), greater than the lattice parameter of the material they are into. Therefore, Wannier-Mott excitons are described with an hydrogenoid model, and are considered "free excitons" as the center of mass of the bound electron-hole pair can move freely in the crystal lattice.

- On the other hand, Frenkel could be seen as the opposite. Generally found in organic semiconductors with small dielectric constant, they are bound with much higher binding energies than Wannier-Mott excitons ($E_b \approx$ 100-1000 meV), and thus, much smaller exciton Bohr radius ($a_B \approx$ few Å). Consequently, they are bound to scales close to that of an atom up to that of a unit cell.

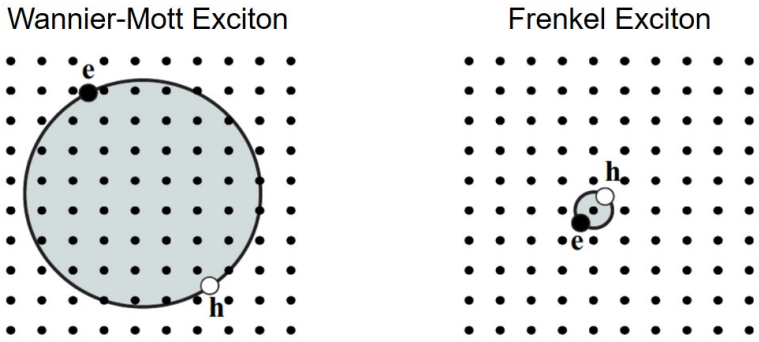

Figure 1.15: Schematic representation of Wannier-Mott and Frenkel excitons. Reproduced from [Fox 2002].

Measurements by Miyata *et al.* indicated binding energies around 16 meV in the orthorhombic γ-MAPI at low temperatures [Miyata *et al.* 2015]. Other works indicated similar binding energy for MAPI and demonstrated that its transition to tetragonal and cubic phases further decreased its binding energy. Furthermore, Galkowski *et al.* showed that changing the A-site cation did not significantly modify the exciton binding energy, leading to similar values in FAPI [Galkowski *et al.* 2016, Zhong *et al.* 2019]. At room

temperature, the thermal energy $k_BT \approx 26$ meV is sufficient to counteract the exciton binding energy of only a few tens of meV in 3D perovskites. Hence, the photogenerated charge carriers in these materials are considered free carriers.

Quantum and dielectric confinements in 2D perovskites

2D perovskite structures are made with alternated inorganic octahedra and spacer layers. The inorganic layer is characterized by its VB, CB, and E_g. The equivalent parameters for organic materials are: the Highest Occupied Molecular Orbital (HOMO) and the Lowest Unoccupied Molecular Orbital (LUMO), separated by the HOMO-LUMO Energy (E_{H-L}). The bandgap energy of the inorganic layer is significantly smaller than the HOMO-LUMO energy of the organic layer ($E_g \approx 2$ eV, while $E_{H-L} \approx 5$ eV) [Tanaka *et al.* 2002]. As a result, the organic layer acts as a potential barrier, and the inorganic part as a potential well. This alternation of potential barriers and wells is called a type I multiple quantum-well, illustrated in Figure 1.16a. Other types exist in the literature, but type I is the general case for most 2D perovskites and will be the only one presented here [Quintero-Bermudez *et al.* 2019, Gao *et al.* 2019].

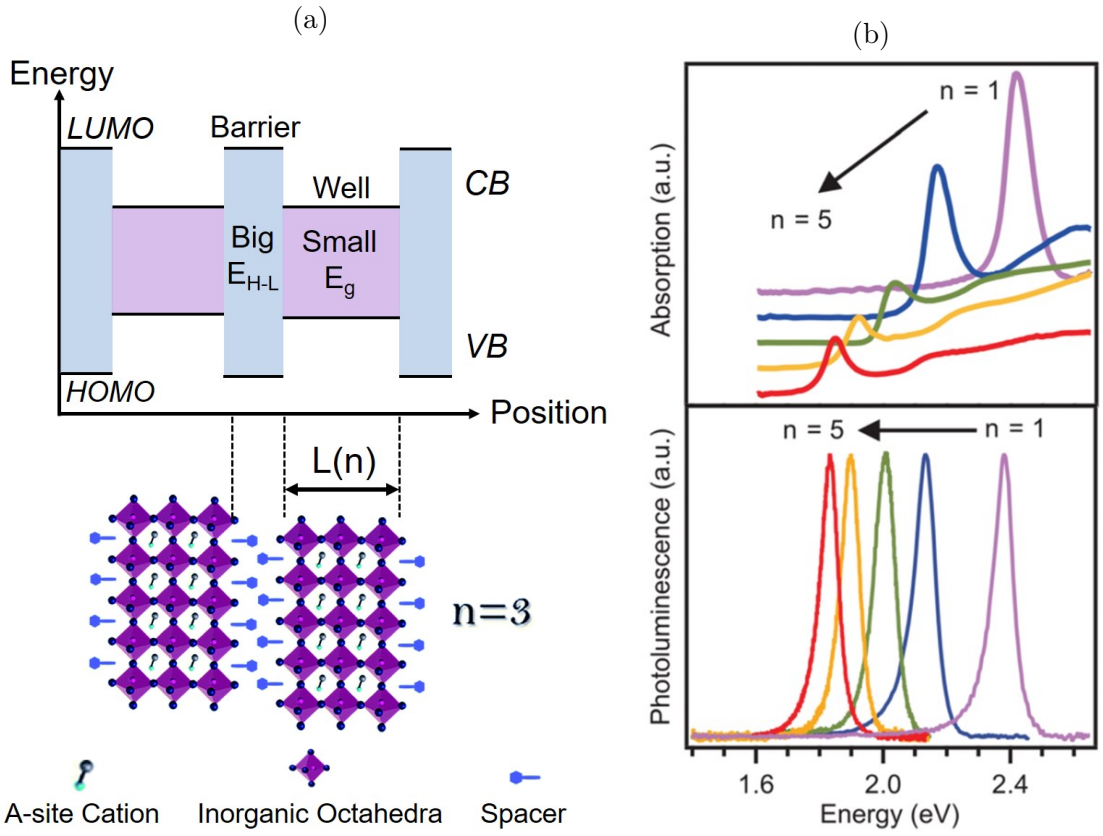

Figure 1.16: (a) Illustration of a type-I multiple quantum well structure in a n=3 RP 2D perovskite. (b) Absorption and PL spectra of $(BA)_2(MA)_{n-1}Pb_nI_{3n+1}$ RP 2D perovskites for n values from 1 to 5. Reproduced from [Blancon *et al.* 2017].

In this type I multiple quantum well, the electrons and holes are spatially confined into the inorganic layer, defining the quantum confinement. When the n-factor value of a RP 2D perovskite phase $(A')_2A_{n-1}B_nX_{3n+1}$ is increased, the size of its inorganic layer

is increased as well (illustrated in Figure 1.16a by the length L(n)). This inorganic layer enlargement leads to a reduction of the electrons and holes quantum confinement and, so, a reduction of the RP 2D perovskite bandgap [Hoye *et al.* 2022]. This phenomenon is illustrated in Figure 1.16b, showing the evolution of absorption and photoluminescence spectra of $(BA)_2(MA)_{n-}Pb_nI_{3n+1}$ RP perovskites regarding their n value.

Several works demonstrated that excitons in 2D perovskites are also Wannier-Mott excitons, with Bohr radius between 1 and 2 nm [Hong *et al.* 1992, Tanaka *et al.* 2002, Lanty *et al.* 2014, Blancon *et al.* 2018]. Their exciton binding energy is much greater than in 3D perovskites, and were estimated close to 202 meV for $(PEA)_2PbI_4$ and 470 meV for $(BA)_2PbI_4$ 2D perovskites. Contrary to 3D perovskites, at room temperature, exciton binding energies in 2D perovskites are greater than k_BT. Hence, excitonic properties heavily drive the behavior of 2D perovskites semiconductors, which is good for light emission purposes, but is detrimental to the electron-hole separation necessary for PV.

Due to quantum confinement, the exciton binding energy in a pure 2D structure should be multiplied by a factor of four in comparison with a 3D structure, leading to exciton binding energies of several tens of meV. However, as mentioned above, excitons binding energies in 2D perovskites are in the order of magnitude of several hundreds of meV. Hence, quantum confinement alone is not enough to explain such high values, and the dielectric confinement effect is also necessary. In the structure, the organic spacer layer has a significantly lower dielectric constant ($\epsilon_{spacer} \approx 2.1$) than the inorganic layer ($\epsilon_{inorganic} \approx 6.1$), and electrons and holes withstand an effective dielectric constant inferior to the dielectric constant of the inorganic layer. This increases the Coulombian interaction between charge carriers and, so, the excitons binding energy [Tanaka and Kondo 2003]. Thus, the exciton binding energy in 2D perovskites can be modulated by changing the organic spacer cation's nature, modifying its dielectric constant.

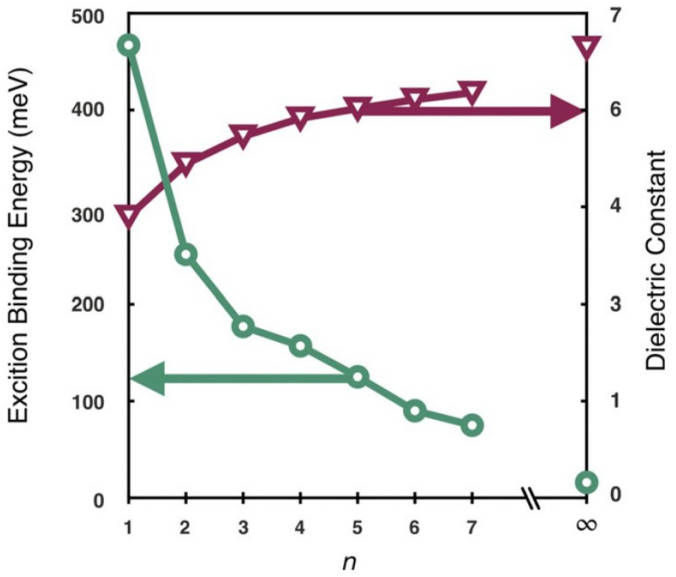

Figure 1.17: Exciton binding energy and high frequency dielectric constant of the RP 2D perovskite $(BA)_2(MA)_{n-1}Pb_nI_{3n+1}$ as a function of its n-factor. ($n{=}\infty$ *values correspond to MAPI*). Reproduced from [Ortiz-Cervantes *et al.* 2019], based on data from [Soe *et al.* 2019] and [Blancon *et al.* 2018].

1.3.3 Applications in photovoltaics

Limits and solutions: towards higher n

In PV, the interest in 3D perovskites has grown constantly since the early 2010s, whereas their 2D counterparts remain marginal. Even though their better stability would be suitable for PV devices, their opto-electronic properties have proven to be problematic for their application in PSCs. Because of the electrons and holes confinement in the quantum well, their bandgap is superior to the one of 3D perovskites (generally > 2 eV), which is sub-optimal for single-junction and tandem solar cells. Furthermore, their high excitons binding energy is also problematic, as it inhibits electron-hole separation and hinders the efficiency of PV devices. 2D perovskites possess anisotropic charge transport, allowing charge carriers transport only along the inorganic layers as the organic spacer layers block charge transport across layers. Therefore, in PSC structures, 2D perovskites must grow perpendicularly to the substrate for good charge extraction in the ETL/HTL, necessary for efficient devices. This concept is depicted in Figure 1.18.

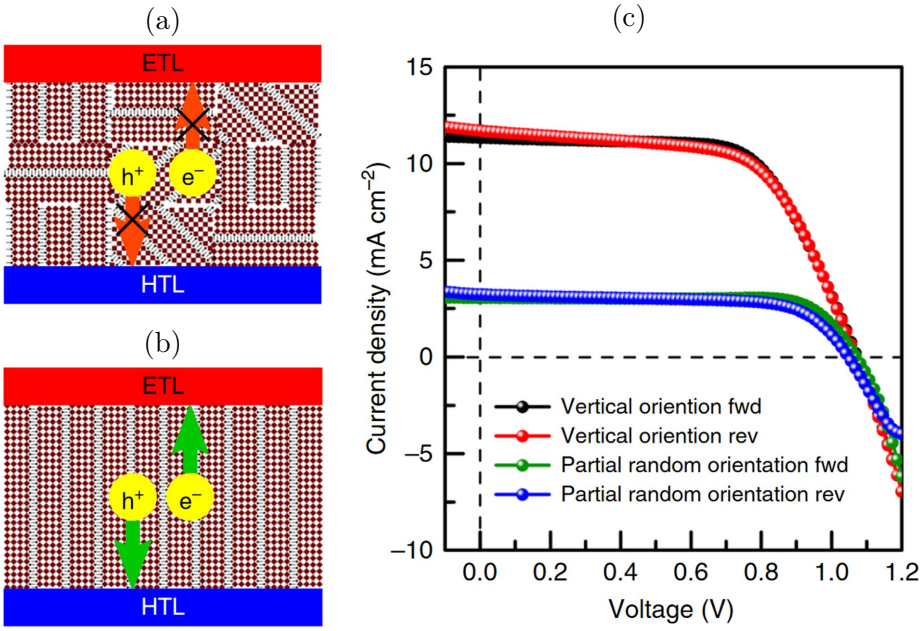

Figure 1.18: Illustration of (a) vertical and (b) random orientation of 2D perovskite phases in a planar PSC ETL/Perovskite/HTL stack. (c) Impact of these orientations on the IV curve of solar cell. Reproduced from [Chen *et al.* 2018].

Increasing the n-factor of the RP 2D perovskite solves a major part of these problems. First, by weakening the quantum confinement of the electrons and holes, it reduces the perovskite bandgap, as shown in Figure 1.16b. Hence, combining this solution with halide mixing allows the modulation of their bandgap closer to optimal values for PV applications. Then, increasing the n-factor weakens confinement effects and leads to lower the exciton binding energy of the structure, visible in Figure 1.17. Finally, higher n-factor are more prone to form 2D perovskite phases in parallel orientation to the substrate [Cao *et al.* 2015, Quintero-Bermudez *et al.* 2018]. As a result, the literature of 2D-based PSCs quickly focused on higher n values. State of the art reviews, such as [Ortiz-Cervantes *et al.* 2019] confirm this statement, with a greater amount of data and better results obtained on devices using n values between 3-5 than for $n < 3$, as visible in Figure 1.19.

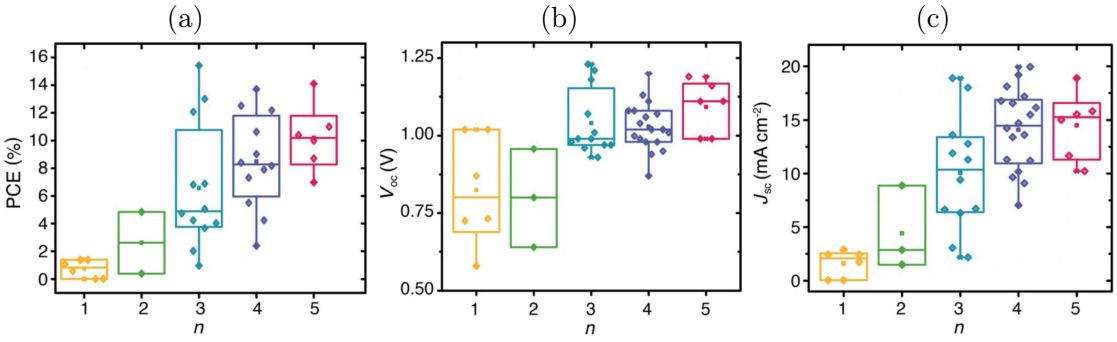

Figure 1.19: Statistical analysis of (a) PCE, (b) V_{OC}, and (c) J_{SC} for lead iodide 2D PSCs as a function of n value. Reproduced from [Ortiz-Cervantes *et al.* 2019].

Promising evolution

The first working PSC using a RP 2D perovskite absorber was revealed by Smith *et al.* [Smith *et al.* 2014]. With a $(PEA)_2(MA)_{n-1}Pb_nI_{3n+1}$ made mainly of n=3 phases ($(PEA)_2(MA)_2Pb_3I_{10}$), they reported better moisture stability of the perovskite material compared to MAPI, and obtained a PCE of 4.73%. The interest in 2D perovskites thrived when Tsai *et al.* fabricated PSCs in a p-i-n architecture based on $(BA)_2(MA)_{n-1}Pb_nI_{3n+1}$ with a majority of n=4 phases $(BA)_2(MA)_3Pb_4I_{13}$. These devices were developed with the "hot-casting" technique, which consisted in spin-coating the perovskite precursor solution on a glass-FTO/PEDOT:PSS stack preheated to 150°C. This method formed a perovskite layer with preferential out-of-plane alignment (perpendicular to the substrate), facilitating charge transport [Tsai *et al.* 2016]. Promising PCEs up to 12.52% were obtained, with better light and moisture stability than MAPI references for both encapsulated and non-encapsulated devices, as shown in Figure 1.20.

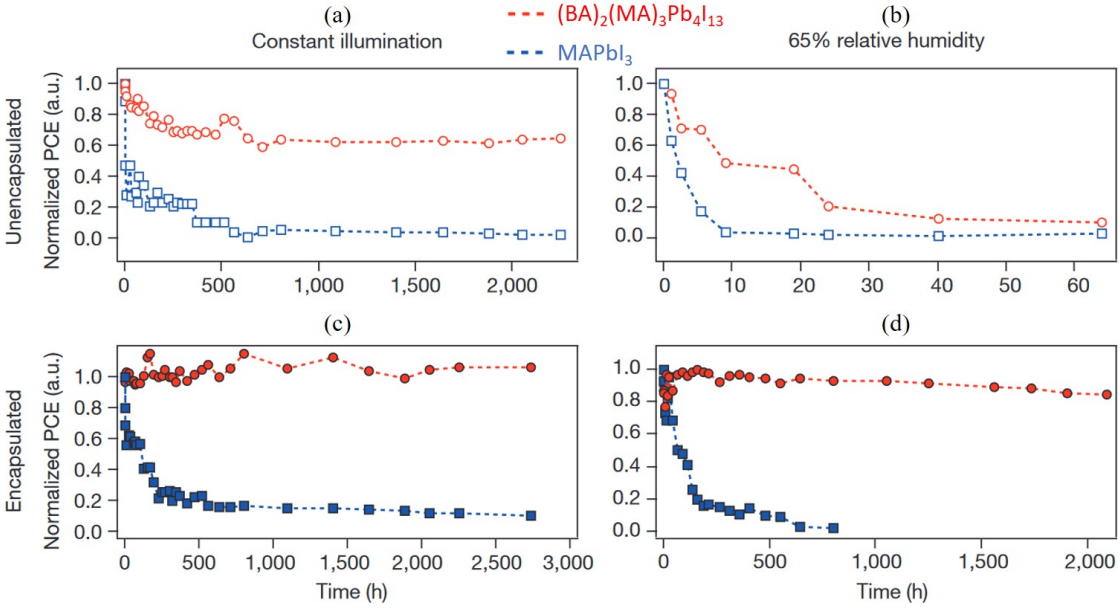

Figure 1.20: PCE evolution under AM1.5G illumination for PSCs without (a) and with (c) encapsulation. PCE evolution under 65% relative humidity for PSCs without (b) and with (d) encapsulation. Reproduced from [Tsai *et al.* 2016].

This paper was one of the first to highlight the potential of 2D perovskites as absorber layer in PSCs with proper optimization. It marked a turning point in the literature and was followed by an increase in the number of papers centered on 2D-based PSCs. This field benefited from the important attention paid towards 3D-based PSCs and the optimization of their architectures (improvement of ETL/HTL, of electrodes, etc). In addition, the optimization of the 2D perovskite absorber itself, through the appearance of new RP spacer cations (such as thiophene-based), [Lai *et al.* 2020], the emergence of DJ and ACI 2D perovskites for solar cell applications, or with the modification of the A-site cation [Lu *et al.* 2020, Zhao *et al.* 2020, Yang *et al.* 2021], led to significant PCE improvement of 2D-based PSCs, eventually reaching 20%, as seen in Figure 1.21.

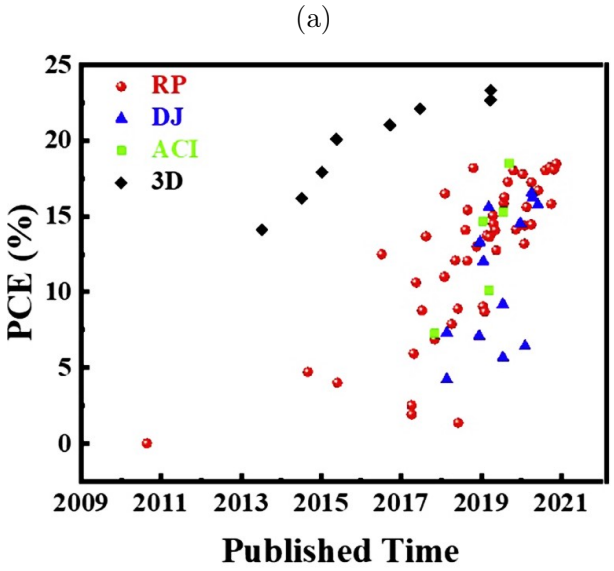

Figure 1.21: Chronological evolution of PCE for PSCs using RP, DJ, or ACI 2D perovskites, compared to 3D PSCs records. Reproduced from [Fu *et al.* 2021].

The last PCE record for 2D-based PSCs was obtained by Zhang and Park in 2022. They applied an ACI 2D perovskite $GA(MA)_nPb_nI_{3n+1}$ with n=5 ($GA(MA)_5Pb_5I_{16}$) in n-i-p devices. Adding an amphoteric imidazolium iodide (ImI) post-treatment on the ACI 2D layer resulted in a 22.26% PCE. This record PCE was associated with important stability, as devices maintained 93.81% of their initial PCE after 1200 hours in ambient conditions (25% relative humidity and 25 °C), while MAPI-based references kept only 18.34% of theirs [Zhang and Park 2022]. Such PCE is fairly close to current PCE records of 3D-based PSCs, and shows the potential for 2D perovskites for PV applications.

1.4 2D/3D perovskite heterostructures

Another application appeared for 2D perovskites in PSCs: mixed-dimensional 2D-3D perovskite, also named 2D/3D heterostructures. These structures combine 2D and 3D perovskites to synthesize 3D-based PSCs that benefit from the stability of 2D perovskites. In the literature, 2D/3D heterostructures have been separated into at least two categories, illustrated in Figure 1.22, each associated with a specific synthesis process [Ortiz-Cervantes *et al.* 2019, Mahmud *et al.* 2021a]:

- 2D bulk incorporation, or mixed 2D/3D perovskite. This structure incorporates spacer cations directly into the 3D perovskite precursor solution. The precursor solution is deposited and annealed to form a layer with 3D and 2D perovskite phases. Some works divide this category into two specific cases: higher spacer concentration in the precursor solution forms a layer with crystallized grains of 2D and 3D perovskite phase. In contrast, low spacer concentration in the precursor solution forms smaller 2D perovskite phases only at the grain boundaries of the 3D grains. However, these two sub-categories present rather close properties and challenges, so we will not distinguish between them.

- 2D surface treatment, or 2D capping layer. This structure first synthesizes a 3D perovskite layer (deposition of a precursor solution and thermal annealing to crystallize the perovskite phase). Then, a precursor solution of spacer cations is deposited on the 3D layer, followed by a second thermal annealing, to crystallize a 2D perovskite layer on top of the 3D bulk.

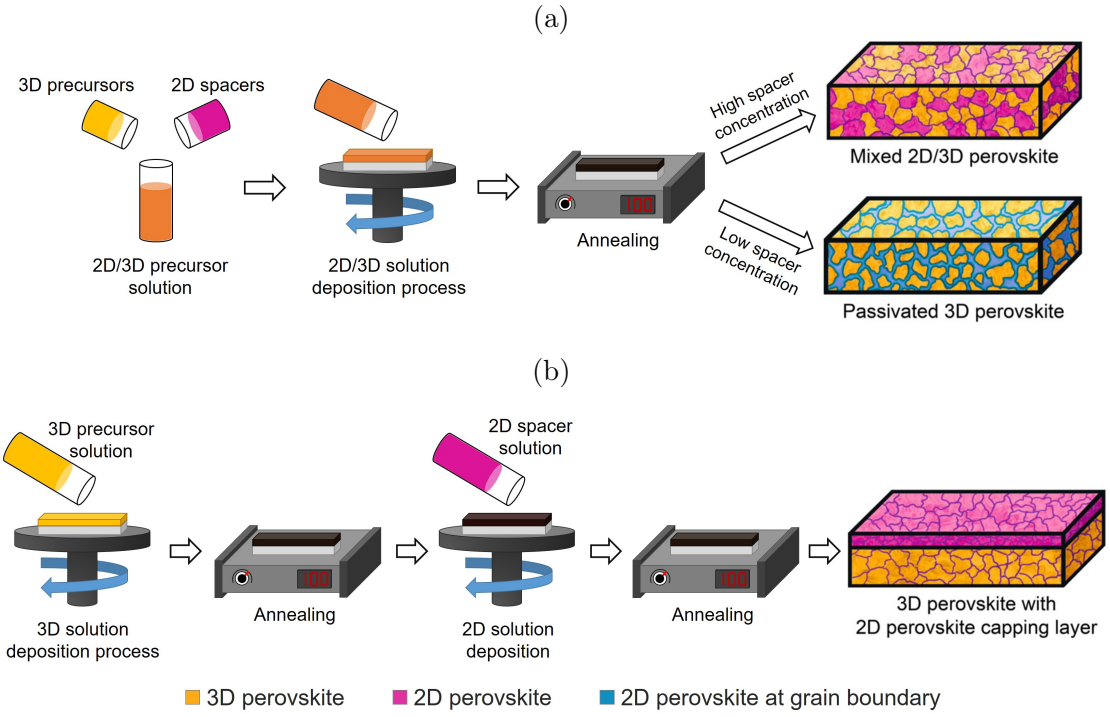

Figure 1.22: Illustration of the deposition method and the resulting 2D/3D heterostructure for (a) bulk incorporation with mixed 2D/3D phases or passivated 3D grains, and (b) 2D surface treatment. Adapted from [Ortiz-Cervantes *et al.* 2019, Mahmud *et al.* 2021a].

The choice of spacer cation to form the 2D perovskite phase in 2D/3D heterostructures has been influenced by the 2D perovskite literature. As a result, many cations have been investigated, as seen in Figure 1.23a, but a significant part of published works applied PEA and BA spacers, which were already the most popular in 2D perovskites. Furthermore, no consensus has yet been found on the best working spacer cations, leaving room for further spacer engineering.

Because 2D/3D heterostructures are an addition to efficient 3D perovskite absorbers, PCEs of 2D/3D materials rapidly reached the ones obtained in purely 3D-based PSCs. In this regard, better PCEs were obtained with surface treatment structures than with bulk incorporation, as seen in Figure 1.23b. This observation could be explained by bulk incorporation structures requiring more thorough optimization of the 2D/3D perovskite absorber, whereas surface treatment only forms a 2D layer on top of an already optimized 3D perovskite. Hence, the record PCE of 2D/3D heterostructures was obtained with surface treatment by Jeong *et al.*, who treated a FAPI perovskite with n-octylammonium iodide ($C_8H_{17}NH_3I$, (n-OAI)) and reached a certified PCE of 24.64%, close to the 25.7% global record for PSCs [Jeong *et al.* 2020].

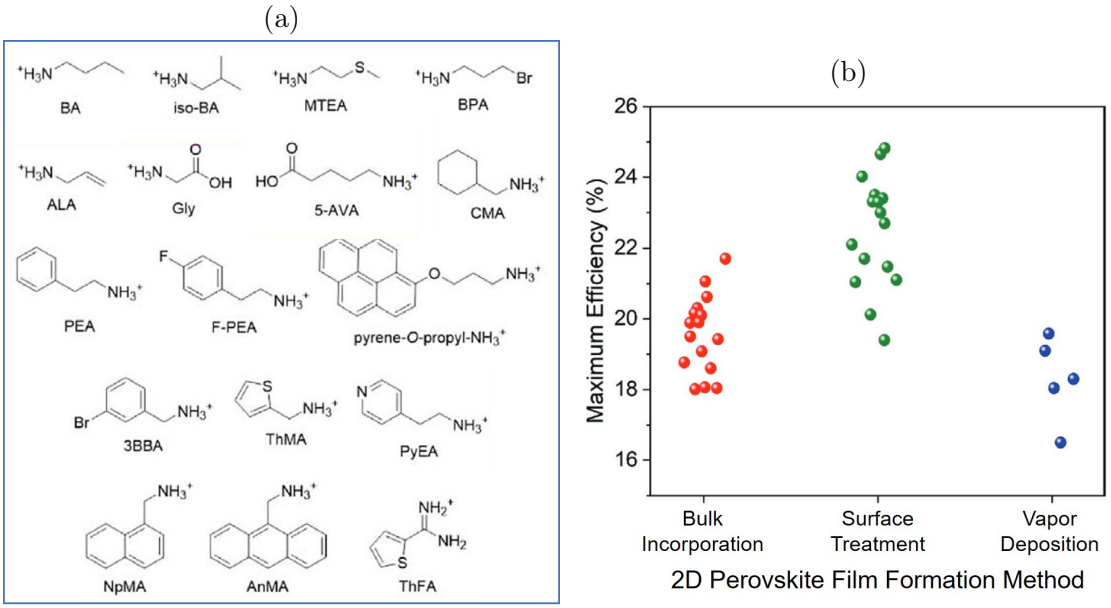

Figure 1.23: (a) Organic spacer cations used in 2D/3D heterostructures for PSCs. Reproduced from [Fu *et al.* 2021]. (b) Distribution of maximum PCE obtained in individual PSC publications using either bulk incorporated, surface treated, or vapor deposited 2D/3D perovskite heterostructures. Reproduced from [Mahmud *et al.* 2021a].

1.4.1 Bulk incorporation

Li *et al.* was one of the first groups to use this strategy when they tried to stabilize α-FAPI by incorporating PEA spacer cation instead of smaller MA or Cs cations, resulting in $FA_xPEA_{1-x}PbI_3$ stoichiometry [Li *et al.* 2017]. They investigated several PEA concentrations to form $FA_xPEA_{1-x}PbI_3$ perovskite with FA/PEA ratio of 10, 20, 40, 60, and ∞ (pure FAPI), and obtained their best PCE of 17.71% with the 40 ratio. By assessing the evolution of optical and structural properties of the perovskite films in ambient conditions with UV-visible spectroscopy and X-ray diffraction, they observed a much better stability of the perovskite material compared to pristine FAPI thanks to the addition of this hydrophobic spacer. Furthermore, the increased stability in ambient conditions of the resulting devices was also revealed. Doing so, they provided a new way to stabilize FAPI without using the more unstable MA cation.

A study from Grancini *et al.* added aminovaleric acid cation ($HOOC(CH_2)_4NH_3^+$, AVA^+) to a MAPI 3D perovskite in an n-i-p architecture, with Spiro-OMeTAD HTL and gold metal electrode. With an optimal 3 mol% AVAI ratio, the formation of 2D perovskite phases was showed with photoluminescence and Raman spectra, leading to a champion PCE reduction from 15.95% to 14.6% compared to pure MAPI. However, it led to better stability, with devices maintaining more than 60% of their initial efficiency after 300 hours of continuous illumination under an argon atmosphere, while pure MAPI devices kept less than 50%. They also developed an HTL-free structure, replacing Spiro-OMeTAD and gold with a hydrophobic carbon electrode. This structure was applied in 0.64 cm^2 cells and 47.6 cm^2 modules using the 3% AVAI-MAPI absorber, leading to respective PCEs of 11.9 and 10.1%. Remarkably, no efficiency loss was measured after more than 10 000 hours in ambient conditions. This result highlighted the impact of both hydrophobicity from the 2D perovskite and the HTL-free structure on device ambient stability [Grancini *et al.* 2017].

The incorporation of BA cation in a double-cation perovskite was studied by Wang *et al.* They obtained a champion PCE of 20.6% with a $BA_{0.05}(FA_{0.83}Cs_{0.17})Pb(I_{0.8}Br_{0.2})_3$ composition, and observed 2D perovskite platelets with perpendicular orientation to the substrate thanks to scanning electron microscopy. They also discussed the mechanisms at stake in the 2D/3D structure, schematized in Figure 1.24. Here, 2D perovskite phases of higher bandgap acted as "barriers" and confined charge carriers in the lower bandgap 3D perovskite grains. This behavior, similar to type-I quantum wells, passivates grain boundaries, preventing charge carriers recombinations at grain boundaries and leading to higher device V_{OC} [Wang *et al.* 2017].

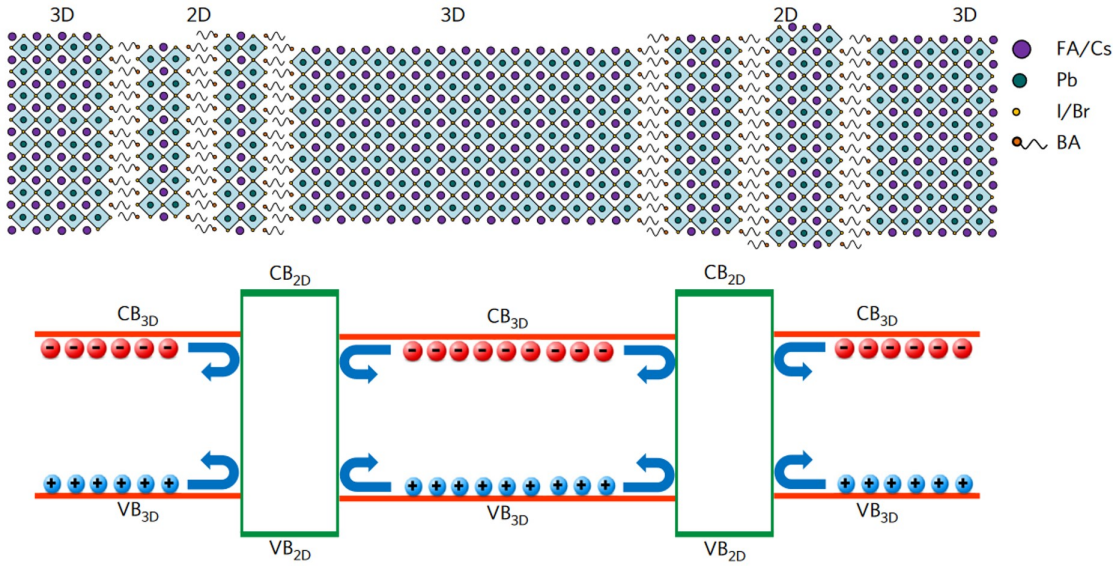

Figure 1.24: Illustration of a mixed-phase 2D–3D heterostructure, and its proposed electronic band offsets. Reproduced from [Wang *et al.* 2017].

Another effect attributed to mixed 2D/3D heterostructures is the suppression of thermal-induced ionic migration within the perovskite layer, responsible for hysteresis effect observed in IV measurements and intrinsic instability [Liu *et al.* 2020, Zheng *et al.* 2020]. Due to the bulky nature of the organic spacers, they provide a physical barrier to ionic motion within the layer and act as a "self-encapsulation," potentially decreasing the hysteresis effect observed in PSCs and increasing their thermal stability.

In bulk incorporation structures, controlling the nucleation of the 2D and 3D perovskite phases to optimize the 2D/3D heterostructure is a major challenge. In this regard, the application of specific additives was discussed. For examples, Ruggeri *et al.* used ammonium thiocyanate (NH_4SCN) to slow down the nucleation and crystallization of 3D domains in a $PEA_2FA_2(Pb_{0.5}Sn_{0.5})_3I_{10}$ perovskite, whereas Kim *et al.* applied lead thiocyanate $Pb(SCN)_2$ additive growth in a mixture of $(FA_{0.65}MA_{0.2}Cs_{0.15})Pb(I_{0.8}Br_{0.2})_3$ and 2 mol% of $PEA(I_xSCN_{1-x})$ to accelerate the 3D perovskite grain growth [Ruggeri *et al.* 2019, Kim *et al.* 2020b].

1.4.2 Surface treatment

Surface treatment 2D/3D heterostructures appeared in the literature the same year as bulk incorporation, with the work of Hu *et al.* released in 2016. After crystallizing a MAPI absorber in an n-i-p architecture, they deposited a mix of phenylethylammonium iodide (PEAI) and methylammonium iodide (MAI) precursors in IPA on the MAPI film and annealed it. Thanks to X-ray diffraction and grazing incidence wide-angle X-ray scattering, they reported the formation of a 20 nm thick RP $(PEA)_2(MA)_4(Pb_5I_{16})$ (n = 5) 2D perovskite layer on top of the MAPI bulk [Hu *et al.* 2016b].

Later, Ma *et al.* changed the nature of the precursor solution used to form the 2D perovskite layer. Instead of spin-coating a mixture of spacer and A-site cations (PEAI and MAI) on the 3D perovskite, they used a solution containing only the spacer cation precursor: cyclopropylammonium iodide ($C_3H_5NH_3I$, CAI) [Ma *et al.* 2016]. Consequently, they formed a 2D CA_2PbI_4 perovskite layer (n = 1) by the reaction of CAI precursors with PbI_2 excess from the 3D perovskite, confirmed by comparing the X-ray diffraction pattern of their 2D/3D structure with the diffractogram of a purely CA_2PbI_4 layer. This synthesis method remains the current standard for developing 2D/3D heterostructures with surface treatment in the literature, with changes only in the nature of the solvent and the spacer cation or in the 3D perovskite's composition. Furthermore, the mechanism describing the reaction between spacer precursor and PbI_2 excess is still central in explaining the formation of the 2D perovskite layer.

The beneficial effects of 2D/3D heterostructures are similar in surface treatment to bulk incorporation configuration, but apply to the interface between the perovskite and the charge transport layer instead of the perovskite layer itself. Thanks to its higher hydrophobicity, demonstrated by contact angle measurements, the 2D perovskite encapsulates the 3D perovskite against moisture, increasing device stability. Several works highlighted this feature by increasing the hydrophobicity of PEA spacer with the addition of fluorine to the molecule, which, after forming a 2D layer, was correlated with better device stability towards moisture compared to non-fluorinated PEA spacer [Zhou *et al.* 2019, Liu *et al.* 2019a, Wang *et al.* 2022]. Sutanto *el al.* studied a 2D/3D heterostructure based on thiophenemethylammonium iodide (SC_5H_5NH3I, TMAI) spacer precursor, deposited on a $Cs_{0.08}FA_{0.8}MA_{0.12}Pb(I_{0.88}Br_{0.12})_3$ perovskite. They obtained similar PCE with an improvement in stability under illumination. They explained it with the ability of the 2D layer to block thermal-induced ionic migration from the 3D perovskite, as seen in Figure 1.25a, thus protecting the HTL from further degradation.

PCE improvement in surface treatment 2D/3D structures was also attributed to passivation effects. The 2D layer should passivate the 3D perovskite surface, decreasing non-radiative recombinations at its interface and leading to higher V_{OC}, while the reduction of ionic migration would reduce current hysteresis [Liu *et al.* 2020, Gharibzadeh *et al.* 2019]. In perovskites, the n-factor increase usually leads to lower energy levels

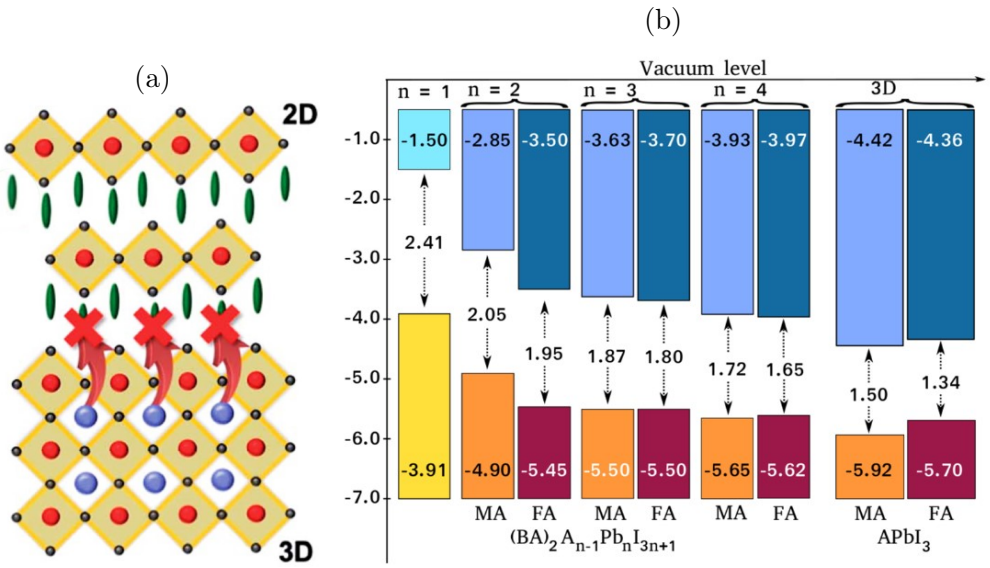

Figure 1.25: (a) Illustration of ionic migration suppression induced by the 2D/3D perovskite interface. Reproduced from [Sutanto *et al.* 2020]. (b) Evolution of energy band alignment for $(BA)_2A_{n-1}Pb_nI_{3n+1}$ perovskites with n = 1, 2, 3, 4, and ∞, with A = MA or FA cations. Reproduced from [Zibouche and Islam 2020].

for both VB and CB, as illustrated in Figure 1.25b. This phenomenon promotes hole transport from higher to lower n-factor phases [Liu *et al.* 2017b, Zibouche and Islam 2020] and is mentioned as electronic passivation. Therefore, in 2D/3D structures, the higher energy level alignment of the 2D layer should promote hole extraction from the 3D perovskite towards the 2D layer while blocking electrons and improving charge extraction. However, passivation of the perovskite/ETL interface was also observed after forming a 2D perovskite at this interface, questioning the real impact of the electronic passivation [Mahmud *et al.* 2020].

With surface treatment, having fine control over the formation of 2D and 3D perovskite phases like in bulk incorporation is unnecessary, because 2D and 3D layers are formed sequentially. However, because the 2D spacer precursor solution is deposited on the 3D layer, its solvent needs to solubilize the spacer precursors without dissolving the 3D perovskite. In this regard, isopropanol (IPA) has been the most popular and efficient solvent, but due to highly polar nature, a potential degradation of the 3D layer was suggested and the use of other solvents, such as chloroform, was reported [Yoo *et al.* 2019, Sidhik *et al.* 2022]. Furthermore, due to the thinness of the 2D layer in typical 2D/3D structures (on the order of few nanometers), assessing the properties of the 2D phase with the already mentioned common characterization techniques (X-ray diffraction, scanning electron microscopy, etc.) is a challenge in itself.

Other processes were explored for the synthesis of the 2D perovskite. Bai *et al.* dissolved PEAI precursor in toluene and used this solution as an anti-solvent [Bai *et al.* 2017]. In doing so, they combined the anti-solvent washing of the 3D perovskite with the 2D perovskite spacer solution deposition, forming a "dimensionally graded layer" instead of a 2D/3D interface. Several works investigated sequential vapor deposition of 2D/3D heterostructures. Still, like in the 3D perovskite literature, such deposition technique remains more marginal and leads to lower PCEs, as illustrated in Figure 1.23b [La-Placa *et al.* 2019, Lin *et al.* 2019].

Finally, the use of spacer cation precursors not converted into a 2D perovskite layer was reviewed. Several groups respectively studied the passivation of a 3D perovskite layer with PEAI, 1-naphthylmethylammonium iodide ($C_{10}H_7CH_2NH_3I$, NMAI), and para-fluorophenylethylammonium iodide (4-FPEAI) spacer cation precursor solutions. Thanks to X-ray photoelectron spectroscopy, they reported the formation of a new layer that modified the material's surface chemistry without forming a 2D perovskite phase, and associated common beneficial effects (surface passivation, reduced charge accumulation, etc.) to this new layer [Jiang *et al.* 2019a, Liang *et al.* 2020, Jiang *et al.* 2021]. Therefore, they questioned the need to create a 2D layer to obtain efficient passivation of the 3D perovskite absorber and suggested that the spacer cation may be sufficient for this purpose, which still needs to be resolved in the literature.

1.5 Summary

This first chapter introduced the general knowledge behind this thesis work. In the first place, this introduction was centered on the physical background of solar cells, starting with sunlight and explaining how it is converted into electricity by solar cells using semiconductor materials. Then, we discussed the theoretical efficiency limit of single-junction solar cells, and how tandem solar cells are able to bypass this limit by combining silicon and hybrid halide perovskite materials.

We presented hybrid halide perovskites, their structure, and the remarkable opto-electronic properties that make them suitable for integration in solar cells. After that, we detailed the development of the perovskite solar cell technology, the main materials and processes used in the literature, and how they evolved through a decade of existence. Despite promising development, perovskite technology must tackle several challenges to enter the photovoltaic market, such as improving its stability. The stability subject led us to hybrid halide 2D perovskites. We revealed the unique nature of this specific class of perovskites and explained how their layered structure dictates their opto-electronic properties. Even though these opto-electronic properties were constraining for solar cell applications and delayed their use, photovoltaic devices using 2D perovskites have eventually been developed, and nowadays, this technology is promising. We covered how 2D and 3D perovskites were combined to improve the stability of 3D perovskite solar cells. We described the two main classes of 2D/3D heterostructures: bulk incorporation and surface treatment, and we explained how these two classes differ and the benefits they provide.

This knowledge helped us to develop a 2D/3D perovskite structure and integrate it into perovskite solar cells. In this regard, it was crucial to investigate the properties of our 2D/3D heterostructure to understand this material more thoroughly and bring answers to the questions that did not make consensus in the literature. Therefore, our efforts were concentrated on the physical properties of the 2D/3D material to establish if a 2D perovskite layer was formed, and if so, which phases were constituting it and what their thickness was. Furthermore, the formation mechanisms of these structures were also not treated extensively in the literature and seemed an important topic to study. For this purpose, we applied common characterization techniques used in perovskites, such as X-ray diffraction, photoluminescence measurements, or X-ray photoemission spectroscopy. All these techniques will be presented in the next chapter, along with the synthesis process of PSCs.

Chapter 2

Experimental processes and methods

This chapter presents all the techniques applied in this work, from the synthesis of samples to their characterization. The first section contextualizes every step of the triple-cation baseline process. The choices made for synthesizing the 2D/3D heterostructure are also justified. The second part provides the theoretical background of each characterization method, from the characterization of perovskite solar cell devices to the physico-chemical properties of the perovskite absorber itself.

Contents

2.1 Fabrication of perovskite solar cells

Our focus in this thesis work was to implement a 2D/3D perovskite heterostructure into the main fabrication process of PSCs of IPVF, called the baseline process. Therefore, we were interested specifically in the development of a 2D treatment, to transform a 3D perovskite absorber into a 2D/3D heterostructure. The baseline process has been the starting point for the development of most samples, whether for device-oriented studies, or for studies dedicated to the perovskite material itself. Hence, this section will detail every step of this process. The architecture is based on a mesoporous n-i-p structure, and the layers will be presented in their fabrication order, corresponding to the order in which sunlight passes through the stack.

2.1.1 Transparent substrate

For the fabrication of samples, the first step was the preparation of transparent conductive oxide (TCO) substrates. We used FTO TEC-7/3.1 commercial samples bought from Solems, which consist of a 3.1 mm thick soda-lime glass, on top of which a 600 nm thick FTO conductive layer is formed by chemical vapor deposition. This FTO layer is indicated with a resistance of around 6-8 Ω/sq. This material was bought in 30x30 cm^2 slabs, which were cut into 2x2 cm^2 cells. For practical reasons regarding the last step of device preparation, solar cells were prepared in batches containing at least 16 samples. This number could, however, be increased if necessary, i.e., for the preparation of samples destined for material studies.

A first pattern was applied to the FTO layer to create an insulated area for the deposition of the metallic cathode. Originally, this pattern was performed with chemical etching of the layer. The sample surface was covered with Kapton tape, except for the soon-to-be-etched line. A combo of zinc powder and hydrochloric acid solution (diluted at 30% in water) was applied on this line to chemically etch the FTO layer of this unprotected line. During this thesis, chemical etching of the FTO layer was replaced with laser patterning. This replacement did not lead to any specific improvement in device results but provided several advantages for the synthesis team, such as a much faster and more reproducible process.

Before moving on to the next stage, etched samples underwent a cleaning procedure of three consecutive ultrasound baths with 50°C heating. The first bath occured in a 2% vol. solution of RBS alkaline detergent in deionized water for 30 minutes. Subsequent baths were realized in acetone and isopropanol for 20 minutes each.

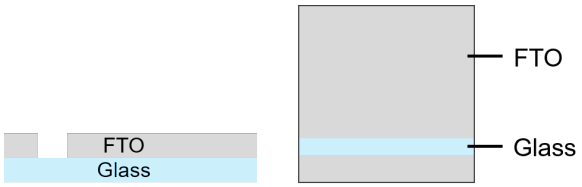

Figure 2.1: Side and top representation of substrates after laser patterning and ultrasonic cleaning.

2.1.2 Titanium oxide ETL

Once cleaned, etched glass-FTO substrates were ready for deposition of the following layer: the titanium oxide ETL, a bilayer made of compact-TiO_2 (c-TiO_2) hole blocking layer and of mesoporous-TiO_2 (m-TiO_2) layer. c-TiO_2 layer formation is one of the processes that was changed during this work. Initially, it was realized using a spray pyrolysis process, later replaced with an Atomic Layer Deposition (ALD) process. Both processes will be presented, as they were each used for a significant part of this work and imply a few modifications on sample preparation.

Compact-TiO_2 by spray pyrolysis

For spray pyrolysis deposition, etched and cleaned substrates were treated with a UV-Ozone cleaner for 15 minutes before being placed on a hot plate at 500°C for 30 minutes of annealing. On the hot plate, samples were lined up into four to five lines in a way that aligned the etched-FTO lines of each sample. Glass slabs were used to separate each sample line, and thin silicon pieces were placed on the substrates to protect them from c-TiO_2 layer spray deposition for proper electrical contact of the cells. This setup is illustrated in Figure 2.2.

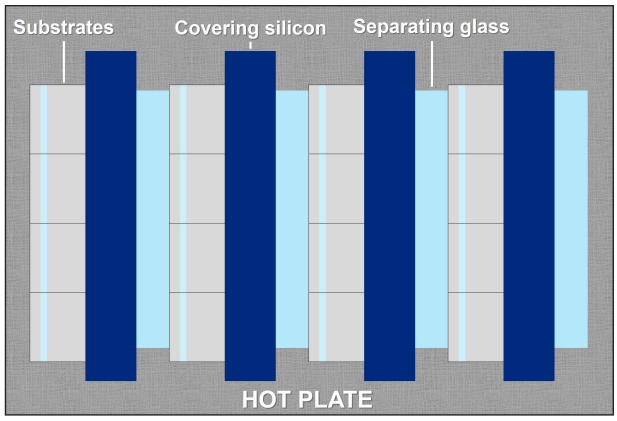

Figure 2.2: Schematized representation of spray pyrolysis deposition setup for c-TiO_2 on glass-FTO substrates.

c-TiO_2 solution was prepared right before deposition from a mix of 2.4 mL of titanium diisopropoxide bis(acetylacetonate) (TAA) (TAA precursor solution diluted at 30 vol.% in IPA), 1.6 mL of acetylacetone, and 36 mL of IPA. This solution was sprayed on the substrates with a nozzle over 20 deposition steps, divided into four runs with different directions for better homogeneity: front to back, back to front, left to right, and right to left. After these 20 steps, a c-TiO_2 layer of around 20 nm was formed on the substrates. Samples were left at 450°C for 15 minutes of annealing and then cooled to room temperature. Even though spray pyrolysis allowed the development of efficient solar cell devices, this method came with some inconveniences:

- **Storage requirements**. TAA solution was hygroscopic, and lesser quality films were obtained in case of its hydration. Thus, it required glovebox environment storage, and the solution must be prepared before deposition.

- **Poor homogeneity and reproducibility**. While considered homogeneous on the scale of a single cell (4 cm^2), over an entire hotplate (> 200 cm^2), large thickness variations of the TiO_2 layer were measured. Furthermore, at IPVF, this process was performed manually, adding a dependency on the operator's gestures to the already significant sensitivity to environmental conditions (moisture, temperature, dust, affecting the aerosol droplets' spread and size). Therefore, the process was very operator-dependant and rather poorly reproducible.

- **High temperatures**. To form a proper layer with spray pyrolysis, high temperatures (> 450 °C) were required, limiting the number of usable substrates (e.g., ITO, that cannot withstand such temperatures), restricting in the same way potential applications of perovskite solar cells.

Compact-TiO_2 by ALD

ALD is a vapor phase deposition technique. It consists of the sequential exposition of a substrate to several molecular precursors. A series of self-limiting chemical reactions between the precursors leads to the growth of a thin film on the substrate. Nowadays, ALD found applications in various photovoltaic technologies, such as the formation of AlO_x layers in PERC silicon solar cells, ZnO layers in thin film architectures, or TiO_2 and SnO_2 ETLs in perovskite devices [Hossain *et al.* 2020]. Various studies demonstrated potential benefits of ALD-TiO_2 compared to spray pyrolysis-TiO_2 [Lu *et al.* 2015,Roelofs *et al.* 2016]. In this regard, a c-TiO_2 ALD process was developed at IPVF in the framework of O. Fournier thesis work [Fournier 2021]. This ALD process consisted of the repetition of a four-steps ALD cycle within a closed reactor, illustrated in Figure 2.3:

1. A first precursor, titanium tetraisopropoxide (TTIP), was introduced in the reactor and chemisorbed on available sites of the substrate surface.

2. The reactor was purged with an inert gas (here N_2) to remove unreacted TTIP.

3. A second precursor, water (H_2O), was introduced in the reactor, and chemisorbed aswell on the substrate surface, reacting with TTIP to form a TiO_2 layer.

4. The reactor was purged once more with N_2 to remove unreacted gaseous H_2O, along with potential byproducts of the reaction.

Compared to spray-pyrolysis, this ALD process presented slight improvements in solar cell device efficiency, while adding several practical advantages:

- **Easier storage**. TTIP and H_2O precursors used for the reaction could be stored in the ALD reactor for weeks without any noticeable degradation of film quality.

- **Homogeneity and reproducibility**. ALD process allowed a good homogeneity of the deposited film over substrates up to 230 cm^2. Furthermore, the deposited layer thickness scaled with the number of ALD cycles, providing fine control over film thickness. Furthermore, good reproducibility of the deposition was observed with this method, which could only be affected by the precursors' quality.

- **Lower temperatures**. c-TiO_2 films could be deposited with ALD at lower temperatures (200 °C), allowing more diverse substrates to be used and expanding potential applications while reducing the energy cost of the process.

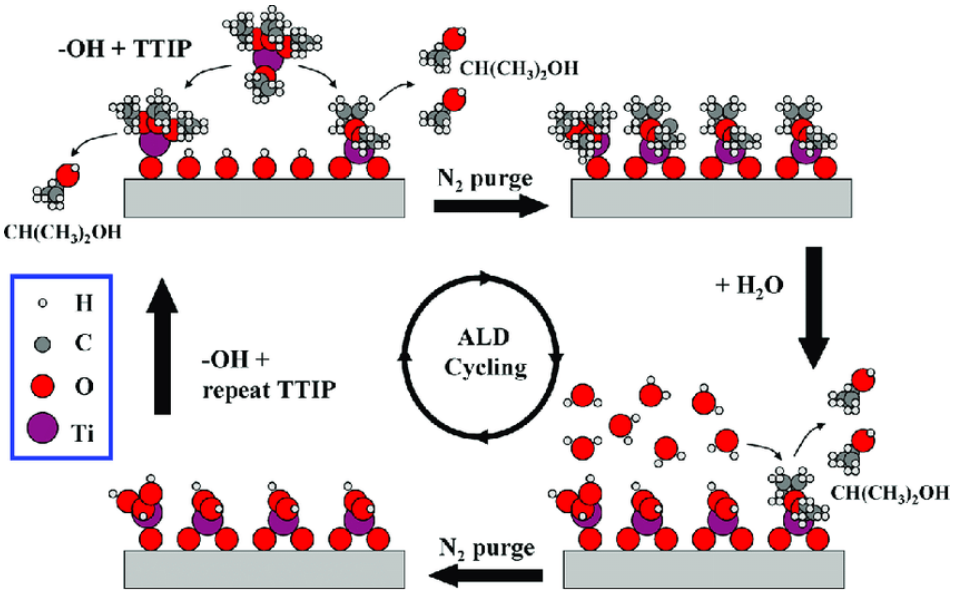

Figure 2.3: Schematic representation of an ALD cycle for the formation of a c-TiO_2 layer. Reproduced from [Hu *et al.* 2016a].

Therefore, ALD was implemented in the baseline process as the new primary method for c-TiO_2 layer synthesis. As a result, glass-FTO substrates underwent laser patterning, ultrasonic cleaning, and ALD c-TiO_2 deposition as 225 cm^2 slabs, with a simpler covering of the substrate top and bottom sides to prevent c-TiO_2 deposition. The slabs were then cut into 4 cm^2 cells for the next step: spin-coating deposition of m-TiO_2 layer.

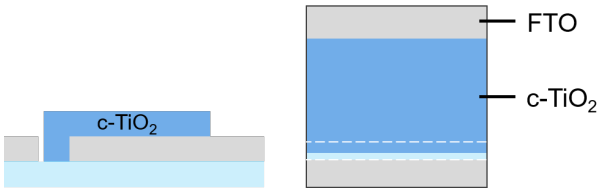

Figure 2.4: Side and top representation of substrates after c-TiO_2 ALD deposition.

Mesoporous-TiO_2 layer by spin-coating

Samples preparation for m-TiO_2 consisted of covering the substrates' top and bottom sides - already masked for c-TiO_2 deposition - with Kapton tape to prevent the deposition of m-TiO_2 layer. Taped substrates were then placed under 15 mins UV-Ozone cleaning.

At least 24 hours before deposition, a m-TiO_2 nanoparticles colloidal solution was prepared with 30 NR-D titania paste diluted in absolute ethanol from Greatcell Solar Materials, with an ethanol:TiO_2 mass ratio of 7:1. The spin-coating deposition of 50 μL of this solution occurred in ambient atmosphere for a duration of 30 s, at a speed of 4000 rpm and a 2000 $rpm.s^{-1}$ acceleration. After deposition, a hot plate annealing up to 500 °C was applied to the substrates following the program described in Table 2.1, resulting in a m-TiO_2 layer of around 120 nm thick.

After cooling to 150 °C, samples were placed in UV-Ozone cleaning for 30 mins before glovebox transfer for the synthesis of the 3D perovskite absorber.

Table 2.1: Annealing parameters of the mesoporous-TiO_2 layer.

Steps	**1**	**2**	**3**	**4**	**5**
Rise time (min)	5	15	5	5	5
Temperature (°C)	125	325	375	450	500
Dwell time (min)	5	5	5	15	15

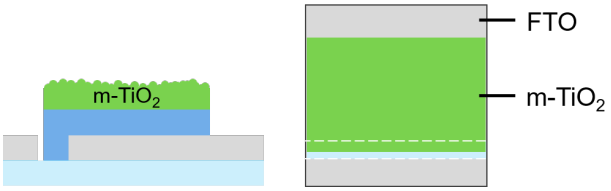

Figure 2.5: Side and top representation of substrates after m-TiO_2 spin-coating.

2.1.3 Triple-cation 3D perovskite absorber

The baseline perovskite composition was already used for a few years when this work started. This process was developed on a FAPI perovskite, presenting better properties than MA-based compositions [Rehman *et al.* 2017]. MA and Cs were combined to FA cations, while Br was added to I halide to optimize the tolerance factor of this FAPI composition, its bandgap, and to stabilize it, preventing the formation of δ-FAPI [Jeon *et al.* 2015, Rehman *et al.* 2015]. These inclusions led to the mixed-halide triple-cation $Cs_{0.05}(MA_{0.17}FA_{0.83})_{0.95}Pb(I_{0.83}Br_{0.17})_3$ 3D perovskite stoichiometry, fairly common in the literature. This composition was completed with a 2.0% stoichiometric PbI_2 excess, revealed as a way to improve device efficiency [Jacobsson *et al.* 2016, Bi *et al.* 2016].

The perovskite precursor solution was obtained by mixing two primary solutions. A first cesium iodide (CsI) solution at 1.5 mol.L^{-1} in DMSO was prepared and stirred overnight at room temperature before use. A second solution was prepared by mixing 0.2 mmol of methylammonium bromide (MABr), 0.2 mmol of lead bromide ($PbBr_2$), 1.0 mmol of formamidinium iodide (FAI), and 1.1 mmol of lead iodide (PbI_2) in 1 mL of an 800 μL DMF / 200 μL DMSO mix (4:1 volume ratio). After 2 hours of stirring at room temperature, 1 mL of this solution was mixed with 42 μL of the CsI solution. This mix was stirred for another 15 mins before deposition. The triple-cation solution was spin-coated on TiO_2-covered substrates following the program shown in Figure 2.6.

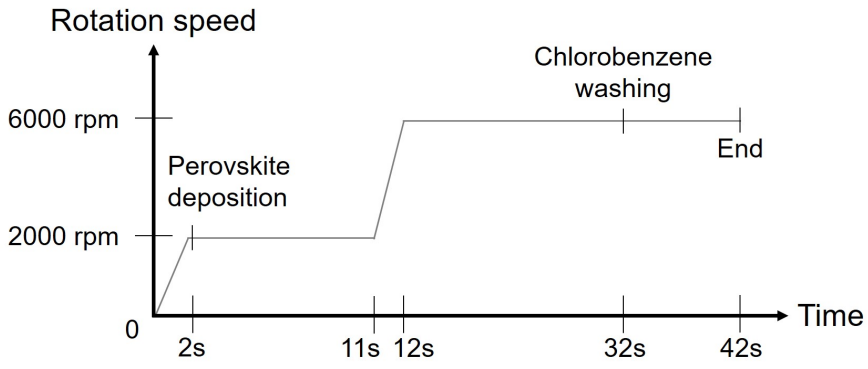

Figure 2.6: Spin-coating program for triple-cation baseline 3D perovskite synthesis.

This program contained two main stages. The first one consisted of a 2000 rpm rotation for 12 s, with a 1000 rpm.s^{-1} acceleration. After 2 s of acceleration, 35 μL of the perovskite solution was deposited on the substrate, and the stage kept rotating for 9 s at 2000 rpm. After accelerating to 6000 rpm in 1 s, the second stage began for 30 s. This stage was dedicated to depositing 100 μL of chlorobenzene antisolvent 12 s before the rotation's end. The intermediate films were then annealed on a hot plate at 100°C for 30 min to crystallize the perovskite film.

Once the 3D perovskite layer crystallized, samples could go through the next step in Section 2.1.4 : 2D solution treatment. Some samples, later designated as "pristine" 3D perovskite, were left without 2D perovskite addition as references.

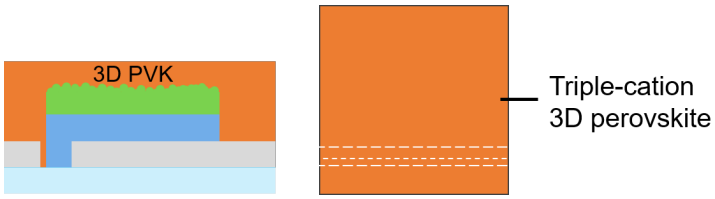

Figure 2.7: Side and top representation of substrates after 3D perovskite synthesis.

2.1.4 2D perovskite addition

For 2D perovskite addition, the choice of 2D/3D structure and 2D spacer cation was based on the knowledge available in the literature at that time, which was still quite an emerging subject. Devices based on 2D/3D structures made with a 2D capping layer on the 3D perovskite absorber seemed more efficient than mixed 2D/3D phases [Yan *et al.* 2018, Kim *et al.* 2019a]. Besides, controlling the formation of the 2D/3D structure appeared easier with two separate layers instead of a single one.

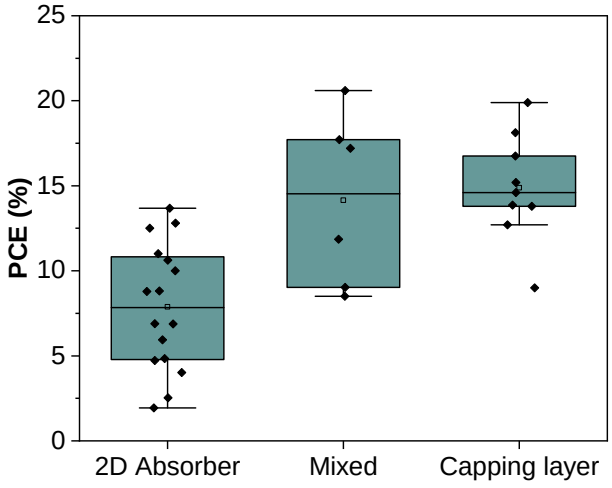

Figure 2.8: PCE of devices using a 2D perovskite absorber, 2D/3D mixed phases, or 2D/3D structures with 2D capping layer. Reproduced from [Yan *et al.* 2018].

Among the many available spacer cations, the investigation of 2D/3D structures began with classic cations already used in 2D perovskite, such as BA or PEA. Significant works based on these spacers proposed noticeable device improvements. Furthermore,

at that time, the LuMIn research group directed by E. Deleporte had already been studying 2D perovskites for more than a decade. More specifically, the team possessed an important experience with PEA-based perovskites. The group had characterized optical and structural properties of various PEA_2PbX_4 phases, studied fluorinated versions of these materials, and developed synthesis methods of monocrystalline phases of PEA_2PbI_4 [Zhang *et al.* 2010, Wei *et al.* 2013, Wei *et al.* 2014, Lédée *et al.* 2017].

Therefore, for developing 2D/3D perovskite heterostructures, we focused on synthesizing a 2D perovskite capping layer on top of the baseline triple-cation 3D perovskite absorber. For the 2D phase spacer cation, preliminary experimentation was conducted on PEAI and 4-FPEAI cation salts. 4-FPEAI was retained as the main cation for this work for a double purpose. First, these tests seemed in agreement with literature data from Section 1.4.2, indicating better device efficiency and stability compared to devices using non-fluorinated PEAI. Furthermore, the presence of fluorine could be used as a probe element in chemical characterizations to track the presence of the 2D cation salt.

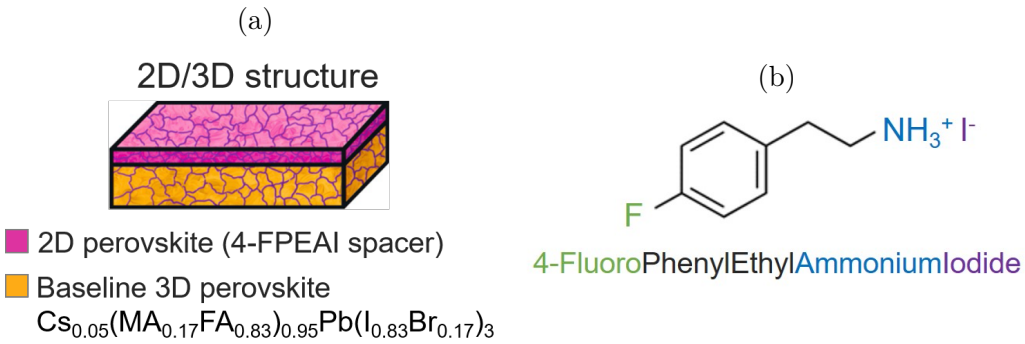

Figure 2.9: (a) Representation of the bi-layer 2D/3D heterostructure used in this work, adapted from [Ortiz-Cervantes *et al.* 2019]. (b) Illustration of the 4-FPEAI spacer molecule used for 2D perovskite treatment.

The synthesis of 4-FPEAI cation salts was realized by G. Trippé-Allard. A solution of para-fluorophenylethylamine (5 mL, 38.1 mmol) in ethanol (20 mL) was added drop by drop to another solution of hydriodic acid (57%, 5.3 mL, 1.05 eq.) and hydrophosphoric acid (0.5 mL) in ethanol (50 mL), cooled to 0°C. The solution was stirred at room temperature for 1 hour before removing the solvent in vacuo. The crude was purified by re-crystallization in ethanol, forming 7.0 g of 4-FPEAI white crystals with a 69% yield.

One of the main constraints of 2D/3D structures in capping layer is to use a solvent solubilizing the 2D cation salt without dissolving the crystallized 3D perovskite. In this regard, IPA was chosen as 2D solution solvent, as it was already significantly used. Hence, 4-FPEAI solution was prepared by dissolving 4-FPEAI crystals in IPA. Typical solution concentrations of 2.5, 5, and 10mg.mL^{-1} were used across this manuscript. This solution was stirred for 2 hours at room temperature. After annealing the 3D layer, 100 μL of the 4-FPEAI solution was spin-coated on each 4-FPEAI treated sample at 4000 rpm for 30 s, with 4000 rpm.s^{-1} acceleration, followed by 100°C annealing for 5 min.

After this second annealing, the formation of a 2D perovskite layer on top of the 3D absorber was supposedly obtained. Samples destined for material characterization were taken out of the glovebox in their current state as so-called half-cells (being either pristine 3D or 4-FPEAI treated half-cells). Meanwhile, samples planned as solar cell devices underwent HTL layer deposition, described in Section 2.1.5.

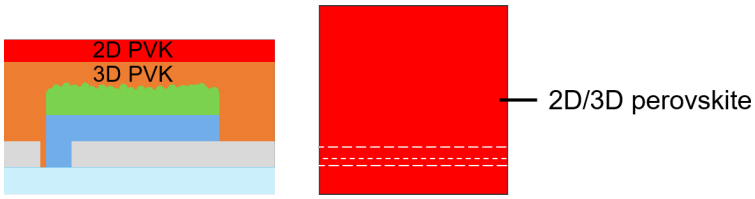

Figure 2.10: Side and top representation of substrates after 2D perovskite layer spin-coating.

2.1.5 Organic HTL layer

The choice of HTL for solar cell devices also evolved during this work. In the early part, Spiro-OMeTAD (2,2',7,7'-tetrakis(N,N-di-p-methoxyphenyl-amine)9,9'-spirobifluorene) was the only HTL used in the baseline process, as it was a well-optimized material and a reference HTL in perovskite solar cells for many years (and remains as of nowadays) [Hawash *et al.* 2018, M. Rombach *et al.* 2021].

To obtain high hole mobility, which is a necessary factor for efficient hole collection and thus, efficient devices, Spiro-OMeTAD needs to be doped. This doping was realized by adding to the Spiro-OMeTAD lithium bistrifluoromethanesulfonimidate (LiTFSI) and tris[2-(1H-pyrazol-1-yl)-4-tert-butylpyridine]cobalt(III) tri[bis(trifluoromethane) sulfonimide] (FK209) p-type dopants, as well as 4-tertbutylpyridine (t-BP). However, these dopants came at a cost, as they were revealed as important sources of intrinsic, moisture, and thermal instability [Lamberti *et al.* 2019, Zhao *et al.* 2017], which was detrimental to device aging and was incompatible with thermal encapsulation processes. The HTL literature has shown more and more interest in other materials, such as poly[bis(4-phenyl)(2,4,6-trimethylphenyl)amine] (PTAA), or copper(I) thiocyanate (CuSCN) [Yang *et al.* 2020a], and has gradually been shifting towards the use of fewer dopants, or even dopant-free materials. [Zhou *et al.* 2018, Pham *et al.* 2020].

Among HTL alternatives, PTAA was chosen at IPVF as a new device route for various reasons. Firstly, undoped PTAA shows a more favorable HOMO energy level position of -5.2 eV, and so, a better energy level alignment than Spiro-OMeTAD [M. Rombach *et al.* 2021]. Therefore, optimal transport properties of the material are obtained with much lower concentrations of dopants than the ones required in Spiro-OMeTAD and excluded the use of FK209 cobalt complex. Consequently, devices using PTAA as the HTL offered better stability than Spiro-based devices, and after some optimization of the layer, quite similar performances. Therefore, PTAA gradually replaced Spiro-OMeTAD as the baseline process HTL and was the exclusive HTL in devices used for stability measurements. After confirming the compatibility of PTAA with the 2D perovskite layer addition, it was also added to this work.

For HTL preparation, regarding the material used, a solution of Spiro-OMeTAD or PTAA was solubilized and stirred at least 2 hours before deposition:

- For Spiro-OMeTAD solution, 110 mg of Spiro-OMeTAD powder was dissolved in 1 mL of chlorobenzene. Right before deposition, this solution was doped with three oxidizing additives: 17 μL of FK209 at 5 mmol.L^{-1}, 25 μL of LiTFSI at 45 mmol.L^{-1}, and 45 μL of a commercial t-BP solution at 310 mmol.L^{-1}.

- For PTAA solution, 10 mg of PTAA powder was dissolved in 1 mL of toluene. As mentioned previously, this solution was only doped with two additives: 2.4 μL of LiTFSI solution and 3.75 μL of t-BP solution.

The HTL was formed by spin-coating on the pristine or 2D-treated perovskite layer 35 μL of HTL solution at 3000 rpm for 30 seconds, after a 1500 rpm.s^{-1} acceleration, without any further annealing. Samples were then taken out of the glovebox for the deposition of a last layer.

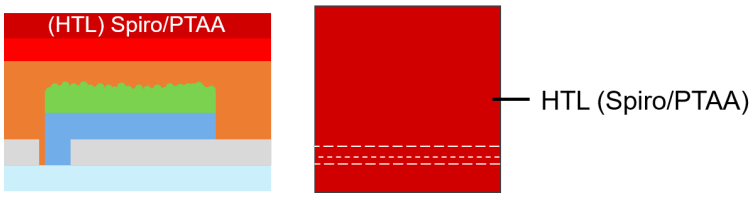

Figure 2.11: Side and top representation of substrates after HTL spin-coating.

2.1.6 Metallic back contact

A 100 nm gold electrode was deposited as the metallic back contact to finalize the fabrication of perovskite solar cells. The substrates' top and bottom edges were chemically etched with DMF down to the FTO layer. Subsequently, a 0.16 mm^2 active area was delimited on the samples. The gold contact was formed on the substrates by E-beam evaporation under vacuum, using a Plassys MEB550S metal evaporator, which is schematized in Figure 2.12a.

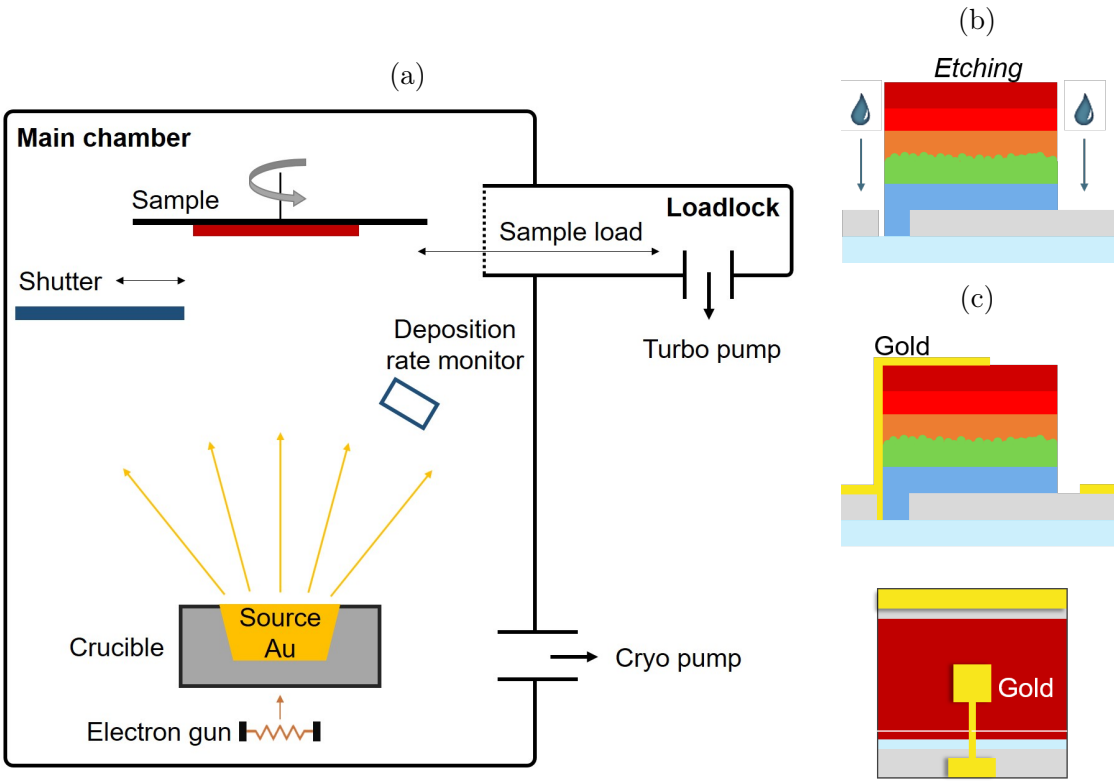

Figure 2.12: (a) Illustration of Plassys MEB550S e-beam evaporator. (b) Side representation of substrates after chemical etching post-HTL deposition. (c) Side and top representation of substrates after gold electrode evaporation.

The procedure consisted in loading the samples into a limited vacuum (10^{-2} mbar) loadlock, before transferring them into the main chamber. There, a cryogenic pump got the chamber to a sufficient vacuum (10^{-7} mbar) for evaporation. Gold was melted and evaporated from a crucible by electronic bombardment. Due to the vacuum, the evaporated metal reached the sample surface and condensated to form a metallic film. The first 10 nm of gold were deposited with a reduced deposition speed of 0.01 nm.s^{-1} to prevent any degradation of the HTL and perovskite layers. The remaining 90 nm were evaporated at a speed of 0.1 nm.s^{-1}. Finally, the cells were removed from the evaporator, and were completed by bringing electrical contacts to the front side with copper tape.

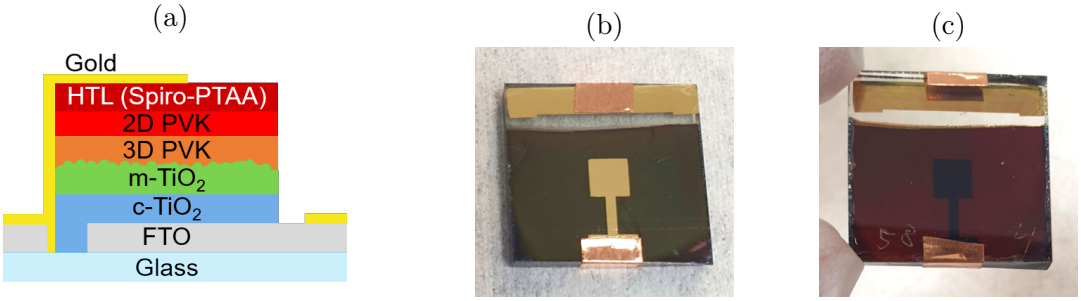

Figure 2.13: (a) Side representation of a baseline perovskite solar cell full stack. Picture of a finalized cell: (b) Back-side, and (c) Front-side.

2.2 Characterization techniques

After describing sample synthesis in the previous section, this section is dedicated to presenting the main characterization methods used, separated between the ones performed on full devices and those on half-cells, focused on characterizing the perovskite material.

2.2.1 Assessing device performances

IV measurements

The most important feature to assess in our solar cell devices was their efficiency, allowed by IV measurements. The theoretical background of such analysis was presented in Section 1.1.2. Therefore, only the measurement setup used will be discussed here.

IV measurements were performed in ambient environmental conditions, with glass-side illumination of the samples. The devices were covered with metallic masks to avoid any influence of the non-active area on the measurements. 3x3 mm^2 aperture masks were used to prevent misalignment between the mask and the 0.16 cm^2 active area, leading to a final 0.09 cm^2 cell active area. By knowing the exact active area of our devices, the current (in mA) measured during IV measurements was converted into current density (in mA.cm^{-2}), leading to the current density-voltage (JV) characterization of the samples.

An Oriel Sol3A AAA-class xenon lamp simulator from Newport was used to illuminate the samples with AM 1.5G solar spectrum filter and a light intensity of 100 mW.cm^{-2}. JV characteristics were obtained within a bias voltage range of -0.2 to 1.2 V with a computer-controlled Keithley 2400, at a scanning speed of 20 mV.s^{-1}. Scans were performed in forward (FW) and reverse (RV) bias directions to detect potential hysteresis. After JV scans, MPP tracking under illumination was performed for a few minutes.

External Quantum Efficiency

Another way to characterize devices was the measure of their External Quantum Efficiency (EQE), which is the ratio between the number of charge carriers collected in a device to the number of incident photons of a given energy.

EQE characterization of a device provides some information on its absorber properties, illustrated in Figure 2.14. An ideal theoretical EQE would show a square shape, with EQE = 0 at $E_{incident} < E_g$, and EQE = 1 for $E_{incident} > E_g$, implying that all photons of each wavelength are absorbed, and the resulting charge carriers are also all collected. However, several phenomena lower the experimental EQE. First, photons need to be absorbed in order to be converted to charge carriers. Hence, in our case EQE signal is limited by the perovskite absorption (spectra shown in Figure 2.16a). Then, an EQE decrease low-wavelength photons indicates front surface defects, as they are absorbed closer to the surface. High absorption from upper layers of the stack (glass substrate and TiO_2) also reduces EQE at lower wavelengths. On the other hand, an EQE decrease for high-wavelength photons indicate back surface defects, but is also caused by the perovskite lower absorption and lower diffusion of the carriers at such wavelengths.

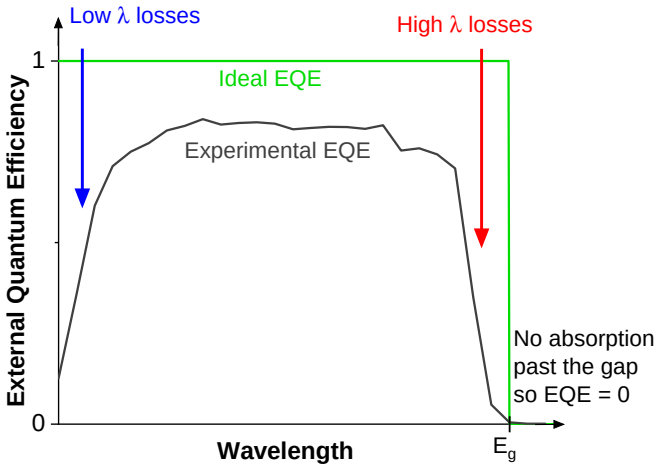

Figure 2.14: Illustration of theoretical and experimental (measured on a pristine 3D perovskite sample) EQE measurements.

In a complementary way to JV characterization, integrating the product of EQE spectrum to the spectral density of incident photons $\Phi(\lambda)$ is also a method to determine device J_{SC}, via the following equation:

$$J_{SC} = -q \int_0^{\infty} EQE(\lambda)\phi(\lambda)d\lambda \tag{2.1}$$

At IPVF, EQE was measured between 300 and 850 nm for perovskite cells using an Oriel IQE 200 system connected to a source meter (Keithley 2400) and a 300 W xenon lamp. Sample illumination was obtained with a monochromator at a power slightly lower than an AM 1.5G solar illumination, resulting in probable differences between J_{SC} measured during JV scans and J_{SC} calculated using EQE data. However, as those differences would occur evenly across samples, they would not be a significant problem.

2.2.2 Optical properties of the material

While previous techniques were performed on complete devices, characterization methods presented onwards were applied on half-cells to describe the perovskite material properties, starting with its optical properties.

Photoluminesence measurements using μ-PL setup

Photoluminescence (PL) is an optical phenomenon describing the production of light by a material (typically semiconductors) under illumination. Enlightening this material with an incident light which energy is superior to the material's bandgap energy leads to the excitation of its electrons. Without any action to collect these excited electrons, they return to their ground state, emitting photons close to the semiconductor's bandgap energy. Steady-state PL measurements (later simplified as PL measurements) characterize a material's radiative properties by collecting the PL signal with a spectrometer and analyzing its spectra. PL spectra were obtained with a homemade micro-PL (μ-PL) experiment from LuMIn lab, simplified and illustrated in Figure 2.15a.

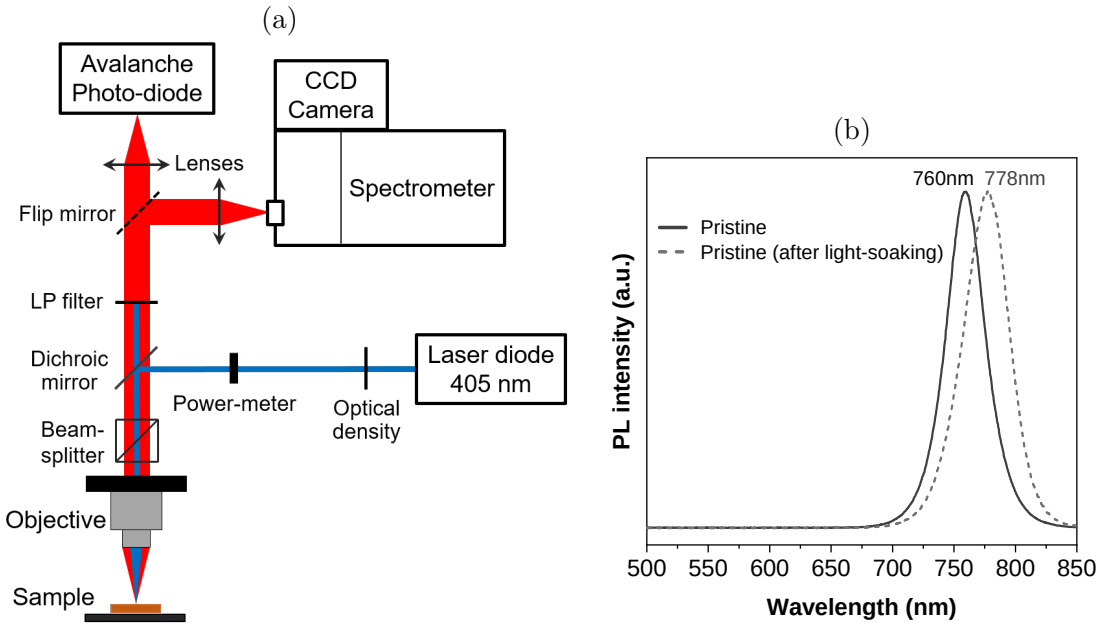

Figure 2.15: (a) Simplified illustration of the micro-photoluminescence setup. (b) PL spectra of a pristine baseline perovskite.

This setup involved exciting the sample with a source focused through a microscope objective and collecting the resulting PL signal. The source used was a PDL 800-D impulsionnal laser diode from PicoQuant, emitting at 405 nm with a repetition rate between 31.25 kHz and 80 MHz. An optical density was put on the beam path to control the exciting power, measured after the density by a power meter from Thorlabs. The loss coefficient was determined by comparing the power measured by the power meter to the power measured after the objective. A dichroic mirror reflected the laser to a Nikon microscope objective with a 40x magnification and a 0.6 numerical aperture, focusing the exciting signal on the sample. The sample luminescence went through the same objective and was separated from the excitation beam with a beam splitter and long-pass filter. A flip mirror was used to send the sample PL on two different paths:

- The first path focused the signal through a Spectrapro 2500i spectrometer, which was collected by a nitrogen-cooled PyLoN CCD camera, both controlled with the LightField software from Princeton Instruments. This path was employed for steady-state PL spectra measurements.
- The second path focused the signal on an ID100 avalanche photodiode from IDQ. This second path was employed for time-resolved PL (TR-PL) measurements, which were not used significantly in this work.

With this setup, the exciting spot was focused on the perovskite layer with a 1.2 μm diameter. This localized excitation could be used to assess the homogeneity of synthesized layers, which is relevant in the case of 2D perovskites as they are often made of a mix of different n-factor values.

The resulting PL spectrum of a pristine baseline sample is shown in Figure 2.15b. During measurements, a shift of the PL signal was observed under illumination. Instantly after light exposure, the perovskite PL peak was located around 760 nm (1.631 eV), and gradually moved to stabilize around 780 nm (1.590 eV) after 1 min of light-soaking with fluences close to 1 $\mu J/cm^2$. This observation is attributed to light-induced phase segregation of iodine phases in the perovskite, already observed in mixed-halide perovskites and slightly decreasing the perovskite bandgap [Draguta *et al.* 2017, Gautam *et al.* 2020].

UV-Visible spectroscopy

UV-Visible (UV-Vis) spectroscopy assesses a material's ability to absorb, reflect, or be transparent to a light source of a specific wavelength. To do so, a monochromator converts a light source into a series of monochromatic radiations directed toward the sample. The incident light intensity is compared to the intensity of the absorbed, reflected, or transmitted beam, providing a measurement of the sample's optical absorption, reflection, or transmission for each wavelength. These features are related to the following equation:

$$100 = A_{\%}(\lambda) + R_{\%}(\lambda) + T_{\%}(\lambda) \tag{2.2}$$

Thus, measuring two of these features allows a calculation of the third one. We measured optical reflection and transmission between 200 and 1300 nm using an Agilent Cary 5000 spectrophotometer. This equipment contained two different light sources: a deuterium arc UV source for wavelengths < 300 nm and a tungsten halogen source for higher wavelengths. It also had two detectors, one for UV-Visible (R928 PMT) and one for IR (Cooled PbS). Absorption was then calculated from reflection and transmission values using Equation 2.2.

This work was focused on the perovskite layer. Therefore, most spectroscopy measurements will have a 400-800 nm range, as higher wavelengths were not energetic enough to interact significantly with the perovskite layer ($E<E_g$). On the other hand, at lower wavelengths, the perovskite layer contribution was marginal in comparison with the other layers of the stack. Optical absorption, reflection, and transmission spectra of pristine perovskite samples illuminated from the perovskite side are shown in Figure 2.16.

These spectra are consistent with PL measurement, showing a drastic absorption increase - related to a reflection and transmission decrease - around 775 nm, close to the emission wavelength. Under 550 nm, almost no light is transmitted through the perovskite layer.

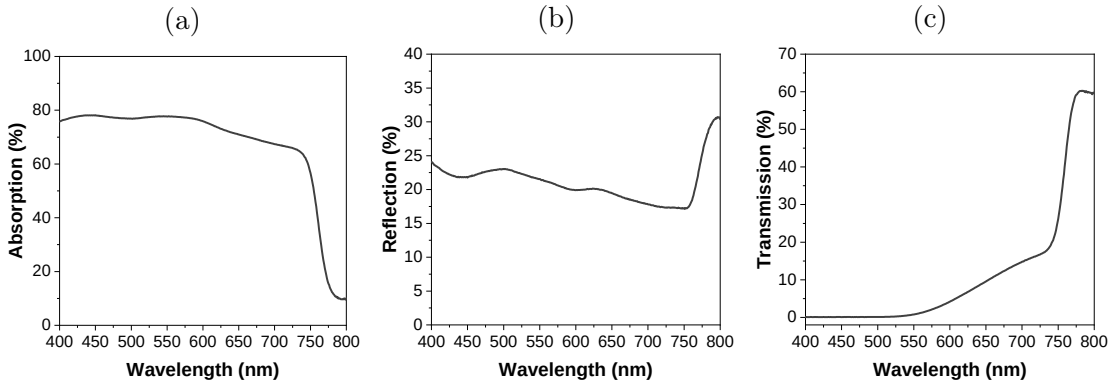

Figure 2.16: (a) Optical absorption, (b) reflection, and (c) transmission of baseline perovskite half-cells (illuminated from perovskite side).

From spectroscopy spectra, it was also possible to estimate an optical bandgap around 1.592 eV ($\approx$ 779 nm) of the perovskite using a Tauc-plot, shown in Figure 2.17. As we established earlier in this manuscript, perovskite shot little Stokes shift, therefore, this estimated value is consistent with PL data.

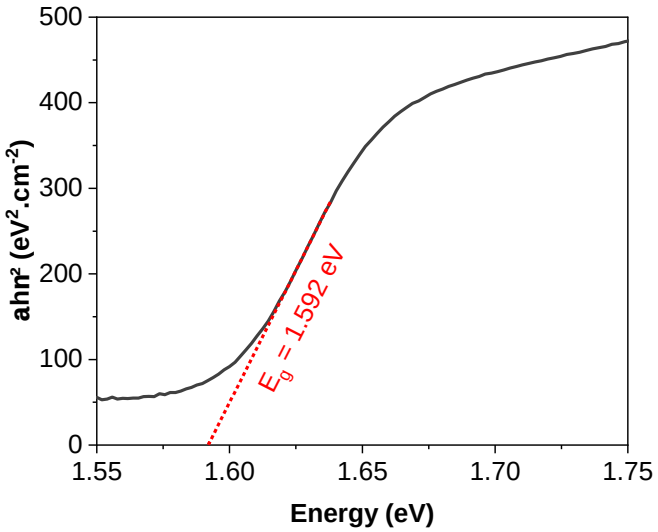

Figure 2.17: Tauc-plot for the determination of baseline perovskite band gap.

2.2.3 Structural, chemical, and topological characterization

Outside of optical techniques, other characterization techniques were applied to the samples to assess their structural, morphological, or chemical properties.

X-Ray crystallography

X-Ray crystallography (or X-Ray Diffraction, XRD) is a characterization method used to determine the crystallographic properties of a material. By sending an X-ray beam on a sample, its crystalline structure diffracts the X-rays into specific directions, based

on the X-ray wavelength, but more importantly, the crystal properties, such as its lattice orientation and size. The intensity and diffraction angle of the resulting X-rays are collected into a diffractogram that identifies the material's crystalline lattice, its dimensions, size, or electronic density. Consequently, it also provides chemical information about the material and various other information.

A variation of this technique, called GIXRD, for Grazing-Incidence X-Ray Diffraction, is based on similar principles to XRD but with the use of small angles (close to the critical angle and typically $< 3°$) for the incident X-ray beam. As a result, more superficial scans are performed, with only a few tens to a few hundreds of nanometers of penetration depth in our case, with the measure of thin films.

For XRD and GIXRD measurements of perovskite samples, we used a Panalytical XRD analyzer (Cu Kα_1 Kα_2 radiations, with λ 1/4 1.5418 Å). The resulting diffractograms were analyzed using HighScore software. An example of a diffractogram measured on a pristine perovskite sample is shown in Figure 2.18.

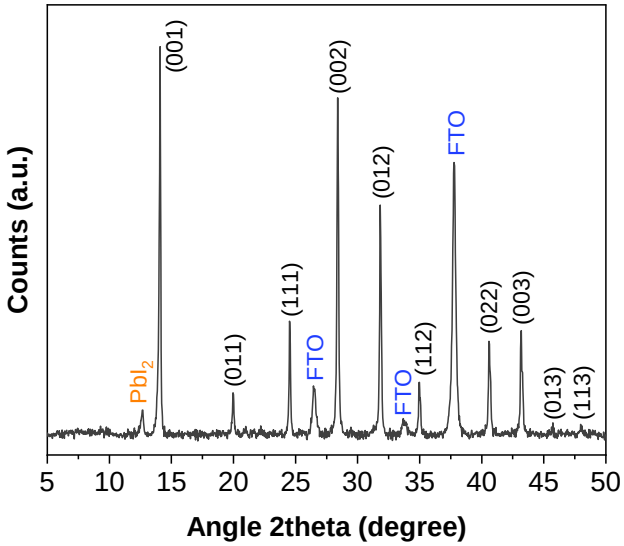

Figure 2.18: XRD diffractogram of pristine baseline perovskite.

First, this diffractogram shows three peaks at 26.4, 33.7, and 37.8° corresponding to the FTO substrate. Secondly, a series of peaks are observed at 14.1, 20.0, 24.5, 28.4, 31.8°, 35.0, 40.6, 43.2, 45.7, and 48.0°. These peaks are attributed to (001), (011), (111), (002), and (012) (112) (022) (003) (013) (113) crystallographic plans of the photo-active black α-phase of the FAPI perovskite, belonging in the Pm3m space group [Weller *et al.* 2015, Zhumekenov *et al.* 2016, Alam and Lewis 2020]. As α-FAPI is the only perovskite phase detected here, it confirms the FA-based nature of the baseline triple-cation perovskite, and that MA or Cs cations only stabilize it without crystallizing significantly on their own. A last peak centered at 12.7° is associated with PbI_2 crystallization, caused by the 2.0% stoichiometric excess introduced in the baseline perovskite precursor solution [Jesper Jacobsson *et al.* 2016].

X-Ray Photoelectron Spectroscopy

To investigate the chemical composition of our perovskite materials, we used X-ray Photoelectron Spectroscopy (XPS). This technique is commonly used in perovskites, as it allows the chemical characterization of the extreme surface (5 to 10 nm) of thin films.

It consists in irradiating a sample by an X-ray source of few keV in ultra-high vacuum (UHV), resulting in the emission of photoelectrons. X-ray absorption and photoelectron emission happen near the sample surface, resulting in a depth probed close to the first 10 nm of the material, which is an important asset to characterize extremely thin 2D layers in surface treatment 2D/3D structures.

Each chemical element produces specific features depending on the level frow which the photoelectrons are produced (from core to valence levels, e.g., 1s, 2s, 2p), and on its binding state (chemical shift). By measuring the kinetic energy of these photoelectrons, the nature of their chemical elements and their intimate atomic networks can be identified. The area of each peak is proportional to the amount of its corresponding element in the scanned area, which allows an accurate quantification of the material's surface stoichiometry and chemistry. The different contributions of the chemical environments, along with the associated proportions, are determined with specific fitting procedures. In addition to studying the extreme surface, it is also possible to investigate the in-depth chemical profile of different elemental species by etching the sample with ionic sputtering, and performing XPS scans in the generated crater.

For XPS analyses, freshly synthesized perovskite samples were transferred to the XPS spectrometer in the dark and under inert atmosphere conditions to ensure the reliability of the analysis. Measurements were carried out with a Thermo Electron K-Alpha+ spectrometer equipped with a monochromated Al-Kα X-Ray source for excitation at 1486.6 eV. The X-ray beam spot was set to 400 μm. Calibration of the spectrometer was done using Cu and Au samples following the ASTM-E-902-94 protocol. The constant analyzer energy (CAE) mode was used and both survey spectra (100 eV pass energy, 1 eV step size, 100 ms dwell time) and high energy resolution spectra (20 eV pass energy, 0.1 ev step size, 100 ms dwell time) were acquired. The total analysis sequence duration was optimized not to exceed 1h to limit the X-ray dose and possible surface alteration. Elements more prone to degradation were acquired first, and two surveys, one at the beginning and one at the end of the analysis, were recorded. This optimized analysis procedure is described in the following work [Cacovich *et al.* 2020]. Thermo Fisher Scientific Avantage© data system was used for data treatment and peak fitting. Energy calibrations were performed regarding the C1s peak located at 284.8 eV. For each experimental condition, a set of ten randomly positioned analysis points was used on several 2x2 cm^2 samples to certify the reliability of the information collected and the homogeneity of samples surface chemistry.

To probe the elemental distribution within the perovskite layers, XPS in-depth profiling was carried out. The elemental depth distribution is obtained by alternating sputtering and acquisition sequences. Each sputtering step lasts for 60 seconds, using a monoatomic Ar^+ gun with an energy of 1000 eV and a 10 mA current density, and is followed by a surface analysis step performed inside the generated crater. Caution has to be taken for the interpretation due to possible bombardment artefacts such as preferential sputtering.

All XPS measurements and data analysis were performed at Institut Lavoisier de Versailles (ILV) by Pia Dally, and later by Mirella Al Katrib, both under the supervision of Muriel Bouttemy.

Scanning Electron Microscopy

Scanning Electron Microscopy (SEM) was this work's main imaging technique. By scanning a sample with a focused, high-energy electron beam (with typical wavelengths of a few tens of picometers) instead of a light source, a SEM microscope can produce images

of this sample with far better resolutions than optical microscopy techniques. In return, measurement scanning has to be performed under high-vacuum on conductive samples (in order to for them to interact, and thus, evacuate electrons). The incident electrons, also called primary electrons, interact with the atoms constituting the sample, producing on each point of impact two main kinds of measurable electron signals:

- Secondary electrons (SE) are low-energy electrons ejected from outer energy levels of the sample atoms due to inelastic scattering with primary electrons. The intensity (associated with its brightness) of the measured SE signal is proportional to the number of secondary electrons detected. Due to their low energy, SE are used for topology imaging, as they originate from the first nanometers of the material.
- Backscattered electrons (BSE) are high-energy primary electrons reflected or backscattered from the sample by elastic scattering interactions with its atoms. BSE are emitted from slightly deeper parts than SE, and are produced in a greater amount by heavier elements. Therefore, the intensity of a BSE signal provides information on the sample's chemical composition.

SEM images were made using a Zeiss Merlin VP Compact field emission scanning electron microscope in the InLensDuo mode, measuring both secondary and back-scattered electrons. Typical magnifications of 10k to 50k were used, with acceleration voltages of 1 kV for surface images. Such acceleration voltage focused more on the topological resolution, with less chemical information about the samples. Example surface image of a pristine perovskite sample is shown in Figure 2.19a, which corresponds to a classical 3D perovskite layer without any additive [Liu *et al.* 2019b, Dehghanipour *et al.* 2020]. Figure 2.19b shows the grain diameter distribution extracted from this surface image, with an average crystalline grains diameter close to 200 nm.

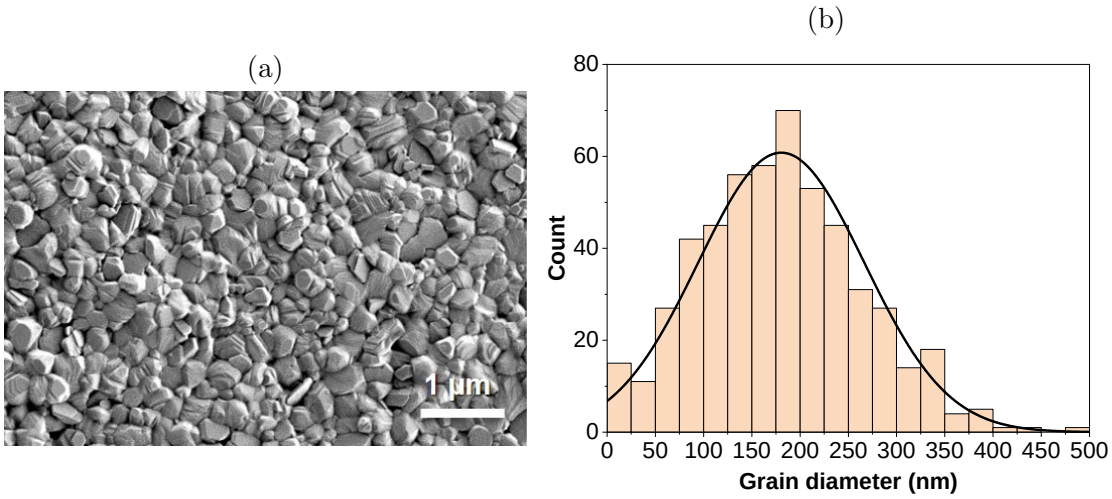

Figure 2.19: (a) SEM surface image of pristine baseline perovskite. (b) Resulting grain diameter distribution.

Cross-section images of the samples were also acquired. Due to the 3 mm thick glass substrate, perovskite cross-section samples were not conductive to electrons and so, were incompatible with SEM. To fix this problem, samples were covered with a few nanometers thick carbon layer during a primary vacuum metallization step, performed in a Denton

Vaccum Desk V Evaporator. Cross-section images were obtained with similar parameters to surface images, with only higher 15 kV acceleration voltages. A cross-section image of a pristine perovskite sample is shown in Figure 2.20, highlighting the thickness of each layer constituting the baseline stack.

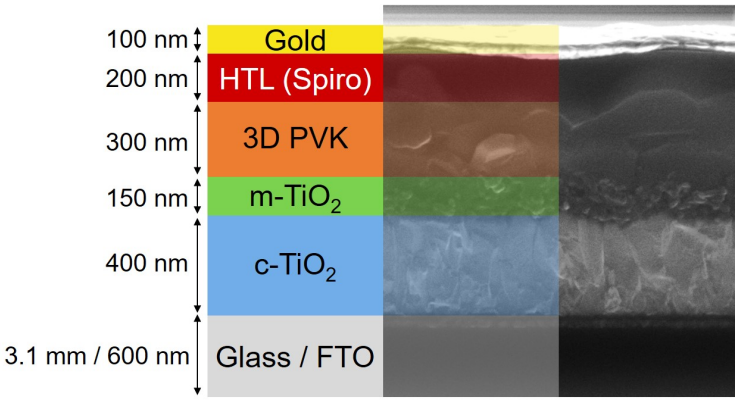

Figure 2.20: Cross-section SEM image of pristine baseline perovskite, with corresponding thickness for each layer of this stack.

Atomic Force Microscopy

Atomic Force Microscopy (AFM) is an imaging technique that can scan the surface topology of most kinds of materials, with a vertical resolution close to 0.1 nm and in-plane resolutions of $\approx$ 1 nm. This technique belongs to the scanning probe microscopy group, involving physical probes to scan the surface of a sample. For AFM, the scanning probe is a sharp tip with a 10 to 20 nm wide apex fixed on a flexible cantilever, and the imaging comes from the interaction between the tip and the surface atoms of the material. Two mains scanning modes are used:

- In the first one, the cantilever oscillates close to its resonance frequency (around 100 kHz) with a constant amplitude, and the tip only touches the sample surface at the bottom of the oscillation, resulting in the "tapping mode" denomination. The sample surface is scanned by assessing the variations in the oscillation amplitude.
- The second method, called the "contact mode", applies a constant contact between the tip and the sample surface, and its topology is scanned by measuring variations of cantilever deflection. This method is more specific than tapping mode and is applied less extensively.

In our case, AFM images (10x10 μm^2) were acquired with an Agilent 5600 LS atomic force microscope, using an ACL probe from AppNano in tapping mode under ambient air. The roughness was extracted from images with Gwyddion software and expressed in (S_q) and (S_a) values. S_q (root mean square (RMS) height) roughness corresponds to the standard deviation of height distribution for all peaks and valleys in the delimited area. On the other hand, S_a (arithmetic mean height) roughness is calculated as the average difference from the absolute height of all peaks to the mean surface. Overall, the values of S_a roughness are inferior to S_q and are less sensitive to abnormal topographic areas, such as large peaks or valleys. The topographic amplitude, which is the height

difference between the highest and the lowest point measured, also gives an indication of the material surface. An example AFM image of a pristine baseline perovskite is shown in Figure 2.21, but will not be discussed until the next chapter.

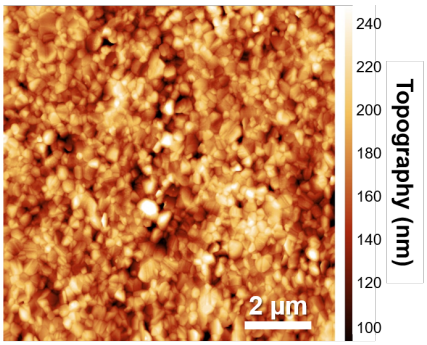

Figure 2.21: Pristine baseline perovskite AFM 10x10 µm^2 topographic scan.

Confocal miscroscopy

Confocal microscopy is an optical imaging technique usually using a light source produced by a laser beam instead of a lamp. A pinhole is placed before the light source to obtain a point illumination. A lens focuses the incident light on the sample, and a second pinhole is placed in front of the detector, optically conjugated with the source pinhole, hence the name confocal. Therefore, out-of-plane signal is eliminated, resulting in a very small depth of field (about 400 nm) but with a far better optical resolution than wide-field microscopes. By gradually moving the microscope's focal plane over several sample depths, it is possible to perform 3D scans of the sample surface.

Confocal images were acquired with an Olympus LEXT OLS5100 confocal microscope using a white light source. S_q and S_a roughness values were extracted from 3D scans of the sample surface with the highest magnification (129x129 μm^2 area). Similarly to AFM, a confocal image of the pristine baseline perovskite and the resulting topographic scan are visible in Figure 2.22, and will not be discussed until later.

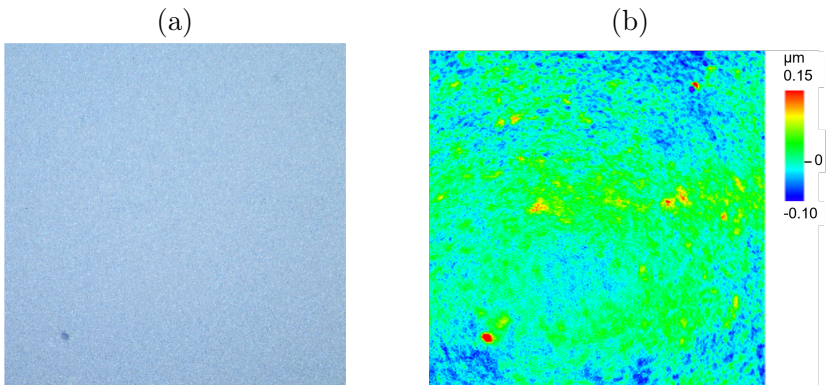

Figure 2.22: Pristine baseline perovskite confocal microscope 129x129 µm^2 (a) white light image, and (b) resulting topographic scan.

2.3 Summary

This chapter presented how the development of 2D/3D perovskite heterostructures was integrated in IPVF's baseline fabrication process of perovskite solar cells. This process relies on a mesoporous n-i-p architecture with the following stack: glass-FTO substrate / compact and mesoporous TiO_2 bilayer / triple-cation 3D perovskite / Spiro-OMeTAD or PTAA / gold electrode. We detailed the techniques for synthesizing each layer of this stack (spin-coating, ALD, metal e-beam evaporation, chemical etchings...) and how they evolved throughout this thesis work. We also explained the process for incorporating a 2D perovskite between the 3D perovskite and HTL layer.

Subsequently, we dealt with the main methods that will be used in this work to characterize the fabricated devices electrically, determine their performance and its evolution over time. Then, the attention was drawn onto characterization methods applied to the perovskite material itself. Some of the presented techniques were completed with example data obtained on the baseline perovskite, to discuss its properties. PL measurements will be used to assess its emission properties and get information on the perovskite bandgap. In addition, UV-Vis spectroscopy will evaluate its transmission, reflection, and absorption properties. On the other hand, several other characterization methods will be used to reveal the physico-chemical properties of the material structure. XRD will characterize the structural features of the 2D/3D structure, while XPS will allow us to obtain important knowledge on the chemical composition of the 2D/3D structure surface and bulk. Lastly, surface scanning and imaging techniques, such as SEM, AFM, and confocal microscopy, will provide information on the material morphology.

Chapter 3

Synthesis parameters of the 2D/3D perovskite structure

This chapter focuses on the understanding of the 2D/3D perovskite structure. The first section presents the fabrication of 2D perovskite references. The second and third sections deal with the characterization of the 2D/3D structure regarding two different synthesis parameters: the 2D solution concentration and the static deposition of this 2D solution. The critical importance of 2D solution concentration on the thickness and morphology of the 2D perovskite formed is revealed. At the same time, static deposition is exposed as an unreliable method to alter the 2D layer. The fourth section is dedicated to photovoltaic device applications. Compared to the pristine 3D material, the 2D/3D material leads to significant efficiency and stability improvements in solar cell devices. Finally, the results obtained on mini-modules show the potential of 2D/3D structures in higher-scale devices.

Contents

3.1 Reference 2D perovskite layer

3.1.1 Fabrication of a pure 2D perovskite

In this work, the main guideline was the formation of a 2D/3D perovskite heterostructure, based on the synthesis process detailed in Section 2.1.4, to improve the performances of PSCs. However, before attributing any potential improvement of solar cell devices to the addition of a 2D perovskite layer, being able to characterize the presence of the 2D perovskite layer was required. This led to the fabrication of reference samples made with a pure n=1 2D perovskite deposited directly on 2x2 cm^2 ITO-coated glass substrates, cleaned with the same sonication process than glass-FTO substrates and treated with UV-Ozone for 30 minutes before glovebox introduction.

While one of the main constraints to design 2D/3D structures was to solubilize the 2D perovskite cation salt without dissolving the crystallized 3D perovskite underneath, the formation of pure 2D perovskite films did not need to comply with this constraint and could be performed more directly. In this regard, an antisolvent process already applied at LuMIn was used and is schematized in Figure 3.1.

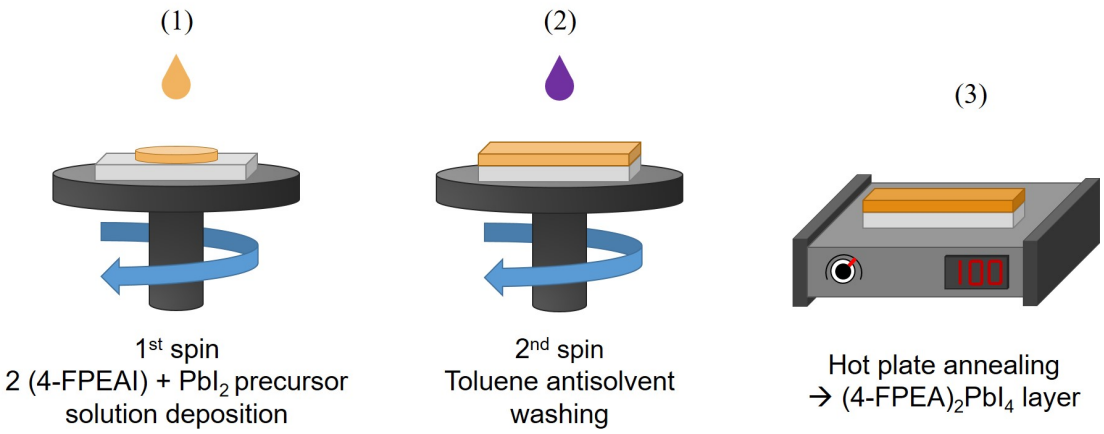

Figure 3.1: Synthesis process of $(4\text{-FPEA})_2PbI_4$ pure 2D perovskite.

This process involved mixing 4-FPEAI cation salts and PbI_2 at a 2:1 molar ratio. This blend was dissolved in a DMF and DMSO mix (4:1 volume ratio) with a 10% weight concentration to form the 2D perovskite precursor solution. 100 μL of this solution was spin-coated in step (1) on the substrate at 2000 rpm for 30 seconds. In step (2), a second run of the same spin-coating program was dedicated to depositing 100 μL of an anti-solvent, here toluene. Crystallization of the perovskite layer was finalized during step (3) with hot plate annealing at 100 °C for 1 min. This reaction process, which is described by the following chemical equation, led to the formation of a $(4\text{-FPEA})_2PbI_4$ n=1 pure 2D perovskite:

$$2(4-FPEAI) + PbI_2 \rightarrow (4-FPEA)_2PbI_4 \tag{3.1}$$

3.1.2 Characterization of the pure 2D layer

Several characterizations were performed on the synthesized films to confirm that this this $(4\text{-FPEA})_2PbI_4$ pure 2D perovskite had the same specific features than in the literature. These features would later be searched in 4-FPEAI treated samples to confirm the presence of a 2D layer on the 3D perovskite. Optical properties of the 2D layer were investigated through UV-Vis spectroscopy and PL measurements, while XRD was performed to look for the structural properties of the materials. The results of these measurements are shown in Figure 3.2.

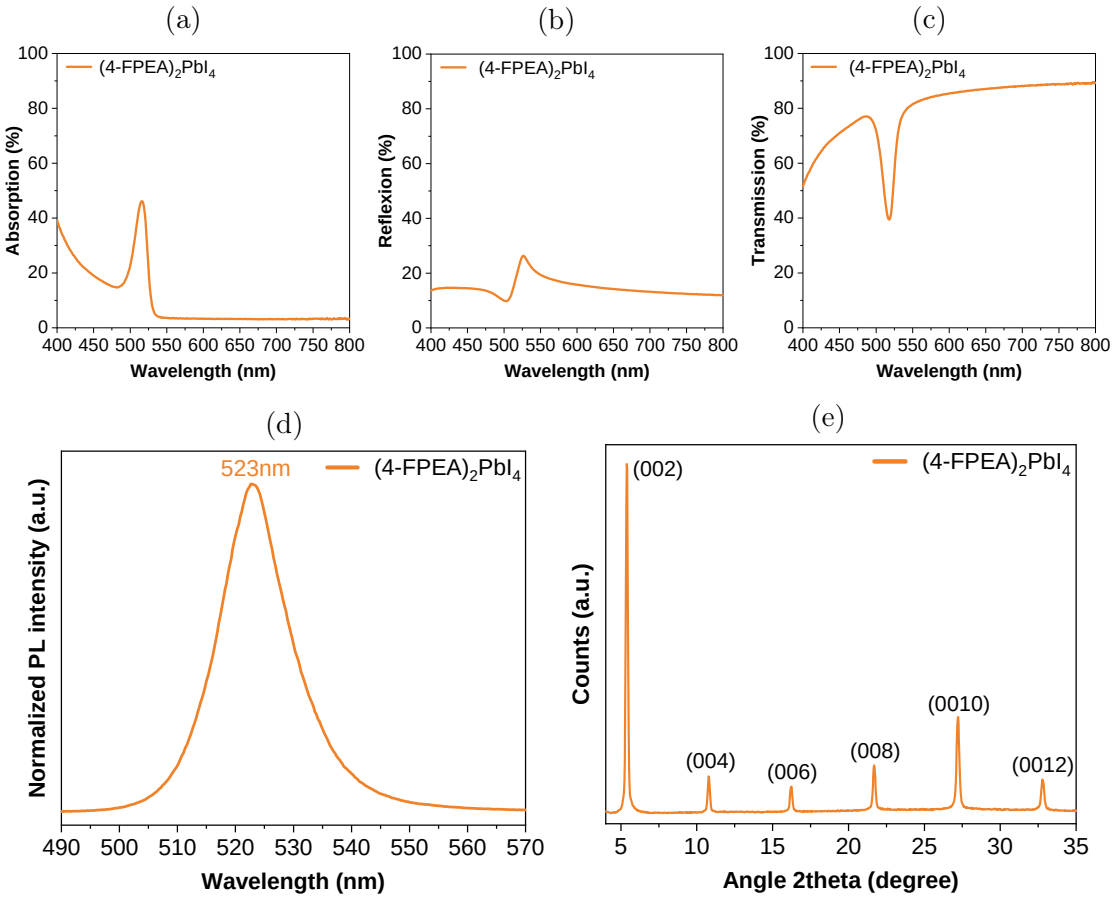

Figure 3.2: (a) Optical absorption, (b) reflection, (c) transmission, (d) PL spectra, and (e) XRD diffractogram of $(4\text{-FPEA})_2PbI_4$ pure 2D perovskite.

Figures 3.2a, 3.2b, 3.2c, and Figure 3.2d confirm the excitonic nature of this 2D perovskite, with negligible absorption at low energies, until the 1s excitonic absorption peak located at 516 nm (2.4 eV). Furthermore, the emission peak seen at 523 nm (2.37 eV) highlights that absorption and emission properties of $(4\text{-FPEA})_2PbI_4$ are nearly identical with its non-fluorinated version $(PEA)_2PbI_4$ [Ledee 2018]. The structural properties are not significantly altered either, as the diffractogram from Figure 3.2e displays peaks located at 5.4, 10.8, 16.3, 21.7, 27.2, and 32.8°, very close to the peaks observed in $(PEA)_2PbI_4$, corresponding to the (002), (004), (006), (008), (0010), and (0012) plans of the 2D perovskite [Ledee 2018, Jiang *et al.* 2019a, Zhou *et al.* 2019]

3.2 Concentration of the spacer cation solution

With pure 2D perovskite references available, our focus shifted to the study of 2D/3D structures. This investigation was realized by tuning the synthesis parameters of of our process, analyzing the effect of this modification on the properties of the 2D/3D material. The first parameter studied was the concentration of the 4-FPEAI precursor solution. Three 4-FPEAI concentrations were used for this IPA solution: 2.5, 5, and 10 mg.mL^{-1}. Theses samples will later be named 2.5 mg.mL^{-1}, 5 mg.mL^{-1}, and 10 mg.mL^{-1}, according to the concentration used.

3.2.1 Identification of 2D perovskite in the 2D/3D structure

XRD was carried out to assess the structural properties of the 2D layer for 4-FPEAI treated samples. Figure 3.3a compares the pure 2D perovskite diffractogram from Figure 3.2e with a pristine 3D perovskite reference and a 10 mg.mL^{-1} sample data.

As discussed in the previous chapter, the 3D perovskite reference features the 14.1, 20.0, 24.5, 28.4, and 31.8° characteristic peaks attributed to the (001), (011), (111), (002), and (012) plans of α-FAPI. Furthermore, the peak centered at 12.7°, attributed to PbI_2 excess, and the FTO peaks at 26.4 and 33.7° are also visible. Figure 3.4 compares Bragg-Brentano and GIXRD diffractograms of a pristine 3D sample, respectively scanning the whole perovskite layer and only its first few tens/hundreds nanometers. This comparison highlights that the PbI_2 peak is mainly localized on the material's surface. A small shift towards higher angles is observed with the transition from XRD to GIXRD, but this difference is observed for all peaks and so, is only caused by the use of a different setup. 10 mg.mL^{-1} sample displays all 3D perovskite peaks, with the addition of two peaks: one at 5.4°, and a second, smaller peak, at 27.2°. These peaks corresponds to the (002) and (0010) peaks seen in the pure 2D reference, suggesting the formation of a 2D perovskite layer on the 3D bulk [Zhou *et al.* 2019]. However, their intensity is significantly lower than the one of peaks from the 3D phase, implying a presumed low thickness.

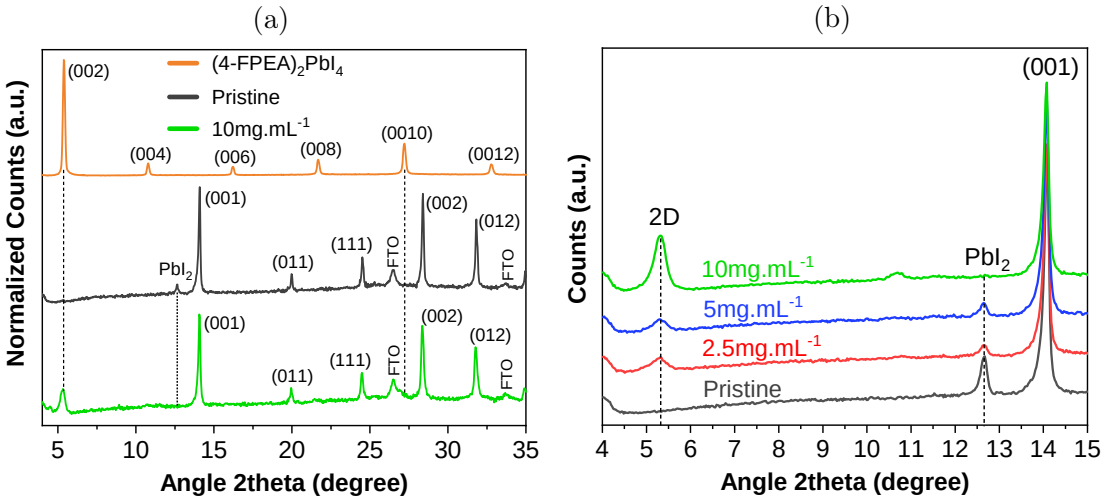

Figure 3.3: (a) XRD patterns of (4-FPEA)$_2$PbI$_4$ pure 2D perovskite, pristine 3D, and 10 mg.mL^{-1} samples. (b) Diffractogram evolution regarding 4-FPEAI solution concentration, zoomed on 2D (002) and 3D (001) perovskites peaks.

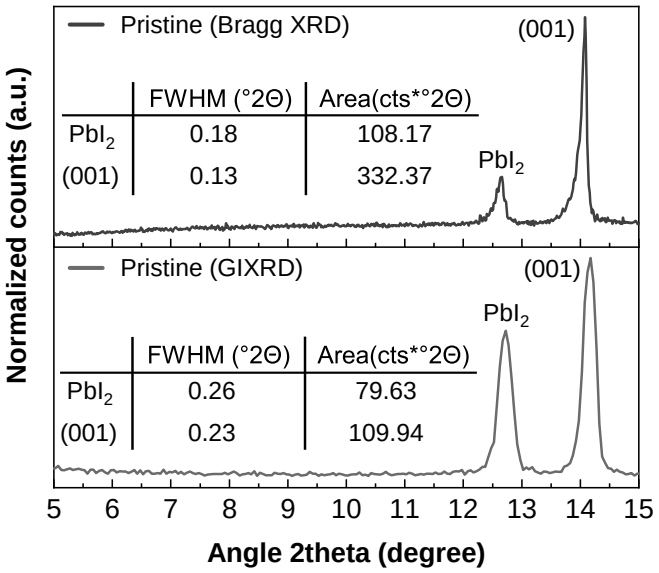

Figure 3.4: Comparison between Bragg-Brentano XRD and GIXRD diffractograms of a pristine 3D perovskite.

Figure 3.3b shows the XRD pattern evolution as a function of 4-FPEAI solution concentration, focused on the first 2D and 3D peaks. While increasing the solution concentration of the 4-FPEAI treatment, two behaviors emerge: the peak at 5.4°, related to the 2D phase, appears and its intensity increases, and secondly, the PbI_2 peak intensity progressively decreases. These observations underline the reaction between the 2D cation salt, here 4-FPEAI, and the PbI_2 excess of the 3D phase surface to form a pure 2D perovskite, similarly to Equation 3.1. Thus, as 4-FPEAI solution concentration increases, the reaction consumes a greater PbI_2 amount, leading to the PbI_2 peak disappearance during XRD measurements for the highest 4-FPEAI solution concentration, in agreement with other works from the literature [Liu *et al.* 2019a, Kim *et al.* 2021]

Optical properties

Optical characterizations were carried out on pristine and 4-FPEAI treated samples to further analyze the deposited 2D layer. UV-Vis absorption, reflection, and transmission spectra obtained by illuminating the samples from the top side are presented in Figures 3.5a, 3.5b, and 3.5c, along with spectra of the $(4\text{-FPEA})_2PbI_4$ pure 2D reference. A significant modification of absorption and reflection of the material is observed with 4-FPEAI treatment, and the reflection pattern of the $(4\text{-FPEA})_2PbI_4$ perovskite seems "added" to the reflectivity of the 3D material, with a slight blue-shift. This leads to a decrease of the material reflectivity, which intensifies with 4-FPEAI solution concentration. Meanwhile, the transmission remain close to zero percent under 525 nm regardless of the samples. Therefore, 4-FPEAI treatment with higher concentrations increases the optical absorption of the stack.

From a purely optical point of view, this phenomenon could benefit to solar cells, as more light reaching the 3D perovskite layer means more possible charge carriers generation. However, the absorption increase is only visible with 2D perovskite side illumination, while our devices have an n-i-p architecture (see Figure 2.13a), and therefore, are enlightened from the 3D perovskite side. Hence, 2D perovskite treatment could be more

beneficial in p-i-n devices, and here, the main interest of spectroscopy measurements is to confirm the presence of the 2D perovskite layer.

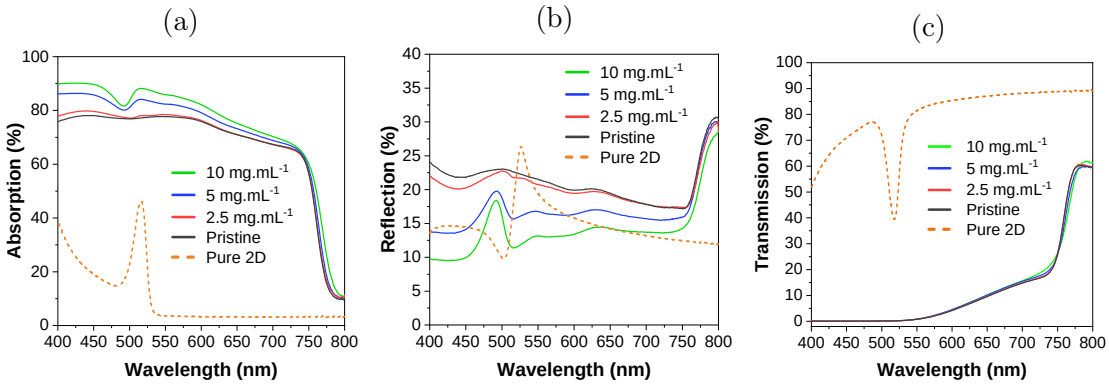

Figure 3.5: (a) Optical absorption, (b) reflection, and (c) transmission of pristine and all 4-FPEAI treated samples, compared to $(4\text{-FPEA})_2PbI_4$ pure 2D perovskite.

PL measurements were also used on the 2D/3D structure. Figure 3.6 shows the PL spectra of pristine and the three 4-FPEAI treated samples, normalized on the 3D perovskite emission. The 3D perovskite peak is located around 760 nm. It remains unchanged regardless of 4-FPEAI solution concentration, confirming that the solutions employed do not affect the emission properties and so, do not damage the 3D perovskite. On the other hand, adding the 2D cation solution leads to the emergence of two new emission peaks around 510 and 552 nm. Increasing 4-FPEAI solution concentration enhances the intensity of these peaks, especially for the first one, relatively to the 3D peak intensity. Thus, we could reasonably assume that they correspond to the excitonic transition of n=1 and n=2 phases of the $(4\text{-FPEA})_2(MA,FA,Cs)_{n-1}Pb_nI_{3n+1}$ RP 2D perovskite formed by the 4-FPEAI treatment, with a predominance for the n=1 phase [Delport *et al.* 2019, Chehade 2022].

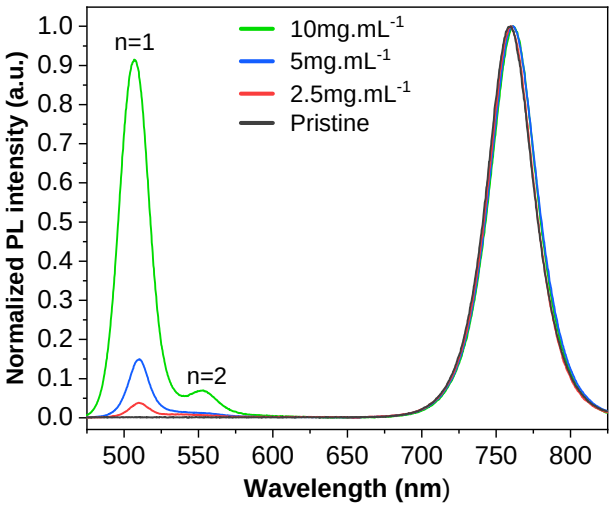

Figure 3.6: PL spectra of pristine 3D and 4-FPEAI treated samples with all three concentrations (2.5, 5, and 10 $mg.mL^{-1}$)

3.2.2 Morphological properties

With XRD and optical characterization data suggesting a significant increase in 2D layer thickness along 4-FPEAI solution concentration, film morphology and coverage was also investigated through SEM and AFM imaging of samples' surface. Resulting SEM images of pristine and 4-FPEAI treated samples for limit 2.5 and 10 mg.mL^{-1} concentrations, showing the most visible surface evolution, are presented in Figure 3.7. The pristine image corresponds to the characteristics presented in Section 2.2.3. Depositing a weakly concentrated solution for the 2.5 mg.mL^{-1} sample visually seems to induce the formation of a thin homogeneous layer, smoothing the space between grains and leveling the surface (see Figure 3.7b). Yet, 3D perovskite grains remain visible underneath, suggesting the low 2D layer thickness. For 10 mg.mL^{-1} concentration, both SEM and AFM in Figures 3.7c and 3.8c show less visible 3D perovskite grains, indicating an increased 2D perovskite thickness. While no general consensus exist on the morphology that should be obtained after 2D solution treatment, our results match with other works in the literature [Dehghanipour *et al.* 2020, He *et al.* 2020, Li *et al.* 2021c].

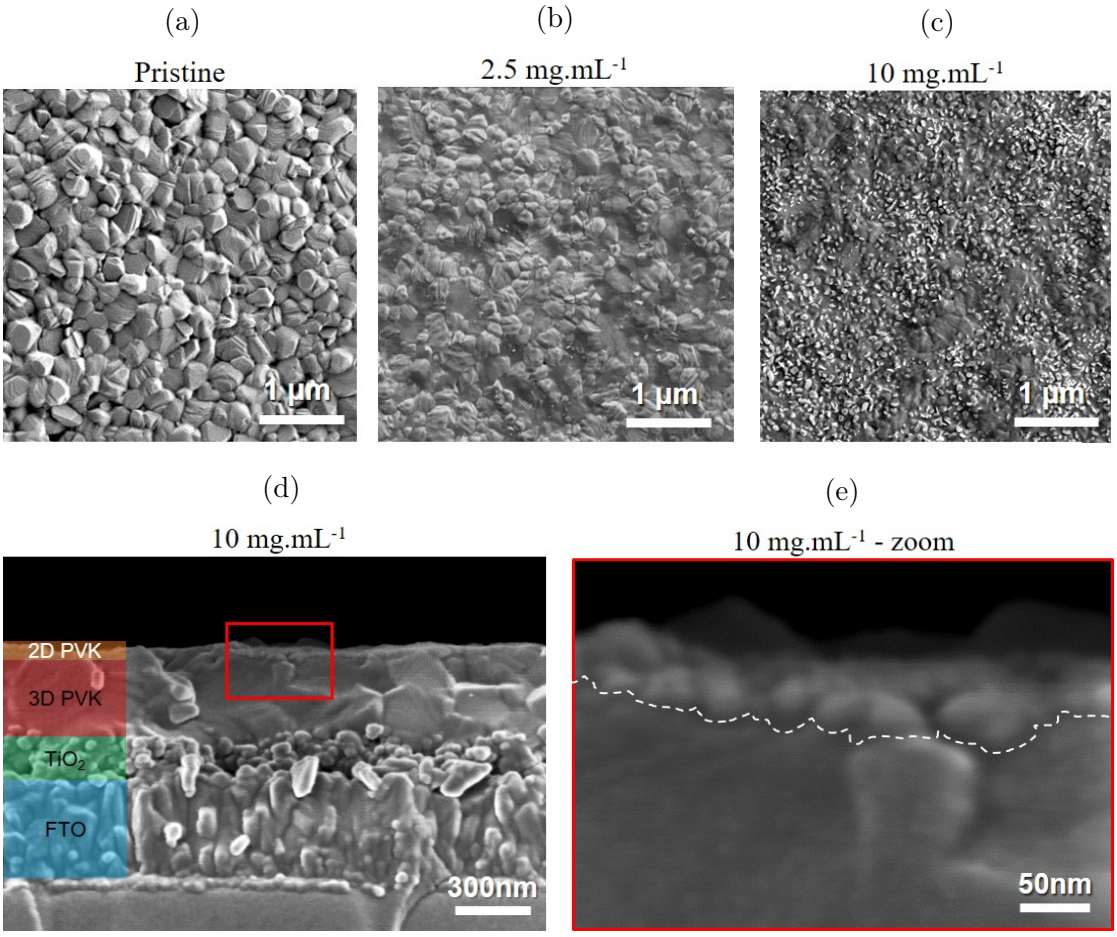

Figure 3.7: SEM surface images of (a) pristine, (b) 2.5 mg.mL^{-1}, and (c) 10 mg.mL^{-1} samples. d) Cross-section SEM image of a 10 mg.mL^{-1} sample, e) zoomed on the 2D perovskite layer.

Cross-section SEM images of the 10 mg.mL^{-1} sample in Figures 3.7d and 3.7e supports the formation of a new layer made of few tens of nanometers wide grains on the

3D perovskite, covering its surface. By correlating this image with the size of the small grains visible on the surface of the 10 mg.mL^{-1} sample in Figure 3.7c, we estimated that the 2D layer thickness for this concentration was around 30 nm or less. Hence, these results confirm the formation of a 2D layer on the 3D perovskite bulk, changing the surface morphology according to the 4-FPEAI solution concentration.

AFM images shown in Figure 3.8 corroborate observations made thanks to SEM images and in the literature. The topographic amplitude shrinks from 150 nm for the pristine sample to 99 nm after 2.5 mg.mL^{-1} treatment, only to increase back close to 140 nm with the 10 mg.mL^{-1} concentration.

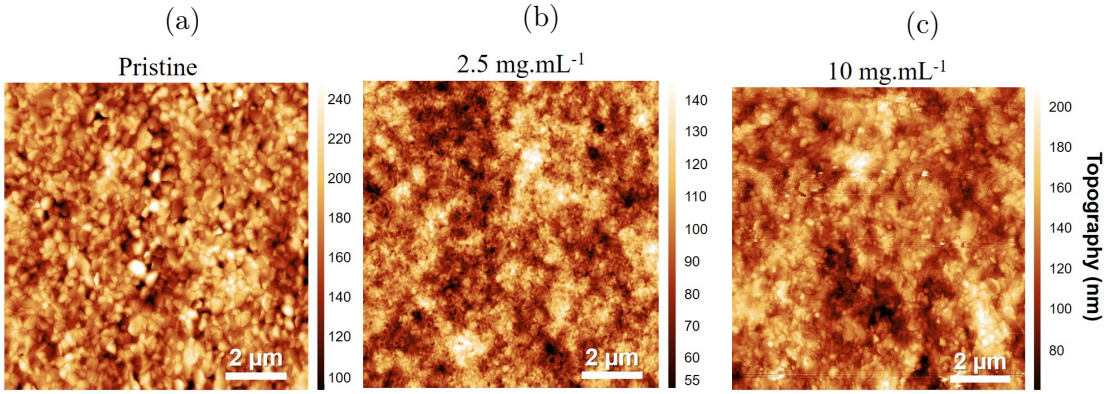

Figure 3.8: AFM 10x10 µm^2 topographic scans of (a) pristine, (b) 2.5 mg.mL^{-1}, and (c) 10 mg.mL^{-1} samples.

A study was performed to determine the impact of 4-FPEAI treatment on the 2D/3D structure surface roughness. In this study, S_q and S_a roughness values of pristine and all 4-FPEAI treated samples were estimated from AFM scan images and were compared to values measured from confocal microscopy images shown in Figure 3.9.

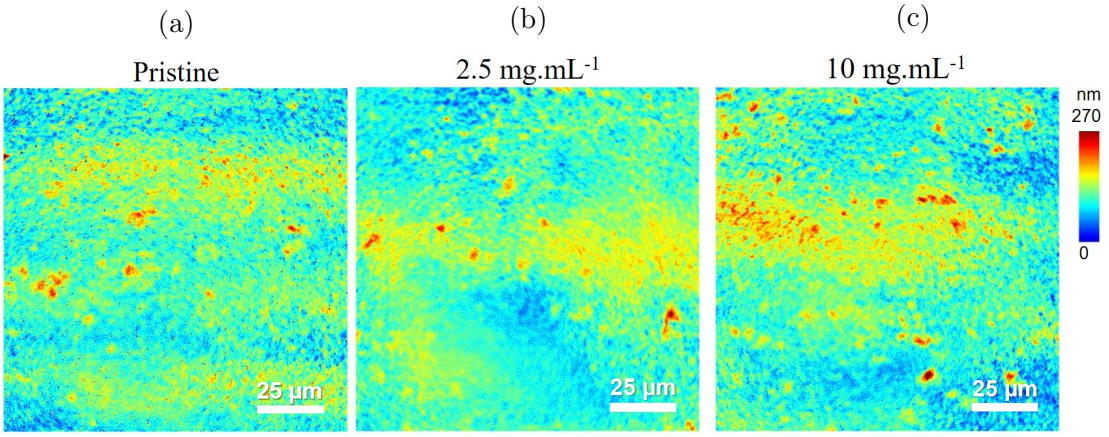

Figure 3.9: Confocal microscope 129x129 µm^2 topographic scans of (a) pristine, (b) 2.5 mg.mL^{-1}, and (c) 10 mg.mL^{-1} samples.

The distribution of measured roughness values is presented in Figure 3.10, and their means are summed-up in Table 3.1. This study confirms that a weakly concentrated 4-FPEAI solution improves surface smoothness due to the 2D top layer formation. As

a result, the average S_q roughness of pristine samples decreases from 25.69 nm to 17.95 nm with 2.5 mg.mL^{-1} 4-FPEAI treatment. Increasing the concentration to 5 mg.mL^{-1} further decreases the roughness to 17.05 nm, however, for the 10 mg.mL^{-1} concentration, the roughness worsens up to a value of 22.20 nm. This observation reveals that forming a significantly thicker 2D layer reduces the smoothness of the surface, in line with the morphological changes (visible sub-micrometer grains inhomogeneous distribution).

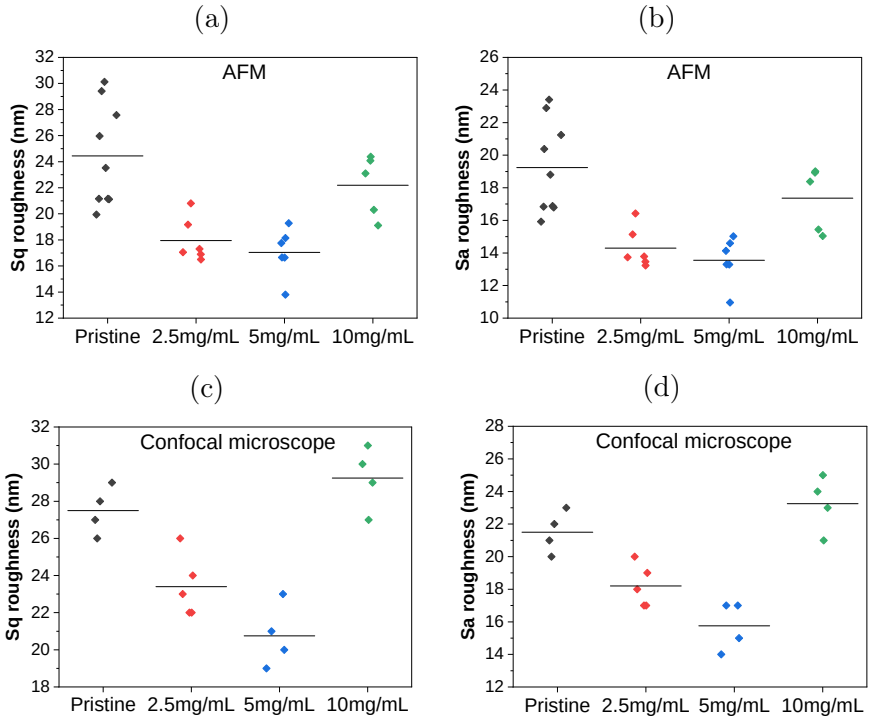

Figure 3.10: Distribution of S_q and S_a roughness measured with (a), (b) an AFM or with (c), (d) a confocal microscope, for pristine, 2.5, 5, and 10 mg.mL^{-1} samples.

Table 3.1: Average S_q and S_a roughness of pristine, 2.5, 5, and 10 mg.mL^{-1} samples, measured either with an AFM or a confocal microscope.

	S_q roughness (nm)		S_a roughness (nm)	
	AFM	Confocal	AFM	Confocal
Pristine	24.4	28	19.2	22
2.5 mg.mL^{-1}	18.0	23	14.3	18
5 mg.mL^{-1}	17.0	21	13.5	16
10 mg.mL^{-1}	22.2	29	17.4	23

Through imaging techniques, a first estimation of the 2D layer thickness was presented for the highest 10 mg.mL^{-1} concentration. However, this result is quite limited for several reasons. First, due to the low amount of 2D perovskite formed for the lower 2.5 and 5 mg.mL^{-1} concentrations, an accurate estimation of the 2D layer thickness is not possible with such techniques. Second, there are more appropriate techniques to establish the 2D layer existence only at the material's surface than imaging techniques.

3.2.3 Chemical characterization using XPS

Surface characterization

On top of previous characterizations, evaluating the surface chemistry of the 2D/3D structure is essential to unveil its formation mechanism. Therefore, XPS surface analyses were performed on all 4-FPEAI treated samples to assess the surface composition modifications consecutive to the 2D process for every concentration. For such thin 2D overlayers (ultimate thickness estimated to 30 nm for 10 mg.mL^{-1}, close to the 10 nm depth probed with XPS), the main challenge is to discriminate spectral contributions from the superimposed 2D and 3D layers, as many elements within both layers are identical, such as carbon, nitrogen, lead, and iodine. Among the remaining elements, the presence of fluorine is direct evidence of the presence of the 2D layer, while bromine and cesium should indicate the 3D layer underneath.

XPS surface analysis was first carried out on pristine 3D and pure 2D perovskites to determine the signals from separate materials, which served as a point of comparison for measurements performed on 4-FPEAI treated samples. Figure 3.11 depicts the results of these measurements, with XPS high-resolution spectra of every element measured at the materials' surface: C1s, N1s, F1s, Pb4f, I3d, Br3d, and Cs3d.

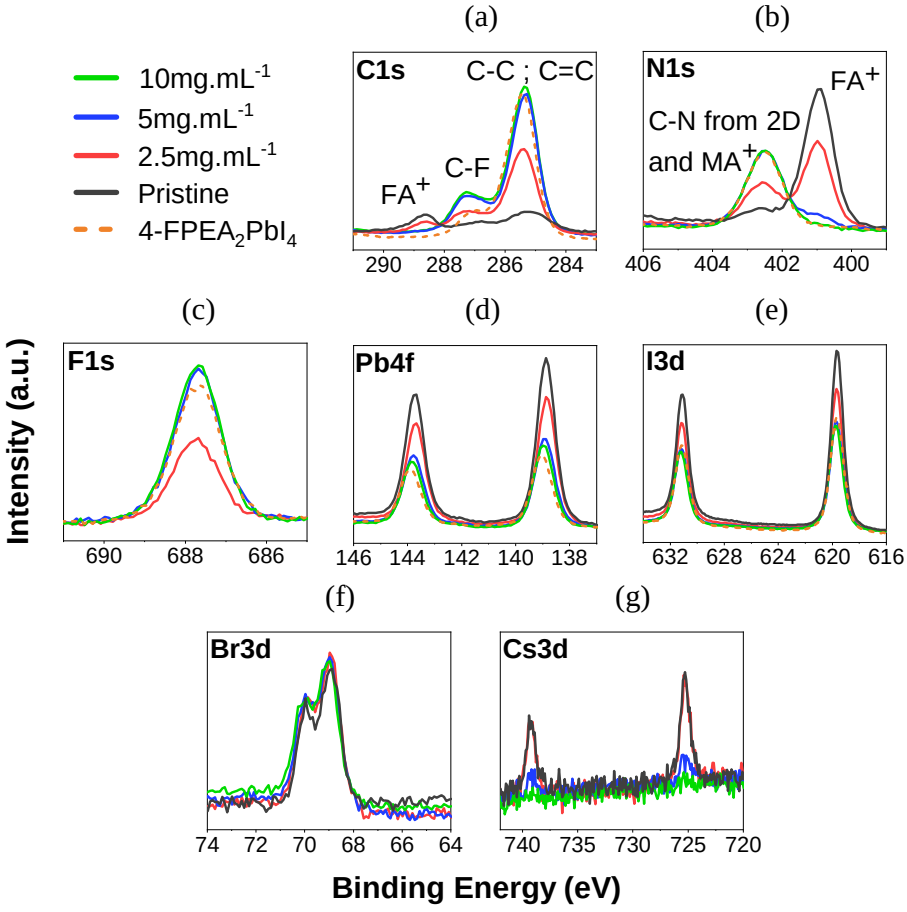

Figure 3.11: XPS high-resolution spectra of (a) C1s, (b) N1s, (c) F1s, (d) Pb4f, (e) I3d, (f) Br3d, and (g) Cs3d of pristine and 4-FPEAI-treated 3D samples (2.5, 5, and 10 mg.mL^{-1}), compared to $(4\text{-FPEA})_2PbI_4$ pure 2D perovskite.

Since the 3D perovskite contains no fluorine, pristine data is not visible for F1s spectra in Figure 3.11c, while Br3d and Cs3d spectra from Figures 3.11f and 3.11g do not display pure 2D perovskite data, as they are not involved in this material.

From a qualitative perspective, the intensity of F1s spectra - related to the C – F contribution - increases with 4-FPEAI solution concentration. Combined with XRD and PL data, this observation evidences the 2D layer presence in every 4-FPEAI treated sample. This is also confirmed by the evolution of C1s spectra, showing a gradual increase of the signal at 287.5 ± 0.2 eV coming from the C - F bonding (while the C - O bonding has close binding energies, the signal was confirmed as a C - F response). Subsequently, we observe a signal decrease of the FA^+ imidine (288.3 ± 0.2 eV) and MA^+ (286.4 ± 0.2 eV) bonds resulting from the 3D perovskite underneath. Similar observations are made on the FA^+ contribution (400.9 ± 0.2 eV) from the N1s spectra, which disappears for the highest 10 mg.mL^{-1} concentration. The C - N bond originating from MA^+ contribution in the 3D perovskite and the C - N bond of the 2D molecule have very close binding energies (402.4 ± 0.2 eV), which explains the increase of this peak for higher 4-FPEAI concentrations, most probably attributed to the 2D layer. Correspondingly, Pb4f and I3d peaks come both from 2D and 3D perovskites. However, the iodine/lead ratio increases from 3.35 for pristine to 3.82 for 10 mg.mL^{-1} sample, getting closer to the one of the pure 2D reference (theoretical I/Pb ratio of 2.5 in the 3D perovskite, and 4 in the 2D). Meanwhile, $Cs3d_{5/2}$ and $Cs3d_{3/2}$ peaks at 725.0 and 739.1 eV, brought only by the 3D perovskite, disappear, meaning that the 2D layer becomes thick enough to prevent the 3D perovskite from being detected by XPS measurements.

Numerous measurements performed for each experimental condition confirmed the spatial homogeneity of the surface composition (400 μm spot size) and the repeatability of measured data. At the same time, SEM and AFM images from Figures 3.7 and 3.8 showed good coverage of the 2D layer formed. Furthermore, Perini *et al.*, who studied the deposition of PEAI, OAI, and OABr spacers on a 3D perovskite composition similar ours, provided high-resolution XPS spectra with identical trends than the ones observed in this work [Perini *et al.* 2021].

Therefore, we conclude that for 2.5 mg.mL^{-1} samples, the measured XPS signal originates from the 2D layer and the 3D perovskite underneath, due to a nanometric 2D layer thickness. By increasing 4-FPEAI solution concentration, the 2D overlayer gets thicker and progressively screens the 3D layer signal, confirming previous correlations between 4-FPEAI solution concentration and 2D layer thickness. Surprisingly, Br3d spectra, contrarily to Cs3d, remain similar between pristine and 4-FPEAI treated samples, while its presence is only expected within the 3D phase. This finding raises a question about bromine distribution in the 2D/3D structure, and its role in the formation mechanism of the 2D perovskite layer, which will be discussed in the next chapter. Using XPS quantitative information, the atomic percentage of every element and corresponding key atomic ratios at the material surface was determined for the pure 2D perovskite, pristine and all 4-FPEAI treated samples. These experimental ratios were compared to the expected ratios obtained from theoretical stoichiometry. The atomic percentages are gathered in Table 3.2, along with the most meaningful C/N ratio. For conciseness purposes, only such tables will be presented for the next studies instead of presenting high-resolution spectra.

Pure 2D and pristine 3D perovskite present very different chemical compositions. Fluorine is exclusive to the 2D phase, and bromine and cesium are found only in the 3D layer. After 2.5 mg.mL^{-1} 4-FPEAI treatment, the surface chemical composition evolves halfway between 2D and 3D perovskite references, confirming that the 2D layer is only

Table 3.2: XPS surface chemical composition of a pristine 3D perovskite, a pure 2D perovskite, and 4-FPEAI treated samples for all concentrations studied.

	Pristine 3D	2.5 mg.mL^{-1}	5 mg.mL^{-1}	10 mg.mL^{-1}	Pure 2D
C1s	31.6 ± 3.5	46.7 ± 1.2	60.0 ± 0.6	62.6 ± 0.4	62.3 ± 0.7
I3d$_{5/2}$	31.5 ± 2.2	21.3 ± 0.5	14.1 ± 0.5	13.0 ± 0.5	16.3 ± 0.4
N1s	18.2 ± 1.1	13.3 ± 0.3	8.8 ± 0.2	7.9 ± 0.3	7.7 ± 0.2
Pb4f$_{7/2}$	9.4 ± 0.6	6.3 ± 0.2	3.8 ± 0.1	3.4 ± 0.1	3.0 ± 0.1
O1s[c]	4.5 ± 1.2	1.9 ± 0.2	1.4 ± 0.6	1.4 ± 1.0	1.6 ± 0.9
F1s[a]	-	5.5 ± 0.2	8.0 ± 0.4	8.3 ± 0.6	8.6 ± 0.2
Cs3d$_{5/2}$[b]	0.6 ± 0.0	0.4 ± 0.0	0.1 ± 0.0	0.1 ± 0.0	-
Br3d[b]	5.2 ± 0.3	4.7 ± 0.1	3.8 ± 0.1	3.4 ± 0.1	-
C/N ratio	1.7	3.5	6.8	7.9	8.1

[a] Only in 4-FPEAI.
[b] Only in 3D perovskite.
[c] Ambient carbonaceous contamination.

a few nanometers thick (lower than the depth probed with XPS), and that the top 2D layer and 3D perovskite underneath are detected. As 4-FPEAI solution concentration increases, the surface chemical composition of 4-FPEAI treated samples tends to the one of a pure 2D perovskite, giving us indications about the thickness evolution of the 2D layer. At the highest 10 mg.mL^{-1} concentration, the chemical composition is almost identical to a pure 2D layer, as illustrated by the C/N ratio. Thus, we conclude that with 5 mg.mL^{-1}, the 2D layer thickness has increased compared to 2.5 mg.mL^{-1}, but remains slightly lower than the 10 nm of XPS scanning depth. At 10 mg.mL^{-1}, however, no more 3D perovskite is detected, and the 2D layer thickness should be greater than 10 nm, supporting the 30 nm thickness estimation made with cross-section SEM. As seen in the high-resolution spectra, the bromine amount within the material's surface remains noteworthy regardless of 4-FPEAI concentration, highlighting the importance of the study performed in the next chapter.

In-depth profiling

To assess the elemental distribution within 2D and 3D layers and to position their interface, XPS in-depth profiling was performed on pristine and 4-FPEAI treated samples, and the results are displayed in Figure 3.12. The procedure for these measurements is detailed in Section 2.2.3. Due to the quick evolution in chemical composition of the surface of 4-FPEAI treated samples, the sputtering steps between each analysis were shortened to 20 seconds. After 200 seconds of etching time, sputtering steps were set back to 60 seconds each, until the TiO_2 layer was reached.

For the pristine sample in Figure 3.12a, after the first sputtering sequence, a radical decrease of the C1s content is observed due to the elimination of superficial adventitious contamination and the degradation of the C-N bounds due to Ar^+ bombardment, in line with the N1s decrease also visible [Cacovich *et al.* 2022]. Going to the second scan, C1s, N1s, and Pb4f amounts are stable along the layer. As the perovskite layer is etched, the iodine/bromine ratio decreases from 6.8 to 4.1, suggesting inhomogeneous

halide distribution, with more iodine towards the 3D perovskite surface, and bromine moving to the bottom of the layer, as shown in the paper above. After 400 seconds, O1s and Ti2p signals increase while the 3D perovskite elements decrease, pinpointing the end of the layer. This evolution is progressive due to the intermixing of 3D perovskite and mesoporous-TiO_2 layers. We consider that the interface between the 3D perovskite and the TiO_2 layer is reached when O1s and Ti2p signals get close to the half of their maximum value, which is estimated for this sample close to 500 seconds of etching, in agreement with other works on the same perovskite [Cacovich *et al.* 2022].

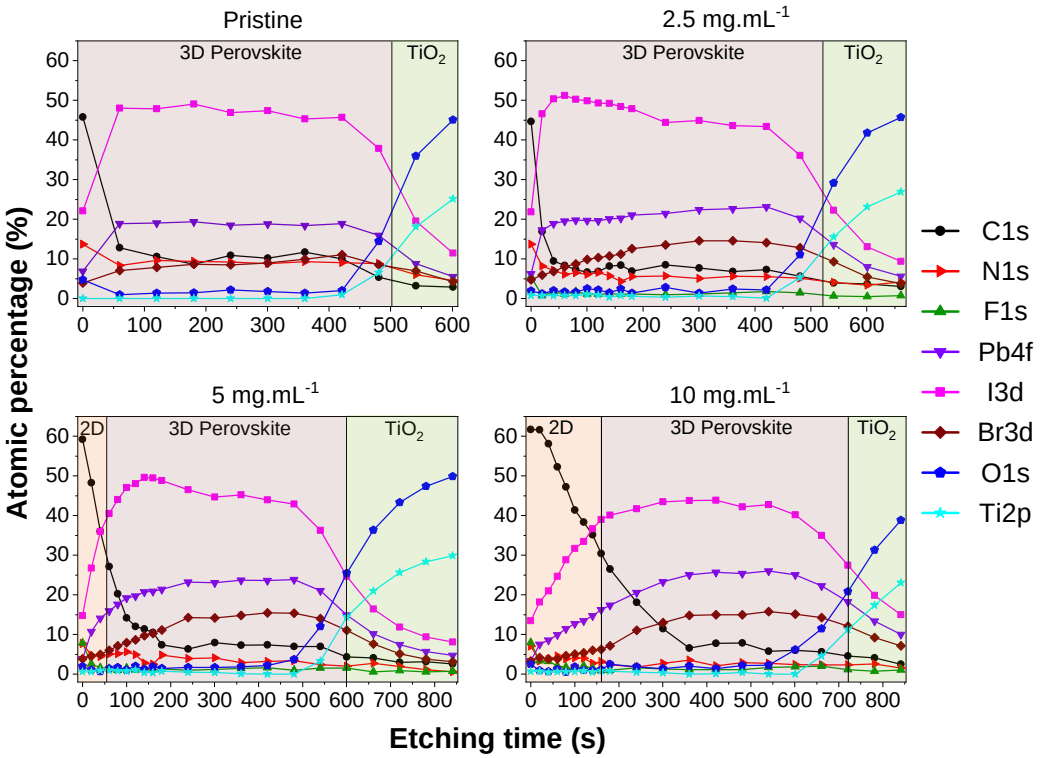

Figure 3.12: Atomic percentage evolution of chemical elements over etching time, for pristine, 2.5, 5, and 10 mg.mL^{-1} samples.

The 2.5 mg.mL^{-1} sample from Figure 3.12b shows equivalent behavior to pristine material, with similar atomic percentages evolution (only more continuous due to more frequent scans), and TiO_2 layer reached after comparable etching times. A 5% fluorine signal in the first scan is the only indication of the 2D perovskite, confirming its shallow thickness. On the other hand, 5 and 10 mg.mL^{-1} samples reveal a different outcome. Correspondingly to the 2D perovskite surface composition seen in Table 3.2, the first scan (performed before any etching) on these samples show higher C1s and lower I3d and Pb4f amounts. The composition gradually moves from a 2D to a 3D perovskite stoichiometry, suggesting a not well defined interface between 2D and 3D phases. F1s signal also confirms the 2D layer presence, but its content decreases after the first scan, stabilizing then around a few percents along the 2D layer profiling. This intensity decrease is however stronger than expected, possibly due to the volatile nature of fluorine, which would get removed from the layer during etching, or because of a 4-FPEAI aggregation in the first few nanometers of the 2D layer. With a more visible 2D layer, it became possible to estimate the interface between 2D and 3D materials.

Just like for the 3D perovskite/TiO_2 interface, the 2D/3D interface was defined as the point when the percentage of I3d and C1s elements is halfway their value in the 2D layer and their value in the 3D perovskite. Therefore, the 2D/3D interface is reached after 60s of etching for the 5 mg.mL^{-1} sample, and 170s for the 10 mg.mL^{-1} sample. Using surface XPS, we estimated the 2D layer thickness to be slightly lower than 10 nm in the 5 mg.mL^{-1} sample. Hence, by considering a constant etching speed in the 2D layer, its thickness should be around 2.8x greater in the 10 mg.mL^{-1} sample than in the 5 mg.mL^{-1} one, leading to a maximum thickness of around 25 to 30 nm, consistent with our previous observations, and with the orders of magnitude found in the literature for such structures [Liu *et al.* 2019a, La-Placa *et al.* 2019].

3.2.4 Solvent washing of the 2D layer

Despite a fairly repeatable process, higher 4-FPEAI solution concentrations combined with small operator-dependant variations during synthesis led to the fabrication of some samples with unusually thick 2D layers. As seen in Figures 3.13, 3.14a, and 3.14b, this kind of sample, named "thick 10 mg.mL^{-1}", exhibits more intense 2D contributions during XRD measurements, and shows a drastically different morphology in comparison with classic 10 mg.mL^{-1} samples, with big flakes instead of a quite uniform layer with smaller grains on top. In addition to the more intense 2D peaks, the diffractogram of the thick 10 mg.mL^{-1} sample shows new peaks regularly distributed at 4.5, 9.0, 17.9, and 22.5°. These peaks do not correspond to a 2D perovskite phase, and so, based on work from Jiang *et al.*, who observed similar phenomenon with PEAI cation salt, we believe they correspond to a crystallized 4-FPEAI phase [Jiang *et al.* 2019a].

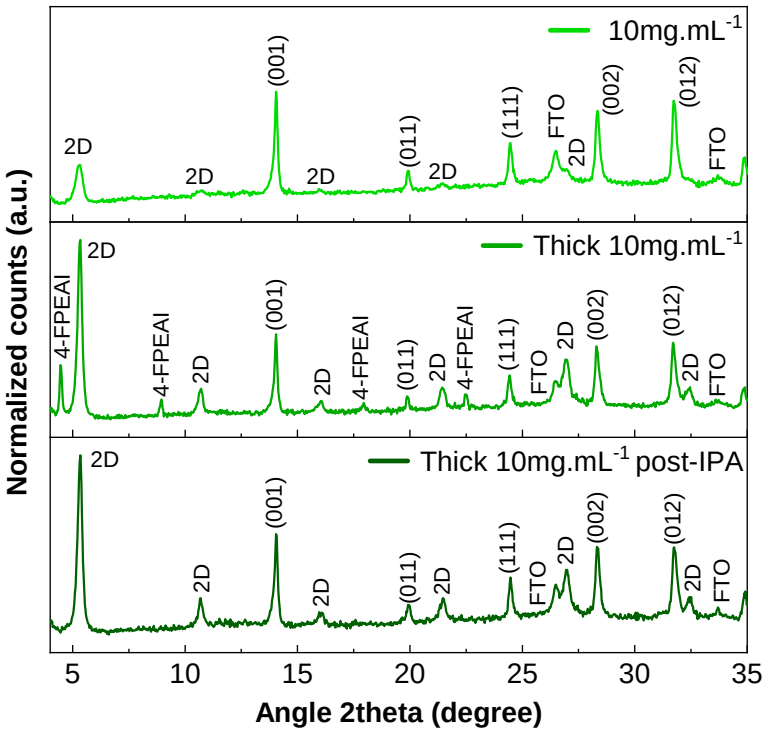

Figure 3.13: XRD patterns of a 10 mg.mL^{-1} sample thick 10 mg.mL^{-1} samples, before and after IPA washing subsequently to 2D perovskite layer annealing.

This phase would be formed after a complete depletion of PbI_2 used by 4-FPEAI to form the 2D perovskite. As a result, excess 4-FPEAI would crystallize on the sample surface during the annealing. As shown in the next subsection, such 2D layer thicknesses are already suboptimal for device applications. Thus, the optoelectronic effects induced by this supplementary cation salt phase were not studied, and instead, a way to remove this compound was explored.

While 4-FPEAI cation salt is solvable in IPA, it should be different for the $(4\text{-FPEA})_2PbI_4$ 2D perovskite phase. Regarding this assumption, after annealing the 2D layer, 100 µL of IPA was spin-coated on the sample's surface as a subsequent washing process. Figures 3.13 and 3.14c display the consequence of this IPA washing. All peaks from the 4-FPEAI crystalline phase disappeared without altering both 2D and 3D phases noticeably. On the sample surface, partial etching of the top layer is observed, and most of the flakes disappeared, leaving what are expected to be small $(4\text{-FPEA})_2PbI_4$ grains (few nanometers to few tens of nanometers). As a result, the surface aspect is much more similar to a classic 10 mg.mL^{-1}, with less visible 3D perovskite grains underneath due to the thicker 2D layer. These observations suggest that IPA is a viable washing solvent to clean the 2D perovskite surface without damaging it.

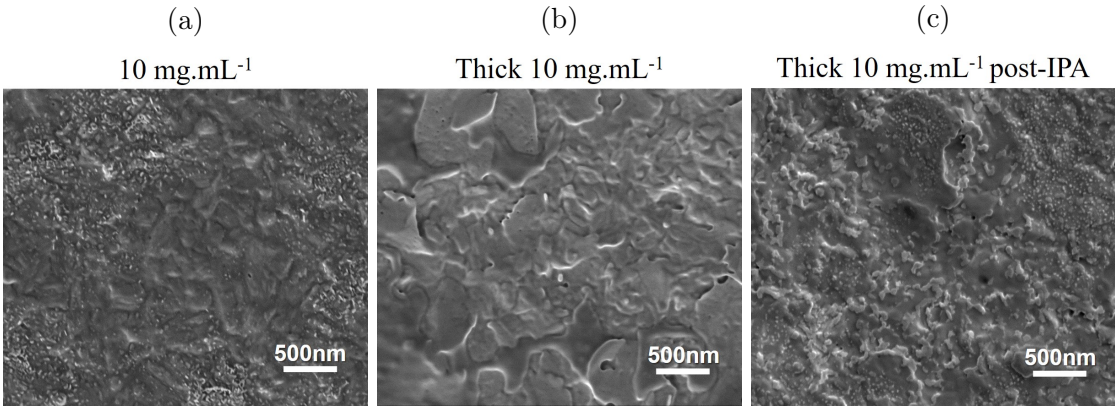

Figure 3.14: SEM images of (b) 10 mg.mL^{-1}, (c) thick 10 mg.mL^{-1}, and (d) IPA-washed thick 10 mg.mL^{-1} samples.

Surface XPS measurements were performed on 10 mg.mL^{-1} 4-FPEAI treated samples, with and without IPA washing, to assess its effect on the 2D perovskite layer. However, samples used for this study are classic 10 mg.mL^{-1} for several reasons. First, thick 10 mg.mL^{-1} samples are uncommon products of the 4-FPEAI treatment process with this concentration. Secondly, it was not possible to discriminate thick 10 mg.mL^{-1} samples and standard ones before sending them for XPS measurements, as samples had to be kept in inert atmosphere before measurements to prevent surface contamination as much as possible. Finally, we did not want to increase further 4-FPEAI concentration to try obtaining such samples more repeatably.

Surface chemical composition of 10 mg.mL^{-1} samples before and after IPA washing are presented in Table 3.3. Without IPA washing, sample surface composition is similar to 10 mg.mL^{-1} samples from the previous study in Table 3.2. As a result of IPA washing, the surface chemical composition is modified and the C/N ratio decreases, getting between the ones of 2.5 and 5 mg.mL^{-1} samples. This result could either indicate a significant decrease in the 2D layer thickness or a modification of its stoichiometry. XPS in-depth profiling, shown in Figure 3.15 was used to arbitrate between these two hypotheses.

Table 3.3: XPS surface chemical composition of a pristine 3D perovskite, and 10 mg.mL^{-1} samples without and with IPA washing.

	Pristine 3D	10 mg.mL^{-1}	
			+ IPA washing
C1s	31.6 ± 3.5	63.6 ± 0.1	47.2 ± 0.1
I3d$_{5/2}$	31.5 ± 2.2	13.0 ± 0.1	22.6 ± 0.5
N1s	18.2 ± 1.1	7.9 ± 0.1	10.2 ± 0.2
Pb4f$_{7/2}$	9.4 ± 0.6	3.1 ± 0.0	7.3 ± 0.2
O1s^{c}	4.5 ± 1.2	0.5 ± 0.1	1.8 ± 0.1
F1s^{a}	-	8.8 ± 0.1	6.6 ± 0.2
Cs3d$_{5/2}$^{b}	0.6 ± 0.0	0.0 ± 0.0	0.2 ± 0.0
Br3d^{b}	5.2 ± 0.3	3.2 ± 0.0	4.1 ± 0.1
C/N ratio	1.7	8.1	4.6

[a] Only in 4-FPEAI.
[b] Only in 3D perovskite.
[c] Ambient carbonaceous contamination.

The chemical composition of the 10 mg.mL^{-1} sample in Figure 3.15a evolves similarly to the same sample from Figure 3.12d, and so, will not be commented again. The only difference is that the 3D perovskite/TiO_2 interface is reached later, possibly due to a lower etching rate caused by denser/thicker perovskite layers. After IPA washing, two main changes are visible. First, the 2D layer gets significantly thinner as it is without washing, reducing the etching time required to reach the 2D/3D interface from 185 to 100 seconds (which is closer to a 5 mg.mL^{-1} sample from Figure 3.12c). The second change is the different surface composition, with lower C1s and F1s amounts, and proportionally increased N1s, Pb4f, I3d, and Br3d signals. It confirms that IPA not only removes the crystallized 4-FPEAI phase but also etches the 2D perovskite.

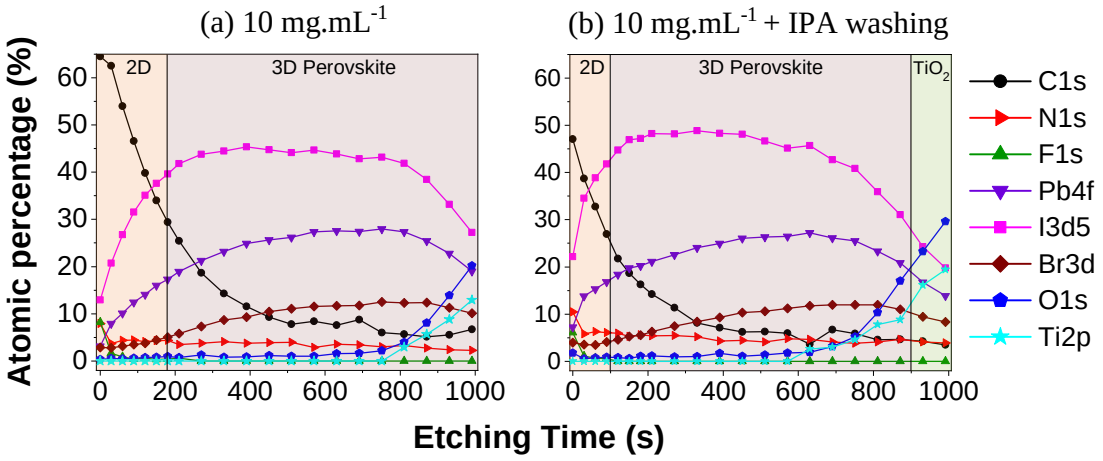

Figure 3.15: Atomic percentage evolution of chemical elements with etching time, (a) a 10 mg.mL^{-1} sample, (b) washed with IPA after 2D perovskite annealing.

This study revealed the possibility of using IPA as a washing solvent to clean a 2D/3D perovskite structure, removing crystallized 2D cation salt from its surface. However, it also highlighted that IPA might not be the best solvent for this purpose, as it noticeably solves the 2D perovskite phase.

3.3 Static deposition of the 2D precursor solution

The previous section investigated the formation of a 2D/3D structure by focusing on 4-FPEAI solution concentration. This study revealed the significant effect of this parameter on the 2D perovskite layer, and provided a better understanding of the 2D/3D structure properties. As presented in the first chapter of this work, the development of industrial-scale devices with greater active areas (> 100 cm^2) is crucial for PSCs. Larger-scale techniques commonly use longer coating windows, i.e., longer times between the deposition of the precursor solution and the extraction of excess solvent, than spin-coating [Yang *et al.* 2017, Howard *et al.* 2019].

Therefore, to acquire more knowledge on the 2D/3D structure and figure out how the formation of a 2D perovskite on a 3D layer could be compatible with such processes, another synthesis parameter was studied in the form of a modified deposition method that would be more comparable to solution processing techniques for larger devices. This new deposition procedure was inspired by several works, which used a prolonged contact between the annealed 3D perovskite and the 2D precursor solution. This prolonged contact was realized either by dipping the samples into the 2D solution, or by depositing this solution for a specific soaking time, and annealing again the samples after removing the excess solvent to form the 2D perovskite [Zhao *et al.* 2016, Wu *et al.* 2020, Teale *et al.* 2020].

3.3.1 Deposition process

So far, after the 3D perovskite crystallization, 100 µL of 4-FPEAI solution in IPA was deposited dynamically during a 30-second spin-coating procedure, followed by a 5 minutes annealing step at 100 °C to form the 2D perovskite. Instead, 100 µL of the 4-FPEAI precursor solution was deposited statically onto the 3D layer and left for a certain amount of soaking time. After reaching the desired time, the same spin-coating and annealing steps were used to remove solution excess from the sample surface and form the 2D perovskite layer (spin-coating was still used to remove excess solvent for practical reasons, the object of this study being the soaking time between 2D precursor solution and the 3D layer). The deposition procedure of these new experimental conditions is illustrated in Figure 3.16.

Based on results from the previous section and the next one dedicated to device applications, the 2.5 mg.mL^{-1} solution concentration was used for this study. Dynamic deposition was compared to static deposition using 10 and 30 seconds soaking times (later designated as dynamic, static 10s, and static 30s). An extra condition, with 5 minutes of soaking time, was also used to investigate the effect of prolonged contact between the 3D perovskite and 4-FPEAI solution. The characterizations performed on this experimental condition are presented in Annex A.2.

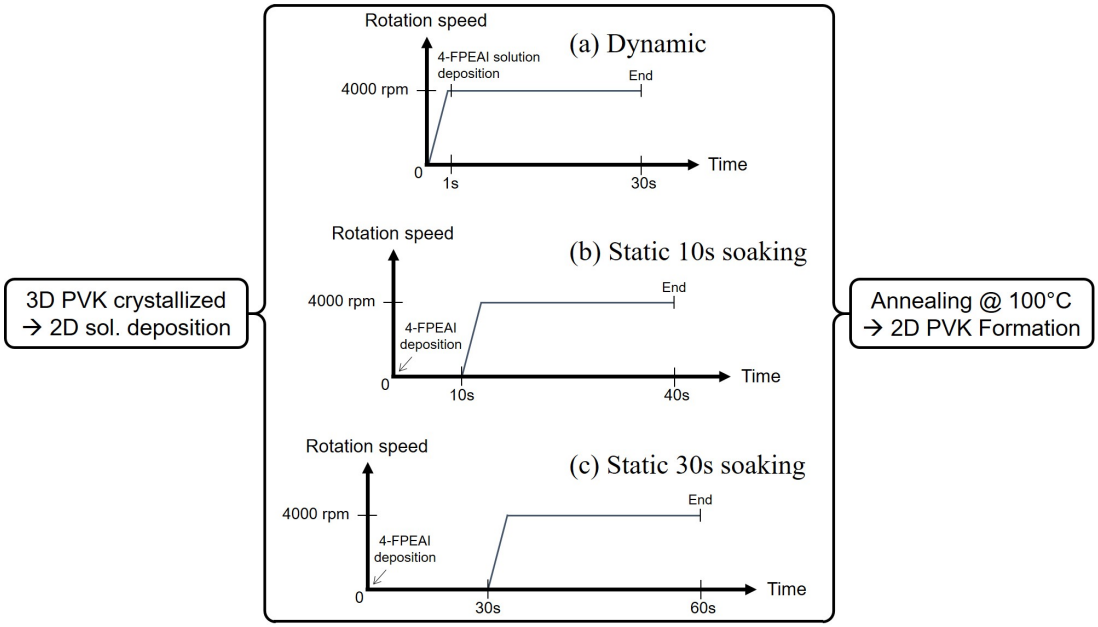

Figure 3.16: Spin-coating deposition procedure for dynamic and static (10 or 30 seconds soaking time) 4-FPEAI treated samples.

3.3.2 Impact on the 2D layer

To analyze the properties of the 2D perovskite layer formed with this static deposition, we used the same characterization methods than in the previous study in Section 3.2.

Optical properties

Looking at absorption and PL spectra from Figure 3.17, increasing the soaking time of 4-FPEAI solution on the 3D perovskite surface leads to a similar result than increasing the solution concentration, but to a considerably lesser extent.

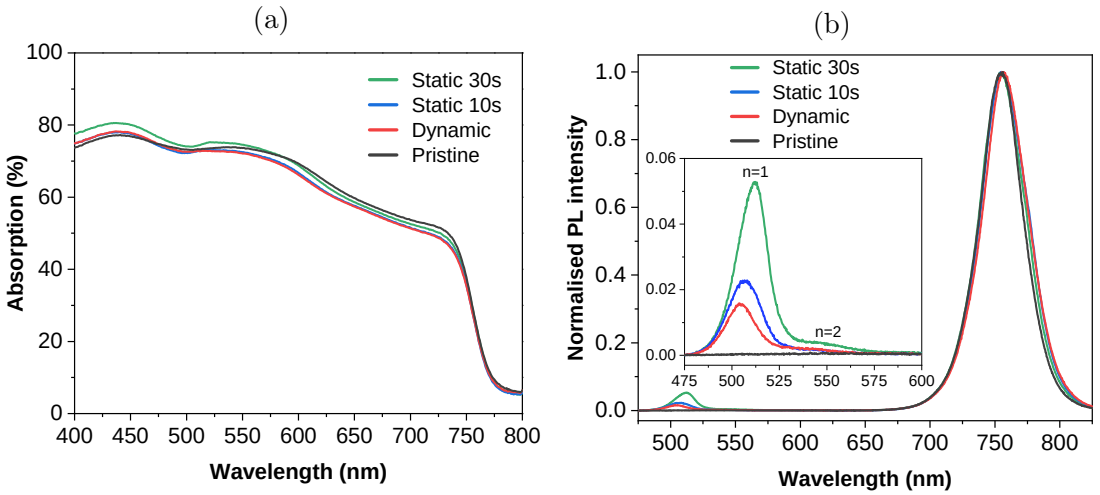

Figure 3.17: (a) Optical absorption and (b) PL spectra of pristine and 4-FPEAI treated samples for all soaking times.

In Figure 3.17a, the difference between the absorption spectra of each condition is insignificant, except for the static 30s. This sample shows similar features to 5 and 10 mg.mL^{-1} samples in Figure 3.5 which are characteristic of the 2D perovskite presence (absorption increase under 550 nm, with an inflection around 500 nm). Nevertheless, these features are comparatively smaller in the static 30s sample than in the 5 mg.mL^{-1} one. Regarding PL spectra from Figure 3.17b, analogous comments can be made on the emission properties of the layer. Increasing soaking time does not affect the 3D perovskite bulk and leads to a brighter 2D phase. However, even with the longest soaking time, the PL signal is only increased by a factor of 3, which is slightly lower than the increase observed by increasing 4-FPEAI solution concentration from 2.5 to 5 mg.mL^{-1}.

Structural and morphological properties

The 2D layer was also characterized with XRD. The resulting zoomed diffractograms in Figure 3.18b corroborate the trend from optical measurements, with a slight increase of the 2D phase signal with longer soaking times. This result would confirm that increasing soaking time forms a greater 2D perovskite amount. Unlike in Figure 3.3b, more 2D perovskite is not correlated with an intensity decrease of the PbI_2 peak. This peak is reduced after dynamic 4-FPEAI solution deposition, but with greater soaking times, it increases back. Furthermore, based on Figure 3.18a, static deposition modifies the 3D perovskite peaks in favor of (011) direction, detrimentally to (001) plans.

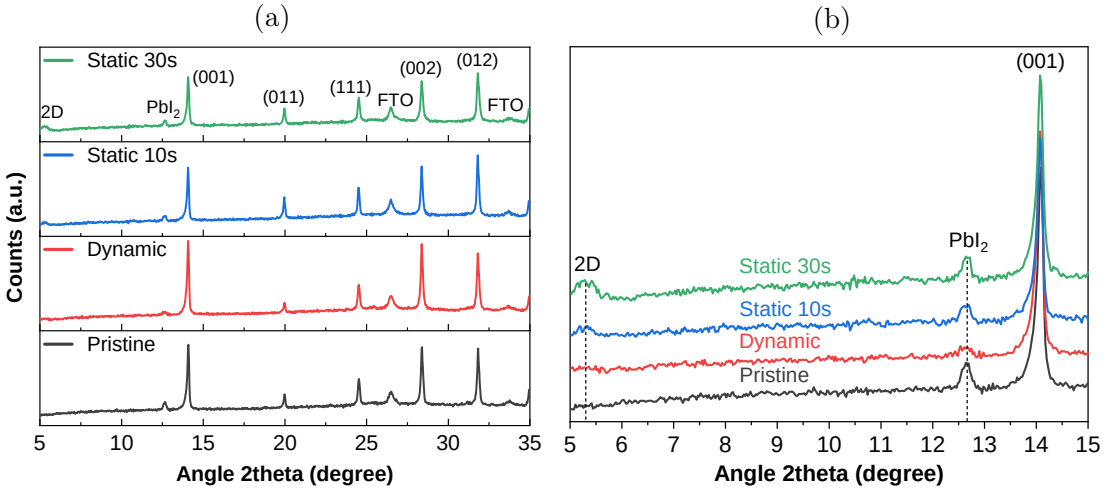

Figure 3.18: (a) XRD pattern of pristine and 4-FPEAI treated (2.5 mg.mL^{-1}) samples for all soaking times, (b) zoomed on first 2D and 3D perovskites peaks.

Both statements are confirmed in Table 3.4, which reports the area of PbI_2, (001), and (011) peaks of the 3D perovskite, extracted from XRD measurements. These data suggest that a prolonged contact between 4-FPEAI solution and the 3D perovskite material leads to the degradation of this layer.

SEM was performed on all 4-FPEAI treated samples. The resulting images shown in Figures 3.19a[a], 3.19b, and 3.19c reveal only a negligible evolution of the 2D layer thickness between all soaking times, and 3D perovskite grains remain visible regardless of the soaking time. As this time increases, a growing number of small grains appear

[a] top-right area masked to hide a hole in the 3D layer unrelated to 4-FPEAI treatment

Table 3.4: XRD parameters of PbI_2 peak, (001) and (011) peaks from the 3D perovskite in pristine and 4-FPEAI treated samples for all soaking times.

	Area (cts×°2Θ)			(001)/PbI_2 ratio	(001)/(011) ratio
	PbI_2	(001)	(011)		
Pristine	49.1	377.8	60.0	7.7	6.3
Dynamic	21.9	443.7	50.85	20.3	8.7
Static 10s	33.6	293.1	112.0	8.7	2.6
Static 30s	30.7	300.4	84.5	9.8	3.6

on the material's surface. For 30 seconds of soaking, these small grains start coalescing into bigger aggregates, suggesting the formation of a more inhomogeneous 2D layer and inducing a rougher surface.

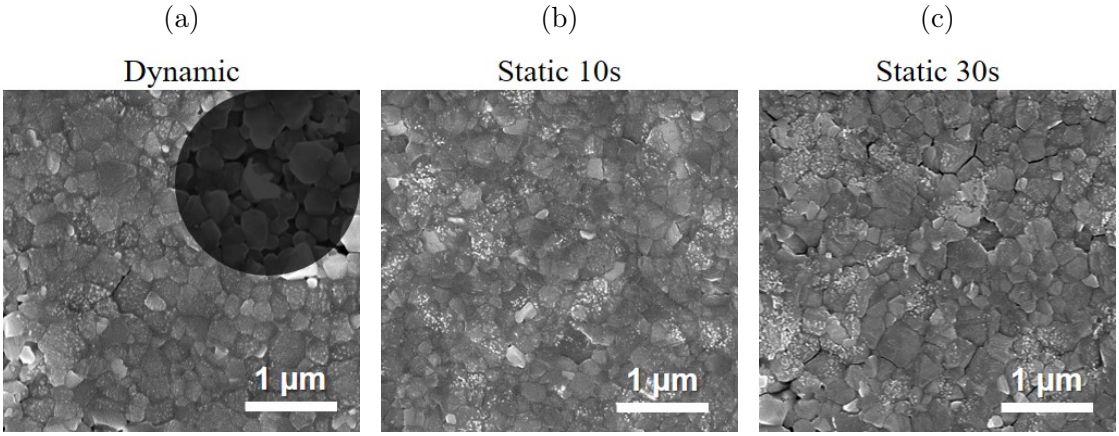

Figure 3.19: SEM images of (a) dynamic, (b) static 10s, and (c) static 30s samples.

Surface roughness was also estimated for each sample. After demonstrating in Section 3.2.2 that AFM and confocal microscopy led to similar results for roughness measurements, only confocal microscopy was used here. The distribution of roughness values, obtained through several measurements, are displayed in Figure 3.20, while average values for each soaking time are presented in Table 3.5.

Due to the irregular segregation of 2D perovskite grains on the material surface observed with SEM, static depositions leads to higher and more inhomogeneous roughness values compared to dynamic deposition.

Table 3.5: Average S_q and S_a roughness of pristine and 4-FPEAI treated samples.

	S_q roughness (nm)	$S_a$roughness (nm)
Pristine	23	18
Dynamic	21	17
Static 10s	31	25
Static 30s	24	19

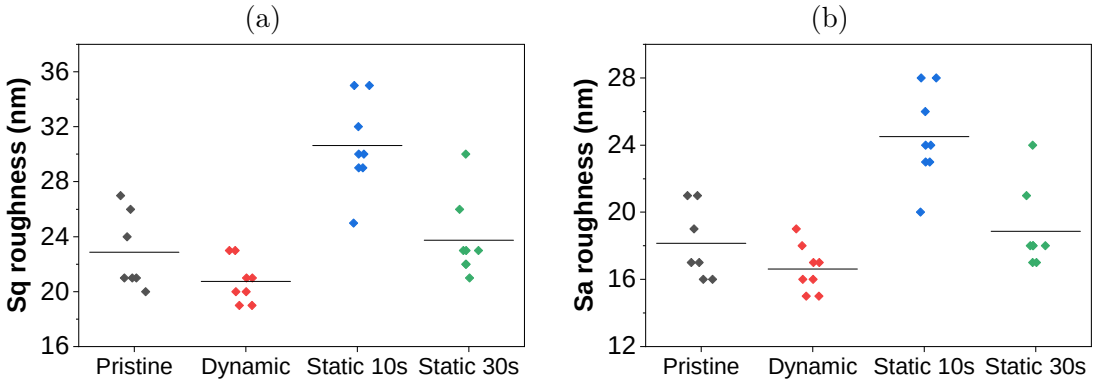

Figure 3.20: Distribution of (a) S_q and (b) S_a roughness measured with confocal microscopy on pristine, and 4-FPEAI treated samples for each soaking time.

Confirmation of the results with XPS

This soaking time study was completed with XPS measurements. Table 3.6 sums-up these measurements and shows the surface atomic percentage measured for each sample. Reference pristine 3D and pure 2D surface compositions are identical to the ones from the 4-FPEAI solution concentration study, as well as the 2.5 mg.mL^{-1} sample, which is labeled here as dynamic. The use of a static deposition does not induce a significant evolution of surface composition. After 10 seconds of soaking, the surface composition is slightly closer to the pure 2D perovskite. However, for 30 seconds of soaking, it comes back closer to the dynamic sample, with increased standard deviation.

Table 3.6: XPS surface chemical composition of pristine 3D perovskite, $(4\text{-FPEA})_2PbI_4$ pure 2D perovskite, and 4-FPEAI treated samples for all soaking times.

	Pristine 3D	2.5 mg.mL^{-1}			Pure 2D
		Dynamic	Static 10s	Static 30s	
C1s	31.6 ± 3.5	46.7 ± 1.2	52.4 ± 1.0	47.4 ± 3.8	62.3 ± 0.7
$I3d_{5/2}$	31.5 ± 2.2	21.3 ± 0.5	17.0 ± 0.7	20.7 ± 4.0	16.3 ± 0.4
N1s	18.2 ± 1.1	13.3 ± 0.3	11.1 ± 0.3	10.3 ± 0.9	7.7 ± 0.2
$Pb4f_{7/2}$	9.4 ± 0.6	6.3 ± 0.2	4.9 ± 0.2	6.5 ± 1.6	3.0 ± 0.1
O1s[c]	4.5 ± 1.2	1.9 ± 0.2	2.3 ± 1.2	3.7 ± 2.2	1.6 ± 0.9
F1s[a]	-	5.5 ± 0.2	6.9 ± 0.8	6.0 ± 0.9	8.6 ± 0.2
$Cs3d_{5/2}$[b]	0.6 ± 0.0	0.3 ± 0.1	0.4 ± 0.1	0.1 ± 0.0	-
Br3d[b]	5.2 ± 0.3	4.7 ± 0.1	5.0 ± 0.2	4.9 ± 0.2	-

[a] Only in 4-FPEAI.
[b] Only in 3D perovskite.
[c] Ambient carbonaceous contamination.

While these results confirm that switching from a dynamic to a static deposition increase the 2D layer thickness, they also reveal that this method is ineffective, for several

reasons. First, with 30 seconds of soaking, most of the characterizations performed provided inhomogeneous results. Secondly, the surface chemical composition of the 5 mg.mL^{-1} sample (see Table 3.2 from the previous study) was much closer to the 2D perovskite reference than static 10s and 30s samples. Therefore, increasing 4-FPEAI solution concentration was more efficient in forming a thicker 2D layer. Therefore, using a static deposition does not provide a good control over layer thickness, and in this regard, increasing 4-FPEAI solution concentration is a much more efficient technique.

Purely based on material properties, the low effect on 2D layer thickness, added to the lack of repeatability in the results obtained, were sufficient to discard the use of soaking time as the main synthesis parameter to control the formation of a 2D/3D structure.

3.3.3 Effect of 2D solution solvent on the 3D perovskite

The last investigation was performed to decorrelate the effects on the 3D perovskite of pure IPA solvent from the effects of the 4-FPEAI solution. The same experimental conditions used in the soaking time study - pristine, dynamic, static 10s, and static 30s - were applied again. However, 2.5 mg.mL^{-1} 4-FPEAI solution in IPA was replaced with pure IPA, leading to the new conditions named pristine, IPA dynamic, IPA static 10s, and IPA static 30s. A sample with 5 minutes soaking time was also added and will be referred as IPA 5mins. These samples were characterized with XRD and SEM. Resulting diffractograms and peak parameters are presented in Figure 3.21 and Table 3.7 and reveal a clear trend.

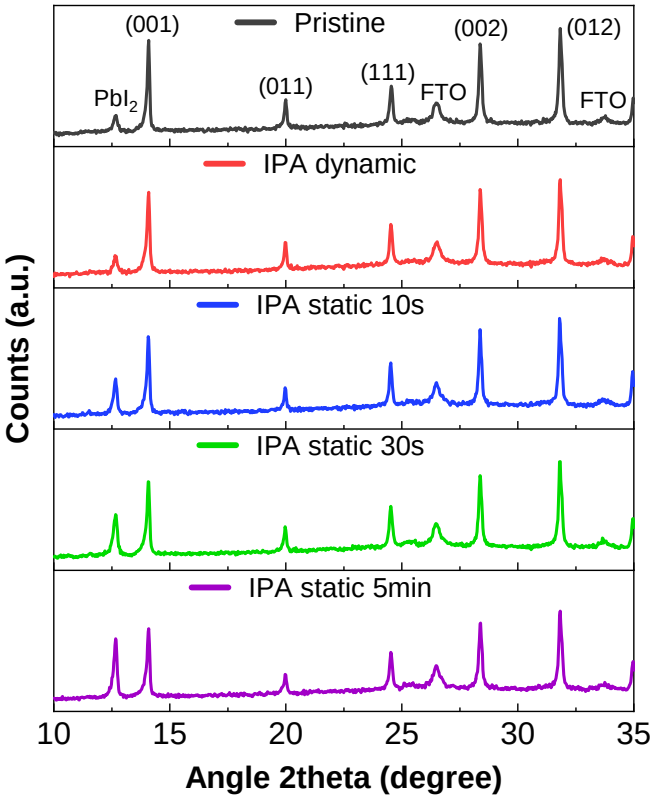

Figure 3.21: XRD pattern of pristine and IPA treated samples using dynamic or static deposition with 10 seconds, 30 seconds, or 5 minutes soaking time.

Here, increasing the soaking time leads to a slight decrease of peaks from the 3D phase while significantly enhancing the PbI_2 peak. This suggests that the 3D phase is more damaged in contact with IPA than in contact with the 4-FPEAI solution. Furthermore, this decrease of 3D perovskite peaks with IPA treatment seems distributed evenly among all crystallographic directions, instead of specifically on the (001) plans as seen with 4-FPEAI treatment.

Table 3.7: XRD parameters of PbI_2 peak and (001) peak from the 3D perovskite in pristine and IPA treated samples.

	Area (cts×°2Θ)			(001)/PbI_2 ratio	(001)/(011) ratio
	PbI_2	(001)	(011)		
Pristine	66.0	270.7	126.7	4.1	2.1
IPA dynamic	61.1	285.8	133.2	4.68	2.1
IPA static 10s	161.5	266.2	141.5	1.65	1.9
IPA static 30s	178.8	276.0	116.4	1.54	2.4
IPA static 5mins	235.3	245.7	121.0	1.04	2.0

SEM images from Figure 3.22 align with XRD observations as the quite uniform pristine 3D layer, after being exposed to IPA for longer times, is progressively degraded. With the dynamic deposition of IPA solvent, this degradation effect remains mild. Switching to static deposition induces more pronounced damages to the layer. After 10 seconds of soaking time, the surface remains fairly homogeneous, with the appearance of a few damaged areas. Increasing soaking time to 30 seconds, most of the surface is altered, and several granular layers at different depths are seen. After 5 minutes of soaking, the layer is entirely damaged and gets a porous aspect, showing numerous holes. While grain size is not modified by IPA, the solvent gradually etched the 3D perovskite in a way that was not seen with the 4-FPEAI treatment.

Therefore, while direct contact with IPA is detrimental to the 3D perovskite layer, this phenomenon is hindered by applying only short soaking times, kept under about ten seconds. Furthermore, the formation of a 2D perovskite layer, driven by the deposition of a 4-FPEAI solution, tempers this degradation effect. To a lesser extent, these results are supported by work from Yoo *et al.* In their work, they considered IPA as a problematic solvent due to its polar protic nature and ability to solubilize FAI, and applied what they called a "selective precursor dissolution (SPD)" strategy. This method consisted in choosing first a solvent considered harmless for the 3D perovskite: chloroform, which had already been used as an anti-solvent for 3D perovskites, and combine it to a 2D cation salt that was soluble in this solvent: n-hexylammonium bromide [Yoo *et al.* 2019].

To conclude, this study raised significant problems regarding the use of a dipping process to form a 2D/3D structure. The formation of a 2D perovskite layer on 3D bulk using short soaking times did not prove to be very problematic in our configuration (4-FPEAI solution in IPA, deposited on a FA-based triple-cation 3D perovskite). More generally, the results obtained on longer soaking times raise a question about the possibility to apply this process in larger devices, as fast excess solvent disposal, trivial in spin-coating deposition, is a more critical issue in large-scale techniques such as blade-coating or slot-die coating. However, Liu *et al.* successfully formed a 2D/3D structure by dipping pristine 3D samples in a 2D precursor solution and annealing it without any excess solvent removal, which could be an interesting approach to investigate [Liu *et al.* 2019a]. Nevertheless, our current process, while being adapted to synthesize 2D/3D

structures with spin-coating, requires further solvent and 2D cation salt engineering to be applied in up-scale deposition methods with longer coating windows.

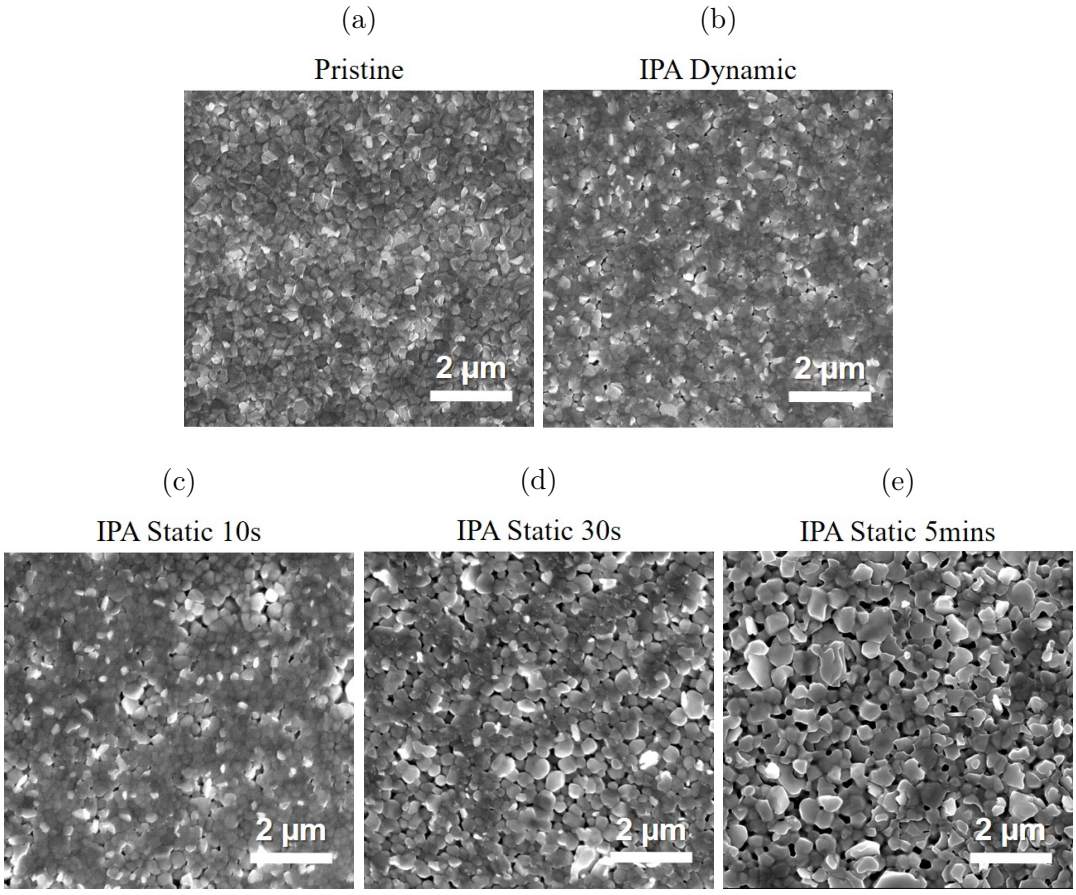

Figure 3.22: SEM surface images of (a) pristine, (b) IPA dynamic, (c) IPA static 10s, (d) IPA static 30s, and (e) IPA static 5mins samples.

3.4 Device applications

In this chapter, Sections 3.2 and 3.3 were focused on a material study of the 2D/3D structure, varying two different synthesis parameters: concentration of the 4-FPEAI solution, and the soaking time of this solution onto the 3D perovskite. The following section will focus on applying the 2D/3D structure in solar cells to improve their performances.

3.4.1 Optimal synthesis parameters

To focus on a single 2D/3D experimental condition, we first investigated which synthesis parameter among the ones studied during this chapter provided the best device performances. On the one hand, we compared the photovoltaic parameters of devices using pristine, dynamic, static 10s, and static 30s materials. On the other hand, this comparison was carried out between 2.5, 5, 7.5, and 10 mg.mL^{-1} 4-FPEAI solution concentrations. The distribution of photovoltaic parameters for each condition is presented in Figure 3.23 for soaking times, and in Figure 3.24 for solution concentrations.

Looking first at the soaking time study, dynamic deposition leads to the best PCEs, along with more repeatable data. More inhomogeneous results are obtained with the use of a 30 seconds soaking time, corroborating the observations made during the material study in Section 3.3. Hence, dynamic deposition was preferred over static deposition for device applications.

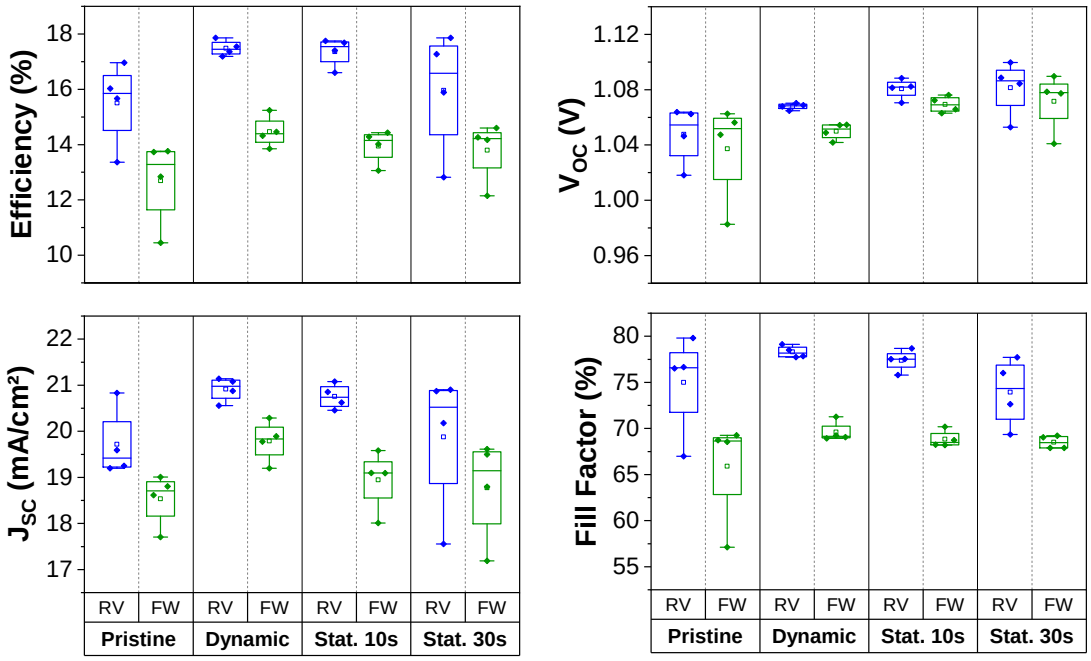

Figure 3.23: PCE, V_{OC}, J_{SC}, and FF distribution of 4-FPEAI treated cells for each soaking time. *(RV: blue, FW: green ; 4 cells/condition)*

Similarly to the material studies, tuning the concentration of the 4-FPEAI solution results in more drastic changes than increasing the deposition soaking time. As a result, the solar cells exhibit significantly altered PV parameters regarding the 4-FPEAI solution concentration used.

The overall best efficiency is obtained with the lowest 2.5 mg.mL^{-1} concentration, and a significant efficiency drop is observed for higher concentrations. Noticeable losses in open-circuit voltage V_{OC} are seen. However, this characteristic is not the main one affected by the 2D layer thickness increase, and fill factor FF shows a more significant and continuous decrease. This suggests that increasing 4-FPEAI solution concentration, is detrimental to device performances and leads to higher resistive losses. The most affected parameter is short-circuit current density (J_{SC}), which is almost halved for higher concentrations. This behavior could be caused by the formation of a too-thick 2D perovskite that would start blocking charge extraction towards the electrodes.

Hence, the use of a 2.5 mg.mL^{-1} 4-FPEAI solution concentration, deposited dynamically on the 3D perovskite, was defined as the routine process for 4-FPEAI treatment of PV devices. It was applied for the following study and all collaborations within IPVF.

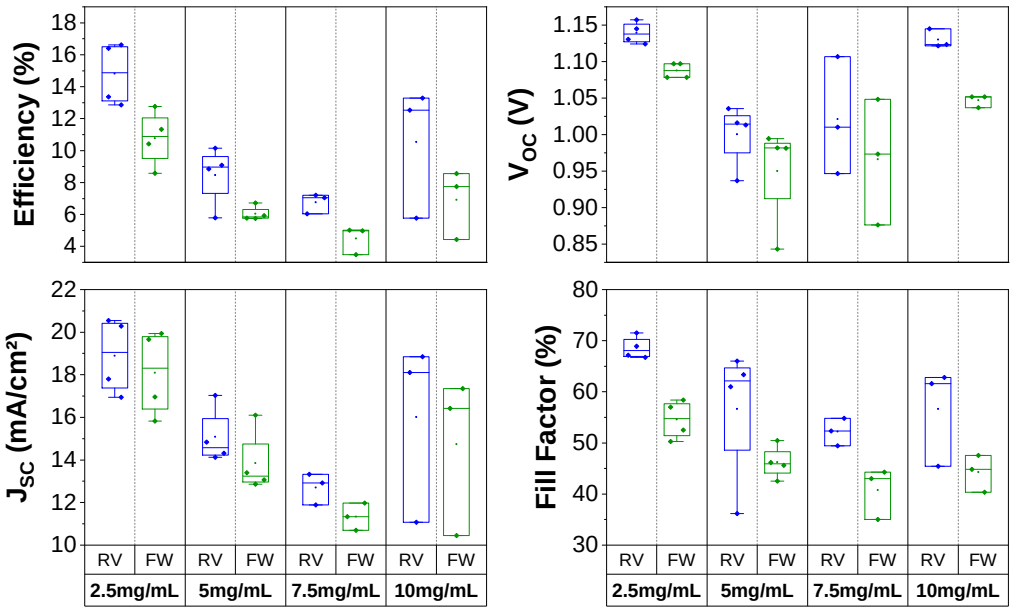

Figure 3.24: PCE, V_{OC}, J_{SC}, and FF distribution of pristine and 4-FPEAI treated cells for each solution concentration. *(RV: blue, FW: green ; 4 cells/condition)*

3.4.2 Device improvement with 2D/3D structure

Efficiency

After choosing the dynamic deposition of a 2.5 mg.mL^{-1} 4-FPEAI solution as the best experimental condition, we focused on assessing its impact on solar cell devices compared to the pristine 3D material. The distribution of photovoltaic parameters for both pristine and 2.5 mg.mL^{-1} devices are presented in Figure 3.25.

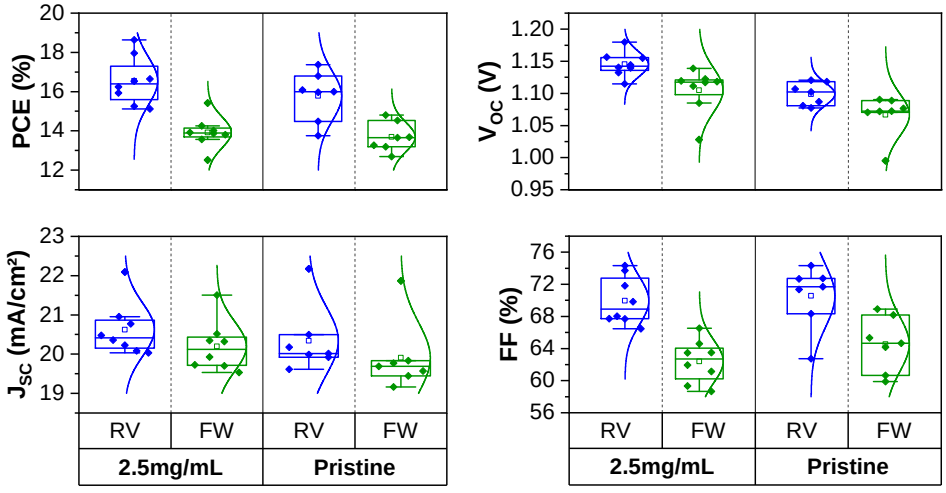

Figure 3.25: PCE, V_{OC}, J_{SC}, and FF distribution of pristine and 2.5 mg.mL^{-1} devices *(8 cells/condition). (RV: blue, FW: green ; 8 cells/condition)*

These results report a systematic significant average V_{OC} improvement of 40 mV with 4-FPEAI treatment. Statistically negligible variations are observed on J_{SC} and FF in

comparison with pristine samples, as J_{SC} undergoes a slight increase, while FF slightly decreases. As a result, 4-FPEAI treatment of the 3D perovskite leads to an average efficiency increase of 0.8% for 2.5 mg.mL^{-1} devices compared to pristine. A moderate J_{SC} improvement is corroborated by the average EQE data from Figure 3.26a, with an integrated J_{SC} going from 18.74 to 19.29 mA/cm^2 with 4-FPEAI treatment.

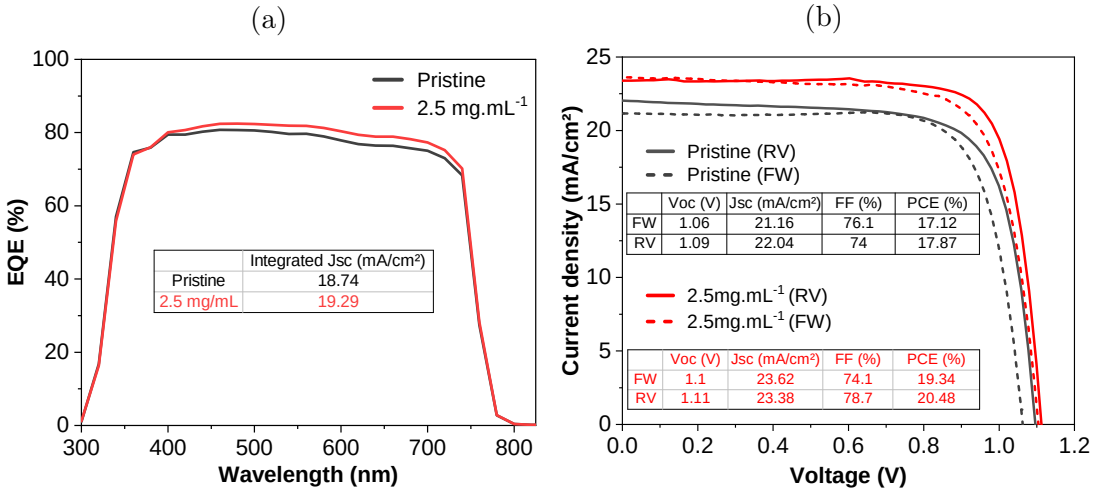

Figure 3.26: (a) PCE, V_{OC}, J_{SC}, and FF distribution of pristine and 2.5 mg.mL^{-1} devices *(8 cells/condition)*. (b) EQE of pristine and 2.5 mg.mL^{-1} devices averaged from devices in (a). (c) JV curve of best working pristine and 2.5 mg.mL^{-1} devices.

Consistently with the literature, the V_{OC} increase is attributed to surface passivation of the 3D perovskite by the 2D layer, inducing a reduction of non-radiative recombinations at the perovskite/HTL interface. Furthermore, the slightly better J_{SC}, in correlation with enhanced EQE for higher wavelengths, would indicate improved charge extraction to the HTL [Li *et al.* 2020b, Kim *et al.* 2021, Mahmud *et al.* 2021a]. Ultimately, the JV characteristic and photovoltaic parameters of best working pristine and 2.5 mg.mL^{-1} devices from Figure 3.26b display encouraging results, with the achievement of a PCE $> 20\%$. Thus, these results validated the potential of our 4-FPEAI treatment process to improve the efficiency of PSCs while pushing us to study it further with, for example, new 3D perovskite compositions or larger-scale devices.

Stability

The effect of 4-FPEAI treatment on device stability was assessed with maximum power point tracking (MPPT) of devices under a continuous 1-sun illumination (without UV) within inert atmosphere and controlled temperature of 25 °C. An important improvement of the stability under illumination is seen in Figure 3.27 with the 2D perovskite addition, with 70% of the initial PCE remaining after 110 hours, compared to 32% for the pristine sample. This result supports a reduction of light-induced ionic migration observed in the literature, which is an important cause of intrinsic perovskite degradation [Huang *et al.* 2019, Zheng *et al.* 2020, Mahmud *et al.* 2021a].

These promising observations reveal the potential of the 2D perovskite layer to improve the stability of 3D perovskite-based PSCs. Pushing further this study by assessing device stability for longer operating times, under ambient conditions, increased humidity,

or thermal stress, would be interesting to obtain a deeper understanding of the 2D/3D structure degradation mechanisms and optimize the devices using this structure.

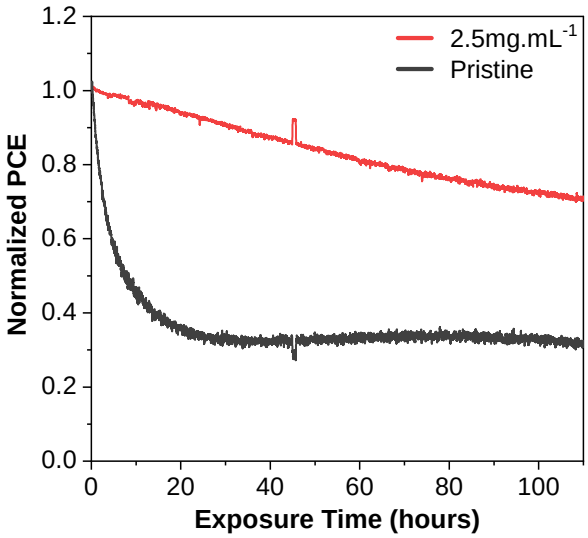

Figure 3.27: Maximum Power Point Tracking (MPPT) of pristine and 2.5 mg.mL^{-1} devices under continuous 1-sun illumination *(without UV)*.

3.4.3 Upscale to mini-modules

On behalf of the good results obtained by adding 4-FPEAI treatment to the triple-cation process for 0.09 cm^2 solar cells, we investigated its applicability to higher-scale devices. Therefore, 4-FPEAI treatment was included in the fabrication process of perovskite mini-modules developed at IPVF.

P1/P2/P3 architecture

Until now, solar cell devices were made using spin-coating deposition on 2x2 cm^2 substrates and with a final active surface of 0.09 cm^2. It was established in IPVF that perovskite films formed by spin-coating were uniformed when deposited on substrates up to 5x5 cm^2 wide. Therefore, in order to keep using spin-coating deposition, the fabrication of mini-modules was realized on such substrates. Hence, the fabrication of mini-modules matched the baseline process detailed in Section 2.1 from ETL to gold cathode, and only solution volumes were adapted when necessary.

With such active areas, one-cell devices would produce much higher photo-currents, leading to a drastic increase in resistive losses. Therefore, mini-modules were divided into smaller "sub-cells" to limit this phenomenon. These sub-cells were all interconnected in series thanks to P1/P2/P3 laser patterning, illustrated in Figure 3.28a. This method consists of a series of three different scribing steps, each one mandatory to obtain functioning devices [Walter *et al.* 2018, Brooks and Nazeeruddin 2021]:

- P1 takes place on glass/FTO substrates, and patterns the FTO layer to insulate the front transparent contact of each individual sub-cell.
- P2 scribing is performed after HTL deposition, down to the FTO layer, to interconnect each sub-cell in series.

- P3 is performed last on the evaporated gold back contact, down to the FTO layer aswell, to separate each sub-cell.

The resulting area between P1 and P3 scribings of each sub-cell no longer produces a collectible electric current and so, becomes a dead area, characterized by its width W_d. Within the dead area, two security areas (SA) are left between P1/P2 and P2/P3 scribings to prevent misalignment in the scribings that would hinder module performances. On the other hand, the working part of each sub-cell is named the active area, characterized by its width W_a. Hence, optimizing the width of dead and security areas is crucial to limit efficiency losses when up-scaling cells to modules.

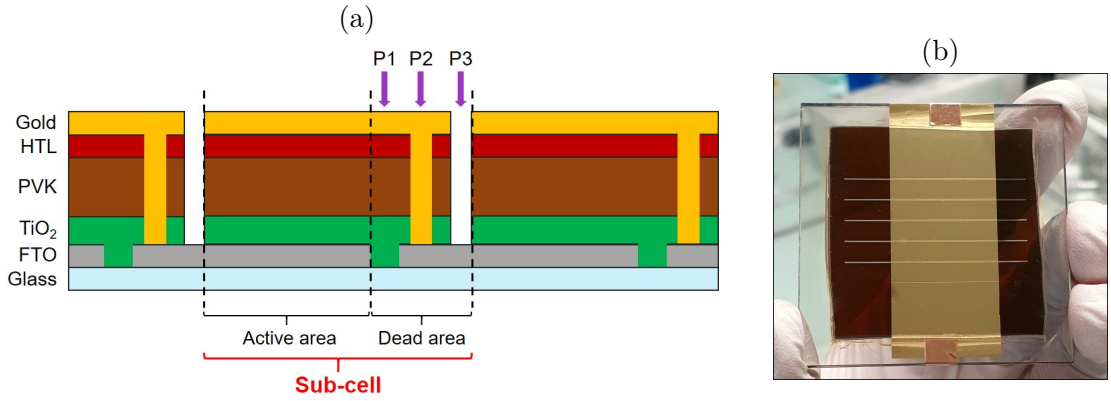

Figure 3.28: (a) Schematic of P1/P2/P3 scribings for perovskite mini-modules. (b) Photo of a 4 cm^2 mini-module used in this study.

These scribings were made with an Innolas ILS LT laser system producing monochromatic 10 ps pulses at 400 kHz either with a 355 nm UV laser or a 532 nm green laser. For P1 scribing, the UV laser was used at maximum power. For P2 and P3, the green laser was used with respective powers of 12.7 W and 0.5 W.

For encapsulation purposes, the whole 5x5 cm^2 substrate could not be used as an active surface. Hence, the mini-module architecture for stability measurements was composed of 5 sub-cells of 0.8 cm^2 each, leading to a total mini-module area of 4 cm^2. The picture of a mini-module in Figure 3.28b shows this architecture. Finally, electrical contacts and encapsulation took place similarly to smaller-scale devices.

Device results

Preliminary results obtained on mini-modules in Figure 3.29 reveal a similar trend to small cells. With 4-FPEAI treatment, a V_{OC} increase from 4.4 to 4.6 V is obtained, which is proportionally close to the results obtained with cells (+ 40 mV for cells, vs. + 200 mV for mini-modules with 4x bigger V_{OC}). Additionally, J_{SC} is also slightly improved, while FF is a bit reduced, resulting in average mini-module efficiency enhanced from 16.81 to 17.70%. This result confirms the similar effect of 4-FPEAI treatment on devices with greater active areas. Furthermore, the PCEs obtained for these mini-modules are fairly close to the state of the art on devices with such active areas deposited by spin-coating, and thus, it would be interesting to pursue this study and perform stability measurements on such mini-modules [Bu *et al.* 2020, Wang *et al.* 2021, Li *et al.* 2022].

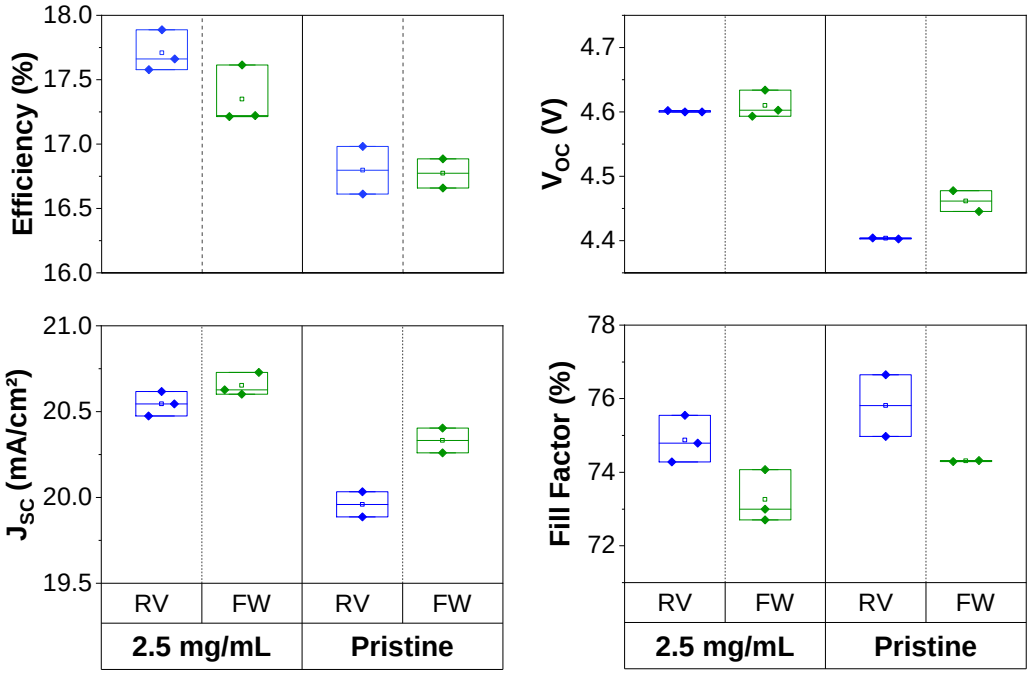

Figure 3.29: PCE, V_{OC}, J_{SC}, and FF distribution of pristine and 2.5 mg.mL^{-1} 4-FPEAI treated mini-modules. *(RV: blue, FW: green ; 3 modules/condition)*

3.5 Summary

This chapter can be summarized as an in-depth study of 2D/3D perovskite heterostructures based on the 4-FPEA 2D spacer and triple-cation 3D perovskite. In this regard, our goal was to improve our understanding of the synthesis, characterization, and application of this material. The pursuit of this objective started with a small first section, dedicated to the production of pure 2D perovskite references.

Then, the second section focused on the synthesis of 2D/3D perovskite structure. Here, we reported the formation of a 2D perovskite layer with mainly n=1 phase, only a few nanometers thick, on top of the 3D perovskite bulk. By increasing 4-FPEAI solution concentration and characterizing the properties of the resulting 2D/3D structure formed, the critical importance of this synthesis parameter on the 2D perovskite formation was revealed. Within the 4-FPEAI solution concentration range used, the 2D layer thickness was increased from a few nanometers to a few tens of nanometers, and its aspect was significantly modified.

The third section was a continuation of the second one. The 2D/3D structure properties were studied under the prism of another synthesis parameter: a static deposition of the 2D solution, with several soaking times between the 4-FPEAI solution and the 3D perovskite. This study revealed the low potential of this method to significantly alter the amount of 2D perovskite formed, paired with irregular results, especially with longer soaking times ($>$ 10 seconds). Furthermore, the detrimental effect of IPA solvent on the 3D perovskite layer was also exposed for these longer soaking times. This phenomenon highlights the importance of more thorough solvent engineering for 2D/3D structures in order to push their usage for device industrialization.

The last section was dedicated to device applications. The best experimental condition for 4-FPEAI treatment was determined, corroborating results obtained in material

studies from previous sections. An overall efficiency and stability improvement was observed with the addition of the 2D perovskite layer, confirming their interest for 3D perovskite-based PSCs. Ultimately, 4-FPEAI treatment was also applied in mini-module devices, up-scaling the active area from 0.09 to 4 cm^2. Promising results were obtained with these bigger devices, revealing the potential of this kind of 2D/3D structure for PSC industrialization, and the need to develop processes compatible with higher-scale deposition methods.

Chapter 4

Formation mechanism of the 2D perovskite layer

This chapter investigates the formation mechanisms of the 2D layer on the 3D perovskite. In the first section, we reveal the 2D layer contamination by bromine from the 3D phase, influencing its optical properties. Then, the bromine content of the layer is quantified with XPS measurements, and a method is proposed to estimate it using only its emission properties. The second section focuses on the 2D layer formation mechanisms leading to this bromine contamination. The third and last section is centered on data that confirms the theorized mechanisms. PbI_2 excess from the 3D perovskite seems to affect how the formation mechanisms occur. A last study highlights how the halide composition of the 2D layer is mainly driven by halides from the 3D perovskite layer over halides from the 2D cation salt.

Contents

4.1 Bromine contamination of the 2D perovskite

4.1.1 Optical shift between pure 2D and 2D/3D

In the previous chapter, Section 3.2.1 showed how a greater concentration of 4-FPEAI cation solution deposited on the 3D perovskite (leading to a greater thickness of the 2D layer) caused the increase of the PL signal detected around 510 nm, as seen in Figure 4.1a. This clear correlation led us to conclude that this PL emission was produced by the 2D perovskite phase. However, the different PL peak position compared to the pure 2D perovskite reference raised a new question. Figure 4.1b shows a comparison between the PL emission from the 2D phase of a 10 mg.mL^{-1} sample, extracted from Figure 4.1a, and the PL emission of a pure $(4\text{-FPEA})_2PbI_4$ 2D perovskite. The PL emission of a pure $(PEA)_2PbI_4$ 2D perovskite made with PEA cation is added to this comparison, to confirm that fluorine from 4-FPEA does not modify the PL position of the resulting 2D perovskite.

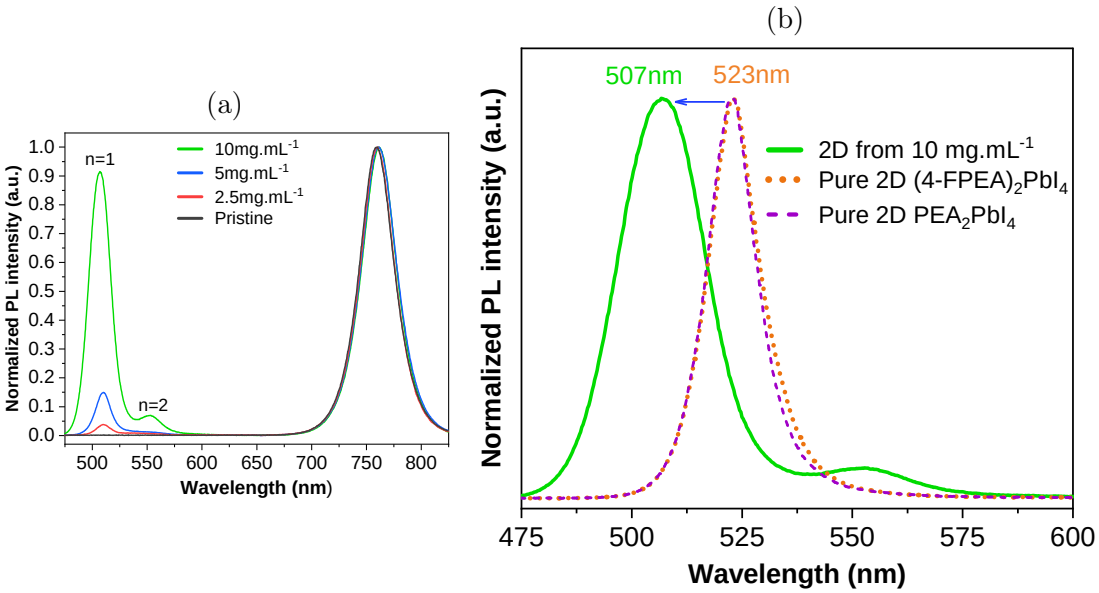

Figure 4.1: (a) PL spectra of pristine 3D and 4-FPEAI treated samples with all three concentrations (2.5, 5, and 10 mg.mL^{-1}). (b) Comparison between PL spectra from the 2D phase of the 10mg.mL^{-1} sample, and from a pure 2D perovskite made with 4-FPEA or PEA cations.

For both 4-FPEA and PEA cations, the 2D perovskite PL signal is centered on 523 nm (2.37 eV), showing that fluorine addition does not affect the bandgap energy of the 2D perovskite formed. Furthermore, this emission wavelength is consistent with data published by LuMIn team on such PEA-based iodide 2D perovskites [Lanty *et al.* 2014, Delport *et al.* 2019]. In comparison, the PL signal from the 2D perovskite formed on top of a 3D layer shows two major differences: the PL is centered on 507 nm (2.44 eV), and the emission peak appears significantly broader.

4.1.2 Effect of bromine absence

Works from Cho *et al.* and Zhou *et al.* presented similar blue-shift on PEAI and 4-FPEAI based 2D perovskite deposited on mixed halide 3D perovskite [Cho *et al.* 2018, Zhou *et al.* 2019]. Zhou *et al.* attributed this PL shift to the quantum confinement effect induced by the "ultrathin" 2D perovskite formed. However, just like tuning the halide of a 3D perovskite allows to stabilize its structure and control its bandgap energy [Noh *et al.* 2013, Eperon *et al.* 2014, Albero *et al.* 2016, T. Hoke *et al.* 2015], tuning the halide in a 2D perovskite has a similar effect, and modifies its excitonic bandgap [Lanty *et al.* 2014, Zhang *et al.* 2010, Jemli 2016]. Thus, another unmentioned factor could cause this PL shift: the presence of bromine in the 2D phase. XPS data presented in Section 3.2.1 showed the presence of Br3d signal in the measurements realized on 4-FPEAI treated samples. If this bromine (initially in the 3D perovskite) was to be found in the 2D phase in a significant amount, it could increase the energy of its n=1 excitonic optical transition from the 2.37 eV initial value with only iodine, to around 2.44 eV, broadening the PL peak due to the presence of a halide mixture.

To confirm if bromine from the 3D perovskite was causing the optical shift observed in 4-FPEAI samples, a new 3D perovskite composition was used. In this composition, called full iodide, all sources of bromine (0.2 mmol of MABr and $PbBr_2$ in the perovskite precursor solution), were replaced with an identical molar amount of their iodide counterparts, leading to the stoichiometry $Cs_{0.05}(MA_{0.17}FA_{0.83})_{0.95}PbI_3$. A 4-FPEAI solution was deposited on the baseline perovskite composition used previously in this work and on the new full iodide composition to form a 2D/3D structure. The properties of the 2D perovskite formed were characterized for both cases. Figure 4.2 schematizes these two experimental conditions and their halide mix differences.

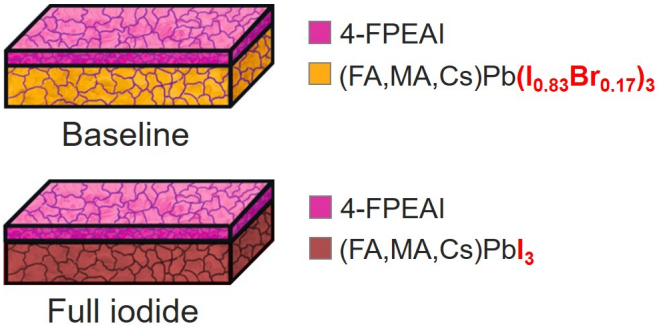

Figure 4.2: Schematic representation of a 2D/3D heterostructure made with baseline or full iodide 3D perovskite compositions.

The first step was to determine the surface chemical composition of full iodide samples treated with 4-FPEAI. XPS measurements were performed on a pristine baseline 3D, a pure $(4\text{-FPEA})_2PbI_4$ 2D perovskite, and baseline and full iodide 3D perovskites treated with 10 $mg.mL^{-1}$ 4-FPEAI solution. Such concentration was used because, as stated in Section 3.2.1, the 2D layer thickness with 10$mg.mL^{-1}$ was greater than the scanning depth of XPS method and so, the measured surface composition is proper to the 2D layer. The atomic percentage quantification for all samples presented above is gathered in Table 4.1.

The first two columns show the surface composition of baseline 3D with and without addition of a 10$mg.mL^{-1}$ solution. After 4-FPEAI treatment, this composition matches the one of the 2D perovskite, with partial substitution of iodine by bromine. Meanwhile,

4-FPEAI treatment of the full iodide 3D material leads to almost identical atomic percentages than the pure 2D reference. This observation confirms that with no bromine involved in the 3D layer, 4-FPEAI treatment forms a $(4\text{-FPEA})_2PbI_4$ 2D perovskite.

Table 4.1: XPS surface chemical composition of a pristine baseline 3D perovskite, baseline and full iodide 3D compositions treated with a 10.mg.mL^{-1} 4-FPEAI solution, and a pure $(4\text{-FPEA})_2PbI_4$ 2D perovskite.

	Baseline 3D	Baseline 3D	Full iodide 3D	Pure 2D
		+ 10.mg.mL^{-1}		
C1s	31.6 ± 3.5	63.4 ± 0.3	63.6 ± 0.4	62.3 ± 0.7
$I3d_{5/2}$	31.5 ± 2.2	12.3 ± 0.2	15.6 ± 0.4	16.3 ± 0.4
N1s	18.2 ± 1.1	8.0 ± 0.1	8.1 ± 0.1	7.7 ± 0.2
$Pb4f_{7/2}$	9.4 ± 0.6	2.8 ± 0.0	2.8 ± 0.1	3.0 ± 0.1
O1s[c]	4.5 ± 1.2	1.2 ± 0.3	0.7 ± 0.1	1.6 ± 0.9
F1s[a]	-	9.0 ± 0.1	9.2 ± 0.2	8.6 ± 0.2
$Cs3d_{5/2}$[b]	0.6 ± 0.0	0.0 ± 0.0	0.1 ± 0.0	-
Br3d[b]	5.2 ± 0.3	3.3 ± 0.1	-	-

[a] Only in 4-FPEAI.
[b] Only in 3D perovskite.
[c] Ambient carbonaceous contamination.

Optical characterizations were performed on baseline and full iodide samples treated with 10 mg.mL^{-1} 4-FPEAI solution to assess the effect of bromine's absence on the 2D layer optical properties. The resulting PL spectra are presented in Figure 4.3. The 3D phase emission moves from 761 nm for the baseline sample to almost 800 nm for the full iodide composition, supporting that removing bromine decreased the 3D perovskite bandgap. The 2D perovskite formed on the baseline 3D shows a main n=1 excitonic peak at 507 nm, with a small contribution from an n=2 phase at 553 nm.

When deposited onto full iodide perovskite, PL intensity of n=1 and n=2 phases remains similar, and a minor signal appears, expected to come from an n=3 phase. This new phase could indicate a better formation or improved emission properties of the 2D layer when a single halide, here iodine, is used in the 2D and 3D compositions instead of an iodine/bromine mix. The emission wavelengths of n=1 and n=2 phases red-shifts to 522 and 571 nm when deposited on the full iodide 3D, closer to the values expected for the excitonic transitions in this material (523 nm for the n=1 phase, see Figure 4.1b).

A mild difference remains between the emission of the n=1 2D phase on the full iodide 3D and the emission of a pure 2D perovskite (522 vs. 523 nm). This difference could be explained by measurement uncertainty between samples. The presence of a 3D bulk under the 2D phase could also modify the dielectric environment of the PbI_4^{2-} inorganic layer, and so the energy of its excitonic transitions (considering the dielectric confinement contributes significantly to the exciton binding energy of the 2D perovskite) [Yaffe *et al.* 2015, Blancon *et al.* 2018]. The small 2D layer thickness, involving specific constraints modifying the bandgap, could also be considered. Nevertheless, this study underlines that these factors remain marginal in the 2D phase PL blue-shift, and highlights the crucial role of bromine presence in the 2D layer composition.

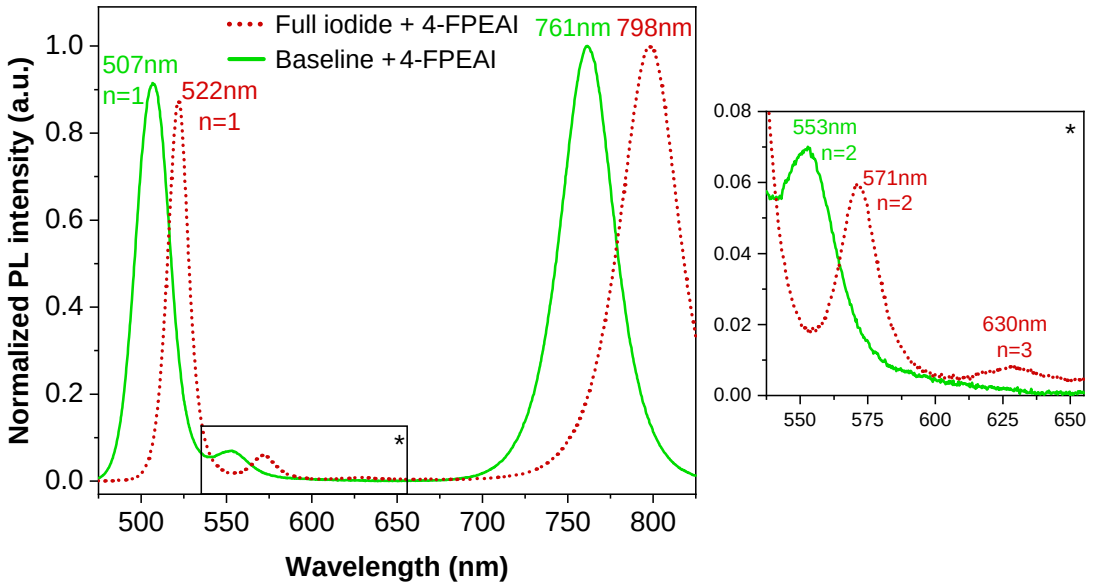

Figure 4.3: PL of baseline and full iodide samples with 4-FPEAI treatment.

Optical absorption was also measured for both compositions with and without 4-FPEAI treatment, and are presented in Figure 4.4. Similarly to PL results from Figure 4.3, the full iodide sample displays a similar absorption to the baseline 3D composition, with only a spectrum shift towards higher wavelengths. With the addition of 4-FPEAI treatment in Figure 4.4b, the absorption from the 3D phase still appears red-shifted, and the excitonic absorption feature of the 2D phase around 520 nm shows a similar red-shift. Thus, removing bromine from the 3D composition reduces both 2D and 3D layers bandgap.

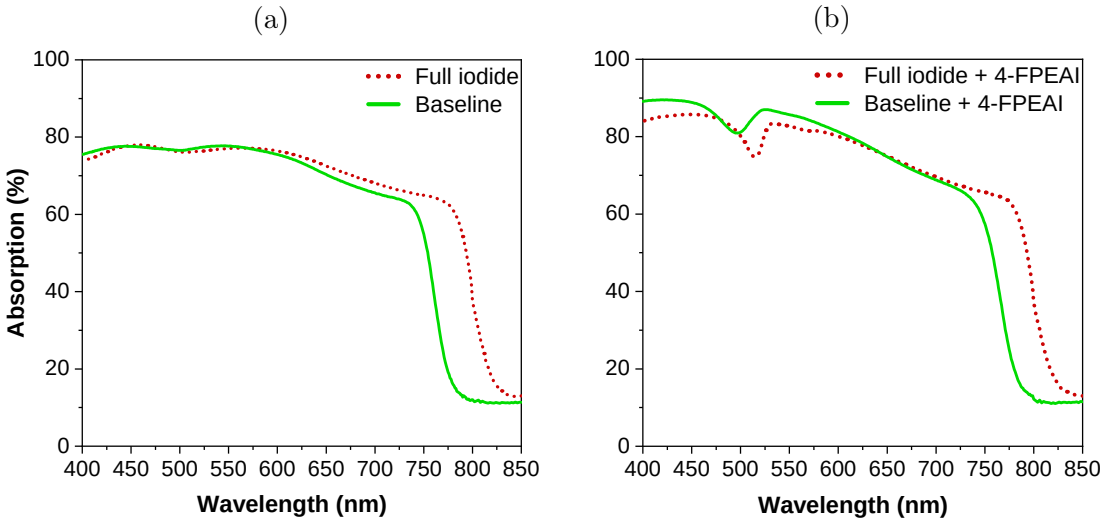

Figure 4.4: (a) Absorption of baseline and full iodide samples without and (b) with 4-FPEAI treatment.

4.1.3 Bromine quantification

After demonstrating that in a 2D/3D structure, the presence of bromine in the 3D perovskite caused a blue-shift of the optical features of the 2D phase, our goal was to determine how much bromine was located in the 2D layer. In this regard, XPS data from 4.1 can be used, as the column "Baseline 3D + 10 mg.mL^{-1}" shows the surface chemical composition of what we expect to be only the 2D layer. This sample shows iodine and bromine percentages of 12.3% and 3.3% (I/Br ratio of 3.74). Therefore, the 2D perovskite layer contains a halide mix close to ($I_{0.789}Br_{0.211}$).

Even though XPS is a very accurate method to probe the surface chemical composition of our perovskite material, we tried to quantify the halide mix in the 2D layer using alternative characterization techniques (less time consuming and easier to implement with no transfer to another lab, etc).

Structural properties

We started by investigating the 2D layer structural properties with XRD measurements. To do so, we synthesized (4-FPEA)$_2$Pb($I_{1-x}Br_x$)$_4$ 2D perovskites samples with x values of 0, 0.5, and 1 by using the process in Section 3.1.1 and gradually replacing 4-FPEAI and PbI_2 by 4-FPEABr and $PbBr_2$ to obtain bromide compositions. Their normalized XRD pattern is compared in Figure 4.5.

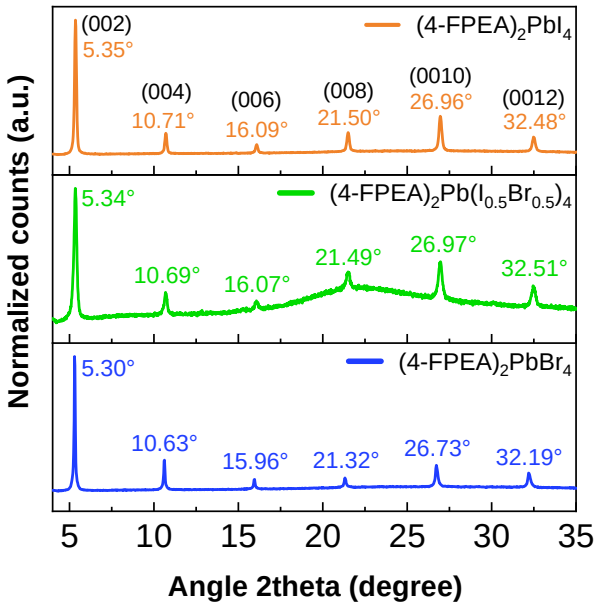

Figure 4.5: XRD diffractogram of (4-FPEA)$_2$Pb($I_{1-x}Br_x$)$_4$ for x = 0 ((4-FPEA)$_2$$PbI_4$), 0.50, and 1 ((4-FPEA)$_2$$PbBr_4$) pure 2D perovskites.

For the halide-mixed 2D perovskite, its peaks get broader and their intensity decrease, resulting in a more intense background signal from the substrate due to signal normalization, and suggesting a thinner or less crystallized layer. The peak diffraction angles are very close to the ones of the iodine-based perovskite, suggesting that the crystal lattice is driven by the bigger iodine halide. With a purely bromide 2D perovskite, the peaks are slightly shifted to lower diffraction angles, related to an increase in the lattice parameter. This angle variation is almost negligible for the (002) peak and gets

more visible with higher order peaks. However, the thin 2D layers formed in 2D/3D structures only produce low signals, and higher order peaks could be used as they were not detected. Hence, this XRD method seemed ineffective to differentiate (I_1Br_0) and ($I_{0.5}Br_{0.5}$) mixtures in a 2D layer using only the first (002) peak. Put in parallel with the ($I_{0.789}Br_{0.211}$) mix estimated above with XPS, it highlighted that a much more extensive study would be necessary to assess the I/Br ratio in the 2D phase from its structural properties, and this approach was quickly abandoned.

Optical properties

Since PL and UV-Vis spectroscopy are simple and rapid non-destructive methods, the layer's optical properties were also considered to determine its iodine/bromine mix, based on previous work from LuMIn team [Lanty *et al.* 2014]. In addition to x = 0, 0.5, and 1 samples, we synthesized more (4-FPEA)$_2$Pb($I_{1-x}Br_x$)$_4$ samples with x values varying gradually from 0 to 0.5. Optical absorption and normalized PL data are respectively shown in Figures 4.6 and 4.7. The 10 mg.mL^{-1} sample spectrum is also included in PL data since the emission of its 2D phase can easily be compared to the spectra of pure 2D perovskites.

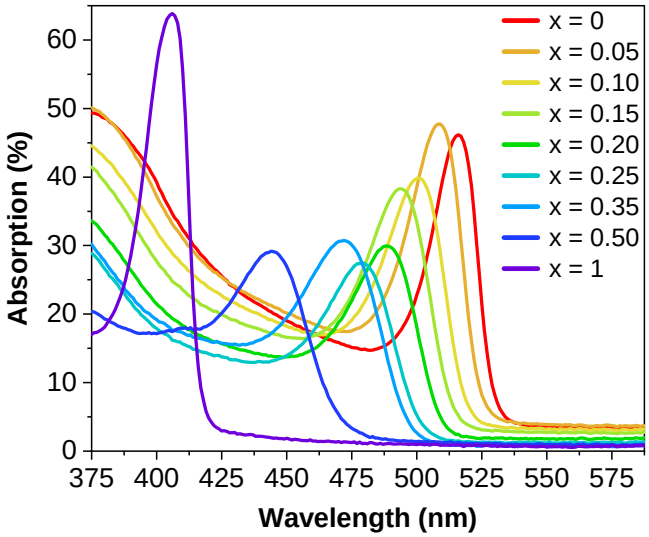

Figure 4.6: Absorption spectra of (4-FPEA)$_2$Pb($I_{1-x}Br_x$)$_4$ pure 2D perovskites for x = 0, 0.05, 0.10, 0.15, 0.20, 0.25, 0.35, 0.50, and 1.

Absorption spectra show clear excitonic peaks for all samples, shifting towards lower wavelengths when substituting iodine with bromine. This known property of halide perovskites is due to an electronic structure modification of the material, which is caused by the hybridization of lead *s* atomic orbitals with the *p* atomic orbitals of the halide (*5p* for iodine, or *4p*) [Jemli 2016, Ledee 2018], and was demonstrated in (4-FPEA)$_2$PbI$_4$ by Even *el al* [Even *et al.* 2012]. PL measurements performed on the same samples reveal a similar trend. As the iodine/bromine mix tends to an equal 50/50 proportion, the distribution between iodine and bromine rich phases gradually increases, leading to greater FWHM. Higher peak asymmetry is also visible due to the development of a tail at lower energies. This tail could arise from defects-related emission [Kahmann *et al.* 2020] or self-trapped excitons [Li *et al.* 2020a, DeCrescent *et al.* 2020] and thus, might indicate a disorder increase in the material and a higher number of defects.

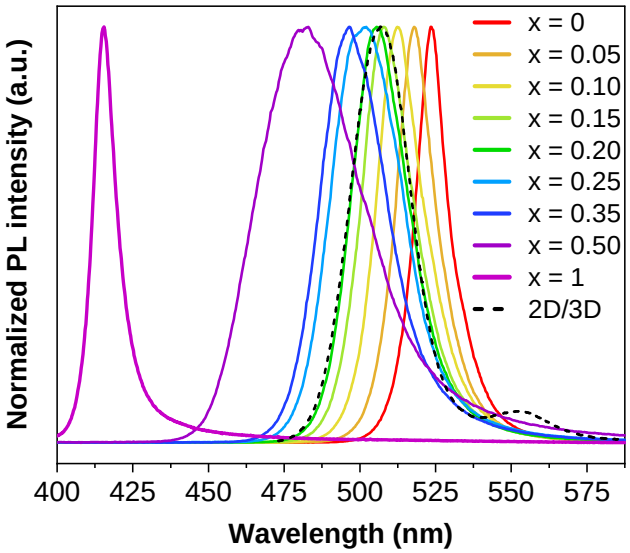

Figure 4.7: Normalized PL spectra of $(4\text{-FPEA})_2Pb(I_{1-x}Br_x)_4$ pure 2D perovskites for x = 0, 0.05, 0.10, 0.15, 0.20, 0.25, 0.35, 0.50, and 1, and of the 2D phase formed on a 3D layer for 10 mg.mL^{-1} concentration.

The absorption and PL wavelengths for each x value were reported in Figure 4.8. A linear evolution of peak position with bromine substitution is observed for both absorption and PL data, confirming bromine's role in opening the bangap of halide perovskites [Lanty *et al.* 2014, Protesescu *et al.* 2015]. We fitted the linear evolution of absorption and PL wavelengths of pure 2D perovskites regarding their halide mix. Applying this fit to the peak from the 2D phase in the 10 mg.mL^{-1} sample, we estimated its halide mix at $(I_{0.798}Br_{0.202})$ (I/Br ratio of 3.95), while this mix was estimated at $(I_{0.789}Br_{0.211})$ (I/Br ratio of 3.74) with XPS analysis. Absorption data could not be used for such estimation, as it was not possible to accurately discriminate the absorption features from the 2D and the 3D phases in 4-FPEAI treated samples.

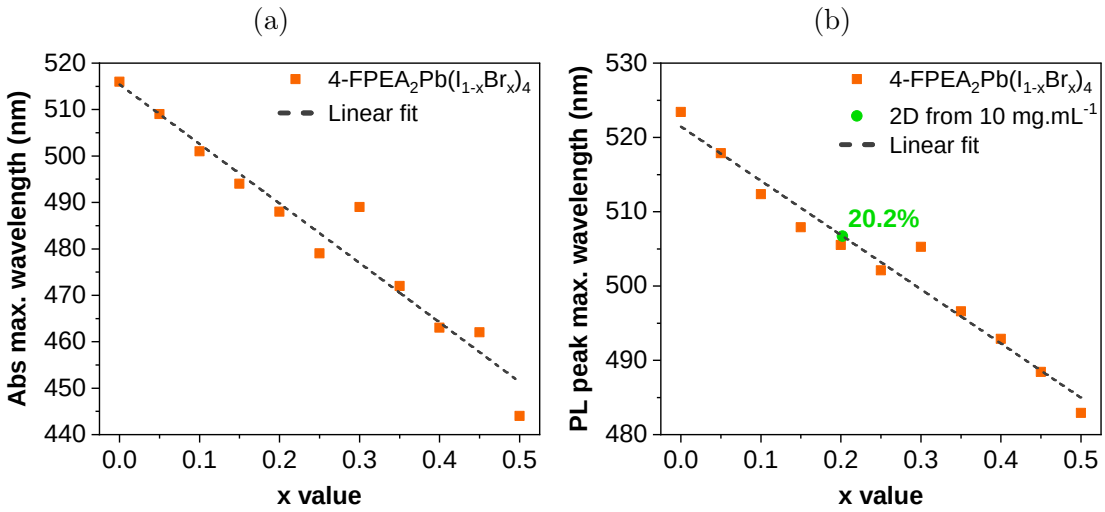

Figure 4.8: (a) Absorption and (b) PL peak position of $(4\text{-FPEA})_2Pb(I_{1-x}Br_x)_4$ perovskites regarding x value.

Therefore, with a difference close to 5% between the bromine content estimated with XPS and with PL, this optical method seems relevant and could be used as a first approximation to estimate the bromine amount of the 2D phase in a 2D/3D structure.

4.2 2D perovskite formation mechanisms

4.2.1 Need for a new mechanism description

In the previous Section 4.1, we demonstrated the contamination of the 2D phase by bromine from the 3D perovskite, leading to the modification of its optical properties. However, the literature consensus for the formation of the 2D layer was based on a reaction between the 4-FPEAI cation and local PbI_2 excess on the 3D perovskite surface following Equation 3.1. Furthermore, this mechanism was confirmed in the previous chapter of this work through XRD measurements from Figure 3.3b. If this mechanism was the only one involved in the 2D perovskite layer formation, the presence of bromine within this 2D layer would not be possible. Based on this affirmation, we presumed that the 2D layer formation was driven by at least another mechanism parallel to the 4-FPEAI/PbI_2 reaction.

4.2.2 Unlikely mechanisms

Reaction with lead bromide

We just argued that a reaction mechanism involving bromine was necessary to explain the formation of a 2D layer containing a significant amount of bromine. In this regard, we first looked at bromine sources in our synthesis process, and thus inspected the precursors used for the 3D perovskite solution. The main source of bromine among the precursors used to make the 3D perovskite is $PbBr_2$. Thus, $PbBr_2$ could interact with 4-FPEAI in the same way as PbI_2 in Equation 3.1 to form a 2D perovskite that would contain both iodine and bromine, based on this reaction:

$$2(4-FPEAI) + PbBr_2 \rightarrow (4-FPEA)_2Pb(I_{0.5}Br_{0.5})_4 \tag{4.1}$$

However, the 3D perovskite precursor solution contained far less $PbBr_2$ than PbI_2 (0.2 mmol of $PbBr_2$ versus 1.1 mmol of PbI_2). Besides, $PbBr_2$ is more reactive than PbI_2 in forming the 3D perovskite [Jesper Jacobsson *et al.* 2016]. Hence, there should not be any $PbBr_2$ in the 3D layer available for reaction with 4-FPEAI. Furthermore, no sign of unreacted $PbBr_2$ was visible in XRD data from Figure 3.3b. Thus, it is likely that when the 4-FPEAI solution is deposited on the 3D surface, bromine is already embedded in the crystallized 3D structure and cannot not get involved in the 2D phase formation, casting aside this mechanism.

Bromine diffusion

In order to explain bromine contamination of the 2D phase, bromine diffusion from the 3D to the 2D layer seemed a viable explanation. Using XPS in-depth profiling, we quantified bromine distribution along material depth for pristine and 10 mg.mL^{-1} samples. Based

on the results presented in Figure 4.9a, both samples show a similar distribution in the 3D layer, with bromine accumulation at the rear interface of the 3D perovskite.

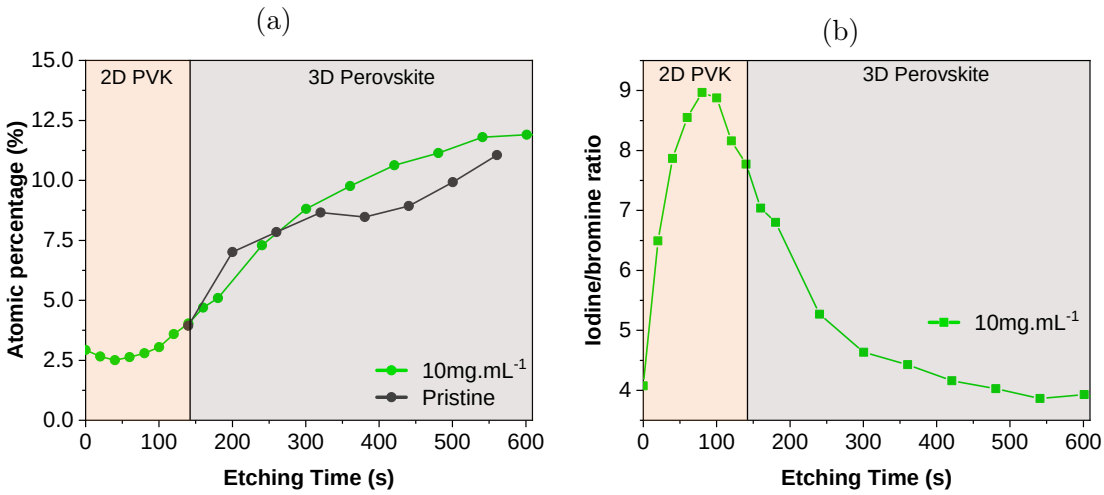

Figure 4.9: (a) Bromine atomic percentage evolution over etching time for pristine and 10mg.mL^{-1} samples. (b) Iodine/bromine ratio evolution evolution over etching time for 10mg.mL^{-1} sample.

This result explained the low bromine amount in the pristine baseline sample shown in Table 4.1 (31.5% of iodine and 5.2% of bromine, corresponding to a halide mix of ($I_{0.86}Br_{0.14}$) in the 3D phase, instead of the ($I_{0.83}Br_{0.17}$) mix of its stoichiometry). However, it does not seem related to the 2D phase, as the bromine amount in the 3D phase is similar for both samples, regardless of 4-FPEAI deposition. In the case of bromine diffusion, the iodine/bromine ratio would progressively decrease as we get closer to the 3D perovskite and the 2D layer gets more bromine-rich. Instead, Figure 4.9b shows that almost the opposite behavior happens, and the surface of the 2D layer has the lowest iodine/bromine ratio. Then, this ratio quickly increases until a maximum is found halfway through the layer, and progressively decreases as we scan deeper in the 3D layer. Finally, XPS measurements performed on 4-FPEAI treated samples for each concentration (Figure 3.11f) reveal a similar bromine amount in the 3D phase, regardless of the 4-FPEAI concentration. This observation contradicted the theory that bromine contamination of the 2D layer would come from bromine diffusion. Instead, it suggested that the 3D perovskite surface is "transformed" into a 2D layer, and most bromine from the 3D phase is reused to constitute this new 2D layer.

4.2.3 Cation substitution

After discarding several mechanisms allowing bromine to infiltrate the 2D layer without being involved in its formation, we were led to assume that bromine, and so the 3D perovskite itself, played a direct role in forming the 2D layer. Thus, we hypothesized that the presence of bromine in the 2D layer is induced by a reaction between 4-FPEAI cation salt and the 3D perovskite, and this reaction is a substitution of the 3D perovskite cations (MA, FA, and Cs) by 4-FPEAI, based on the following reaction:

$$\begin{aligned} &Cs_{0.05}(MA_{0.17}FA_{0.83})_{0.95}Pb(I_{0.83}Br_{0.17})_3 + 2(4-FPEAI) \\ &\rightarrow (4-FPEA)_2Pb(I_yBr_{1-y})_4 + (I,Br)^- + (FA,MA,Cs)^+ \end{aligned} \tag{4.2}$$

Huang *et al.* formulated this reaction for perovskite nanoparticle colloidal solutions, later supported by Mayer *et al.* from LuMIn group [Huang *et al.* 2018a, Mayer *et al.* 2022]. This mechanism was also proposed in chemical vapor deposited perovskite thin films [Huang *et al.* 2018b, Lin *et al.* 2019], and we speculate that it would also happen in our solution-processed perovskite thin films. This mechanism would reorganize the very surface of the 3D perovskite into a 2D layer. Chen *et al.* demonstrated this phenomena in a MAPI thin-film exposed to a C6 gas [Chen *et al.* 2021]. Meanwhile, Tan *et al.* suggested that this phenomena could be induced in FAPI perovskite by IPA solvent itself, leading to FA vacancies and a more PbI_2-rich surface [Tan *et al.* 2021], while Liu *et al.* theorized that the non-photoactive phase δ-FAPI was converted into a 2D perovskite phase [Liu *et al.* 2019a]. The greater complexation of Pb^{2+} with Br^- than with I^- would favor the formation of bromine-rich 2D phases before iodine-rich ones. This explanation would justify the lower iodine/bromine ratio in the 2D layer ($I_{0.789}Br_{0.211}$, ratio of 3.74) than in the 3D perovskite surface ($I_{0.858}Br_{0.142}$, ratio of 6.0) observed in Table 4.1 [Yoon *et al.* 2016].

To form the $A'_2AB_2X_7$ n=2 phase visible in PL measurements, small A-site cations from the 3D perovskite are mandatory. However, IPA's highly polar nature makes it an efficient solvent to solubilize FA and MA [Yoo *et al.* 2019]. As a result, both compounds might be eliminated along with excess solvent during the spin-coating of 4-FPEAI solution and by solvent evaporation during the 2D layer annealing, explaining their disappearance from XPS measurements. Meanwhile, Cs^+ ions are not soluble in IPA and would not be evacuated from the surface as efficiently as FA and MA. However, due to their inorganic nature, they are also less favorable for ionic exchange, leading to a predominance of the n=1 phase due to the small number of A-site cations available [Liu *et al.* 2021b]. Hence, we could not determine which free A-site cations are used during the reconstruction of the 3D perovskite outer surface to form n>1 phases, and we assume that all A-site cations (FA, MA, and Cs) are involved. For clarity, byproducts of the reaction in Equation 4.2 were presented in their ionic form, with 3D perovskite cations $(FA, MA, Cs)^+$ on one side, and halide anions $(I, Br)^-$ on the other. However, we do not know how these species are evacuated, which could happen in the form of various molecule combinations, such as FAI, FABr, MABr...

To sum up, a substitution of the 3D perovskite cations (FA, MA, and Cs) by 4-FPEAI would form the 2D perovskite layer, reorganizing the material surface to form a 2D phase with a significant amount of bromine.

4.3 Support to cation substitution hypothesis

We established that the 2D layer formation is linked to the 3D perovskite by a substitution process of the 3D perovskite cations with 4-FPEAI. Even though this mechanism was proposed based on a significant amount of experimental work and literature data, at this stage, it remained a theory. Without any means to demonstrate this theory directly, we deepened our study with new kinds of samples to support its relevance.

4.3.1 Lead iodide excess in the 3D perovskite

Section 3.2.1 of the previous chapter presented the first mechanism for the 2D perovskite formation: the reaction of 4-FPEAI with PbI_2 excess from the 3D perovskite surface. Later, another mechanism was discussed in Section 4.2 of the current chapter, based on a substitution of the 3D perovskite A-site cations (FA, MA, and Cs) by 4-FPEAI. If these two mechanisms exist, they should occur concurrently for the 2D perovskite formation.

In this regard, new 3D perovskite compositions were designed, with a modification of the PbI_2 content in the 3D bulk. IPVF baseline 3D perovskite process used a 2.0% PbI_2 stoichiometric excess. Two variations of this excess were made: by reducing PbI_2 precursor amount from 1.1 to 1.0 mmol, the excess was transformed into a deficiency of -6.2% PbI_2, and by increasing it from 1.1 to 1.2 mmol, the excess was accentuated to 9.0%. These three perovskite compositions were treated with a $5mg.mL^{-1}$ 4-FPEAI solution to examine the 2D/3D structure formation with different PbI_2 amount available. These experimental conditions are illustrated in Figure 4.10.

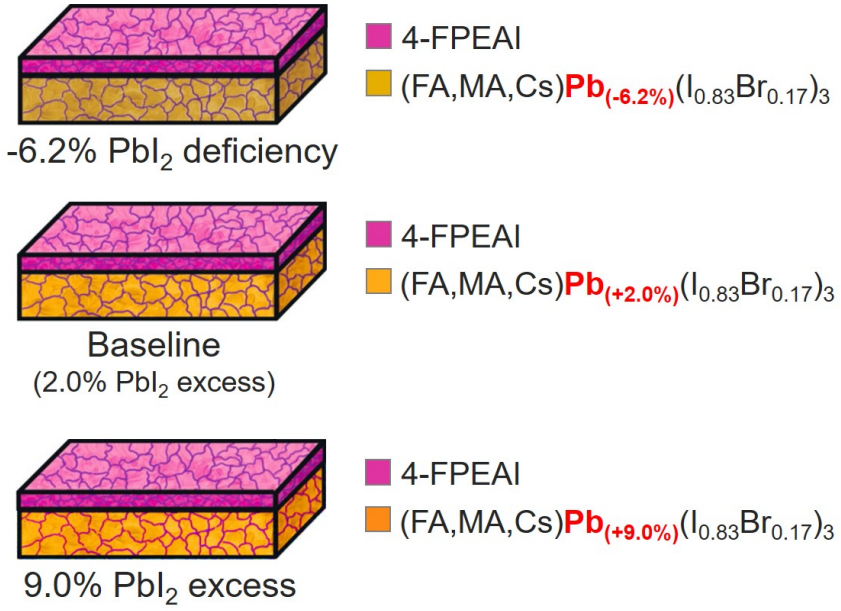

Figure 4.10: Schematic representation of 2D/3D heterostructures made with 3D perovskites containing a -6.2%, 2.0% (baseline), or 9.0% PbI_2 excess.

Impact on 2D perovskite formation

Figures 4.11a and 4.11b compare the diffractograms between pristine and 4-FPEAI treated samples to study how the 2D layer formation is affected. Figure 4.11b displays comparable 2D peaks regardless of the PbI_2 excess, implying similar 2D perovskite layer thicknesses. The main difference in these diffractograms is the 12.7° PbI_2 peak. This peak is not visible for both -6.2% and 2.0% samples, but for different reasons. For the -6.2% PbI_2 deficiency, it does not appear due to the lower PbI_2 amount in the 3D layer composition, preventing pure PbI_2 crystallization after the 3D perovskite formation. GIXRD performed on this sample in Figure 4.11c confirmed this assertion, as it shows the complete absence of the PbI_2 peak.

On the other hand, for the 2.0% excess, PbI_2 was fully consumed by reaction with 4-FPEAI, as explained previously in Section 3.2.1, leading to the peak disappearance after 4-FPEAI treatment. Similar behavior is observed for the 9.0% sample. However, in this case, the PbI_2 peak does not disappear but only decreases after 2D treatment, suggesting that a significant amount of crystallized PbI_2 remains in the layer even after 4-FPEAI deposition. The reason could be a PbI_2 excess located in the bulk of the layer, that was not depleted due to the superficial nature of 4-FPEAI treatment. An other possibility could be that 4-FPEAI was the limiting reactant in the reaction with PbI_2.

SEM images from Figures 4.11d and 4.11e, comparing pristine 3D perovskites with 2.0 and 9.0% excesses, show an increase of crystallized PbI_2 grains at the material surface, supporting a stronger XRD PbI_2 peak.

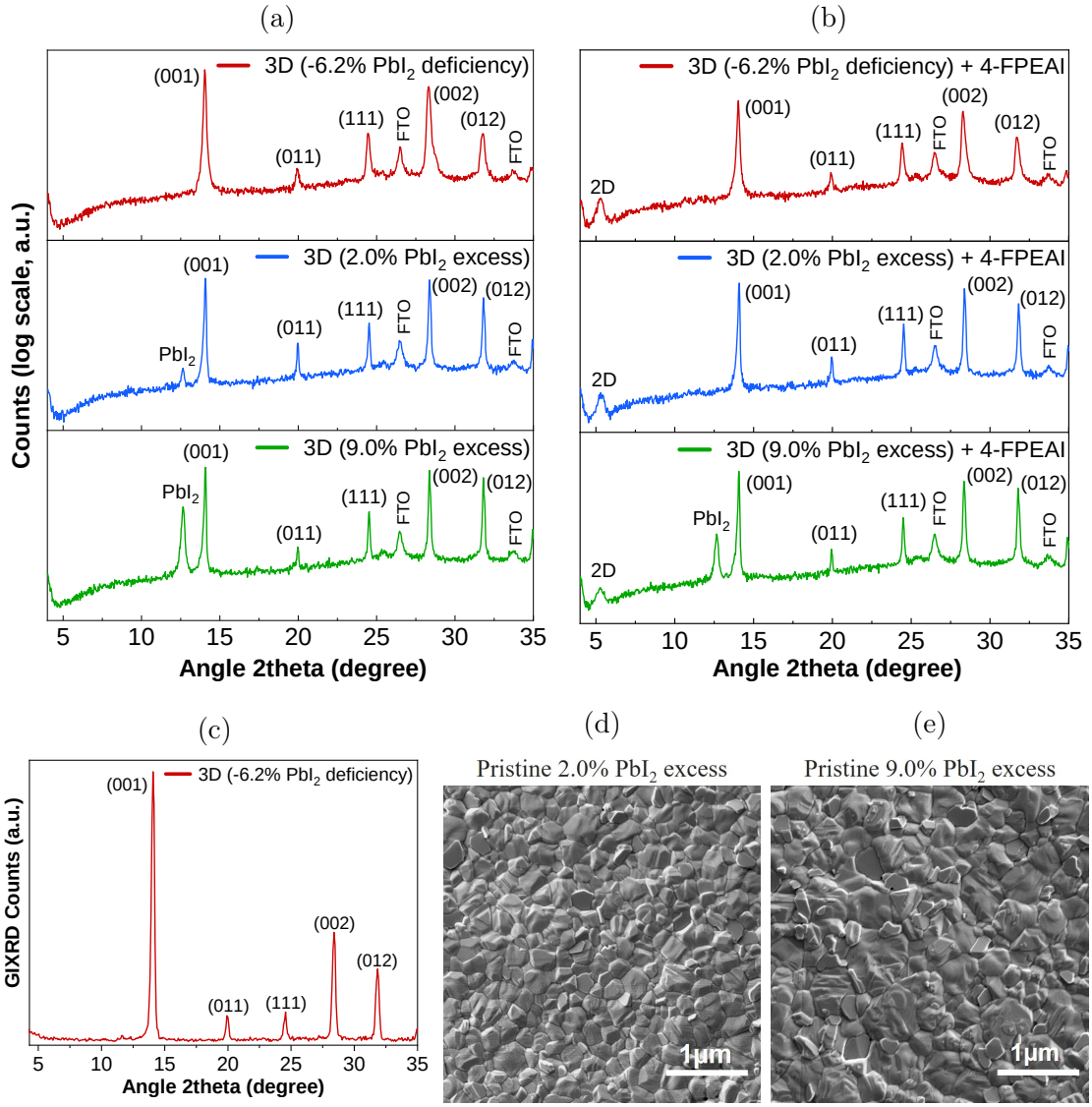

Figure 4.11: Bragg XRD diffractograms of 3D perovskites with a -6.2%, 2.0%, or 9.0% PbI_2 excess (a) without, and (b) with 5 $mg.mL^{-1}$ 4-FPEAI solution treatment. (c) GIXRD diffractogram of a -6.2% PbI_2 deficiency 3D perovskite. SEM image of pristine 3D perovskites with (d) 2.0%, and (e) 9.0% PbI_2 excess.

PL emission shift

PL measurements were performed on these samples. The results in Figure 4.12a show a trend similar to XRD data, with only a slight intensity variation of the 2D phase signals between all conditions. However, a slight blue-shift of the 2D peak is visible for the -6.2% PbI_2 deficiency. For this reason, we plotted in Figure 4.12b the wavelength position of 2D PL peaks measured on several samples for each PbI_2 excess. On average, the 2D emission peaks are respectively located at 508.5 ± 1.0, 510.3 ± 0.7, and 510.5 ± 0.9 nm for the -6.2%, 2.0%, and 9.0% PbI_2 excesses. Thus, with a lower PbI_2 amount in the 3D layer, the 2D phase is blue-shifted.

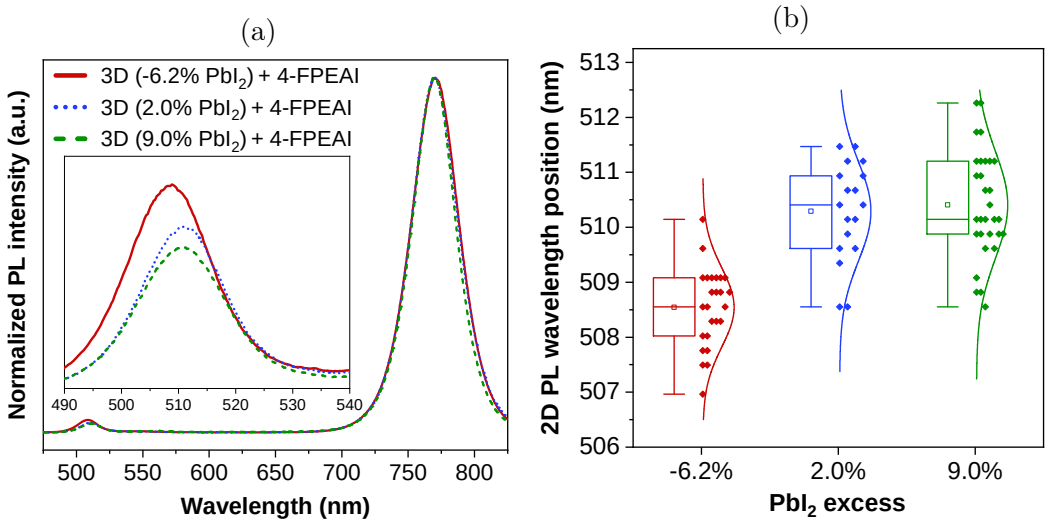

Figure 4.12: (a) PL spectra and (b) Distribution of 2D phase PL position, for 3D perovskites with -6.2%, 2.0%, or 9.0% PbI_2 excesses, treated with 5 mg.mL^{-1} 4-FPEAI solution.

Two phenomena might cause this shift. First, with no PbI_2 available from the 3D phase, the cation substitution mechanism would be favored to form the 2D phase. As this mechanism, unlike the reaction with PbI_2, involves bromine, the 2D layer formed would contain slightly more bromine, leading to the PL blue-shift. Second, by reducing PbI_2 excess in the 3D layer, its iodine/bromine ratio would be decreased, which would be transferred to the 2D phase during cation substitution. The 2.0 and 9.0% excesses show similar PL position, revealing that increasing the amount of PbI_2 in the 3D perovskite does not favor the 4-FPEAI/PbI_2 reaction and form an more iodine-rich 2D layer.

Similarly, Figure 4.13 compares the distribution of 2D emission peaks for each 4-FPEAI concentration. These peaks are located at 509.4 ± 1.2 and 509.9 ± 0.5 nm for 2.5 and and 5 mg.mL^{-1} samples, and are slighly blue-shifted to 507.8 ± 1.3 nm for 10 mg.mL^{-1} samples. In Chapter 3, we established that 4-FPEAI reacts with PbI_2 excess to form the 2D perovskite, consuming this PbI_2. Figure 3.3b showed that with a 4-FPEAI concentration of 10 mg.mL^{-1}, PbI_2 peak vanished from XRD data. In this chapter, we stated that 4-FPEAI also reacts with the 3D perovskite by cation substitution. Thus, we assumed that for high 4-FPEAI concentrations, PbI_2 becomes the limiting reactant of the 4-FPEAI/PbI_2 reaction, and eventually stops it. The cation substitution then becomes the only reaction forming 2D perovskite. Since this mechanism involves bromine, the resulting 2D phase is slightly more bromine-rich, and its PL gets blue-shifted.

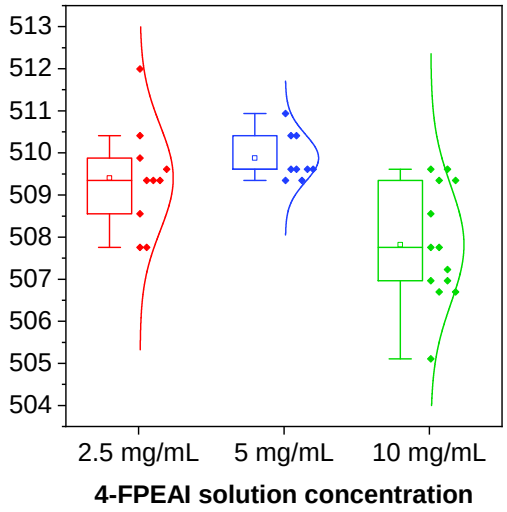

Figure 4.13: Distribution of 2D phase PL position for baseline 3D perovskite composition treated with 2.5, 5, or 10 mg.mL^{-1} 4-FPEAI solution.

Confirmation with chemical composition

To conclude on the impact of PbI_2 excess on the 2D phase formation, XPS measurements were carried out. New samples were made for XPS characterization with similar experimental conditions, but using a 10 mg.mL^{-1} 4-FPEAI solution instead of a 5 mg.mL^{-1} one, to from a thicker 2D layer and prevent the 3D layer from being scanned. The results of measurements performed on baseline (2.0% excess), -6.2%, and 9.0% excess samples before and after 4-FPEAI treatment are summed up in Table 4.2.

Without 4-FPEAI treatment, the table shows comparable compositions for all samples, with only slight differences. Decreasing PbI_2 excess in the layer leads to a lower I/Br ratio in comparison with the baseline sample, suggesting a more bromine-rich surface with a PbI_2 deficiency. On the other hand, increasing PbI_2 excess increases lead contribution and also leads to a higher I/Br ratio, hinting a greater amount of PbI_2 at the surface. This result is consistent with the observation of an intense PbI_2 peak in the XRD diffractogram of this sample.

After 4-FPEAI treatment, the result is significantly different between each sample. For 9.0% PbI_2 excess, surface composition remains close to the baseline one, with slight increase in iodine and lead contributions due to the presence of remaining PbI_2. On the other hand, in the -6.2% sample, atomic percentages are closer to the 3D perovskite, with the C/N ratio being reduced from 7.9 to 5.9 in comparison with the baseline sample, suggesting that the 3D phase was also scanned, and so, that the 2D layer formed with lower PbI_2 amount is thinner. The I/Br ratio is also higher in baseline than is -6.2% sample after 4-FPEAI treatment. This observation corroborates a higher bromine amount in the 2D layer than for the baseline sample, which is consistent with the blue-shift observed in the position of its PL (see Figure 4.12b). On the opposite, I/Br ratio is higher in 9.0% than in baseline sample. However, due to the presence of remaining PbI_2 at the sample's surface, this ratio is not representative of the 2D phase.

After analysing 2D phase composition with surface XPS, XPS in-depth profiling was realized on 4-FPEAI treated baseline, -6.2% deficiency, and 9.0% excess 3D compositions to investigate the 2D layer thickness. These measurements are presented in Figure 4.14.

Table 4.2: XPS surface chemical composition of baseline, -6.2% PbI_2, and 9.0% PbI_2 3D perovskites, with and without 10.mg.mL^{-1} 4-FPEAI treatment.

	Baseline	-6.2% PbI_2	9% PbI_2	Baseline	-6.2% PbI_2	9% PbI_2
				+ 10.mg.mL^{-1}		
C1s	31.6 ± 3.5	30.5 ± 0.2	31.9 ± 0.5	63.4 ± 0.3	58.5 ± 0.5	64.1 ± 0.1
$I3d_{5/2}$	31.5 ± 2.2	31.3 ± 0.2	34.6 ± 0.5	12.3 ± 0.2	14.2 ± 0.3	13.5 ± 0.0
N1s	18.2 ± 1.1	20.6 ± 0.2	15.7 ± 0.1	8.0 ± 0.1	10.0 ± 0.3	7.7 ± 0.1
$Pb4f_{7/2}$	9.4 ± 0.6	9.4 ± 0.0	11.4 ± 0.2	2.8 ± 0.0	4.2 ± 0.1	3.3 ± 0.0
O1s[c]	4.5 ± 1.2	0.9 ± 0.1	1.1 ± 0.0	1.2 ± 0.3	0.5 ± 0.3	0.6 ± 0.1
F1s[a]	-	-	-	9.0 ± 0.1	6.7 ± 0.2	8.1 ± 0.1
$Cs3d_{5/2}$[b]	0.6 ± 0.0	0.5 ± 0.0	0.4 ± 0.0	0.0 ± 0.0	0.5 ± 0.0	0.1 ± 0.1
Br3d[b]	5.2 ± 0.3	6.0 ± 0.1	4.6 ± 0.0	3.3 ± 0.1	5.4 ± 0.1	2.7 ± 0.1
C/N ratio	1.7	1.5	2.0	7.9	5.9	8.3
I/Br ratio	6.1	5.2	7.5	3.7	2.6	5.0

[a] Only in 4-FPEAI.
[b] Only in 3D perovskite.
[c] Ambient carbonaceous contamination.

For the baseline sample, O1s and Ti2p atomic percentage profiles show that the rear interface of the 3D perovskite in still not reached after 1000s, but approaching. With the -6.2% deficiency, similar O1s and Ti2p signals are obtained after 900 seconds of etching, suggesting that the 3D layer was either thinner or easier to etch due to a smaller PbI_2 amount. In contrary, for 9.0% excess sample, at the etching's end, O1s and Ti2p signals are still very low, implying that the TiO_2 layer was not reached, either due to a thicker or harder to etch 3D perovskite because of higher PbI_2 amount.

Focusing on the 2D phase, we considered that the 2D/3D interface was reached when the C1s percentage got close to 30%, which is the surface C1s percentage of a pristine 3D perovskite and corresponds to half of the atomic percentage on either side of the interface. With this postulate, the time to reach the 2D/3D interface is almost equivalent for the three samples. For 4-FPEAI treated baseline sample, this time is close to 175 seconds. By reducing PbI_2 amount in the 3D phase for -6.2% sample, the 2D/3D interface is reached after 150 seconds. This is consistent with the assumption on 2D layer thickness decrease made based on data from Table 4.2. Oppositely, for 9.0% excess sample, 200 seconds of etching are necessary to reach the 3D perovskite, hinting a thicker 2D layer.

Therefore, we conclude that modifying PbI_2 excess of the 3D phase is not a viable solution to modify the 2D perovskite, as its impact on the formation of a thin 2D passivation layer is weak. Furthermore, by modifying this PbI_2 excess, the 2D phase halide composition seems altered. By increasing PbI_2 amount, a slight increase in iodine content is measured, but not significant enough to be detected through PL measurements. On the opposite, with lower PbI_2 excess, a 2D layer is still formed with a higher bromine amount, leading to small blue-shift of its PL. This results confirms the existence of another formation mechanism for the 2D layer, outside of the reaction with PbI_2.

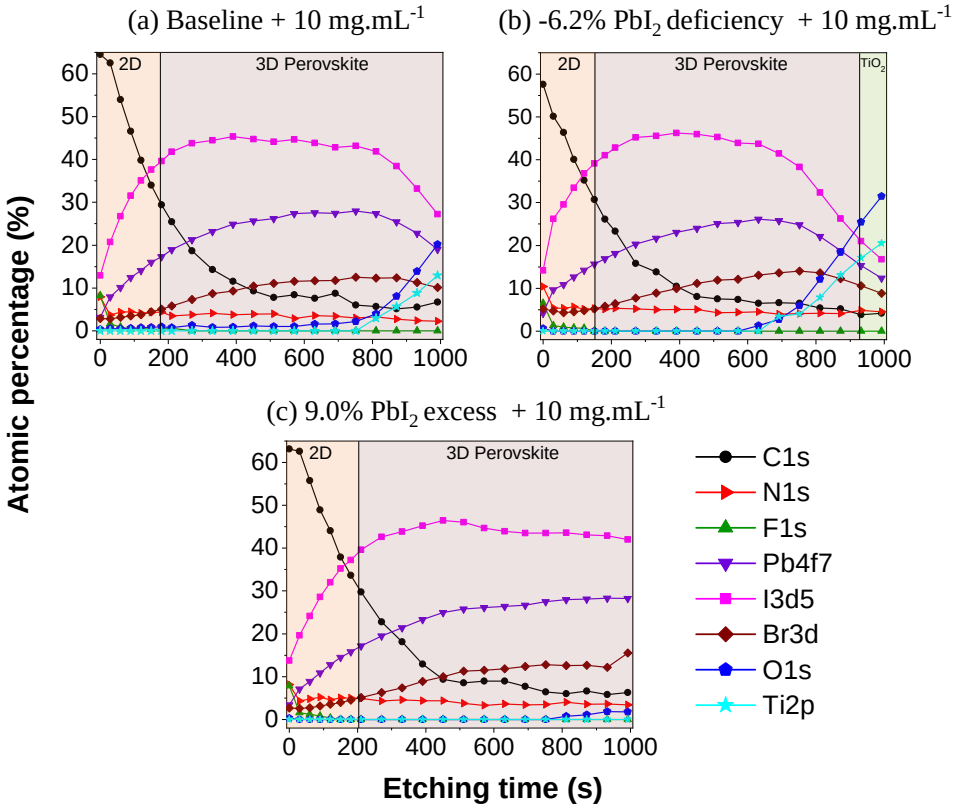

Figure 4.14: Atomic percentage evolution of chemical elements over etching time, for (a) Baseline, (b) -6.2% PbI_2 deficiency, and (c) 9.0% PbI_2 excess 3D perovskites treated with 10.mg.mL^{-1} 4-FPEAI solution.

4.3.2 Contribution of halide mix in 3D perovskite and 2D molecule on 2D perovskite halide composition

Section 4.1 revealed a contamination of the 2D layer by bromine from the 3D perovskite, and Section 4.2.3 proposed a cation substitution of 3D perovskite cations by 4-FPEAI to explain this contamination. In this regard, a final investigation was performed to assess the importance of cation substitution in the final composition of the 2D perovskite layer. To form the 2D layer of the 2D/3D structure, two elements are involved: the 3D perovskite (FA,MA,Cs)PbX_3 (X designates the 3D perovskite halides), and the 2D cation salt 4-FPEAY (Y is the 2D cation salt halides). The study consisted to modify either X or Y halides, and to characterize the optical emission of the resulting layer. In this regard, three different 3D perovskites were used:

- The full iodide configuration, used in Section 4.1.2, with the stoichiometry $Cs_{0.05}(MA_{0.17}FA_{0.83})_{0.95}PbI_3$. $\mathbf{X = I}$
- Baseline composition, mainly used along this manuscript.
  Stoichiometry: $Cs_{0.05}(MA_{0.17}FA_{0.83})_{0.95}Pb(I_{0.83}Br_{0.17})_3$. $\mathbf{X = I_{0.83}Br_{0.17}}$
- A new design, where iodine sources were replaced by bromine counterparts (except CsI), leading to the stoichiometry $Cs_{0.05}(MA_{0.17}FA_{0.83})_{0.95}Pb(I_{0.02}Br_{0.98})_3$. This design was named bromine-rich. $\mathbf{X \approx Br}$

Each composition was treated with a 10mg.mL^{-1} solution of 4-FPEAI, 4-FPEABr, or 4-FPEAI$_{0.5}$Br$_{0.5}$, and each X-Y set was characterized with PL. Figures 4.15 and 4.16, Figures 4.17 and 4.18, and Figures 4.19 and 4.20 display the experimental conditions and PL spectra, respectively for full iodide, baseline, and bromine-rich configurations.

4-FPEAI, 4-FPEABr, and 4-FPEAI/Br on full iodide configuration X = I

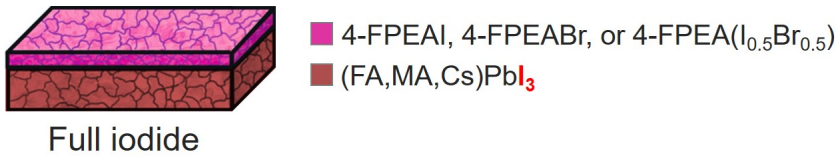

Figure 4.15: Schematic representation of 2D/3D heterostructures made with full iodide 3D perovskite composition.

An observation of full iodide samples in Figure 4.16 reveals that switching Y halide from iodine to bromine slightly blue-shifts 3D perovskite emission, shown in the top-right corner. This phenomenon could be explained by an infiltration of Y halides in the 3D bulk during 2D solution deposition, slightly altering its emission bandgap.

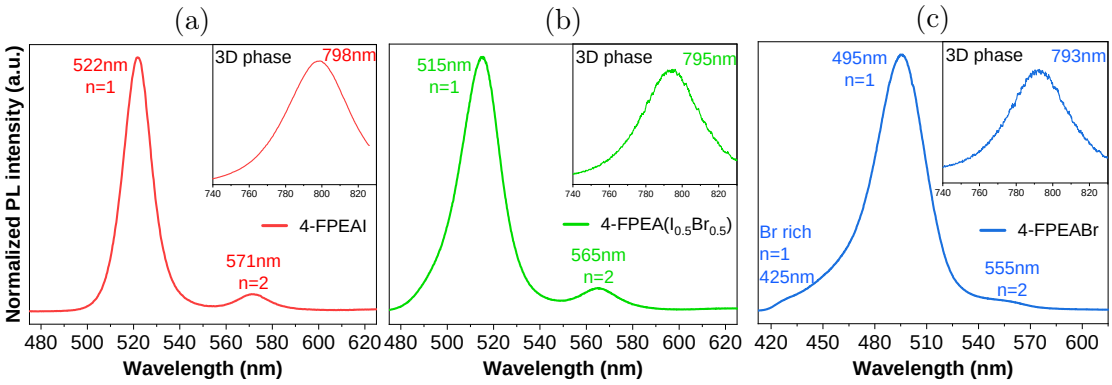

Figure 4.16: PL spectra of full iodide 3D perovskite treated with a 10mg.mL^{-1} solution of (a) 4-FPEAI, (b) 4-FPEA(I$_{0.5}$Br$_{0.5}$), or (c) 4-FPEABr cation.

Focusing on 2D layer emission, n=1 and n=2 phases are visible at 522 and 571 nm for Y = iodine in Figure 4.16a. When Y becomes an iodine/bromine mix (Figure 4.16b), these peaks get wider and blue-shift to 515 and 565 nm, corresponding to the formation of a 2D layer with higher bromine content. With Y = bromine in Figure 4.16c, the n=1 emission further blue-shifts to 495 nm, widens again (indicating an even higher bromine content in the 2D layer), and displays two tails. The first one corresponds to the n=2 phase that blue-shifted to 555 nm and started merging with the main n=1 peak. The second tail is located around 425 nm, close to the emission of the (4-FPEA)$_2$PbBr$_4$ perovskite (412 nm, see Figure 4.7), and so, is expected to be the emission of a 2D perovskite phase segregated with a majority of bromine. Such photo-induced halide segregation is more common in bromine-rich perovskites [T. Hoke *et al.* 2015, Bush *et al.* 2018], and would be channeled by 4-FPEABr cation salt bringing a significant amount of bromine into the reaction.

The linear fit from Figure 4.8b was used to estimate the halide mix of 2D layers in each configuration, which are summed up in the "Measured" columns of Table 4.3. For full iodide/4-FPEAI, without any bromine involved, the 2D layer PL is similar to the $(4\text{-FPEA})_2PbI_4$ reference. On the other hand, adding bromine in Y halides leads to halide mixes estimated at $(I_{0.91}Br_{0.09})$ for full iodide/4-FPEA(I,Br) configuration, and $(I_{0.64}Br_{0.36})$ for full iodide/4-FPEABr configuration.

From the reactants in the cation substitution Equation 4.2, three X halide anions are brought by the 3D perovskite, while the 2D cation salt brings two Y halides. Hence, the 3D perovskite would contribute to 60% of halides, and the 2D molecule to 40%. The halide mix expected with this model are indicated in the "Expected" columns of Table 4.3 for each configuration. However, the 2D perovskite layer contains only four halide anions, while five halides were brought into the reaction. This method, based on counting halides provided by each reactant to predict the halide mix of the 2D layer, should therefore be considered with parsimony.

Table 4.3: Estimated halide mix of 2D layers for each full iodide configuration.

2D/3D configuration	Measured		Expected	
	I (%)	Br (%)	I (%)	Br (%)
Full iodide + 4-FPEAI	100	0	100	0
Full iodide + 4-FPEA($I_{0.5}Br_{0.5}$)	90.7	9.3	80	20
Full iodide + 4-FPEABr	63.7	36.3	60	40

4-FPEAI, 4-FPEABr, and 4-FPEAI/Br on baseline configuration $\mathbf{X = I_{0.83}Br_{0.17}}$

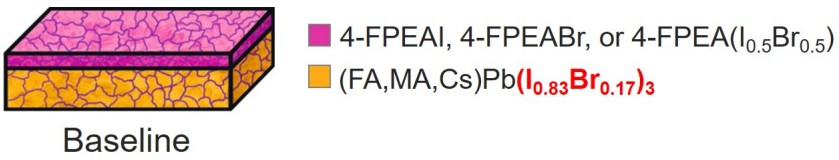

Figure 4.17: Schematic representation of 2D/3D heterostructures made with baseline 3D perovskite composition.

Baseline configurations in Figure 4.18 reveal a significant blue-shift visible for all samples, due to the 16.7% of bromine in the 3D perovskite stoichiometry. Applying the fit to these configurations gives the estimations presented in Table 4.4, showing a more linear evolution than full iodide configurations.

Table 4.4: Estimated halide mix of 2D layers for each baseline configuration.

2D/3D configuration	Measured		Expected	
	I (%)	Br (%)	I (%)	Br (%)
Baseline + 4FPEAI	79.8	20.2	90	10
Baseline + 4-FPEA($I_{0.5}Br_{0.5}$)	66.4	33.6	70	30
Baseline + 4-FPEABr	51.0	49.0	50	50

For baseline/4-FPEAI configuration, adding 16.7% of bromine in the 3D precursor solution leads to 20% of bromine in the 2D perovskite. Replacing 4-FPEAI by 4-FPEABr only increases bromine content from 20 to 49%. A similar result was observed in full iodide configuration, as replacing 4-FPEAI with 4-FPEABr increased bromine amount estimated in the 2D layer from 0 to 36%. These results suggest that the 3D perovskite is the major contributor in the halide composition of the resulting 2D layer, and so, they highlight the importance of the 3D perovskite stoichiometry.

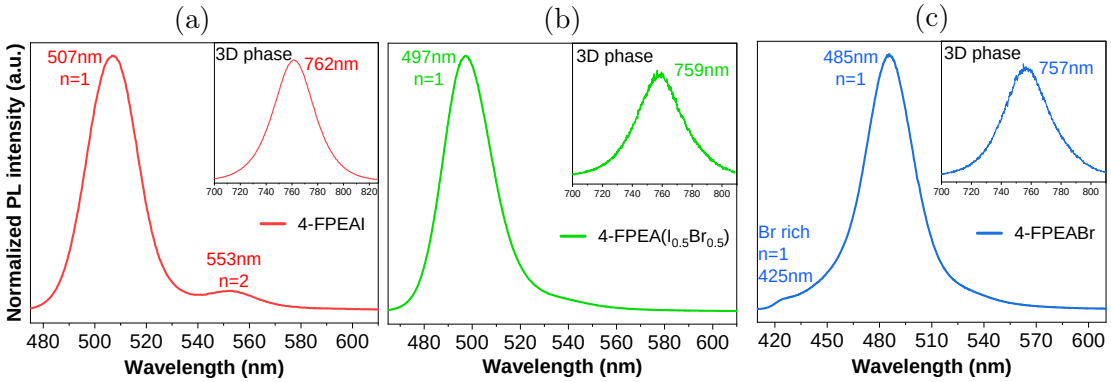

Figure 4.18: PL spectra of baseline 3D perovskite treated with a 10mg.mL^{-1} solution of (a) 4-FPEAI, (b) 4-FPEA($I_{0.5}Br_{0.5}$), or (c) 4-FPEABr cation.

4-FPEAI, 4-FPEABr, and 4-FPEAI/Br on bromide rich configuration X = Br

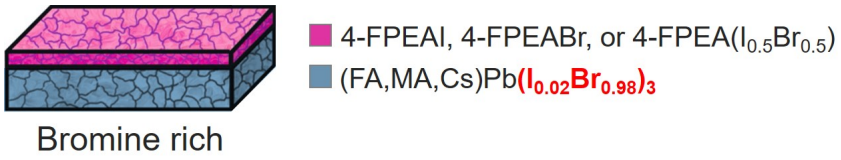

Figure 4.19: Schematic representation of 2D/3D heterostructures made with bromine-rich 3D perovskite composition.

As the 3D phase rely on bromine instead of iodine, bromine-rich samples display different results in Figure 4.20. The 3D emission is moved around 545 nm, and still blue-shifts slightly when Y halide is replaced from iodine to bromine.

Using 4-FPEABr solution, the PL spectrum in Figure 4.20a can be compared to iodine-based 3D perovskites. Distinct peaks are seen at 417, 445, and 477 nm, attributed to n=1, n=2, and n=3 phases of a bromide $(4\text{-FPEA})_2A_{n-1}Pb_nBr_{3n+1}$ 2D perovskite. With Y = iodine/bromine mix, the 2D emission turns into a large band from 410 to 510 nm due to the formation of 2D phases with various iodine/bromine mixes. Two peaks stand out at 424 and 448 nm, expected as the n=1 and n=2 phases of the bromide 2D perovskite, red-shifted due to higher iodine amount. Another n=3 peak might be located around 477 nm, but this peak is not clearly defined as it seems to have merged with the more intense n=2 peak. Switching to Y = iodine, the emission band is significantly red-shifted, and two peaks are visible at 464 and 506 nm. The first peak would come from

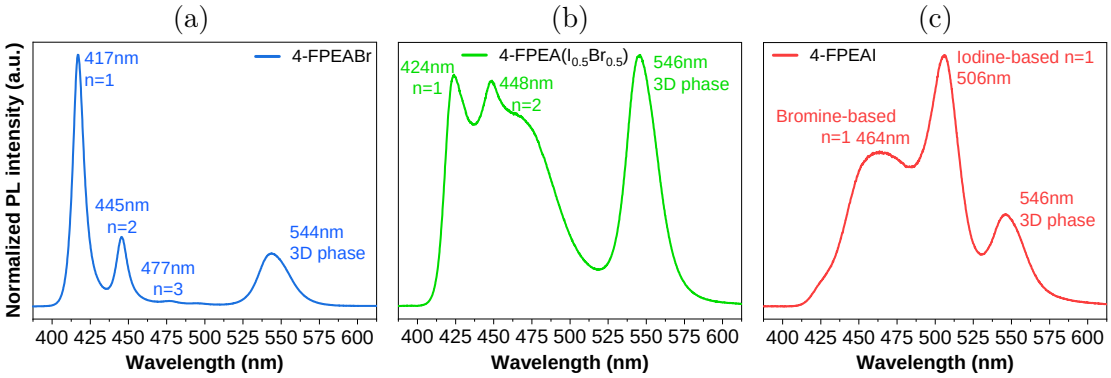

Figure 4.20: PL spectra of full bromide 3D perovskite treated with a 10mg.mL^{-1} solution of (a) 4-FPEAI, (b) 4-FPEA($I_{0.5}Br_{0.5}$), or (c) 4-FPEABr cation.

the segregation of a bromine-based 2D phase, red-shifted to 464 nm due to a noticeable iodine amount. The second peak originates from an iodine-based 2D phase, blue-shifted to 506 nm because of bromine inclusion. The iodine-based peak would be more intense than the bromine-based peak due to re-absorption by the low-bandgap (iodine) phase of photons generated by the high-bandgap (bromine) phase.

This study provided a compelling amount of data. It unravelled the greater importance of halides from the 3D perovskite than the 2D cation on the composition of the 2D layer formed. It also shows interesting development potential for further knowledge on the 2D perovskite formation.

4.4 Summary

This chapter focused on the formation mechanism of the 2D/3D perovskite structure. Starting from observing a PL blue-shift of the 2D layer, we exposed the important role of bromine from the 3D phase in this blue-shift. We observed that the 2D layer was contaminated by bromine from the 3D perovskite, which affected its optical properties. The amount of bromine in the 2D layer was quantified with XPS measurements and later, we proposed a method to accurately determine this amount using only the optical emission properties of the 2D layer.

Confirming bromine contamination of the 2D perovskite led us to the necessity of a mechanism involving the 3D perovskite layer. After discarding various phenomena, we proposed a reaction in which 4-FPEAI substitutes the 3D perovskite cations (i.e., FA, MA, and Cs) to form a 2D perovskite layer containing a significant amount of bromine.

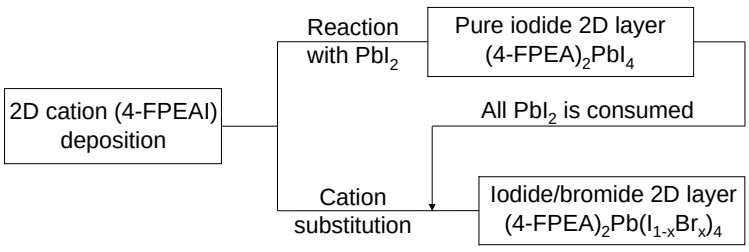

Figure 4.21: Expected formation of a 4-FPEAI based 2D layer on a 3D perovskite.

Finally, the third section consisted of various experiments made to support or contradict the theorized mechanisms. Modifying the PbI_2 excess in the 3D perovskite has proven to be a quite ineffective method of affecting the 2D perovskite layer thickness, but gave a better understanding of its formation mechanisms and how they occur. The last study revealed how the halides from the 3D perovskite prevail on the halide composition of the 2D phase, and thus, highlighted the importance of the cation substitution mechanism to form the 2D layer on top of a 3D perovskite.

Chapter 5

Exploration perspectives of alkylammonium cations

This last chapter explores the synthesis of a 2D/3D heterostructure based on the n-octylammonium spacer cation. In the first section, we study the properties of the 2D/3D structure regarding the 2D precursor solution concentration and highlight the formation of a layer constituted mainly of n=2 RP phases, which differs from the 4-FPEAI treatment. The presence of bromine from the 3D layer is found in these 2D phases. However, more information would be required to conclude on the formation mechanisms. The second section is dedicated to applying n-OAI treatment in solar cells. Interestingly, the n-OAI spacer improves device efficiency and stability in a very similar way to 4-FPEAI.

Contents

In previous chapters, we studied 2D/3D heterostructures based on 4-FPEAI. Chapter 3 focused on the properties of the 2D/3D structure, and we proposed a new perspective on the 2D layer formation mechanisms in Chapter 4. As described in Chapter 1, many cations have been used in the literature to form 2D/3D materials. While n-butylammmonium (n-BA) spacer cation is most common in 2D perovskites, various works established that n-octylammonium (n-OA) was the optimal alkyl-chain length for 2D/3D structures [de Holanda *et al.* 2019, Kim *et al.* 2019b]. Furthermore, very high PCE were obtained with 2D/3D structures based on n-OAI cation salt [Jeong *et al.* 2020]. After wondering if the drastically different shapes of n-OA and 4-FPEA cation molecules could influence the resulting 2D/3D structure, we applied our experience to explore the formation of 2D/3D structures based on n-OA.

5.1 OAI-based 2D perovskite references

2D perovskite references were fabricated with n-OAI cation salt to assess their features. Their synthesis was performed identically to $(4\text{-FPEA})_2PbI_4$ references from Section 3.1.1. For the precursor solution, n-OAI and PbI_2 (2:1 molar ratio) were dissolved in a DMF/DMSO (4:1) mix with 10% weight concentration. 100 μL of this solution was spin-coated on the substrate at 2000 rpm for 30 s, followed by a second run to deposit 100 μL of toluene anti-solvent. Last, 100 °C hot plate annealing for 1 min crystallized the $(\text{n-OA})_2PbI_4$ n=1 pure 2D perovskite. We characterized their optical and structural properties with UV-Vis spectroscopy, PL, and XRD, shown in Figures 5.1 and 5.2.

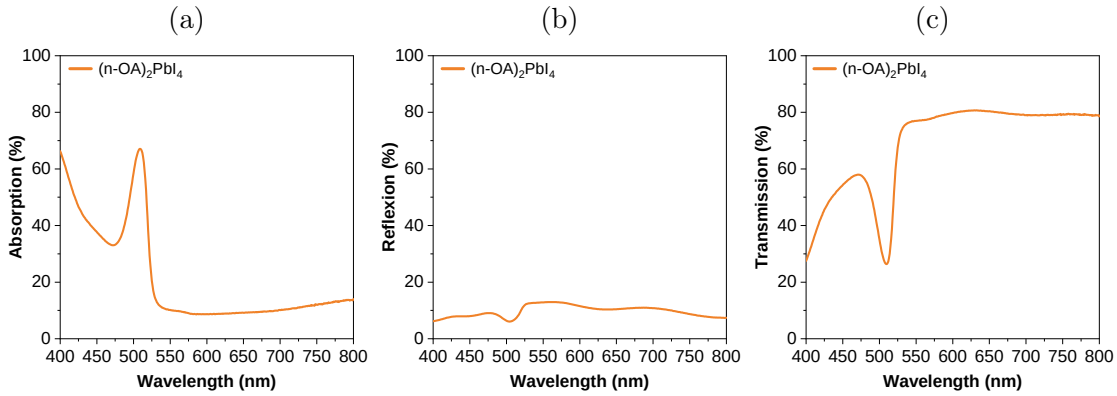

Figure 5.1: (a) Optical absorption, (b) reflection, and (c) transmission of $(\text{n-OA})_2PbI_4$ reference 2D perovskite.

The properties of the resulting perovskite agree with the literature [Sheikh *et al.* 2019] and are analogous to the properties of the pure 2D references based on the 4-FPEA spacer, with some noticeable differences. First, its optical properties are similar, with only a slight blue-shift of the 1s excitonic absorption peak to 509 nm (2.44 eV) and of the emission peak to 521 nm (2.38 eV). Figure 5.2b also reveals that replacing 4-FPEA with n-OAI increased the lattice parameter of the resulting perovskite and moved its peaks to lower angles. As a result, the (002), (004), (006), (008), (0010), and (0012) peaks are found at 4.7, 9.5, 14.2, 18.9, 23.7, and 28.5°. The (0014) peak shifted within the scan range and is detected at 33.4°.

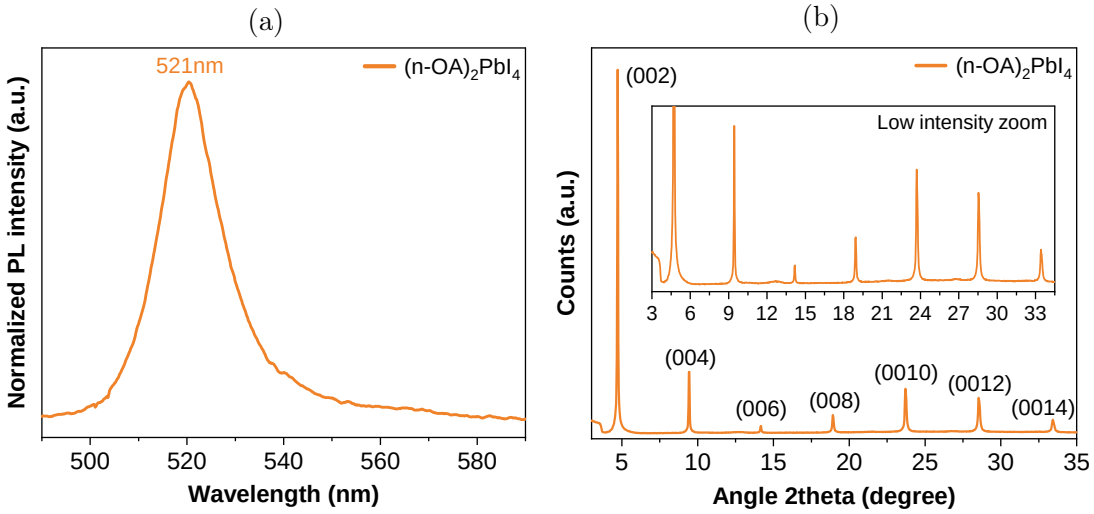

Figure 5.2: (a) PL spectra and (b) Diffractogram of $(n\text{-}OA)_2PbI_4$ 2D perovskite.

5.2 Properties of the 2D/3D heterostructure

5.2.1 Identification of the 2D phase

To study 2D/3D heterostructures made with n-OAI, we applied the same synthesis process used in this thesis work and described in Section 2.1.4. Instead of 4-FPEAI, n-OAI spacer cation precursor was solubilized in IPA with similar solution concentrations of 2.5, 5, and 10 mg.mL^{-1}. This solution was dynamically deposited on the 3D perovskite and annealed for 5 minutes at 100°C.

The structural properties of 2D/3D structures were assessed with XRD. Figure 5.3a compares the diffractogram of an n-OAI 10 mg.mL^{-1} sample with pure 2D and pristine 3D references.

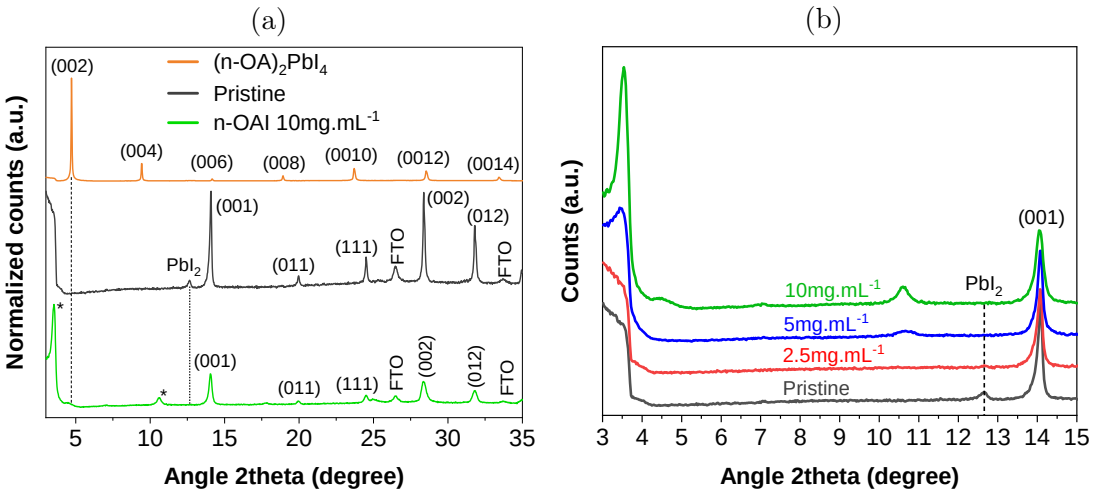

Figure 5.3: (a) XRD patterns of $(n\text{-}OA)_2PbI_4$ pure 2D perovskite, pristine 3D, and 10 mg.mL^{-1} samples. (b) Diffractogram evolution regarding n-OAI solution concentration, focused on the 3-15° diffraction angle range.

For all samples, intense background noise is seen between 3 and 4° due to low measurement angles (its intensity is constant, so it is less visible in the highly crystallized 2D reference than in 3D samples). The n-OAI treated sample features (001), (011), (111), (002), and (012) peaks of the 3D perovskite phase. A short peak is detected at 4.5° and likely corresponds to the (002) plan of the $(n\text{-}OA)_2PbI_4$ phase. New peaks appear at 3.5 and 10.6° but do not match any peak visible in the 2D perovskite reference shown in Figure 5.2b. Figure 5.3b displays the evolution of XRD pattern as the n-OAI solution concentration increases, focused on low angles. The two peaks at 3.5 and 10.6° appear more intense as n-OAI concentration increases. The 4.5° peak is only seen for the highest concentration. Furthermore, the PbI_2 peak also disappears after n-OAI treatment, which suggests that n-OAI reacted with PbI_2 excess from the 3D phase to form a new phase, similarly to 4-FPEAI treatment. However, unlike with 4-FPEAI, this phase does not correspond to the n=1 $(n\text{-}OA)_2PbI_4$ 2D perovskite.

UV-Vis spectroscopy and PL measurements were carried out on these samples to understand better the 2D/3D interface from its optical properties. Absorption spectra shown in Figure 5.4a reveal an identical behavior to 4-FPEAI treatment, with an increase in optical absorption of the perovskite material that is further enhanced with higher 2D solution concentration. Similarly, an absorption feature is added to the absorption of the 3D perovskite. This feature looks like the excitonic peak of the 2D phase. With 4-FPEAI treatment, it was slightly blue-shifted in comparison with the $(4\text{-}FPEA)_2PbI_4$ 2D reference, which was later attributed to the presence of bromine in the 2D layer. However, for n-OAI treatment, this feature is red-shifted further than the emission of the $(n\text{-}OA)_2PbI_4$ 2D reference in Figure 5.1a, which raised questions about its nature.

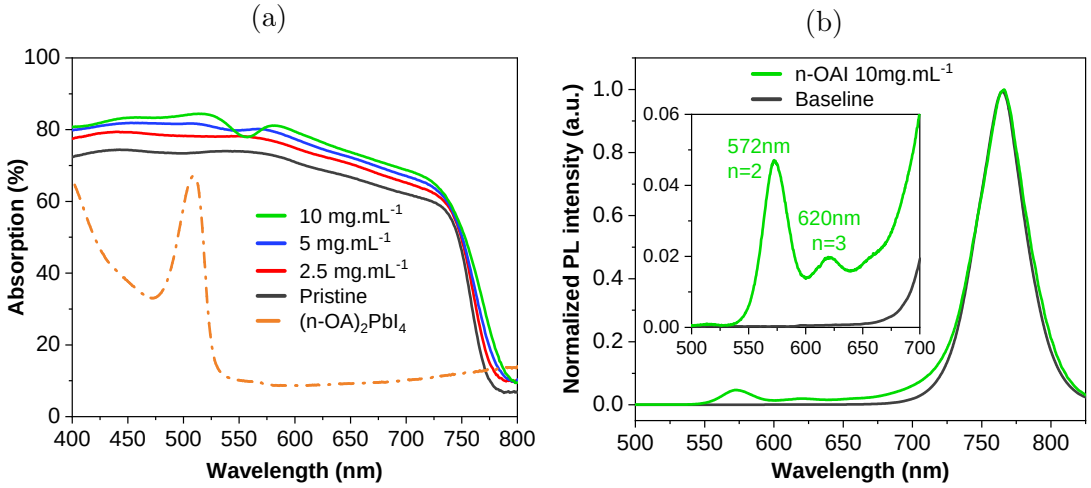

Figure 5.4: (a) Optical absorption of pristine and n-OAI treated samples for all concentrations (2.5, 5, and 10 $mg.mL^{-1}$), compared to $(n\text{-}OA)_2PbI_4$ 2D reference. (b) PL spectra of pristine n-OAI treated samples with 10 $mg.mL^{-1}$.

PL measurements from Figure 5.4b confirmed these observations. As 2.5 and 5 $mg.mL^{-1}$ samples did not differ from pristine material, only the 10 $mg.mL^{-1}$ PL spectrum is presented. With this concentration, a tiny emission peak is hardly distinguished at 515 nm, and more intense peaks are seen at 572 and 620 nm. Such wavelength positions would likely be attributed to n=1, n=2, and n=3 phases of the $(n\text{-}OA)_2(A)_{n-1}Pb_nI_{3n+1}$ RP perovskite. Thus, unlike 4-FPEAI treatment which formed a majority of 2D n=1 perovskite, RP n=2 phases would be formed predominantly with the n-OAI spacer cation,

leading to XRD peaks that do not match the 2D n=1 $(n\text{-}OA)_2PbI_4$ reference. Such behavior was already discussed by Sutanto *et al.*, who observed the formation of either n=1 or n=2 phases in 2D/3D structures regarding the spacer cation used for the 3D perovskite surface treatment [Sutanto *et al.* 2020]. Furthermore, the formation of less emissive n=2 phases would explain the lower emission intensity of 2D phases obtained with n-OAI instead of 4-FPEAI treatment.

5.2.2 Morphology

SEM was used to investigate if n-OAI treatment (forming n=2 RP phases) resulted in a different surface morphology than 4-FPEAI treatment (leading to n=1 2D phases). The resulting images of n-OAI treated samples for every concentration are shown in Figure 5.5. For the lowest 2.5 $mg.mL^{-1}$ concentration, the 3D perovskite grains are still clearly visible on most of the sample surface, and only specific areas show a smoothing effect, with the appearance of platelet-like grains. This surface suggests the inhomogeneous formation of a very thin 2D perovskite layer, which would not be seen by XRD or PL measurements. The 3D grains are less visible after increasing the concentration to 5 $mg.mL^{-1}$, and more platelet-like grains are formed evenly on the surface. Finally, with 10 $mg.mL^{-1}$ n-OAI treatment, the platelet-like grains merged into a more continuous layer. As a result, the 3D perovskite grains can hardly be distinguished anymore.

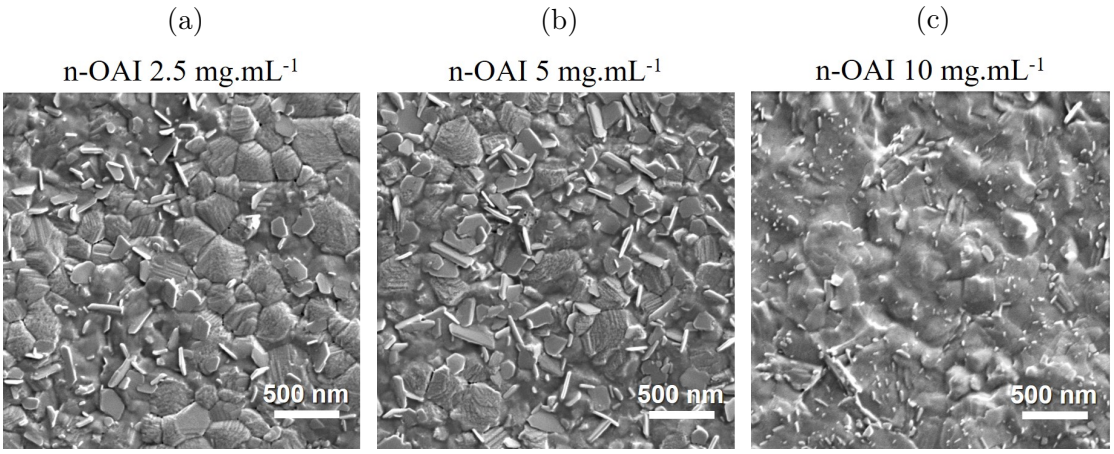

Figure 5.5: SEM surface images of n-OAI treated samples with (a) 2.5 $mg.mL^{-1}$, (b) 5 $mg.mL^{-1}$, and (c) 10 $mg.mL^{-1}$ solution concentration.

After observing the evolution of surface morphology induced by n-OAI treatment through SEM imaging, we used confocal microscopy to assess if surface roughness followed a similar evolution. Figures 5.6a and 5.6b compare the distribution of S_q and S_a roughness of n-OAI treated samples for all concentrations with 4-FPEAI treated references.

Due to lesser optimization of n-OAI treatment, micrometric-sized aggregates are visible on the sample surface (see Figures 5.6c and 5.6d). These aggregates lead to a more inhomogeneous distribution of S_q roughness in Figure 5.6a, with some unusually larger values. As mentioned in Section 2.2.3, S_a roughness in Figure 5.6b is less sensitive than S_q roughness to abnormal topology such as these aggregates, leading to its more homogeneous distribution.

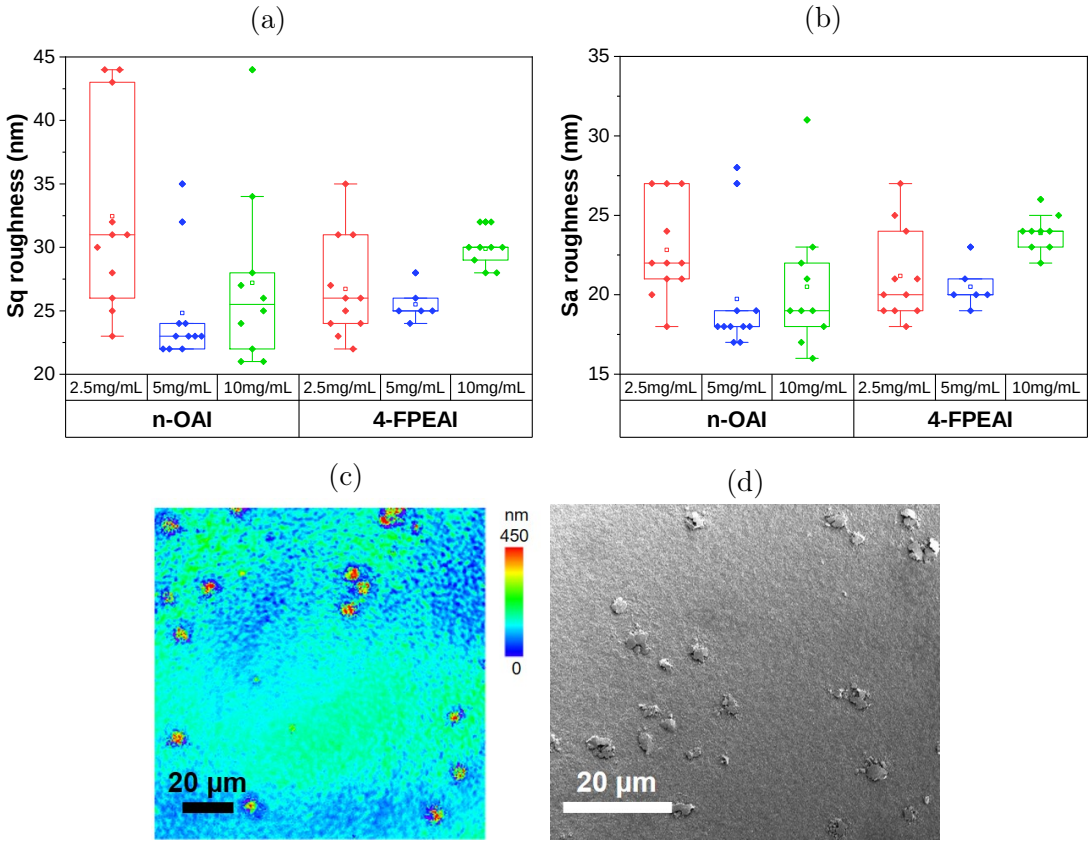

Figure 5.6: Distribution of (a) S_q and (b) S_a roughness measured with confocal microscopy on 4-FPEAI and n-OAI treated samples, for 2.5, 5, and 10 mg.mL^{-1} 2D precursor solution concentrations. (c) Confocal and (d) SEM image of 2.5 mg.mL^{-1} n-OAI treated samples, with visible micrometric sized aggregates.

Table 5.1 summarizes the average value for each experimental condition. Although SEM images revealed a slightly different outcome of n-OAI and 4-FPEAI treatment on surface morphology, roughness measurements, on the other hand, suggest a shared trend. Increasing the 2D solution concentration from 2.5 to 5 mg.mL^{-1} leads to a smoother layer, with the average S_a roughness being reduced from 23 to 20 nm. Interestingly, while SEM images would have suggested a smoother surface for the 10 mg.mL^{-1} samples due to the continuous layer formed, it is not the case, and the average S_a roughness is increased from 20 to 21 nm between 5 and 10 mg.mL^{-1} samples.

Table 5.1: Average S_q and S_a roughness of 4-FPEAI and n-OAI treated samples for 2.5, 5, and 10 mg.mL^{-1} solution concentration.

	n-OAI		4-FPEAI	
	S_q (nm)	S_a (nm)	S_q (nm)	S_a (nm)
2.5 mg.mL^{-1}	32	23	27	21
5 mg.mL^{-1}	25	20	26	21
10 mg.mL^{-1}	27	21	30	24

5.2.3 Insight on bromine contamination and mechanisms

The experimental method from Section 4.1.2 was reused to determine if bromine from the 3D layer was still involved in forming the RP 2D perovskite phases characterized above. 10 mg.mL^{-1} n-OAI treatment was applied on baseline and full iodide 3D perovskite compositions and we characterized their optical properties.

Absorption spectra of baseline and full iodide references without n-OAI treatment in Figure 5.7a are comparable to the same references from Figure 4.4a, and the full iodide sample is red-shifted compared to the baseline composition. After n-OAI addition (see Figure 5.7b), the absorption feature of the 2D phase, close to 580 nm for the baseline composition, is red-shifted to 595 nm for the full iodide perovskite. Therefore, the optical absorption of the 2D/3D structure suggests that bromine from the 3D layer is involved in forming the 2D phase with n-OAI treatment.

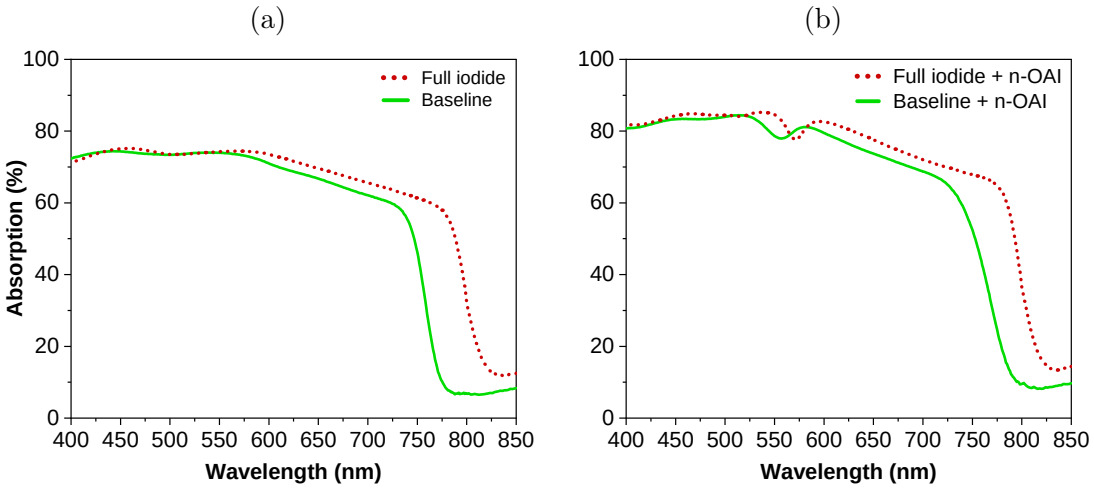

Figure 5.7: Optical absorption of baseline and full iodide samples (a) without and (b) with 10 mg.mL^{-1} n-OAI treatment.

As expected, PL measurements from Figure 5.8 show a red-shifted 3D phase emission, from 766 to 796 nm, when bromine is removed from its composition. Meanwhile, the 2D phases show a different behavior. First, with the full iodide perovskite, the PL intensity of the 2D phases is increased (remarkably for the n=2 phase, more mildly for the n=3 phase), and emission peaks appear for the n=1 and n=4 phases. The position of the n=1 peak (522 nm) matches the emission of the (n-OA)$_2$PbI$_4$, confirming its nature, suggesting that the mixed-halide composition is unfavorable to form n=1 pure 2D perovskite. Additionally, a red-shift is observed for the emission of 2D phases (515 to 522 nm for n=1 and 620 to 628 nm for n=3). Surprisingly, this shift does not apply to both compositions' main n=2 peak, positioned at 572 nm.

Therefore, these preliminary optical characterizations lead us to assume that the formation of 2D perovskite phases with n-OAI involves bromine from the 3D layer and so, involves the cation substitution mechanism. However, they should be pushed further to confirm the results obtained.

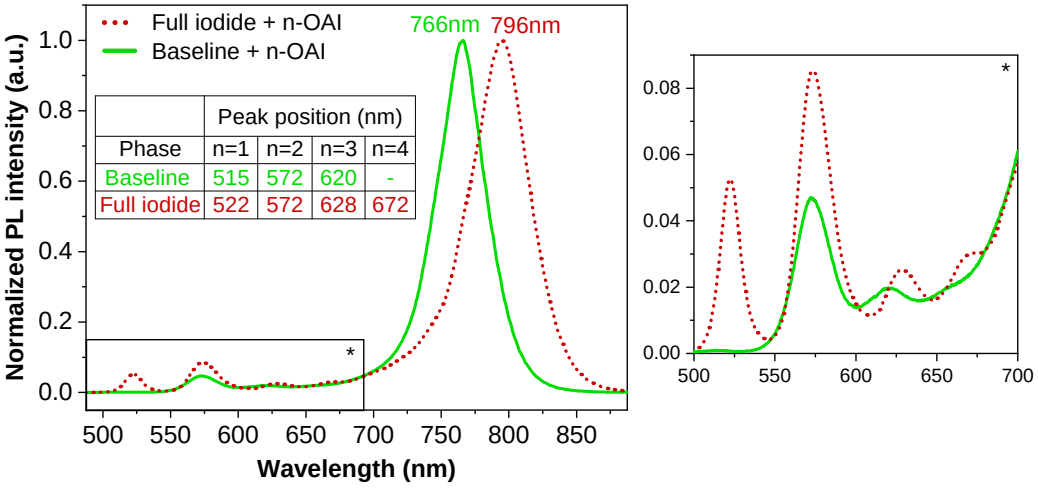

Figure 5.8: PL spectra of 10 mg.mL^{-1} OAI treated baseline and full iodide samples.

5.3 Application in solar cells

In collaboration with the postdoctoral researcher V. S. Nguyen from IPVF, the effect of n-OAI treatment on solar cell devices was also investigated. A concentration of 3 mg.mL^{-1} was chosen, close to 4-FPEAI treatment. Figure 5.9 compares the distribution of photovoltaic parameters between pristine and n-OAI 3 mg.mL^{-1} devices.

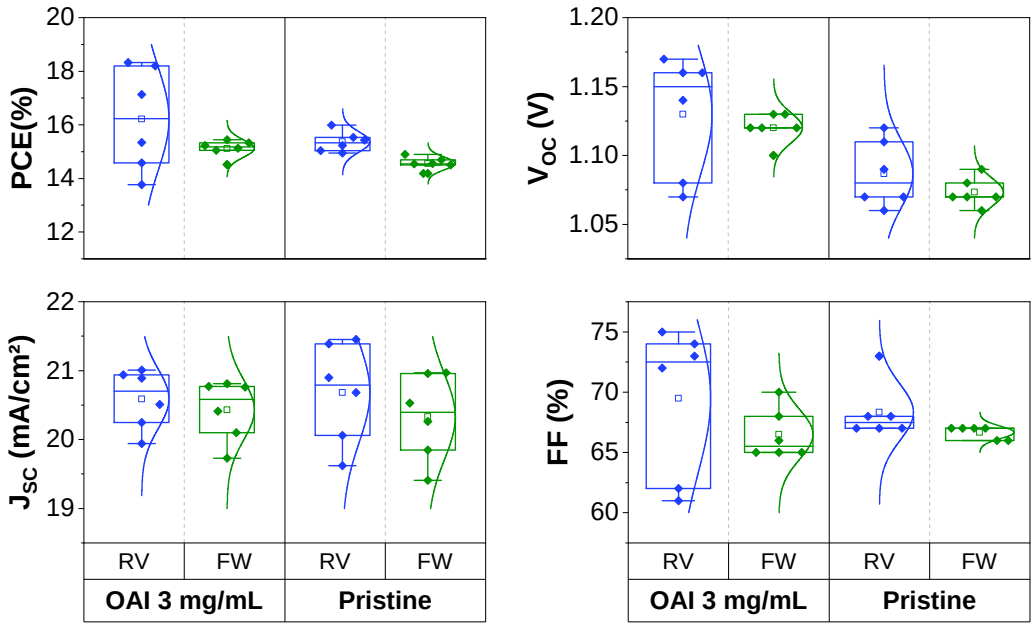

Figure 5.9: (a) Photovoltaic parameters (PCE, V_{OC}, J_{SC}, and FF) distribution of pristine and 3 mg.mL^{-1} n-OAI treated devices *(6 cells/condition)*.

The impact of n-OAI treatment on device efficiency is similar to that obtained with 4-FPEAI treatment. A PCE increase is seen with n-OAI treatment, related to a V_{OC} improvement, while J_{SC} and FF do not show any statistically significant variation. Furthermore, with an average PCE rising from 15.36 to 16.22% and an average V_{OC} going

from 1.09 to 1.13 V, the value of this improvement is almost identical to the ones observed with 4-FPEAI (+ 0.8% PCE, + 40 mV increase). This result agrees with the literature and confirms that an OAI-based 2D layer also passivates the 3D perovskite surface and improves the perovskite/HTL interface [Kim *et al.* 2019b, Mahmud *et al.* 2021b].

The influence of n-OAI and 4-FPEAI treatment on stability was assessed with MPPT. This tracking was performed in the same conditions as in Section 3.4.2 (continuous 1-sun illumination without UV, inert atmosphere, 25°C controlled temperature). The results, shown in Figure 5.10, confirmed the similar effect of both treatments on stability under illumination, with respectively 75% and 70% of the initial PCE remaining after 110 hours for n-OAI and 4-FPEAI treated cells, compared to 32% for the pristine sample.

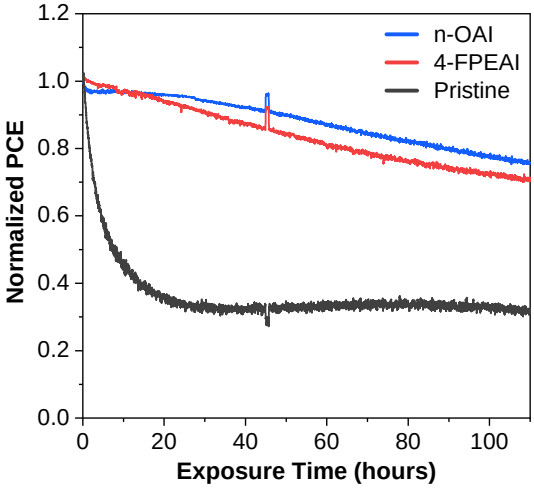

Figure 5.10: MPPT of pristine, 4-FPEAI treated, or n-OAI treated devices under continuous 1-sun illumination *(without UV)*.

Such results suggest that 2D/3D heterostructures improve the efficiency and stability of 3D-based PSCs similarly, regardless of the spacer cation nature. This result corroborates the discussion made at the end of Section 3.3.3 about the potential greater importance of the solvent than of the spacer for the 2D solution.

5.4 Summary

This work introduced the study of 2D/3D heterostructures based on the n-OA spacer cation. We first fabricated and characterized 2D perovskite references made with n-OAI precursor, before focusing on the study of the 2D/3D perovskite structure itself. After assessing in Chapter 3 that the 2D precursor solution concentration was a crucial factor to modify the thickness of the 2D layer formed with 4-FPEAI, we varied this synthesis parameter in a similar way. We highlighted that replacing 4-FPEAI by n-OAI formed a 2D layer that seemed constituted mainly of n=2 RP phases instead of n=1 2D perovskite phases. However, these different phases did not affect significantly the morphology of the layer, and its thickness seemed to evolve similarly than with 4-FPEAI treatment.

To determine if bromine was involved in the formation of perovskite phases induced by n-OAI treatment, we conducted a preliminary study dedicated to apply n-OAI treatment on baseline and full iodide 3D perovskite compositions. This exploration study suggested that bromine from the 3D perovskite impacted the optical properties of the

2D layer. This result would confirm that the 3D perovskite, and so the cation substitution mechanism, is still involved in the formation of the 2D phase with n-OAI treatment. For the development of this study, fabricating and characterizing OAI-based n=2 RP references, performing new optical characterizations on baseline and full iodide compositions, and using XPS would be necessary. This development would allow to conclude on the formation mechanisms of the 2D layer involved during n-OAI treatment, and would provide more information on the nature of the 2D spacer cation in 2D/3D structures.

Interestingly, with the application of n-OAI in solar cells, 4-FPEAI and n-OAI treatment were found to improve similarly both efficiency and stability of devices. This result suggests that prioritizing the choice of solvent for the 2D precursor solution before the choice of spacer cation could be relevant for 2D/3D heterostructures in solar cells. Nevertheless, an extensive comparative study between 4-FPEAI and n-OAI treatments would be interesting to assess the beneficial effects of each spacer cation.

Conclusion and perspectives

This thesis occurred as a collaboration between the research group led by E. Deleporte in LuMIn laboratory, specialized in the optical study of 2D perovskites, and IPVF's IMPACTS program, which develops perovskite-silicon tandem cells. This work consisted in the study of 2D/3D perovskite heterostructures, which were not studied in these labs before the start of this PhD.

The first chapter provided a general context to this study. It highlighted how perovskite solar cells appeared as relevant candidates for photovoltaics, and in particular for low-cost tandem cells, one of the most promising solutions to develop the photovoltaic industry. So far, the development of perovskite solar cells has been astonishing, and they reached similar efficiency (25.7%) than silicon technology in only a decade. Several issues still need to be solved for perovskite technology to enter the photovoltaic market on a large scale. Among these challenges, device stability is crucial to ensure good energy and economic paybacks. Despite important progress in the stability of perovskite solar cells through composition and interface engineering, further improvements are necessary. In this regard, 2D perovskites, based on big organic spacer cations and a layered structure, stood out thanks to better intrinsic and extrinsic stability than their 3D counterpart. Optimizing their specific structure made their application as the main absorber in perovskite solar cells promising. However, their most popular application is combining them with 3D perovskites to form 2D/3D perovskite heterostructures. Two different approaches have been studied: synthesizing a single perovskite layer made with mixed 2D and 3D perovskite phases, or forming a thin 2D layer on the surface of a 3D absorber. These alternatives have both proved to improve 3D-based perovskite solar cells by enhancing their intrinsic and extrinsic stability, and increasing their efficiency.

The development of perovskite solar cells using 2D/3D heterostructures was presented in Chapter 2. This development started from a 3D perovskite-based solar cell fabrication process designed at IPVF called the baseline process. The techniques used to synthesize each layer of the devices were detailed (spin-coating, ALD, metal e-beam evaporation...). The main challenge of this thesis was the integration of 2D/3D heterostructures in the baseline process. We focused on the more promising surface treatment 2D/3D structures. Thanks to the important knowledge of the LuMIn group in PEA-based 2D perovskites, 4-FPEAI was chosen as the main material to form our 2D/3D structures. The measurement of IV characteristics was central in assessing the effect of the 2D/3D heterostructures on the efficiency and stability of solar cell devices. UV-Vis spectroscopy and PL measurements were used to evaluate the optical properties of the perovskite material itself. XRD and XPS were crucial to assess structural and chemical properties of the material. Imaging techniques such as SEM, AFM, and confocal microscopy provided information on the morphology of the 2D/3D structure.

When this work started, the study of some 2D/3D perovskite heterostructures had already begun in the literature. Still, no consensus existed on some of their properties (thickness of the 2D layer, phases formed, surface aspect). Hence, the main goal of the third chapter was to understand our 2D/3D material. A 2D perovskite layer, only a few nanometers thin and constituted mainly of n=1 phases, was formed on the 3D perovskite by the reaction of 4-FPEAI with PbI_2. The concentration of 4-FPEAI precursor solution was revealed as a major factor to alter the thickness of the 2D layer formed. Increasing 4-FPEAI solution concentration from 2.5 to 10 $mg.mL^{-1}$ thickened the 2D layer from a few nanometers to a few tens of nanometers, significantly changing the morphology of the layer. Applying each solution concentration in solar cell devices highlighted that a thin 2D layer was more optimal for improved efficiency. On the other hand, increasing the soaking time between the 4-FPEAI solution and 3D perovskite did not alter the amount of 2D perovskite formed in a relevant way. Furthermore, this method was exposed as very inconsistent, due to IPA solvent being detrimental to the 3D perovskite layer for longer soaking times. This study underlined that solvent engineering is necessary to extend 2D/3D perovskite structures to large-scale deposition techniques. Applying it to perovskite solar cells, 4-FPEAI treatment significantly improved device efficiency and stability, and we obtained a promising record efficiency of 20.48% on 0.09 cm^2 devices. An efficiency close to 18% was reached with 4 cm^2 mini-modules, further confirming the relevance of integrating 2D/3D heterostructures in the baseline process of solar cells.

Despite the properties of the 2D layer in 2D/3D structures matching the ones of $(4\text{-FPEA})_2PbI_4$ 2D perovskite references, a blue-shift was observed in its optical properties. Identifying the cause of this blue-shift was necessary to figure out how the 2D layer formation, and was the subject of the fourth chapter. XPS measurements revealed the presence of bromine in the 2D layer and quantified its halide mix to 79% of iodine and 21% of bromine. Removing bromine from the 3D perovskite composition allowed us to confirm that bromine was the cause of the 2D layer blue-shift. We proposed a method to accurately assess the amount of bromine in the 2D phase of a 2D/3D structure using only its PL emission. The formation mechanism presented in Chapter 3 and generally accepted in the literature could not explain the presence of bromine in the 2D layer. Therefore, we hypothesized that 4-FPEAI substitutes the A-site cations of the 3D perovskite to form a 2D layer containing bromine. Modifying PbI_2 excess in the 3D perovskite, we confirmed the existence of this mechanism. Additionally, focusing on the formation of 2D/3D structures with various halide compositions for the 3D perovskite and 2D cation salt provided new supporting arguments. By revealing that the two mechanisms are concurrent in forming the 2D layer and highlighting the importance of the cation substitution mechanism, these studies bring new insights into the synthesis mechanisms of 3D/2D perovskite heterostructures and improve their understanding.

In the fifth chapter, we used our knowledge of 2D/3D structures to study their formation with another spacer cation, n-octylammonium. Based on the spacer cation used, the formation of the 2D layer is modified. While 4-FPEAI forms mostly n=1 2D perovskite phases, n-OAI instead forms a majority of n=2 phases. These different phases do not lead to significantly different 2D layer morphology or thickness. The improvements obtained on device efficiency and stability also suggested that 2D perovskite layers similarly improve a 3D perovskite material, regardless of the spacer cation. Based on the optical properties of the 2D phase, the presence of bromine within the layer was suggested, implying that n-OAI involved the cation substitution mechanism to form the n=2 RP phases. However, further analysis is required to confirm the mechanisms at stake with this other cation with more certainty.

Perspectives

To sum-up this thesis work, we successfully developed 2D/3D perovskite heterostructures and integrated them in perovskite solar cells. Furthermore, we provided new insight into their synthesis mechanisms, which could be beneficial for future development.

This study was performed with a very empirical approach, based on specific characterization methods applied to various experimental conditions, to understand how 2D/3D perovskite structures are formed. Therefore, some aspects of these materials were not treated extensively during this work, and exploring them could significantly improve its comprehensiveness. For example, understanding how 2D/3D structures enhance the efficiency of solar cells is crucial to improve them further. In this regard, focusing on the opto-electronic properties of the material and the devices through time-resolved photoluminescence or dark-current voltage would provide important information on the passivation effects induced by the 2D layer. Similarly, an important asset could be the characterization of energy level alignment in 2D/3D perovskite solar cells using ultraviolet photoelectron spectroscopy (UPS) and inverse photoemission spectroscopy (IPES).

In addition, our work on the 2D/3D structure formation mechanisms was limited by the characterization techniques available. For instance, grazing-incidence wide-angle x-ray scattering (GIWAXS) could have helped us to determine the orientation of the perovskite phases in the 2D layer. Likewise, assessing in real time the evolution of the perovskite material during 2D treatment with *in-situ* techniques, such as *in-situ* PL, would allow us to confirm the formation mechanisms proposed. The stability study of solar cell devices should also be extended, with more samples, longer aging times, and more aging conditions (thermal stress, high relative humidity, continuous illumination).

This study was based on a triple-cation 3D perovskite composition. However, the perovskite literature is moving towards other compositions, such as (FA, Cs) double-cation perovskites. Therefore, the relevance of 2D/3D structures should be investigated for these new compositions. Using novel spacer cations, such as di-ammonium cations forming Dion-Jacobson 2D perovskites, could also benefit 2D/3D structures. Solvent engineering is also essential to ensure minimal degradation of the 3D perovskite phase and to develop stable 2D/3D structures. It could be mandatory to integrate such structures in devices made with large-scale deposition techniques [Sidhik *et al.* 2022].

The evolution of the perovskite solar cell literature confirms the relevance of this work. At the beginning of this thesis, 2D/3D heterostructures were still a developing topic, with bulk incorporation and surface treatment structures being studied in relatively equal proportions. Nowadays, 2D/3D structures have become a hot topic. Capping layer has become the dominant structure, and many published works use such 2D/3D perovskites (sometimes without even mentioning it), highlighting that this material has become much more common. An ever-increasing number of spacers are being used. Many of them have proven their efficiency, such as 4-FPEAI. However, none stand out as the reference to follow, leaving room for further exploration.

From a broader perspective, there is still a long way to go in understanding and solving the stability challenge raised by perovskite solar cells regarding the myriad solutions proposed in the literature. However, the rapid development towards higher stability and good efficiencies has attracted substantial interest. Thus, if its other challenges, like large-scale industrial production, were overcome, perovskite solar cells could have a major impact on the photovoltaic market and global energy production.

Appendix

A.1 List of conferences and publications

Publications

T. Campos, P. Dally, S. Gbegnon, A. Blaizot, G. Trippé-Allard, M. Provost, M. Bouttemy, A. Duchatelet, D. Garrot, J. Rousset, E. Deleporte. 'Unraveling the Formation Mechanism of the 2D/3D Perovskite Heterostructure for Perovskite Solar Cells Using Multi-Method Characterization'. *J. Phys. Chem. C* **vol. 126**, no. 31, pp. 13527–13538 (2022)

G. Garcia-Arellano, G. Trippé-Allard, **T. Campos**, F. Bernardot, L. Legrand, D. Garrot, E. Deleporte, C. Testelin, M. Chamarro. 'Unexpected Anisotropy of the Electron and Hole Landé G-Factors in Perovskite CH3NH3PbI3 Polycrystalline Films'. *Nanomaterials (Basel)* **vol. 12**, no. 9, p 1399 (2022)

Conferences

French conferences

Journée des Pérovskites Halogénées (GDR HPERO), 31 march-2 april 2021, videoconference. **Poster communication**. *Study of 2D/3D halide perovskite heterostructure to improve the stability of photovoltaic devices.* T. Campos, E. Deleporte, A. Duchatelet, D. Garrot, G. Trippé-Allard, J. Rousset

Journée des Pérovskites Halogénées (GDR HPERO), 16-18 march 2022, Ecully. **Oral communication**. *Study of Synthesis Parameters on the Formation and Physical Properties of 2D/3D Hybrid Halide Perovskite Heterostructures for Solar Cells.* Thomas Campos, P. Dally, M. Bouttemy, G. Trippé-Allard, A. Duchatelet, D. Garrot, J. Rousset, E. Deleporte

Journées Nationales du PhotoVoltaïque, 29 november-2 december 2022, Dourdan. **Oral communication**. *Etude du mécanisme de formation d'une hétérostructure de pérovskites 2D/3D appliquée pour des cellules photovoltaïques.* T. Campos, P. Dally, S. Gbegnon, A. Blaizot, G. Trippé-Allard, M. Provost, M. Bouttemy, A. Duchatelet, D. Garrot, J. Rousset, E. Deleporte

International conferences

MRS Spring Meeting, 8-13 May 2022, Honolulu, Hawaii. **Oral communication**. Symposium EQ05: Semiconductor Physics of Halide Perovskites - From Fundamentals to Devices. *Study of synthesis parameters on the formation of 2D/3D hybrid halide perovskite heterostructures, for photovoltaic applications* T. Campos, Pia Dally, M. Bouttemy, G. Trippé-Allard, A. Duchatelet, D. Garrot, J. Rousset, E. Deleporte.

Momentom International Congress, 8-10 march 2023, Gif-sur-Yvette. **Oral communication**. *Study of the formation of 2D/3D perovskite heterostructures for solar cells.* Thomas Campos, P. Dally, M. Bouttemy, G. Trippé-Allard, A. Duchatelet, D. Garrot, J. Rousset, E. Deleporte

A.2 Static deposition with 5 mins soaking time

Optical properties

Based on absorption and PL spectra from Figure A.1, using increasing to 5 minutes the soaking time of 4-FPEAI solution on the 3D perovskite surface produces interesting results. The absorption spectra in Figure A.1a is greatly modified in comparison with the pristine sample. First, the overall absorption is decreased due to low surface due to a more reflective surface. Second, a strong absorption feature associated to the 2D layer is visible around 500 nm. This observation is confirmed by the PL spectrum from Figure A.1b. The use of a long soaking time leads to the appearance of several peaks around 519, 552, 600, and 632 nm. These peaks are attributed to n=1, n=2, n=3, and n=4 phases of the (4-FPEA)$_2$(MA,FA,Cs)$_{n-1}$Pb$_n$I$_{3n+1}$ RP perovskite, and their intensity (the n=1 peak is significantly more intense than the 3D perovskite peak) suggest the formation of an high amount of 2D perovskite.

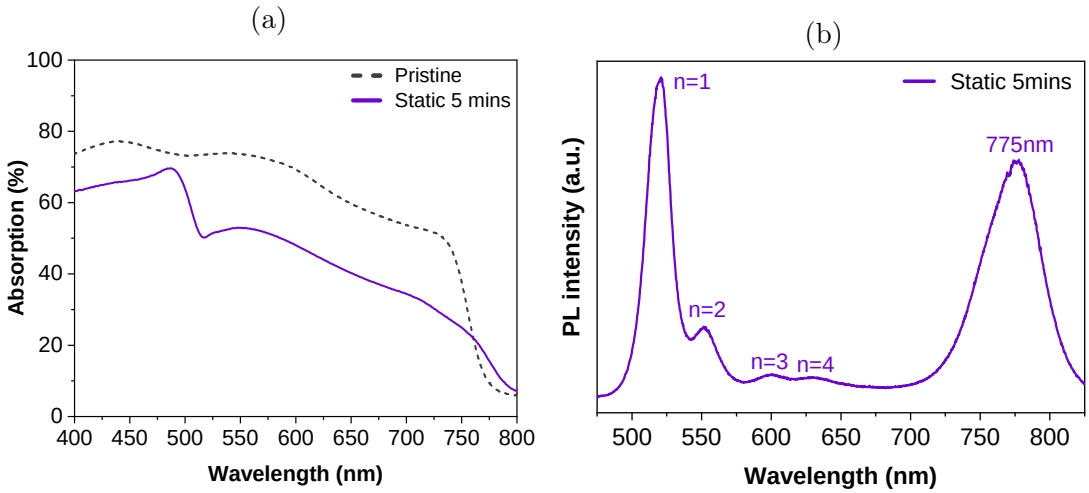

Figure A.1: (a) Optical absorption and (b) PL spectra of a 4-FPEAI treated sample with 5 mins soaking time.

Structural and morphological properties

XRD and SEM were also used to characterize these samples. The diffractogram in Figure A.2a supports the optical measurements, as peaks from both the 2D and 3D perovskites are visible. More importantly, unlike any other experimental condition, all peaks of the 2D perovskite phase are visible in the 2D/3D structure, and their intensity is also higher than the 3D phase peaks, further suggesting a high amount of 2D perovskite.

Finally, surface and cross-section SEM images confirmed the high amount of 2D perovskite formed with such soaking time. The cross-section image in Figure A.2d shows a new layer of 2D perovskite close to 100 nm thick on the 3D bulk. However, the surface image in Figure A.2b reveals that this high amount of 2D perovskite does not form an homogeneous thick 2D layer. Instead, the 2D phases crystallized in large aggregates, few tens micrometers wide. The second SEM from Figure A.2c, acquired with a higher magnification, confirms the inhomogeneity of the 2D phases formed, as the 3D perovskite grains are still visible between the large 2D aggregates.

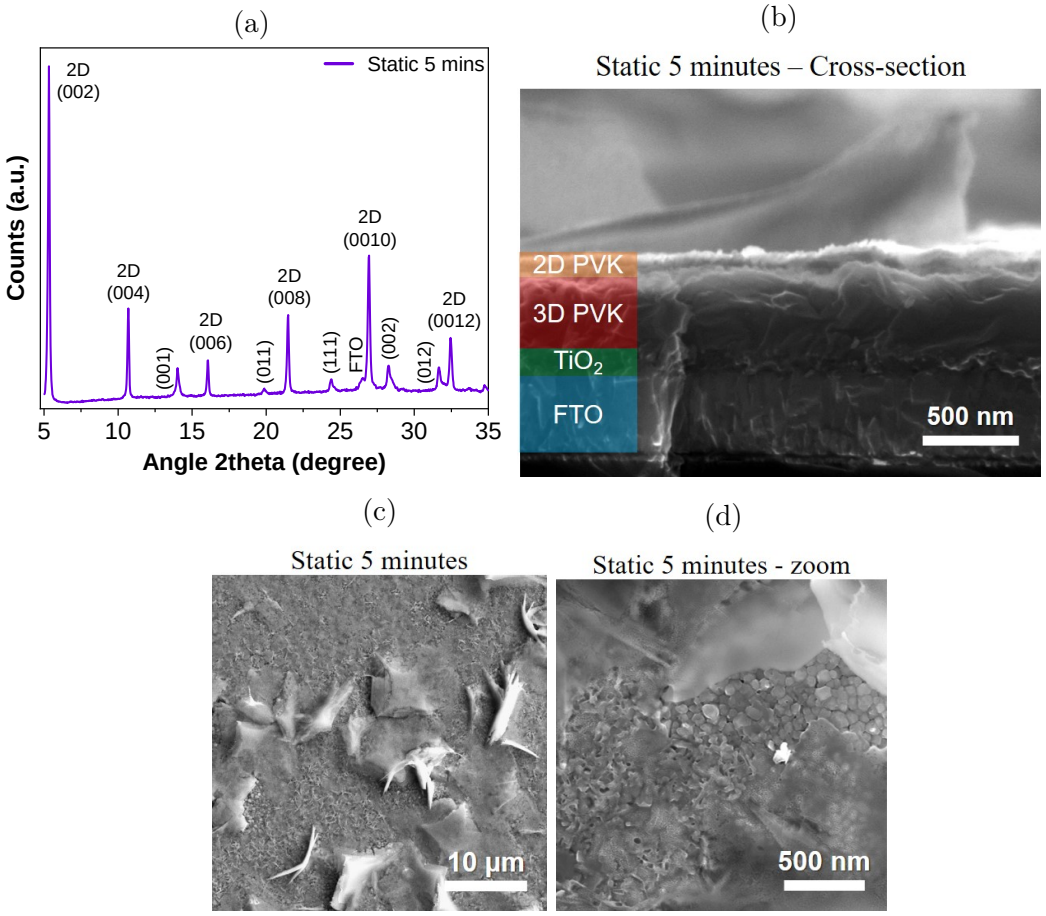

Figure A.2: (a) Diffractogram, (b) cross-section SEM image, (c) SEM surface image, and (d) SEM surface image focused on the 3D perovskite grains of a 4-FPEAI treated sample with 5 mins soaking time.

Thus, these samples seem to confirm the observations made in the soaking time study from Section 3.3. While increasing soaking can form higher 2D perovskite amount, this greater quantity comes at the expense of the homogeneity of the layer formed, if it can be designated as such.

Bibliography

[Ahn *et al.* 2015] N. Ahn, D.-Y. Son, I.-H. Jang, S. M. Kang, M. Choi and N.-G. Park. 'Highly Reproducible Perovskite Solar Cells with Average Efficiency of 18.3% and Best Efficiency of 19.7% Fabricated via Lewis Base Adduct of Lead(II) Iodide'. *Journal of the American Chemical Society*, **vol. 137**, no. 27, pp. 8696–8699 (2015) (cited p. 18)

[Akhil *et al.* 2021] S. Akhil, S. Akash, A. Pasha, B. Kulkarni, M. Jalalah, M. Alsaiari, F. A. Harraz and R. G. Balakrishna. 'Review on perovskite silicon tandem solar cells: Status and prospects 2T, 3T and 4T for real world conditions'. *Materials & Design*, **vol. 211**, p. 110138 (2021) (cited p. 14)

[Al-Ashouri *et al.* 2019] A. Al-Ashouri, A. Magomedov, M. Roß, M. Jošt, M. Talaikis, G. Chistiakova, T. Bertram, J. A. Márquez, E. Köhnen, E. Kasparavičius, S. Levcenco, L. Gil-Escrig, C. J. Hages, R. Schlatmann, B. Rech, T. Malinauskas, T. Unold, C. A. Kaufmann, L. Korte, G. Niaura, V. Getautis and S. Albrecht. 'Conformal monolayer contacts with lossless interfaces for perovskite single junction and monolithic tandem solar cells'. *Energy & Environmental Science*, **vol. 12**, no. 11, pp. 3356–3369 (2019) (cited p. 20)

[Alam and Lewis 2020] F. Alam and D. J. Lewis. 'Thin films of formamidinium lead iodide (FAPI) deposited using aerosol assisted chemical vapour deposition (AACVD)'. *Scientific Reports*, **vol. 10**, no. 1, p. 22245 (2020) (cited p. 54)

[Albero *et al.* 2016] J. Albero, A. M. Asiri and H. García. 'Influence of the composition of hybrid perovskites on their performance in solar cells'. *Journal of Materials Chemistry A*, **vol. 4**, no. 12, pp. 4353–4364 (2016) (cited p. 95)

[Anaya *et al.* 2017] M. Anaya, G. Lozano, M. E. Calvo and H. Míguez. 'ABX3 Perovskites for Tandem Solar Cells'. *Joule*, **vol. 1**, no. 4, pp. 769–793 (2017) (cited p. ix, 17)

[Andreani *et al.* 2019] L. C. Andreani, A. Bozzola, P. Kowalczewski, M. Liscidini and L. Redorici. 'Silicon solar cells: Toward the efficiency limits'. *Advances in Physics: X*, **vol. 4**, no. 1, p. 1548305 (2019) (cited p. 16)

[Ashcroft and Mermin 1976] N. W. Ashcroft and N. D. Mermin. *Solid State Physics*. Holt, Rinehart and Winston (1976). ISBN 978-0-03-083993-1 (cited p. 9)

[Azmi *et al.* 2018] R. Azmi, W. T. Hadmojo, S. Sinaga, C.-L. Lee, S. C. Yoon, I. H. Jung and S.-Y. Jang. 'High-Efficiency Low-Temperature ZnO Based Perovskite Solar Cells Based on Highly Polar, Nonwetting Self-Assembled Molecular Layers'. *Advanced Energy Materials*, **vol. 8**, no. 5, p. 1701683 (2018) (cited p. 24)

[Babayigit *et al.* 2016] A. Babayigit, A. Ethirajan, M. Muller and B. Conings. 'Toxicity of organometal halide perovskite solar cells'. *Nature Materials*, **vol. 15**, no. 3, pp. 247–251 (2016) (cited p. 24)

[Bai *et al.* 2017] Y. Bai, S. Xiao, C. Hu, T. Zhang, X. Meng, H. Lin, Y. Yang and S. Yang. 'Dimensional Engineering of a Graded 3D–2D Halide Perovskite Interface Enables Ultrahigh Voc Enhanced Stability in the p-i-n Photovoltaics'. *Advanced Energy Materials*, **vol. 7**, no. 20, p. 1701038 (2017) (cited p. 37)

[Baker *et al.* 2017] J. A. Baker, Y. Mouhamad, K. E. Hooper, D. Burkitt, M. Geoghegan and T. M. Watson. 'From spin coating to roll-to-roll: Investigating the challenge of upscaling lead halide perovskite solar cells'. *IET Renewable Power Generation*, **vol. 11**, no. 5, pp. 546–549 (2017) (cited p. 23)

[Baranowski and Plochocka 2020] M. Baranowski and P. Plochocka. 'Excitons in Metal-Halide Perovskites'. *Advanced Energy Materials*, **vol. 10**, no. 26, p. 1903659 (2020) (cited p. 17)

[Becquerel 1839] E. Becquerel. 'Mémoire sur les effets électriques produits sous l'inuence des rayons solaires'. https://gallica.bnf.fr/ark:/12148/bpt6k2968p (1839) (cited p. 8)

[Bercegol *et al.* 2018] A. Bercegol, F. J. Ramos, A. Rebai, T. Guillemot, D. Ory, J. Rousset and L. Lombez. 'Slow Diffusion and Long Lifetime in Metal Halide Perovskites for Photovoltaics'. *The Journal of Physical Chemistry C*, **vol. 122**, no. 43, pp. 24570–24577 (2018) (cited p. 16)

[Bi *et al.* 2016] D. Bi, W. Tress, M. I. Dar, P. Gao, J. Luo, C. Renevier, K. Schenk, A. Abate, F. Giordano, J.-P. Correa Baena, J.-D. Decoppet, S. M. Zakeeruddin, M. K. Nazeeruddin, M. Grätzel and A. Hagfeldt. 'Efficient luminescent solar cells based on tailored mixed-cation perovskites'. *Science Advances*, **vol. 2**, no. 1, p. e1501170 (2016) (cited p. 44)

[Blancon *et al.* 2017] J.-C. Blancon, H. Tsai, W. Nie, C. C. Stoumpos, L. Pedesseau, C. Katan, M. Kepenekian, C. M. M. Soe, K. Appavoo, M. Y. Sfeir, S. Tretiak, P. M. Ajayan, M. G. Kanatzidis, J. Even, J. J. Crochet and A. D. Mohite. 'Extremely efficient internal exciton dissociation through edge states in layered 2D perovskites'. *Science*, **vol. 355**, no. 6331, pp. 1288–1292 (2017) (cited p. ix, 28)

[Blancon *et al.* 2018] J.-C. Blancon, A. V. Stier, H. Tsai, W. Nie, C. C. Stoumpos, B. Traoré, L. Pedesseau, M. Kepenekian, F. Katsutani, G. T. Noe, J. Kono, S. Tretiak, S. A. Crooker, C. Katan, M. G. Kanatzidis, J. J. Crochet, J. Even and A. D. Mohite. 'Scaling law for excitons in 2D perovskite quantum wells'. *Nature Communications*, **vol. 9**, no. 1, p. 2254 (2018) (cited p. ix, 29, 96)

[Blancon *et al.* 2020] J.-C. Blancon, J. Even, C. C. Stoumpos, M. G. Kanatzidis and A. D. Mohite. 'Semiconductor physics of organic–inorganic 2D halide perovskites'. *Nature Nanotechnology*, **vol. 15**, no. 12, pp. 969–985 (2020) (cited p. ix, 25, 26)

[Boeglin 2022] W. Boeglin. '18. PN-Junction — Modern Lab Experiments documentation'. https://wanda.fiu.edu/boeglinw/courses/Modern_lab_manual3/pn_junction.html (2022) (cited p. viii, 11)

[Borchert *et al.* 2017] J. Borchert, R. L. Milot, J. B. Patel, C. L. Davies, A. D. Wright, L. Martínez Maestro, H. J. Snaith, L. M. Herz and M. B. Johnston. 'Large-Area, Highly Uniform Evaporated Formamidinium Lead Triiodide Thin Films for Solar Cells'. *ACS Energy Letters*, **vol. 2**, no. 12, pp. 2799–2804 (2017) (cited p. 19)

[Boriskina and Chen 2014] S. V. Boriskina and G. Chen. 'Exceeding the solar cell Shockley–Queisser limit via thermal up-conversion of low-energy photons'. *Optics Communications*, **vol. 314**, pp. 71–78 (2014) (cited p. 13)

[BP 2022] BP. 'Statistical Review of World Energy | 71st edition'. https://www.bp.com/en/global/corporate/energy-economics/statistical-review-of-world-energy.html (2022) (cited p. viii, 3)

[Brehier *et al.* 2006] A. Brehier, R. Parashkov, J. S. Lauret and E. Deleporte. 'Strong exciton-photon coupling in a microcavity containing layered perovskite semiconductors'. *Applied Physics Letters*, **vol. 89**, no. 17, p. 171110 (2006) (cited p. 24)

[Brooks and Nazeeruddin 2021] K. G. Brooks and M. K. Nazeeruddin. 'Laser Processing Methods for Perovskite Solar Cells and Modules'. *Advanced Energy Materials*, **vol. 11**, no. 29, p. 2101149 (2021) (cited p. 88)

[Bu *et al.* 2017] T. Bu, X. Liu, Y. Zhou, J. Yi, X. Huang, L. Luo, J. Xiao, Z. Ku, Y. Peng, F. Huang, Y.-B. Cheng and J. Zhong. 'A novel quadruple-cation absorber for universal hysteresis elimination for high efficiency and stable perovskite solar cells'. *Energy & Environmental Science*, **vol. 10**, no. 12, pp. 2509–2515 (2017) (cited p. 21)

[Bu *et al.* 2020] T. Bu, X. Liu, J. Li, W. Huang, Z. Wu, F. Huang, Y.-B. Cheng and J. Zhong. 'Dynamic Antisolvent Engineering for Spin Coating of 10 × 10 cm2 Perovskite Solar Module Approaching 18%'. *Solar RRL*, **vol. 4**, no. 2, p. 1900263 (2020) (cited p. 89)

[Bush *et al.* 2018] K. A. Bush, K. Frohna, R. Prasanna, R. E. Beal, T. Leijtens, S. A. Swifter and M. D. McGehee. 'Compositional Engineering for Efficient Wide Band Gap Perovskites with Improved Stability to Photoinduced Phase Segregation'. *ACS Energy Letters*, **vol. 3**, no. 2, pp. 428–435 (2018) (cited p. 110)

[Cacovich *et al.* 2020] S. Cacovich, D. Messou, A. Bercegol, S. Béchu, A. Yaiche, H. Shafique, J. Rousset, P. Schulz, M. Bouttemy and L. Lombez. 'Light-Induced Passivation in Triple Cation Mixed Halide Perovskites: Interplay between Transport Properties and Surface Chemistry'. *ACS Applied Materials & Interfaces*, **vol. 12**, no. 31, pp. 34784–34794 (2020) (cited p. 55)

[Cacovich *et al.* 2022] S. Cacovich, P. Dally, G. Vidon, M. Legrand, S. Gbegnon, J. Rousset, J.-B. Puel, J.-F. Guillemoles, P. Schulz, M. Bouttemy and A. Etcheberry. 'In-Depth Chemical and Optoelectronic Analysis of Triple-Cation Perovskite Thin Films by Combining XPS Profiling and PL Imaging'. *ACS Applied Materials & Interfaces*, **vol. 14**, no. 30, pp. 34228–34237 (2022) (cited p. 72, 73)

[Cao *et al.* 2015] D. H. Cao, C. C. Stoumpos, O. K. Farha, J. T. Hupp and M. G. Kanatzidis. '2D Homologous Perovskites as Light-Absorbing Materials for Solar Cell Applications'. *Journal of the American Chemical Society*, **vol. 137**, no. 24, pp. 7843–7850 (2015) (cited p. 30)

[Cheacharoen *et al.* 2018] R. Cheacharoen, C. C. Boyd, G. F. Burkhard, T. Leijtens, J. A. Raiford, K. A. Bush, S. F. Bent and M. D. McGehee. 'Encapsulating perovskite solar cells to withstand damp heat and thermal cycling'. *Sustainable Energy & Fuels*, **vol. 2**, no. 11, pp. 2398–2406 (2018) (cited p. 24)

[Chehade 2022] G. Chehade. *Dynamique de Recombinaison et Propriétés Excitoniques Dans Les Pérovskites Hybrides 2D*. These de doctorat, université Paris-Saclay (2022) (cited p. 66)

[Chen *et al.* 2018] A. Z. Chen, M. Shiu, J. H. Ma, M. R. Alpert, D. Zhang, B. J. Foley, D.-M. Smilgies, S.-H. Lee and J. J. Choi. 'Origin of vertical orientation in two-dimensional metal halide perovskites and its effect on photovoltaic performance'. *Nature Communications*, **vol. 9**, no. 1, p. 1336 (2018) (cited p. ix, 30)

[Chen *et al.* 2021] S. Chen, J. Zhang, J. Piao and Z. Fu. 'Ion-exchange-induced MAPbI3 thin-film 3D–2D and 3D–1D conversions: Unveiling structural transformations in films via synergistic and competitive approaches'. *New Journal of Chemistry*, **vol. 45**, no. 16, pp. 7103–7108 (2021) (cited p. 103)

[Cheng and Ding 2021] Y. Cheng and L. Ding. 'Perovskite/Si tandem solar cells: Fundamentals, advances, challenges, and novel applications'. *SusMat*, **vol. 1**, no. 3, pp. 324–344 (2021) (cited p. 14)

[Cho *et al.* 2018] K. T. Cho, G. Grancini, Y. Lee, E. Oveisi, J. Ryu, O. Almora, M. Tschumi, P. A. Schouwink, G. Seo, S. Heo, J. Park, J. Jang, S. Paek, G. Garcia-Belmonte and M. K. Nazeeruddin. 'Selective growth of layered perovskites for stable and efficient photovoltaics'. *Energy & Environmental Science*, **vol. 11**, no. 4, pp. 952–959 (2018) (cited p. 95)

[Conings *et al.* 2015] B. Conings, J. Drijkoningen, N. Gauquelin, A. Babayigit, J. D'Haen, L. D'Olieslaeger, A. Ethirajan, J. Verbeeck, J. Manca, E. Mosconi, F. D. Angelis and H.-G. Boyen. 'Intrinsic Thermal Instability of Methylammonium Lead Trihalide Perovskite'. *Advanced Energy Materials*, **vol. 5**, no. 15, p. 1500477 (2015) (cited p. 20)

[Dai *et al.* 2019] X. Dai, Y. Deng, C. H. V. Brackle and J. Huang. 'Meniscus fabrication of halide perovskite thin films at high throughput for large area and low-cost solar panels'. *International Journal of Extreme Manufacturing*, **vol. 1**, no. 2, p. 022004 (2019) (cited p. 23)

[de Holanda *et al.* 2019] M. S. de Holanda, R. Szostak, P. E. Marchezi, L. G. T. A. Duarte, J. C. Germino, T. D. Z. Atvars and A. F. Nogueira. 'In Situ 2D Perovskite Formation and the Impact of the 2D/3D Structures on Performance and Stability of Perovskite Solar Cells'. *Solar RRL*, **vol. 3**, no. 9, p. 1900199 (2019) (cited p. 116)

[de Quilettes *et al.* 2015] D. W. de Quilettes, S. M. Vorpahl, S. D. Stranks, H. Nagaoka, G. E. Eperon, M. E. Ziffer, H. J. Snaith and D. S. Ginger. 'Impact of microstructure on local carrier lifetime in perovskite solar cells'. *Science*, **vol. 348**, no. 6235, pp. 683–686 (2015) (cited p. 16)

[De Wolf *et al.* 2014] S. De Wolf, J. Holovsky, S.-J. Moon, P. Löper, B. Niesen, M. Ledinsky, F.-J. Haug, J.-H. Yum and C. Ballif. 'Organometallic Halide Perovskites: Sharp Optical Absorption Edge and Its Relation to Photovoltaic Performance'. *The Journal of Physical Chemistry Letters*, **vol. 5**, no. 6, pp. 1035–1039 (2014) (cited p. ix, 16, 17)

[DeCrescent *et al.* 2020] R. A. DeCrescent, X. Du, R. M. Kennard, N. R. Venkatesan, C. J. Dahlman, M. L. Chabinyc and J. A. Schuller. 'Even-Parity Self-Trapped Excitons Lead to Magnetic Dipole Radiation in Two-Dimensional Lead Halide Perovskites'. *ACS Nano*, **vol. 14**, no. 7, pp. 8958–8968 (2020) (cited p. 99)

[Dehghanipour *et al.* 2020] M. Dehghanipour, A. Behjat and H. A. Bioki. 'Fabrication of stable and efficient 2D/3D perovskite solar cells through post-treatment with TBABF4'. *Journal of Materials Chemistry C* (2020) (cited p. 56, 67)

[Delport *et al.* 2019] G. Delport, G. Chehade, F. Lédée, H. Diab, C. Milesi-Brault, G. Trippé-Allard, J. Even, J.-S. Lauret, E. Deleporte and D. Garrot. 'Exciton–Exciton Annihilation in Two-Dimensional Halide Perovskites at Room Temperature'. *The Journal of Physical Chemistry Letters*, **vol. 10**, no. 17, pp. 5153–5159 (2019) (cited p. 66, 94)

[Ding *et al.* 2016] X. Ding, J. Liu and T. A. L. Harris. 'A review of the operating limits in slot die coating processes'. *AIChE Journal*, **vol. 62**, no. 7, pp. 2508–2524 (2016) (cited p. 23)

[Ding *et al.* 2022] G. Ding, Y. Zheng, X. Xiao, H. Cheng, G. Zhang, Y. Shi and Y. Shao. 'Sustainable development of perovskite solar cells: Keeping a balance between toxicity and efficiency'. *Journal of Materials Chemistry A*, **vol. 10**, no. 15, pp. 8159–8171 (2022) (cited p. 24)

[Dolzhenko *et al.* 1986] Y. I. Dolzhenko, T. Inabe and Y. Maruyama. 'In Situ X-Ray Observation on the Intercalation of Weak Interaction Molecules into Perovskite-Type Layered Crystals (C9H19NH3)2PbI4 and (C10H21NH3)2CdCl4'. *Bulletin of the Chemical Society of Japan*, **vol. 59**, no. 2, pp. 563–567 (1986) (cited p. 24)

[Domanski *et al.* 2016] K. Domanski, J.-P. Correa-Baena, N. Mine, M. K. Nazeeruddin, A. Abate, M. Saliba, W. Tress, A. Hagfeldt and M. Grätzel. 'Not All That Glitters Is Gold: Metal-Migration-Induced Degradation in Perovskite Solar Cells'. *ACS Nano*, **vol. 10**, no. 6, pp. 6306–6314 (2016) (cited p. 23)

[Draguta *et al.* 2017] S. Draguta, O. Sharia, S. J. Yoon, M. C. Brennan, Y. V. Morozov, J. S. Manser, P. V. Kamat, W. F. Schneider and M. Kuno. 'Rationalizing the light-induced phase separation of mixed halide organic–inorganic perovskites'. *Nature Communications*, **vol. 8**, no. 1, p. 200 (2017) (cited p. 52)

[Duong *et al.* 2017] T. Duong, H. K. Mulmudi, Y. Wu, X. Fu, H. Shen, J. Peng, N. Wu, H. T. Nguyen, D. Macdonald, M. Lockrey, T. P. White, K. Weber and K. Catchpole. 'Light and Electrically Induced Phase Segregation and Its Impact on the Stability of Quadruple Cation High Bandgap Perovskite Solar Cells'. *ACS Applied Materials & Interfaces*, **vol. 9**, no. 32, pp. 26859–26866 (2017) (cited p. 21)

[Egger *et al.* 2016] D. A. Egger, A. M. Rappe and L. Kronik. 'Hybrid Organic–Inorganic Perovskites on the Move'. *Accounts of Chemical Research*, **vol. 49**, no. 3, pp. 573–581 (2016) (cited p. 15)

[Ehrler *et al.* 2020] B. Ehrler, E. Alarcón-Lladó, S. W. Tabernig, T. Veeken, E. C. Garnett and A. Polman. 'Photovoltaics Reaching for the Shockley–Queisser Limit'. *ACS Energy Letters*, **vol. 5**, no. 9, pp. 3029–3033 (2020) (cited p. viii, 13)

[Eperon *et al.* 2014] G. E. Eperon, S. D. Stranks, C. Menelaou, M. B. Johnston, L. M. Herz and H. J. Snaith. 'Formamidinium lead trihalide: A broadly tunable perovskite for efficient planar heterojunction solar cells'. *Energy & Environmental Science*, **vol. 7**, no. 3, pp. 982–988 (2014) (cited p. 20, 95)

[Even *et al.* 2012] J. Even, L. Pedesseau, M.-A. Dupertuis, J.-M. Jancu and C. Katan. 'Electronic model for self-assembled hybrid organic/perovskite semiconductors: Reverse band edge electronic states ordering and spin-orbit coupling'. *Physical Review B*, **vol. 86**, no. 20, p. 205301 (2012) (cited p. 99)

[Fournier 2021] O. Fournier. *Synthèse Par ALD et Caractérisation de Couches Extractrices d'électrons Pour Application Dans Les Cellules Solaires à Base de Pérovskite.* These de doctorat, Université Paris sciences et lettres (2021) (cited p. 42)

[Fox 2002] M. Fox. 'Optical Properties of Solids'. *American Journal of Physics*, **vol. 70**, no. 12, pp. 1269–1270 (2002) (cited p. ix, 27)

[Frenkel 1931] J. Frenkel. 'On the Transformation of light into Heat in Solids. I'. *Physical Review*, **vol. 37**, no. 1, pp. 17–44 (1931) (cited p. 27)

[Fu *et al.* 2019] Z. Fu, M. Xu, Y. Sheng, Z. Yan, J. Meng, C. Tong, D. Li, Z. Wan, Y. Ming, A. Mei, Y. Hu, Y. Rong and H. Han. 'Encapsulation of Printable Mesoscopic Perovskite Solar Cells Enables High Temperature and Long-Term Outdoor Stability'. *Advanced Functional Materials*, **vol. 29**, no. 16, p. 1809129 (2019) (cited p. 24)

[Fu *et al.* 2021] W. Fu, H. Chen and A. K. Y. Jen. 'Two-dimensional perovskites for photovoltaics'. *Materials Today Nano*, **vol. 14**, p. 100117 (2021) (cited p. ix, x, 26, 32, 34)

[Galkowski *et al.* 2016] K. Galkowski, A. Mitioglu, A. Miyata, P. Plochocka, O. Portugall, G. E. Eperon, J. Tse-Wei Wang, T. Stergiopoulos, S. D. Stranks, H. J. Snaith and R. J. Nicholas. 'Determination of the exciton binding energy and effective masses for methylammonium and formamidinium lead tri-halide perovskite semiconductors'. *Energy & Environmental Science*, **vol. 9**, no. 3, pp. 962–970 (2016) (cited p. 27)

[Gao *et al.* 2019] Y. Gao, E. Shi, S. Deng, S. B. Shiring, J. M. Snaider, C. Liang, B. Yuan, R. Song, S. M. Janke, A. Liebman-Peláez, P. Yoo, M. Zeller, B. W. Boudouris, P. Liao, C. Zhu, V. Blum, Y. Yu, B. M. Savoie, L. Huang and L. Dou. 'Molecular engineering of organic–inorganic hybrid perovskites quantum wells'. *Nature Chemistry*, **vol. 11**, no. 12, pp. 1151–1157 (2019) (cited p. 28)

[Gao *et al.* 2020] X.-X. Gao, W. Luo, Y. Zhang, R. Hu, B. Zhang, A. Züttel, Y. Feng and M. K. Nazeeruddin. 'Stable and High-Efficiency Methylammonium-Free Perovskite Solar Cells'. *Advanced Materials*, **vol. 32**, no. 9, p. 1905502 (2020) (cited p. 20)

[Gatti *et al.* 2017] T. Gatti, E. Menna, M. Meneghetti, M. Maggini, A. Petrozza and F. Lamberti. 'The Renaissance of fullerenes with perovskite solar cells'. *Nano Energy*, **vol. 41**, pp. 84–100 (2017) (cited p. 20)

[Gautam *et al.* 2020] S. K. Gautam, M. Kim, D. R. Miquita, J.-E. Bourée, B. Geffroy and O. Plantevin. 'Reversible Photoinduced Phase Segregation and Origin of Long Carrier Lifetime in Mixed-Halide Perovskite Films'. *Advanced Functional Materials*, **vol. 30**, no. 28, p. 2002622 (2020) (cited p. 52)

[Geisz *et al.* 2020] J. F. Geisz, R. M. France, K. L. Schulte, M. A. Steiner, A. G. Norman, H. L. Guthrey, M. R. Young, T. Song and T. Moriarty. 'Six-junction III–V solar cells with 47.1% conversion efficiency under 143 Suns concentration'. *Nature Energy*, **vol. 5**, no. 4, pp. 326–335 (2020) (cited p. 14)

[Gharibzadeh *et al.* 2019] S. Gharibzadeh, B. Abdollahi Nejand, M. Jakoby, T. Abzieher, D. Hauschild, S. Moghadamzadeh, J. A. Schwenzer, P. Brenner, R. Schmager, A. A. Haghighirad, L. Weinhardt, U. Lemmer, B. S. Richards, I. A. Howard and U. W. Paetzold. 'Record Open-Circuit Voltage Wide-Bandgap Perovskite Solar Cells Utilizing 2D/3D Perovskite Heterostructure'. *Advanced Energy Materials*, **vol. 9**, no. 21, p. 1803699 (2019) (cited p. 36)

[Goldschmidt 1926] V. M. Goldschmidt. 'Die Gesetze der Krystallochemie'. *Naturwissenschaften*, **vol. 14**, no. 21, pp. 477–485 (1926) (cited p. 15)

[Grancini *et al.* 2017] G. Grancini, C. Roldán-Carmona, I. Zimmermann, E. Mosconi, X. Lee, D. Martineau, S. Narbey, F. Oswald, F. De Angelis, M. Graetzel and M. K. Nazeeruddin. 'One-Year stable perovskite solar cells by 2D/3D interface engineering'. *Nature Communications*, **vol. 8**, p. 15684 (2017) (cited p. 35)

[Green *et al.* 2022] M. A. Green, E. D. Dunlop, J. Hohl-Ebinger, M. Yoshita, N. Kopidakis, K. Bothe, D. Hinken, M. Rauer and X. Hao. 'Solar cell efficiency tables (Version 60)'. *Progress in Photovoltaics: Research and Applications*, **vol. 30**, no. 7, pp. 687–701 (2022) (cited p. 4, 18, 21, 23)

[Gribov and Zinov'ev 2003] B. G. Gribov and K. V. Zinov'ev. 'Preparation of High-Purity Silicon for Solar Cells'. *Inorganic Materials*, **vol. 39**, no. 7, pp. 653–662 (2003) (cited p. 17)

[Hawash *et al.* 2018] Z. Hawash, L. K. Ono and Y. Qi. 'Recent Advances in Spiro-MeOTAD Hole Transport Material and Its Applications in Organic–Inorganic Halide Perovskite Solar Cells'. *Advanced Materials Interfaces*, **vol. 5**, no. 1, p. 1700623 (2018) (cited p. 47)

[He *et al.* 2020] Q. He, M. Worku, L. Xu, C. Zhou, H. Lin, A. J. Robb, K. Hanson, Y. Xin and B. Ma. 'Facile Formation of 2D–3D Heterojunctions on Perovskite Thin Film Surfaces for Efficient Solar Cells'. *ACS Applied Materials & Interfaces*, **vol. 12**, no. 1, pp. 1159–1168 (2020) (cited p. 67)

[Heo *et al.* 2016] J. H. Heo, M. H. Lee, M. H. Jang and S. H. Im. 'Highly efficient CH3NH3PbI3-xClx mixed halide perovskite solar cells prepared by re-dissolution and crystal grain growth via spray coating'. *Journal of Materials Chemistry A*, **vol. 4**, no. 45, pp. 17636–17642 (2016) (cited p. 23)

[Hirst and Ekins-Daukes 2011] L. C. Hirst and N. J. Ekins-Daukes. 'Fundamental losses in solar cells'. *Progress in Photovoltaics: Research and Applications*, **vol. 19**, no. 3, pp. 286–293 (2011) (cited p. viii, 13)

[Hong *et al.* 1992] X. Hong, T. Ishihara and A. V. Nurmikko. 'Dielectric confinement effect on excitons in ${\mathrm{PbI}}_{4}$-based layered semiconductors'. *Physical Review B*, **vol. 45**, no. 12, pp. 6961–6964 (1992) (cited p. 29)

[Hossain *et al.* 2020] M. A. Hossain, K. T. Khoo, X. Cui, G. K. Poduval, T. Zhang, X. Li, W. M. Li and B. Hoex. 'Atomic layer deposition enabling higher efficiency solar cells: A review'. *Nano Materials Science*, **vol. 2**, no. 3, pp. 204–226 (2020) (cited p. 42)

[Howard *et al.* 2019] I. A. Howard, T. Abzieher, I. M. Hossain, H. Eggers, F. Schackmar, S. Ternes, B. S. Richards, U. Lemmer and U. W. Paetzold. 'Coated and Printed Perovskites for Photovoltaic Applications'. *Advanced Materials*, **vol. 31**, no. 26, p. 1806702 (2019) (cited p. 77)

[Hoye *et al.* 2022] R. L. Z. Hoye, J. Hidalgo, R. A. Jagt, J.-P. Correa-Baena, T. Fix and J. L. MacManus-Driscoll. 'The Role of Dimensionality on the Optoelectronic Properties of Oxide and Halide Perovskites, and their Halide Derivatives'. *Advanced Energy Materials*, **vol. 12**, no. 4, p. 2100499 (2022) (cited p. 29)

[Hu *et al.* 2016a] H. Hu, B. Dong, H. Hu, F. Chen, M. Kong, Q. Zhang, T. Luo, L. Zhao, Z. Guo, J. Li, Z. Xu, S. Wang, D. Eder and L. Wan. 'Atomic Layer Deposition of TiO2 for a High-Efficiency Hole-Blocking Layer in Hole-Conductor-Free Perovskite Solar Cells Processed in Ambient Air'. *ACS Applied Materials & Interfaces*, **vol. 8**, no. 28, pp. 17999–18007 (2016) (cited p. x, 43)

[Hu *et al.* 2016b] Y. Hu, J. Schlipf, M. Wussler, M. L. Petrus, W. Jaegermann, T. Bein, P. Müller-Buschbaum and P. Docampo. 'Hybrid Perovskite/Perovskite Heterojunction Solar Cells'. *ACS Nano*, **vol. 10**, no. 6, pp. 5999–6007 (2016) (cited p. 36)

[Hu *et al.* 2018] L. Hu, M. Li, K. Yang, Z. Xiong, B. Yang, M. Wang, X. Tang, Z. Zang, X. Liu, B. Li, Z. Xiao, S. Lu, H. Gong, J. Ouyang and K. Sun. 'PEDOT:PSS monolayers to enhance the hole extraction and stability of perovskite solar cells'. *Journal of Materials Chemistry A*, **vol. 6**, no. 34, pp. 16583–16589 (2018) (cited p. 20)

[Huang *et al.* 2018a] W. Huang, S. Sadhu, P. Sapkota and S. Ptasinska. 'In situ identification of cation-exchange-induced reversible transformations of 3D and 2D perovskites'. *Chemical Communications*, **vol. 54**, no. 46, pp. 5879–5882 (2018) (cited p. 103)

[Huang *et al.* 2018b] W. Huang, Y. Wang and S. K. Balakrishnan. 'Controllable transformation between 3D and 2D perovskites through cation exchange'. *Chemical Communications*, **vol. 54**, no. 57, pp. 7944–7947 (2018) (cited p. 103)

[Huang *et al.* 2019] Z. Huang, A. H. Proppe, H. Tan, M. I. Saidaminov, F. Tan, A. Mei, C.-S. Tan, M. Wei, Y. Hou, H. Han, S. O. Kelley and E. H. Sargent. 'Suppressed Ion Migration in Reduced-Dimensional Perovskites Improves Operating Stability'. *ACS Energy Letters*, **vol. 4**, no. 7, pp. 1521–1527 (2019) (cited p. 87)

[IEA 2021a] IEA. 'Global Energy Review 2021'. https://www.iea.org/reports/global-energy-review-2021 (2021) (cited p. viii, 2)

[IEA 2021b] IEA. 'Key World Energy Statistics 2021'. https://www.iea.org/reports/key-world-energy-statistics-2021 (2021) (cited p. viii, 1, 2)

[IEA 2021c] IEA. 'Net Zero by 2050'. https://www.iea.org/reports/net-zero-by-2050 (2021) (cited p. viii, 2, 4)

[IEA 2022a] IEA. 'Solar PV'. https://www.iea.org/reports/solar-pv (2022) (cited p. 8)

[IEA 2022b] IEA. 'World Energy Outlook 2022'. https://www.iea.org/reports/world-energy-outlook-2022 (2022) (cited p. 2)

[IPCC 2018] IPCC. 'Global Warming of 1.5 ºC'. https://www.ipcc.ch/sr15/ (2018) (cited p. 1)

[Ishihara *et al.* 1989] T. Ishihara, J. Takahashi and T. Goto. 'Exciton state in two-dimensional perovskite semiconductor (C10H21NH3)2PbI4'. *Solid State Communications*, **vol. 69**, no. 9, pp. 933–936 (1989) (cited p. 24)

[Jacobsson *et al.* 2016] T. J. Jacobsson, J.-P. Correa-Baena, E. Halvani Anaraki, B. Philippe, S. D. Stranks, M. E. F. Bouduban, W. Tress, K. Schenk, J. Teuscher, J.-E. Moser, H. Rensmo and A. Hagfeldt. 'Unreacted PbI2 as a Double-Edged Sword for Enhancing the Performance of Perovskite Solar Cells'. *Journal of the American Chemical Society*, **vol. 138**, no. 32, pp. 10331–10343 (2016) (cited p. 44)

[Jacobsson *et al.* 2022] T. J. Jacobsson, A. Hultqvist, A. García-Fernández, A. Anand, A. Al-Ashouri, A. Hagfeldt, A. Crovetto, A. Abate, A. G. Ricciardulli, A. Vijayan, A. Kulkarni, A. Y. Anderson, B. P. Darwich, B. Yang, B. L. Coles, C. A. R. Perini, C. Rehermann, D. Ramirez, D. Fairen-Jimenez, D. Di Girolamo, D. Jia, E. Avila, E. J. Juarez-Perez, F. Baumann, F. Mathies, G. S. A. González, G. Boschloo, G. Nasti, G. Paramasivam, G. Martínez-Denegri, H. Näsström, H. Michaels, H. Köbler, H. Wu, I. Benesperi, M. I. Dar, I. Bayrak Pehlivan, I. E. Gould, J. N. Vagott, J. Dagar, J. Kettle, J. Yang, J. Li, J. A. Smith, J. Pascual, J. J. Jerónimo-Rendón, J. F. Montoya, J.-P. Correa-Baena, J. Qiu, J. Wang, K. Sveinbjörnsson, K. Hirselandt, K. Dey, K. Frohna, L. Mathies, L. A. Castriotta, M. H. Aldamasy, M. Vasquez-Montoya, M. A. Ruiz-Preciado, M. A. Flatken, M. V. Khenkin, M. Grischek, M. Kedia, M. Saliba, M. Anaya, M. Veldhoen, N. Arora, O. Shargaieva, O. Maus, O. S. Game, O. Yudilevich, P. Fassl, Q. Zhou, R. Betancur, R. Munir, R. Patidar, S. D. Stranks, S. Alam, S. Kar, T. Unold, T. Abzieher, T. Edvinsson, T. W. David, U. W. Paetzold, W. Zia, W. Fu, W. Zuo, V. R. F. Schröder, W. Tress, X. Zhang, Y.-H. Chiang, Z. Iqbal, Z. Xie and E. Unger. 'An open-access database and analysis tool for perovskite solar cells based on the FAIR data principles'. *Nature Energy*, **vol. 7**, no. 1, pp. 107–115 (2022) (cited p. ix, 21, 22)

[Jang *et al.* 2015] D. M. Jang, K. Park, D. H. Kim, J. Park, F. Shojaei, H. S. Kang, J.-P. Ahn, J. W. Lee and J. K. Song. 'Reversible Halide Exchange Reaction of Organometal Trihalide Perovskite Colloidal Nanocrystals for Full-Range Band Gap Tuning'. *Nano Letters*, **vol. 15**, no. 8, pp. 5191–5199 (2015) (cited p. 17)

[Jemli 2016] K. Jemli. *Synthése et Auto-Assemblage de Molécules de Pérovskite Pour La Photonique et Le Marquage*. Ph.D. thesis, Université Paris Saclay (COmUE) ; Faculté des sciences de Bizerte (Tunisie) (2016) (cited p. 95, 99)

[Jemli *et al.* 2015] K. Jemli, P. Audebert, L. Galmiche, G. Trippé-Allard, D. Garrot, J.-S. Lauret and E. Deleporte. 'Two-Dimensional Perovskite Activation with an Organic Luminophore'. *ACS Applied Materials & Interfaces*, **vol. 7**, no. 39, pp. 21763–21769 (2015) (cited p. 26)

[Jeon *et al.* 2014] N. J. Jeon, J. H. Noh, Y. C. Kim, W. S. Yang, S. Ryu and S. I. Seok. 'Solvent engineering for high-performance inorganic–organic hybrid perovskite solar cells'. *Nature Materials*, **vol. 13**, no. 9, pp. 897–903 (2014) (cited p. 18)

[Jeon *et al.* 2015] N. J. Jeon, J. H. Noh, W. S. Yang, Y. C. Kim, S. Ryu, J. Seo and S. I. Seok. 'Compositional engineering of perovskite materials for high-performance solar cells'. *Nature*, **vol. 517**, no. 7535, pp. 476–480 (2015) (cited p. 44)

[Jeong *et al.* 2020] M. Jeong, I. W. Choi, E. M. Go, Y. Cho, M. Kim, B. Lee, S. Jeong, Y. Jo, H. W. Choi, J. Lee, J.-H. Bae, S. K. Kwak, D. S. Kim and C. Yang. 'Stable perovskite solar cells with efficiency exceeding 24.8% and 0.3-V voltage loss'. *Science*, **vol. 369**, no. 6511, pp. 1615–1620 (2020) (cited p. 34, 116)

[Jesper Jacobsson *et al.* 2016] T. Jesper Jacobsson, J.-P. Correa-Baena, M. Pazoki, M. Saliba, K. Schenk, M. Grätzel and A. Hagfeldt. 'Exploration of the compositional space for mixed lead halogen perovskites for high efficiency solar cells'. *Energy & Environmental Science*, **vol. 9**, no. 5, pp. 1706–1724 (2016) (cited p. 54, 101)

[Jiang *et al.* 2019a] Q. Jiang, Y. Zhao, X. Zhang, X. Yang, Y. Chen, Z. Chu, Q. Ye, X. Li, Z. Yin and J. You. 'Surface passivation of perovskite film for efficient solar cells'. *Nature Photonics*, **vol. 13**, no. 7, pp. 460–466 (2019) (cited p. 38, 63, 74)

[Jiang *et al.* 2019b] Y. Jiang, L. Qiu, E. J. Juarez-Perez, L. K. Ono, Z. Hu, Z. Liu, Z. Wu, L. Meng, Q. Wang and Y. Qi. 'Reduction of lead leakage from damaged lead halide perovskite solar modules using self-healing polymer-based encapsulation'. *Nature Energy*, **vol. 4**, no. 7, pp. 585–593 (2019) (cited p. 24)

[Jiang *et al.* 2020] X. Jiang, F. Wang, Q. Wei, H. Li, Y. Shang, W. Zhou, C. Wang, P. Cheng, Q. Chen, L. Chen and Z. Ning. 'Ultra-high open-circuit voltage of tin perovskite solar cells via an electron transporting layer design'. *Nature Communications*, **vol. 11**, no. 1, p. 1245 (2020) (cited p. 20)

[Jiang *et al.* 2021] X. Jiang, S. Chen, Y. Li, L. Zhang, N. Shen, G. Zhang, J. Du, N. Fu and B. Xu. 'Direct Surface Passivation of Perovskite Film by 4-Fluorophenethylammonium Iodide toward Stable and Efficient Perovskite Solar Cells'. *ACS Applied Materials & Interfaces*, **vol. 13**, no. 2, pp. 2558–2565 (2021) (cited p. 38)

[Jordan *et al.* 2016] D. C. Jordan, S. R. Kurtz, K. VanSant and J. Newmiller. 'Compendium of photovoltaic degradation rates'. *Progress in Photovoltaics: Research and Applications*, **vol. 24**, no. 7, pp. 978–989 (2016) (cited p. 23)

[Juarez-Perez *et al.* 2019] E. J. Juarez-Perez, L. K. Ono and Y. Qi. 'Thermal degradation of formamidinium based lead halide perovskites into sym-triazine and hydrogen cyanide observed by coupled thermogravimetry-mass spectrometry analysis'. *Journal of Materials Chemistry A*, **vol. 7**, no. 28, pp. 16912–16919 (2019) (cited p. 20)

[Jung *et al.* 2019] M. Jung, S.-G. Ji, G. Kim and S. I. Seok. 'Perovskite precursor solution chemistry: From fundamentals to photovoltaic applications'. *Chemical Society Reviews*, **vol. 48**, no. 7, pp. 2011–2038 (2019) (cited p. 18)

[Kahmann *et al.* 2020] S. Kahmann, E. K. Tekelenburg, H. Duim, M. E. Kamminga and M. A. Loi. 'Extrinsic nature of the broad photoluminescence in lead iodide-based Ruddlesden–Popper perovskites'. *Nature Communications*, **vol. 11**, no. 1, p. 2344 (2020) (cited p. 99)

[Karunakaran *et al.* 2019] S. K. Karunakaran, G. M. Arumugam, W. Yang, S. Ge, S. N. Khan, X. Lin and G. Yang. 'Recent progress in inkjet-printed solar cells'. *Journal of Materials Chemistry A*, **vol. 7**, no. 23, pp. 13873–13902 (2019) (cited p. 23)

[Ke *et al.* 2017] W. Ke, C. C. Stoumpos, I. Spanopoulos, L. Mao, M. Chen, M. R. Wasielewski and M. G. Kanatzidis. 'Efficient Lead-Free Solar Cells Based on Hollow {en}MASnI3 Perovskites'. *Journal of the American Chemical Society*, **vol. 139**, no. 41, pp. 14800–14806 (2017) (cited p. 17)

[Khenkin *et al.* 2020] M. V. Khenkin, E. A. Katz, A. Abate, G. Bardizza, J. J. Berry, C. Brabec, F. Brunetti, V. Bulović, Q. Burlingame, A. Di Carlo, R. Cheacharoen, Y.-B. Cheng, A. Colsmann, S. Cros, K. Domanski, M. Dusza, C. J. Fell, S. R. Forrest, Y. Galagan, D. Di Girolamo, M. Grätzel, A. Hagfeldt, E. von Hauff, H. Hoppe, J. Kettle, H. Köbler, M. S. Leite, S. F. Liu, Y.-L. Loo, J. M. Luther, C.-Q. Ma, M. Madsen, M. Manceau, M. Matheron, M. McGehee, R. Meitzner, M. K. Nazeeruddin, A. F. Nogueira, Ç. Odabaşı, A. Osherov, N.-G. Park, M. O. Reese, F. De Rossi, M. Saliba, U. S. Schubert, H. J. Snaith, S. D. Stranks, W. Tress, P. A. Troshin, V. Turkovic, S. Veenstra, I. Visoly-Fisher, A. Walsh, T. Watson, H. Xie, R. Yıldırım, S. M. Zakeeruddin, K. Zhu and M. Lira-Cantu. 'Consensus statement for stability assessment and reporting for perovskite photovoltaics based on ISOS procedures'. *Nature Energy*, **vol. 5**, no. 1, pp. 35–49 (2020) (cited p. 23)

[Kieslich *et al.* 2014] G. Kieslich, S. Sun and A. K. Cheetham. 'Solid-state principles applied to organic–inorganic perovskites: New tricks for an old dog'. *Chemical Science*, **vol. 5**, no. 12, pp. 4712–4715 (2014) (cited p. 15)

[Kim *et al.* 2012] H.-S. Kim, C.-R. Lee, J.-H. Im, K.-B. Lee, T. Moehl, A. Marchioro, S.-J. Moon, R. Humphry-Baker, J.-H. Yum, J. E. Moser, M. Grätzel and N.-G. Park. 'Lead Iodide Perovskite Sensitized All-Solid-State Submicron Thin Film Mesoscopic Solar Cell with Efficiency Exceeding 9%'. *Scientific Reports*, **vol. 2**, no. 1, p. 591 (2012) (cited p. 18)

[Kim *et al.* 2014] J. Kim, S.-H. Lee, J. H. Lee and K.-H. Hong. 'The Role of Intrinsic Defects in Methylammonium Lead Iodide Perovskite'. *The Journal of Physical Chemistry Letters*, **vol. 5**, no. 8, pp. 1312–1317 (2014) (cited p. 17)

[Kim *et al.* 2016] H. Kim, K.-G. Lim and T.-W. Lee. 'Planar heterojunction organometal halide perovskite solar cells: Roles of interfacial layers'. *Energy & Environmental Science*, **vol. 9**, no. 1, pp. 12–30 (2016) (cited p. 15)

[Kim *et al.* 2019a] H. Kim, K. A. Huynh, S. Y. Kim, Q. V. Le and H. W. Jang. '2D and Quasi-2D Halide Perovskites: Applications and Progress'. *physica status solidi (RRL) – Rapid Research Letters*, **vol. n/a**, no. n/a, p. 1900435 (2019) (cited p. 45)

[Kim *et al.* 2019b] H. Kim, S.-U. Lee, D. Y. Lee, M. J. Paik, H. Na, J. Lee and S. I. Seok. 'Optimal Interfacial Engineering with Different Length of Alkylammonium Halide for Efficient and Stable Perovskite Solar Cells'. *Advanced Energy Materials*, **vol. 9**, no. 47, p. 1902740 (2019) (cited p. 116, 123)

[Kim *et al.* 2019c] M. Kim, G.-H. Kim, T. K. Lee, I. W. Choi, H. W. Choi, Y. Jo, Y. J. Yoon, J. W. Kim, J. Lee, D. Huh, H. Lee, S. K. Kwak, J. Y. Kim and D. S.

Kim. 'Methylammonium Chloride Induces Intermediate Phase Stabilization for Efficient Perovskite Solar Cells'. *Joule*, **vol. 3**, no. 9, pp. 2179–2192 (2019) (cited p. 24)

[Kim *et al.* 2020a] B. Kim, J. Kim and N. Park. 'First-principles identification of the charge-shifting mechanism and ferroelectricity in hybrid halide perovskites'. *Scientific Reports*, **vol. 10**, no. 1, p. 19635 (2020) (cited p. viii, 15, 16)

[Kim *et al.* 2020b] D. Kim, H. J. Jung, I. J. Park, B. W. Larson, S. P. Dunfield, C. Xiao, J. Kim, J. Tong, P. Boonmongkolras, S. G. Ji, F. Zhang, S. R. Pae, M. Kim, S. B. Kang, V. Dravid, J. J. Berry, J. Y. Kim, K. Zhu, D. H. Kim and B. Shin. 'Efficient, stable silicon tandem cells enabled by anion-engineered wide-bandgap perovskites'. *Science*, **vol. 368**, no. 6487, pp. 155–160 (2020) (cited p. 36)

[Kim *et al.* 2021] E.-B. Kim, M. S. Akhtar, H.-S. Shin, S. Ameen and M. K. Nazeeruddin. 'A review on two-dimensional (2D) and 2D-3D multidimensional perovskite solar cells: Perovskites structures, stability, and photovoltaic performances'. *Journal of Photochemistry and Photobiology C: Photochemistry Reviews*, **vol. 48**, p. 100405 (2021) (cited p. 65, 87)

[Klampaftis *et al.* 2009] E. Klampaftis, D. Ross, K. R. McIntosh and B. S. Richards. 'Enhancing the performance of solar cells via luminescent down-shifting of the incident spectrum: A review'. *Solar Energy Materials and Solar Cells*, **vol. 93**, no. 8, pp. 1182–1194 (2009) (cited p. 13)

[Kojima *et al.* 2009] A. Kojima, K. Teshima, Y. Shirai and T. Miyasaka. 'Organometal Halide Perovskites as Visible-Light Sensitizers for Photovoltaic Cells'. *Journal of the American Chemical Society*, **vol. 131**, no. 17, pp. 6050–6051 (2009) (cited p. 4, 18)

[Kost *et al.* 2021] C. Kost, S. Shammugam, V. Fluri, D. Peper, A. Davoodi Memar and T. Schlegl. 'Study: Levelized Cost of Electricity - Renewable Energy Technologies - Fraunhofer ISE'. https://www.ise.fraunhofer.de/en/publications/studies/cost-of-electricity.html (2021) (cited p. 3)

[Kwon *et al.* 2014] Y. S. Kwon, J. Lim, H.-J. Yun, Y.-H. Kim and T. Park. 'A diketopyrrolopyrrole-containing hole transporting conjugated polymer for use in efficient stable organic–inorganic hybrid solar cells based on a perovskite'. *Energy & Environmental Science*, **vol. 7**, no. 4, pp. 1454–1460 (2014) (cited p. 23)

[La-Placa *et al.* 2019] M.-G. La-Placa, L. Gil-Escrig, D. Guo, F. Palazon, T. J. Savenije, M. Sessolo and H. J. Bolink. 'Vacuum-Deposited 2D/3D Perovskite Heterojunctions'. *ACS Energy Letters*, pp. 2893–2901 (2019) (cited p. 37, 74)

[Lai *et al.* 2020] H. Lai, D. Lu, Z. Xu, N. Zheng, Z. Xie and Y. Liu. 'Organic-Salt-Assisted Crystal Growth and Orientation of Quasi-2D Ruddlesden–Popper Perovskites for Solar Cells with Efficiency over 19%'. *Advanced Materials*, **vol. 32**, no. 33, p. 2001470 (2020) (cited p. 32)

[Lal *et al.* 2017] N. N. Lal, Y. Dkhissi, W. Li, Q. Hou, Y.-B. Cheng and U. Bach. 'Perovskite Tandem Solar Cells'. *Advanced Energy Materials*, **vol. 7**, no. 18, p. 1602761 (2017) (cited p. viii, 14)

[Lamberti *et al.* 2019] F. Lamberti, T. Gatti, E. Cescon, R. Sorrentino, A. Rizzo, E. Menna, G. Meneghesso, M. Meneghetti, A. Petrozza and L. Franco. 'Evidence of Spiro-OMeTAD De-doping by tert-Butylpyridine Additive in Hole-Transporting Layers for Perovskite Solar Cells'. *Chem*, **vol. 5**, no. 7, pp. 1806–1817 (2019) (cited p. 47)

[Lanty *et al.* 2014] G. Lanty, K. Jemli, Y. Wei, J. Leymarie, J. Even, J.-S. Lauret and E. Deleporte. 'Room-Temperature Optical Tunability and Inhomogeneous Broadening in 2D-Layered Organic–Inorganic Perovskite Pseudobinary Alloys'. *The Journal of Physical Chemistry Letters*, **vol. 5**, no. 22, pp. 3958–3963 (2014) (cited p. 29, 94, 95, 99, 100)

[Ledee 2018] F. Ledee. *Cristallisation et Fonctionnalisation de Pérovskites Hybrides Halogénées à 2-Dimensions Pour Le Photovoltaïque et l'émission de Lumière*. Ph.D. thesis, Université Paris-Saclay (2018) (cited p. 63, 99)

[Lédée *et al.* 2017] F. Lédée, G. Trippé-Allard, H. Diab, P. Audebert, D. Garrot, J.-S. Lauret and E. Deleporte. 'Fast growth of monocrystalline thin films of 2D layered hybrid perovskite'. *CrystEngComm*, **vol. 19**, no. 19, pp. 2598–2602 (2017) (cited p. 46)

[Lee *et al.* 2012] M. M. Lee, J. Teuscher, T. Miyasaka, T. N. Murakami and H. J. Snaith. 'Efficient Hybrid Solar Cells Based on Meso-Superstructured Organometal Halide Perovskites'. *Science*, **vol. 338**, no. 6107, pp. 643–647 (2012) (cited p. 16, 18)

[Lee *et al.* 2014] J.-W. Lee, D.-J. Seol, A.-N. Cho and N.-G. Park. 'High-Efficiency Perovskite Solar Cells Based on the Black Polymorph of HC(NH2)2PbI3'. *Advanced Materials*, **vol. 26**, no. 29, pp. 4991–4998 (2014) (cited p. 20)

[Lee *et al.* 2019] J.-W. Lee, S.-G. Kim, J.-M. Yang, Y. Yang and N.-G. Park. 'Verification and mitigation of ion migration in perovskite solar cells'. *APL Materials*, **vol. 7**, no. 4, p. 041111 (2019) (cited p. 23)

[Lee *et al.* 2021] H. B. Lee, N. Kumar, B. Tyagi, S. He, R. Sahani and J.-W. Kang. 'Bulky Organic Cations Engineered Lead-halide Perovskites: A Review on Dimensionality and Optoelectronic Applications'. *Materials Today Energy*, p. 100759 (2021) (cited p. 25)

[Li *et al.* 2004] C. Li, K. C. K. Soh and P. Wu. 'Formability of ABO3 perovskites'. *Journal of Alloys and Compounds*, **vol. 372**, no. 1, pp. 40–48 (2004) (cited p. 15)

[Li *et al.* 2008] C. Li, X. Lu, W. Ding, L. Feng, Y. Gao and Z. Guo. 'Formability of ABX3 (X = F, Cl, Br, I) halide perovskites'. *Acta Crystallographica Section B: Structural Science*, **vol. 64**, no. 6, pp. 702–707 (2008) (cited p. 15)

[Li *et al.* 2015] X. Li, M. Ibrahim Dar, C. Yi, J. Luo, M. Tschumi, S. M. Zakeeruddin, M. K. Nazeeruddin, H. Han and M. Grätzel. 'Improved performance and stability of perovskite solar cells by crystal crosslinking with alkylphosphonic acid ω-ammonium chlorides'. *Nature Chemistry*, **vol. 7**, no. 9, pp. 703–711 (2015) (cited p. 24)

[Li *et al.* 2016] Z. Li, M. Yang, J.-S. Park, S.-H. Wei, J. J. Berry and K. Zhu. 'Stabilizing Perovskite Structures by Tuning Tolerance Factor: Formation of Formamidinium and Cesium Lead Iodide Solid-State Alloys'. *Chemistry of Materials*, **vol. 28**, no. 1, pp. 284–292 (2016) (cited p. 21)

[Li *et al.* 2017] N. Li, Z. Zhu, C.-C. Chueh, H. Liu, B. Peng, A. Petrone, X. Li, L. Wang and A. K.-Y. Jen. 'Mixed Cation FAxPEA1–xPbI3 with Enhanced Phase and Ambient Stability toward High-Performance Perovskite Solar Cells'. *Advanced Energy Materials*, **vol. 7**, no. 1, p. 1601307 (2017) (cited p. 34)

[Li *et al.* 2018] Z. Li, T. R. Klein, D. H. Kim, M. Yang, J. J. Berry, M. F. A. M. van Hest and K. Zhu. 'Scalable fabrication of perovskite solar cells'. *Nature Reviews Materials*, **vol. 3**, no. 4, pp. 1–20 (2018) (cited p. ix, 22)

[Li *et al.* 2020a] J. Li, J. Ma, X. Cheng, Z. Liu, Y. Chen and D. Li. 'Anisotropy of Excitons in Two-Dimensional Perovskite Crystals'. *ACS Nano*, **vol. 14**, no. 2, pp. 2156–2161 (2020) (cited p. 99)

[Li *et al.* 2020b] J. Li, M. Wu, G. Yang, D. Zhang, Z. Wang, D. Zheng and J. Yu. 'Bottom-up passivation effects by using 3D/2D mix structure for high performance p-i-n perovskite solar cells'. *Solar Energy*, **vol. 205**, pp. 44–50 (2020) (cited p. 87)

[Li *et al.* 2021a] D. Li, D. Zhang, K.-S. Lim, Y. Hu, Y. Rong, A. Mei, N.-G. Park and H. Han. 'A Review on Scaling Up Perovskite Solar Cells'. *Advanced Functional Materials*, **vol. 31**, no. 12, p. 2008621 (2021) (cited p. ix, 22, 23)

[Li *et al.* 2021b] J. Li, R. Xia, W. Qi, X. Zhou, J. Cheng, Y. Chen, G. Hou, Y. Ding, Y. Li, Y. Zhao and X. Zhang. 'Encapsulation of perovskite solar cells for enhanced stability: Structures, materials and characterization'. *Journal of Power Sources*, **vol. 485**, p. 229313 (2021) (cited p. 24)

[Li *et al.* 2021c] Q. Li, Q. Shu, Y. Wang, D.-Y. Zhou, F. Wang, Q. Yuan, S. Yi, H. Wang and L. Feng. 'Interfacial Engineering by In Situ Building of a 3D/2D Heterojunction for Inverted CsPbI2Br Solar Cells: Beyond Moisture Proof'. *ACS Applied Energy Materials* (2021) (cited p. 67)

[Li *et al.* 2022] Z. Li, X. Wang, Z. Wang, Z. Shao, L. Hao, Y. Rao, C. Chen, D. Liu, Q. Zhao, X. Sun, C. Gao, B. Zhang, X. Wang, L. Wang, G. Cui and S. Pang. 'Ammonia for post-healing of formamidinium-based Perovskite films'. *Nature Communications*, **vol. 13**, no. 1, p. 4417 (2022) (cited p. 89)

[Liang *et al.* 2020] L. Liang, H. Luo, J. Hu, H. Li and P. Gao. 'Efficient Perovskite Solar Cells by Reducing Interface-Mediated Recombination: A Bulky Amine Approach'. *Advanced Energy Materials*, **vol. 10**, no. 14, p. 2000197 (2020) (cited p. 38)

[Lin *et al.* 2019] D. Lin, T. Zhang, J. Wang, M. Long, F. Xie, J. Chen, B. Wu, T. Shi, K. Yan, W. Xie, P. Liu and J. Xu. 'Stable and scalable 3D-2D planar heterojunction perovskite solar cells via vapor deposition'. *Nano Energy*, **vol. 59**, pp. 619–625 (2019) (cited p. 37, 103)

[Liu *et al.* 2017a] C. Liu, W. Li, H. Li, C. Zhang, J. Fan and Y. Mai. 'C60 additive-assisted crystallization in CH3NH3Pb0.75Sn0.25I3 perovskite solar cells with high stability and efficiency'. *Nanoscale*, **vol. 9**, no. 37, pp. 13967–13975 (2017) (cited p. 24)

[Liu *et al.* 2017b] J. Liu, J. Leng, K. Wu, J. Zhang and S. Jin. 'Observation of Internal Photoinduced Electron and Hole Separation in Hybrid Two-Dimentional Perovskite Films'. *Journal of the American Chemical Society*, **vol. 139**, no. 4, pp. 1432–1435 (2017) (cited p. 37)

[Liu *et al.* 2017c] Z. Liu, A. Zhu, F. Cai, L. Tao, Y. Zhou, Z. Zhao, Q. Chen, Y.-B. Cheng and H. Zhou. 'Nickel oxide nanoparticles for efficient hole transport in p-i-n and n-i-p perovskite solar cells'. *Journal of Materials Chemistry A*, **vol. 5**, no. 14, pp. 6597–6605 (2017) (cited p. 20)

[Liu *et al.* 2019a] Y. Liu, S. Akin, L. Pan, R. Uchida, N. Arora, J. V. Milić, A. Hinderhofer, F. Schreiber, A. R. Uhl, S. M. Zakeeruddin, A. Hagfeldt, M. I. Dar and M. Grätzel. 'Ultrahydrophobic 3D/2D fluoroarene bilayer-based water-resistant perovskite solar cells with efficiencies exceeding 22%'. *Science Advances*, **vol. 5**, no. 6, p. eaaw2543 (2019) (cited p. 36, 65, 74, 83, 103)

[Liu *et al.* 2019b] Z. Liu, D. Liu, H. Chen, L. Ji, H. Zheng, Y. Gu, F. Wang, Z. Chen and S. Li. 'Enhanced Crystallinity of Triple-Cation Perovskite Film via Doping NH4SCN'. *Nanoscale Research Letters*, **vol. 14**, no. 1, p. 304 (2019) (cited p. 56)

[Liu *et al.* 2020] C. Liu, J. Sun, W. L. Tan, J. Lu, T. R. Gengenbach, C. R. McNeill, Z. Ge, Y.-B. Cheng and U. Bach. 'Alkali Cation Doping for Improving the Structural Stability of 2D Perovskite in 3D/2D PSCs'. *Nano Letters*, **vol. 20**, no. 2, pp. 1240–1251 (2020) (cited p. 35, 36)

[Liu *et al.* 2021a] L. Liu, J. Lu, H. Wang, Z. Cui, G. Giorgi, Y. Bai and Q. Chen. 'A-site phase segregation in mixed cation perovskite'. *Materials Reports: Energy*, **vol. 1**, no. 4, p. 100064 (2021) (cited p. 23)

[Liu *et al.* 2021b] T. Liu, J. Zhang, M. Qin, X. Wu, F. Li, X. Lu, Z. Zhu and A. K.-Y. Jen. 'Modifying Surface Termination of CsPbI3 Grain Boundaries by 2D Perovskite Layer for Efficient and Stable Photovoltaics'. *Advanced Functional Materials*, **vol. 31**, no. 15, p. 2009515 (2021) (cited p. 103)

[Lu *et al.* 2015] H. Lu, Y. Ma, B. Gu, W. Tian and L. Li. 'Identifying the optimum thickness of electron transport layers for highly efficient perovskite planar solar cells'. *Journal of Materials Chemistry A*, **vol. 3**, no. 32, pp. 16445–16452 (2015) (cited p. 42)

[Lu *et al.* 2020] D. Lu, G. Lv, Z. Xu, Y. Dong, X. Ji and Y. Liu. 'Thiophene-Based Two-Dimensional Dion–Jacobson Perovskite Solar Cells with over 15% Efficiency'. *Journal of the American Chemical Society*, **vol. 142**, no. 25, pp. 11114–11122 (2020) (cited p. 32)

[Lynas *et al.* 2021] M. Lynas, B. Z. Houlton and S. Perry. 'Greater than 99% consensus on human caused climate change in the peer-reviewed scientific literature'. *Environmental Research Letters*, **vol. 16**, no. 11, p. 114005 (2021) (cited p. 1)

[M. Rombach *et al.* 2021] F. M. Rombach, S. A. Haque and T. J. Macdonald. 'Lessons learned from spiro-OMeTAD and PTAA in perovskite solar cells'. *Energy & Environmental Science*, **vol. 14**, no. 10, pp. 5161–5190 (2021) (cited p. 47)

[Ma *et al.* 2016] C. Ma, C. Leng, Y. Ji, X. Wei, K. Sun, L. Tang, J. Yang, W. Luo, C. Li, Y. Deng, S. Feng, J. Shen, S. Lu, C. Du and H. Shi. '2D/3D perovskite hybrids as moisture-tolerant and efficient light absorbers for solar cells'. *Nanoscale*, **vol. 8**, no. 43, pp. 18309–18314 (2016) (cited p. 36)

[Ma *et al.* 2017] F. Ma, J. Li, W. Li, N. Lin, L. Wang and J. Qiao. 'Stable α/δ phase junction of formamidinium lead iodide perovskites for enhanced near-infrared emission'. *Chemical Science*, **vol. 8**, no. 1, pp. 800–805 (2017) (cited p. 15, 21)

[Mahmud *et al.* 2020] M. A. Mahmud, T. Duong, Y. Yin, H. T. Pham, D. Walter, J. Peng, Y. Wu, L. Li, H. Shen, N. Wu, N. Mozaffari, G. Andersson, K. R. Catchpole, K. J. Weber and T. P. White. 'Double-Sided Surface Passivation of 3D Perovskite Film for High-Efficiency Mixed-Dimensional Perovskite Solar Cells'. *Advanced Functional Materials*, **vol. 30**, no. 7, p. 1907962 (2020) (cited p. 37)

[Mahmud *et al.* 2021a] M. A. Mahmud, T. Duong, J. Peng, Y. Wu, H. Shen, D. Walter, H. T. Nguyen, N. Mozaffari, G. D. Tabi, K. R. Catchpole, K. J. Weber and T. P. White. 'Origin of Efficiency and Stability Enhancement in High-Performing Mixed Dimensional 2D-3D Perovskite Solar Cells: A Review'. *Advanced Functional Materials*, **vol. n/a**, no. n/a, p. 2009164 (2021) (cited p. x, 32, 33, 34, 87)

[Mahmud *et al.* 2021b] M. A. Mahmud, H. T. Pham, T. Duong, Y. Yin, J. Peng, Y. Wu, W. Liang, L. Li, A. Kumar, H. Shen, D. Walter, H. T. Nguyen, N. Mozaffari, G. D. Tabi, G. Andersson, K. R. Catchpole, K. J. Weber and T. P. White. 'Combined Bulk and Surface Passivation in Dimensionally Engineered 2D-3D Perovskite Films via Chlorine Diffusion'. *Advanced Functional Materials*, **vol. 31**, no. 46, p. 2104251 (2021) (cited p. 123)

[Mao *et al.* 2019] L. Mao, C. C. Stoumpos and M. G. Kanatzidis. 'Two-Dimensional Hybrid Halide Perovskites: Principles and Promises'. *Journal of the American Chemical Society*, **vol. 141**, no. 3, pp. 1171–1190 (2019) (cited p. 24, 25)

[Mayer *et al.* 2022] C. R. Mayer, H. Levy-Falk, M. Rémond, G. Trippé-Allard, F. Fossard, M. Vallet, M. Lepeltier, N. Guiblin, J.-S. Lauret, D. Garrot and E. Deleporte. 'Synthesis of highly calibrated CsPbBr3 nanocrystal perovskites by soft chemistry'. *Chemical Communications*, **vol. 58**, no. 40, pp. 5960–5963 (2022) (cited p. 103)

[Meadows *et al.* 1972] D. H. Meadows, D. L. Meadows, J. Randers and i. W. Behrens III. *The Limits to Growth* (1972). ISBN 0-87663-165-0 (cited p. 1)

[Mei *et al.* 2014] A. Mei, X. Li, L. Liu, Z. Ku, T. Liu, Y. Rong, M. Xu, M. Hu, J. Chen, Y. Yang, M. Grätzel and H. Han. 'A hole-conductor–free, fully printable mesoscopic perovskite solar cell with high stability'. *Science*, **vol. 345**, no. 6194, pp. 295–298 (2014) (cited p. 23)

[Meillaud *et al.* 2006] F. Meillaud, A. Shah, C. Droz, E. Vallat-Sauvain and C. Miazza. 'Efficiency limits for single-junction and tandem solar cells'. *Solar Energy Materials and Solar Cells*, **vol. 90**, no. 18, pp. 2952–2959 (2006) (cited p. 14)

[Menéndez-Proupin *et al.* 2014] E. Menéndez-Proupin, P. Palacios, P. Wahnón and J. C. Conesa. 'Self-consistent relativistic band structure of the $\mathrm{CH}{}_{3}\mathrm{NH}{}_{3}\mathrm{PbI}{}_{3}$ perovskite'. *Physical Review B*, **vol. 90**, no. 4, p. 045207 (2014) (cited p. 15)

[Min *et al.* 2021] H. Min, D. Y. Lee, J. Kim, G. Kim, K. S. Lee, J. Kim, M. J. Paik, Y. K. Kim, K. S. Kim, M. G. Kim, T. J. Shin and S. Il Seok. 'Perovskite solar cells with atomically coherent interlayers on SnO2 electrodes'. *Nature*, **vol. 598**, no. 7881, pp. 444–450 (2021) (cited p. 20, 22)

[Mitzi 2001] D. B. Mitzi. 'Templating and structural engineering in organic–inorganic perovskites'. *Journal of the Chemical Society, Dalton Transactions*, , no. 1, pp. 1–12 (2001) (cited p. ix, 25)

[Mitzi *et al.* 1999] D. B. Mitzi, K. Chondroudis and C. R. Kagan. 'Design, Structure, and Optical Properties of Organic-Inorganic Perovskites Containing an Oligothiophene Chromophore'. *Inorganic Chemistry*, **vol. 38**, no. 26, pp. 6246–6256 (1999) (cited p. 24, 25)

[Miyata *et al.* 2015] A. Miyata, A. Mitioglu, P. Plochocka, O. Portugall, J. T.-W. Wang, S. D. Stranks, H. J. Snaith and R. J. Nicholas. 'Direct measurement of the exciton binding energy and effective masses for charge carriers in organic–inorganic tri-halide perovskites'. *Nature Physics*, **vol. 11**, no. 7, pp. 582–587 (2015) (cited p. 17, 27)

[Motta *et al.* 2015] C. Motta, F. El-Mellouhi, S. Kais, N. Tabet, F. Alharbi and S. Sanvito. 'Revealing the role of organic cations in hybrid halide perovskite CH3NH3PbI3'. *Nature Communications*, **vol. 6**, no. 1, p. 7026 (2015) (cited p. ix, 16, 17)

[Nakajima *et al.* 1983] T. Nakajima, H. Yamauchi, T. Goto, M. Yoshizawa, T. Suzuki and T. Fujimura. 'Magnetic and elastic properties of (CH3NH3)2FeCl4 and (C2H5NH3)2FeCl4'. *Journal of Magnetism and Magnetic Materials*, **vol. 31–34**, pp. 1189–1190 (1983) (cited p. 24)

[Noh *et al.* 2013] J. H. Noh, S. H. Im, J. H. Heo, T. N. Mandal and S. I. Seok. 'Chemical Management for Colorful, Efficient, and Stable Inorganic–Organic Hybrid Nanostructured Solar Cells'. *Nano Letters*, **vol. 13**, no. 4, pp. 1764–1769 (2013) (cited p. 95)

[NREL] NREL. 'Reference Air Mass 1.5 Spectra'. https://www.nrel.gov/grid/solar-resource/spectra-am1.5.html (cited p. viii, 9)

[NREL 2021] NREL. 'Life Cycle Assessment Harmonization'. https://www.nrel.gov/analysis/life-cycle-assessment.html (2021) (cited p. 3)

[NREL 2022] NREL. 'Best Research-Cell Efficiency Chart'. https://www.nrel.gov/pv/cell-efficiency.html (2022) (cited p. 18, 21)

[Ortiz-Cervantes *et al.* 2019] C. Ortiz-Cervantes, P. Carmona-Monroy and D. Solis-Ibarra. 'Two-Dimensional Halide Perovskites in Solar Cells: 2D or not 2D?' *ChemSusChem*, **vol. 12**, no. 8, pp. 1560–1575 (2019) (cited p. ix, x, 29, 30, 31, 32, 33, 46)

[Ouedraogo *et al.* 2020] N. A. N. Ouedraogo, Y. Chen, Y. Y. Xiao, Q. Meng, C. B. Han, H. Yan and Y. Zhang. 'Stability of all-inorganic perovskite solar cells'. *Nano Energy*, **vol. 67**, p. 104249 (2020) (cited p. 21)

[Park *et al.* 2017] Y. H. Park, I. Jeong, S. Bae, H. J. Son, P. Lee, J. Lee, C.-H. Lee and M. J. Ko. 'Inorganic Rubidium Cation as an Enhancer for Photovoltaic Performance and Moisture Stability of HC(NH2)2PbI3 Perovskite Solar Cells'. *Advanced Functional Materials*, **vol. 27**, no. 16, p. 1605988 (2017) (cited p. 21)

[Pascoe *et al.* 2017] A. R. Pascoe, Q. Gu, M. U. Rothmann, W. Li, Y. Zhang, A. D. Scully, X. Lin, L. Spiccia, U. Bach and Y.-B. Cheng. 'Directing nucleation and growth kinetics in solution-processed hybrid perovskite thin-films'. *Science China Materials*, **vol. 60**, no. 7, pp. 617–628 (2017) (cited p. 18)

[Pérez-del-Rey *et al.* 2018] D. Pérez-del-Rey, P. P. Boix, M. Sessolo, A. Hadipour and H. J. Bolink. 'Interfacial Modification for High-Efficiency Vapor-Phase-Deposited Perovskite Solar Cells Based on a Metal Oxide Buffer Layer'. *The Journal of Physical Chemistry Letters*, **vol. 9**, no. 5, pp. 1041–1046 (2018) (cited p. 19)

[Perini *et al.* 2021] C. A. R. Perini, E. Rojas-Gatjens, M. Rovello, A. F. C. Mendez, J. Hidalgo, Y. An, R. Li, C. Silva-Acuña and J.-P. Correa-Baena. 'Preventing bulky cation diffusion in lead halide perovskite solar cells'. *ChemRxiv* (2021) (cited p. 71)

[Pham *et al.* 2020] H. D. Pham, T. C.-J. Yang, S. M. Jain, G. J. Wilson and P. Sonar. 'Development of Dopant-Free Organic Hole Transporting Materials for Perovskite Solar Cells'. *Advanced Energy Materials*, **vol. 10**, no. 13, p. 1903326 (2020) (cited p. 47)

[Philippe *et al.* 2015] B. Philippe, B.-W. Park, R. Lindblad, J. Oscarsson, S. Ahmadi, E. M. J. Johansson and H. Rensmo. 'Chemical and Electronic Structure Characterization of Lead Halide Perovskites and Stability Behavior under Different Exposures—A Photoelectron Spectroscopy Investigation'. *Chemistry of Materials*, **vol. 27**, no. 5, pp. 1720–1731 (2015) (cited p. 23)

[Protesescu *et al.* 2015] L. Protesescu, S. Yakunin, M. I. Bodnarchuk, F. Krieg, R. Caputo, C. H. Hendon, R. X. Yang, A. Walsh and M. V. Kovalenko. 'Nanocrystals of Cesium Lead Halide Perovskites (CsPbX3, X = Cl, Br, and I): Novel Optoelectronic Materials Showing Bright Emission with Wide Color Gamut'. *Nano Letters*, **vol. 15**, no. 6, pp. 3692–3696 (2015) (cited p. 100)

[Qi *et al.* 2020] W. Qi, X. Zhou, J. Li, J. Cheng, Y. Li, M. J. Ko, Y. Zhao and X. Zhang. 'Inorganic material passivation of defects toward efficient perovskite solar cells'. *Science Bulletin*, **vol. 65**, no. 23, pp. 2022–2032 (2020) (cited p. 24)

[Quan *et al.* 2016] L. N. Quan, M. Yuan, R. Comin, O. Voznyy, E. M. Beauregard, S. Hoogland, A. Buin, A. R. Kirmani, K. Zhao, A. Amassian, D. H. Kim and E. H. Sargent. 'Ligand-Stabilized Reduced-Dimensionality Perovskites'. *Journal of the American Chemical Society*, **vol. 138**, no. 8, pp. 2649–2655 (2016) (cited p. 26)

[Quintero-Bermudez *et al.* 2018] R. Quintero-Bermudez, A. Gold-Parker, A. H. Proppe, R. Munir, Z. Yang, S. O. Kelley, A. Amassian, M. F. Toney and E. H. Sargent. 'Compositional and orientational control in metal halide perovskites of reduced dimensionality'. *Nature Materials*, **vol. 17**, no. 10, pp. 900–907 (2018) (cited p. 30)

[Quintero-Bermudez *et al.* 2019] R. Quintero-Bermudez, A. H. Proppe, A. Mahata, P. Todorović, S. O. Kelley, F. De Angelis and E. H. Sargent. 'Ligand-Induced Surface Charge Density Modulation Generates Local Type-II Band Alignment in Reduced-Dimensional Perovskites'. *Journal of the American Chemical Society*, **vol. 141**, no. 34, pp. 13459–13467 (2019) (cited p. 28)

[Ravi *et al.* 2020] V. K. Ravi, B. Mondal, V. V. Nawale and A. Nag. 'Don't Let the Lead Out: New Material Chemistry Approaches for Sustainable Lead Halide Perovskite Solar Cells'. *ACS Omega*, **vol. 5**, no. 46, pp. 29631–29641 (2020) (cited p. 24)

[Rehman *et al.* 2015] W. Rehman, R. L. Milot, G. E. Eperon, C. Wehrenfennig, J. L. Boland, H. J. Snaith, M. B. Johnston and L. M. Herz. 'Charge-Carrier Dynamics and Mobilities in Formamidinium Lead Mixed-Halide Perovskites'. *Advanced Materials*, **vol. 27**, no. 48, pp. 7938–7944 (2015) (cited p. 44)

[Rehman *et al.* 2017] W. Rehman, D. P. McMeekin, J. B. Patel, R. L. Milot, M. B. Johnston, H. J. Snaith and L. M. Herz. 'Photovoltaic mixed-cation lead mixed-halide perovskites: Links between crystallinity, photo-stability and electronic properties'. *Energy & Environmental Science*, **vol. 10**, no. 1, pp. 361–369 (2017) (cited p. 21, 44)

[Richter *et al.* 2013] A. Richter, M. Hermle and S. W. Glunz. 'Reassessment of the Limiting Efficiency for Crystalline Silicon Solar Cells'. *IEEE Journal of Photovoltaics*, **vol. 3**, no. 4, pp. 1184–1191 (2013) (cited p. 3, 13)

[Roelofs *et al.* 2016] K. E. Roelofs, V. L. Pool, D. A. Bobb-Semple, A. F. Palmstrom, P. K. Santra, D. G. Van Campen, M. F. Toney and S. F. Bent. 'Impact of Conformality and Crystallinity for Ultrathin 4 nm Compact TiO2 Layers in Perovskite Solar Cells'. *Advanced Materials Interfaces*, **vol. 3**, no. 21, p. 1600580 (2016) (cited p. 42)

[Rong *et al.* 2018] Y. Rong, Y. Hu, A. Mei, H. Tan, M. I. Saidaminov, S. I. Seok, M. D. McGehee, E. H. Sargent and H. Han. 'Challenges for commercializing perovskite solar cells'. *Science*, **vol. 361**, no. 6408, p. eaat8235 (2018) (cited p. ix, 20)

[Rose 1840] G. Rose. 'Ueber einige neue Mineralien des Urals'. *Journal für Praktische Chemie*, **vol. 19**, no. 1, pp. 459–468 (1840) (cited p. 15)

[Ross and Nozik 1982] R. T. Ross and A. J. Nozik. 'Efficiency of hot-carrier solar energy converters'. *Journal of Applied Physics*, **vol. 53**, no. 5, pp. 3813–3818 (1982) (cited p. 13)

[Ruggeri *et al.* 2019] E. Ruggeri, M. Anaya, K. Gałkowski, G. Delport, F. U. Kosasih, A. Abfalterer, S. Mackowski, C. Ducati and S. D. Stranks. 'Controlling the Growth Kinetics and Optoelectronic Properties of 2D/3D Lead–Tin Perovskite Heterojunctions'. *Advanced Materials*, **vol. 31**, no. 51, p. 1905247 (2019) (cited p. 36)

[Saliba *et al.* 2016] M. Saliba, T. Matsui, K. Domanski, J.-Y. Seo, A. Ummadisingu, S. M. Zakeeruddin, J.-P. Correa-Baena, W. R. Tress, A. Abate, A. Hagfeldt and M. Grätzel. 'Incorporation of rubidium cations into perovskite solar cells improves photovoltaic performance'. *Science*, **vol. 354**, no. 6309, pp. 206–209 (2016) (cited p. ix, 21)

[Schulz *et al.* 2019] P. Schulz, D. Cahen and A. Kahn. 'Halide Perovskites: Is It All about the Interfaces?' *Chemical Reviews*, **vol. 119**, no. 5, pp. 3349–3417 (2019) (cited p. 23)

[Seo *et al.* 2017] Y.-H. Seo, E.-C. Kim, S.-P. Cho, S.-S. Kim and S.-I. Na. 'High-performance planar perovskite solar cells: Influence of solvent upon performance'. *Applied Materials Today*, **vol. 9**, pp. 598–604 (2017) (cited p. 18)

[Sheikh *et al.* 2019] T. Sheikh, A. Shinde, S. Mahamuni and A. Nag. 'Dual excitonic emissions and structural phase transition of octylammonium lead iodide 2D layered perovskite single crystal'. *Materials Research Express*, **vol. 6**, no. 12, p. 124002 (2019) (cited p. 116)

[Shockley and Queisser 1961] W. Shockley and H. J. Queisser. 'Detailed Balance Limit of Efficiency of p-n Junction Solar Cells'. *Journal of Applied Physics*, **vol. 32**, no. 3, p. 510 (1961) (cited p. 13)

[Sidhik *et al.* 2022] S. Sidhik, Y. Wang, M. De Siena, R. Asadpour, A. J. Torma, T. Terlier, K. Ho, W. Li, A. B. Puthirath, X. Shuai, A. Agrawal, B. Traore, M. Jones, R. Giridharagopal, P. M. Ajayan, J. Strzalka, D. S. Ginger, C. Katan, M. A. Alam, J. Even, M. G. Kanatzidis and A. D. Mohite. 'Deterministic fabrication of 3D/2D perovskite bilayer stacks for durable and efficient solar cells'. *Science*, **vol. 377**, no. 6613, pp. 1425–1430 (2022) (cited p. 37, 127)

[Slotcavage *et al.* 2016] D. J. Slotcavage, H. I. Karunadasa and M. D. McGehee. 'Light-Induced Phase Segregation in Halide-Perovskite Absorbers'. *ACS Energy Letters*, **vol. 1**, no. 6, pp. 1199–1205 (2016) (cited p. 23)

[Smith *et al.* 2014] I. C. Smith, E. T. Hoke, D. Solis-Ibarra, M. D. McGehee and H. I. Karunadasa. 'A Layered Hybrid Perovskite Solar-Cell Absorber with Enhanced Moisture Stability'. *Angewandte Chemie International Edition*, **vol. 53**, no. 42, pp. 11232–11235 (2014) (cited p. 31)

[Soe *et al.* 2019] C. M. M. Soe, G. P. Nagabhushana, R. Shivaramaiah, H. Tsai, W. Nie, J.-C. Blancon, F. Melkonyan, D. H. Cao, B. Traoré, L. Pedesseau, M. Kepenekian, C. Katan, J. Even, T. J. Marks, A. Navrotsky, A. D. Mohite, C. C. Stoumpos and M. G. Kanatzidis. 'Structural and thermodynamic limits of layer thickness in 2D halide perovskites'. *Proceedings of the National Academy of Sciences*, **vol. 116**, no. 1, pp. 58–66 (2019) (cited p. ix, 29)

[Song *et al.* 2016] Z. Song, A. Abate, S. C. Watthage, G. K. Liyanage, A. B. Phillips, U. Steiner, M. Graetzel and M. J. Heben. 'Perovskite Solar Cell Stability in Humid Air: Partially Reversible Phase Transitions in the PbI2-CH3NH3I-H2O System'. *Advanced Energy Materials*, **vol. 6**, no. 19, p. 1600846 (2016) (cited p. 20)

[Stoumpos *et al.* 2013] C. C. Stoumpos, C. D. Malliakas and M. G. Kanatzidis. 'Semiconducting Tin and Lead Iodide Perovskites with Organic Cations: Phase Transitions, High Mobilities, and Near-Infrared Photoluminescent Properties'. *Inorganic Chemistry*, **vol. 52**, no. 15, pp. 9019–9038 (2013) (cited p. 15)

[Stranks *et al.* 2013] S. D. Stranks, G. E. Eperon, G. Grancini, C. Menelaou, M. J. P. Alcocer, T. Leijtens, L. M. Herz, A. Petrozza and H. J. Snaith. 'Electron-Hole Diffusion Lengths Exceeding 1 Micrometer in an Organometal Trihalide Perovskite Absorber'. *Science*, **vol. 342**, no. 6156, pp. 341–344 (2013) (cited p. 16)

[Sun and Yin 2017] Q. Sun and W.-J. Yin. 'Thermodynamic Stability Trend of Cubic Perovskites'. *Journal of the American Chemical Society*, **vol. 139**, no. 42, pp. 14905–14908 (2017) (cited p. 15)

[Sutanto *et al.* 2020] A. A. Sutanto, N. Drigo, V. I. E. Queloz, I. Garcia-Benito, A. R. Kirmani, L. J. Richter, P. A. Schouwink, K. T. Cho, S. Paek, M. K. Nazeeruddin and G. Grancini. 'Dynamical evolution of the 2D/3D interface: A hidden driver behind perovskite solar cell instability'. *Journal of Materials Chemistry A*, **vol. 8**, no. 5, pp. 2343–2348 (2020) (cited p. x, 37, 119)

[T. Hoke *et al.* 2015] E. T. Hoke, D. J. Slotcavage, E. R. Dohner, A. R. Bowring, H. I. Karunadasa and M. D. McGehee. 'Reversible photo-induced trap formation in mixed-halide hybrid perovskites for photovoltaics'. *Chemical Science*, **vol. 6**, no. 1, pp. 613–617 (2015) (cited p. 23, 95, 110)

[Tan *et al.* 2021] S. Tan, T. Huang, I. Yavuz, R. Wang, M. H. Weber, Y. Zhao, M. Abdelsamie, M. E. Liao, H.-C. Wang, K. Huynh, K.-H. Wei, J. Xue, F. Babbe, M. S. Goorsky, J.-W. Lee, C. M. Sutter-Fella and Y. Yang. 'Surface Reconstruction of Halide Perovskites During Post-treatment'. *Journal of the American Chemical Society* (2021) (cited p. 103)

[Tanaka and Kondo 2003] K. Tanaka and T. Kondo. 'Bandgap and exciton binding energies in lead-iodide-based natural quantum-well crystals'. *Science and Technology of Advanced Materials*, **vol. 4**, no. 6, pp. 599–604 (2003) (cited p. 29)

[Tanaka *et al.* 2002] K. Tanaka, F. Sano, T. Takahashi, T. Kondo, R. Ito and K. Ema. 'Two-dimensional Wannier excitons in a layered-perovskite-type crystal (C6H13NH3)2PbI4'. *Solid State Communications*, **vol. 122**, no. 5, pp. 249–252 (2002) (cited p. 28, 29)

[Tavakoli *et al.* 2019] M. M. Tavakoli, P. Yadav, D. Prochowicz, M. Sponseller, A. Osherov, V. Bulović and J. Kong. 'Controllable Perovskite Crystallization via Antisolvent Technique Using Chloride Additives for Highly Efficient Planar Perovskite Solar Cells'. *Advanced Energy Materials*, **vol. 9**, no. 17, p. 1803587 (2019) (cited p. 24)

[Teale *et al.* 2020] S. Teale, A. H. Proppe, E. H. Jung, A. Johnston, D. H. Parmar, B. Chen, Y. Hou, S. O. Kelley and E. H. Sargent. 'Dimensional Mixing Increases the Efficiency of 2D/3D Perovskite Solar Cells'. *The Journal of Physical Chemistry Letters*, **vol. 11**, no. 13, pp. 5115–5119 (2020) (cited p. 77)

[Todorov *et al.* 2016] T. Todorov, O. Gunawan and S. Guha. 'A road towards 25% efficiency and beyond: Perovskite tandem solar cells'. *Molecular Systems Design & Engineering*, **vol. 1**, no. 4, pp. 370–376 (2016) (cited p. viii, 14)

[Tsai *et al.* 2016] H. Tsai, W. Nie, J.-C. Blancon, C. C. Stoumpos, R. Asadpour, B. Harutyunyan, A. J. Neukirch, R. Verduzco, J. J. Crochet, S. Tretiak, L. Pedesseau, J. Even, M. A. Alam, G. Gupta, J. Lou, P. M. Ajayan, M. J. Bedzyk, M. G. Kanatzidis and A. D. Mohite. 'High-efficiency two-dimensional Ruddlesden–Popper perovskite solar cells'. *Nature*, **vol. 536**, no. 7616, pp. 312–316 (2016) (cited p. ix, 31)

[Turren-Cruz *et al.* 2018] S.-H. Turren-Cruz, A. Hagfeldt and M. Saliba. 'Methylammonium-free, high-performance, and stable perovskite solar cells on a planar architecture'. *Science*, **vol. 362**, no. 6413, pp. 449–453 (2018) (cited p. 20)

[VDMA 2022] VDMA. 'International Technology Roadmap for Photovoltaic (ITRPV) 2022'. https://www.vdma.org/international-technology-roadmap-photovoltaic (2022) (cited p. viii, 3)

[Vos 1980] A. D. Vos. 'Detailed balance limit of the efficiency of tandem solar cells'. *Journal of Physics D: Applied Physics*, **vol. 13**, no. 5, p. 839 (1980) (cited p. 14)

[Wali *et al.* 2018] Q. Wali, N. K. Elumalai, Y. Iqbal, A. Uddin and R. Jose. 'Tandem perovskite solar cells'. *Renewable and Sustainable Energy Reviews*, **vol. 84**, pp. 89–110 (2018) (cited p. 4, 14)

[Walter *et al.* 2018] A. Walter, S.-J. Moon, B. A. Kamino, L. Löfgren, D. Sacchetto, F. Matteocci, B. Taheri, J. Bailat, A. Di Carlo, C. Ballif and S. Nicolay. 'Closing the Cell-to-Module Efficiency Gap: A Fully Laser Scribed Perovskite Minimodule With

16% Steady-State Aperture Area Efficiency'. *IEEE Journal of Photovoltaics*, **vol. 8**, no. 1, pp. 151–155 (2018) (cited p. 88)

[Wang *et al.* 2013] Y. Wang, T. Gould, J. F. Dobson, H. Zhang, H. Yang, X. Yao and H. Zhao. 'Density functional theory analysis of structural and electronic properties of orthorhombic perovskite CH3NH3PbI3'. *Physical Chemistry Chemical Physics*, **vol. 16**, no. 4, pp. 1424–1429 (2013) (cited p. 15)

[Wang *et al.* 2017] Z. Wang, Q. Lin, F. P. Chmiel, N. Sakai, L. M. Herz and H. J. Snaith. 'Efficient ambient-air-stable solar cells with 2D–3D heterostructured butylammonium-caesium-formamidinium lead halide perovskites'. *Nature Energy*, **vol. 2**, no. 9, p. 17135 (2017) (cited p. x, 35)

[Wang *et al.* 2019] R. Wang, M. Mujahid, Y. Duan, Z.-K. Wang, J. Xue and Y. Yang. 'A Review of Perovskites Solar Cell Stability'. *Advanced Functional Materials*, **vol. 29**, no. 47, p. 1808843 (2019) (cited p. 23)

[Wang *et al.* 2021] Y. Wang, C. Duan, P. Lv, Z. Ku, J. Lu, F. Huang and Y.-B. Cheng. 'Printing strategies for scaling-up perovskite solar cells'. *National Science Review*, **vol. 8**, no. 8, p. nwab075 (2021) (cited p. 89)

[Wang *et al.* 2022] L. Wang, Q. Zhou, Z. Zhang, W. Li, X. Wang, Q. Tian, X. Yu, T. Sun, J. Wu, B. Zhang and P. Gao. 'A guide to use fluorinated aromatic bulky cations for stable and high-performance 2D/3D perovskite solar cells: The more fluorination the better?' *Journal of Energy Chemistry*, **vol. 64**, pp. 179–189 (2022) (cited p. 36)

[Wannier 1937] G. H. Wannier. 'The Structure of Electronic Excitation Levels in Insulating Crystals'. *Physical Review*, **vol. 52**, no. 3, pp. 191–197 (1937) (cited p. 27)

[Wei *et al.* 2013] Y. Wei, P. Audebert, L. Galmiche, J.-S. Lauret and E. Deleporte. 'Synthesis, optical properties and photostability of novel fluorinated organic–inorganic hybrid (R –NH $_3$) $_2$ Pb X $_4$ semiconductors'. *Journal of Physics D: Applied Physics*, **vol. 46**, no. 13, p. 135105 (2013) (cited p. 46)

[Wei *et al.* 2014] Y. Wei, P. Audebert, L. Galmiche, J.-S. Lauret and E. Deleporte. 'Photostability of 2D Organic-Inorganic Hybrid Perovskites'. *Materials*, **vol. 7**, no. 6, pp. 4789–4802 (2014) (cited p. 46)

[Weller *et al.* 2015] M. T. Weller, O. J. Weber, J. M. Frost and A. Walsh. 'Cubic Perovskite Structure of Black Formamidinium Lead Iodide, α-[HC(NH2)2]PbI3, at 298 K'. *The Journal of Physical Chemistry Letters*, **vol. 6**, no. 16, pp. 3209–3212 (2015) (cited p. 21, 54)

[Wu *et al.* 2020] T. Wu, D. Cui, X. Liu, X. Meng, Y. Wang, T. Noda, H. Segawa, X. Yang, Y. Zhang and L. Han. 'Efficient and Stable Tin Perovskite Solar Cells Enabled by Graded Heterostructure of Light-Absorbing Layer'. *Solar RRL*, **vol. 4**, no. 9, p. 2000240 (2020) (cited p. 77)

[Xiang and Tress 2019] W. Xiang and W. Tress. 'Review on Recent Progress of All-Inorganic Metal Halide Perovskites and Solar Cells'. *Advanced Materials*, **vol. 31**, no. 44, p. 1902851 (2019) (cited p. 21)

[Xiang *et al.* 2021] Y. Xiang, X. Mo, X. Li, K. Huang, P. He, G. Dai and J. Yang. 'Progress on growth of metal halide perovskites by vapor-phase synthesis and their applications'. *Journal of Physics D: Applied Physics*, **vol. 55**, no. 7, p. 073001 (2021) (cited p. 19)

[Xiao *et al.* 2014] M. Xiao, F. Huang, W. Huang, Y. Dkhissi, Y. Zhu, J. Etheridge, A. Gray-Weale, U. Bach, Y.-B. Cheng and L. Spiccia. 'A Fast Deposition-Crystallization Procedure for Highly Efficient Lead Iodide Perovskite Thin-Film Solar Cells'. *Angewandte Chemie International Edition*, **vol. 53**, no. 37, pp. 9898–9903 (2014) (cited p. 18)

[Xing *et al.* 2013] G. Xing, N. Mathews, S. Sun, S. S. Lim, Y. M. Lam, M. Grätzel, S. Mhaisalkar and T. C. Sum. 'Long-Range Balanced Electron- and Hole-Transport Lengths in Organic-Inorganic CH3NH3PbI3'. *Science*, **vol. 342**, no. 6156, pp. 344–347 (2013) (cited p. 16)

[Xiong *et al.* 2018] L. Xiong, Y. Guo, J. Wen, H. Liu, G. Yang, P. Qin and G. Fang. 'Review on the Application of SnO2 in Perovskite Solar Cells'. *Advanced Functional Materials*, **vol. 28**, no. 35, p. 1802757 (2018) (cited p. 20)

[Yaffe *et al.* 2015] O. Yaffe, A. Chernikov, Z. M. Norman, Y. Zhong, A. Velauthapillai, A. van der Zande, J. S. Owen and T. F. Heinz. 'Excitons in ultrathin organic-inorganic perovskite crystals'. *Physical Review B*, **vol. 92**, no. 4, p. 045414 (2015) (cited p. 96)

[Yan *et al.* 2018] J. Yan, W. Qiu, G. Wu, P. Heremans and H. Chen. 'Recent progress in 2D/quasi-2D layered metal halide perovskites for solar cells'. *Journal of Materials Chemistry A*, **vol. 6**, no. 24, pp. 11063–11077 (2018) (cited p. x, 45)

[Yang *et al.* 2015] W. S. Yang, J. H. Noh, N. J. Jeon, Y. C. Kim, S. Ryu, J. Seo and S. I. Seok. 'High-performance photovoltaic perovskite layers fabricated through intramolecular exchange'. *Science*, **vol. 348**, no. 6240, pp. 1234–1237 (2015) (cited p. 18)

[Yang *et al.* 2017] M. Yang, Z. Li, M. O. Reese, O. G. Reid, D. H. Kim, S. Siol, T. R. Klein, Y. Yan, J. J. Berry, M. F. A. M. van Hest and K. Zhu. 'Perovskite ink with wide processing window for scalable high-efficiency solar cells'. *Nature Energy*, **vol. 2**, no. 5, pp. 1–9 (2017) (cited p. 77)

[Yang *et al.* 2020a] Y. Yang, M. T. Hoang, D. Yao, N. D. Pham, V. T. Tiong, X. Wang and H. Wang. 'Spiro-OMeTAD or CuSCN as a preferable hole transport material for carbon-based planar perovskite solar cells'. *Journal of Materials Chemistry A*, **vol. 8**, no. 25, pp. 12723–12734 (2020) (cited p. 47)

[Yang *et al.* 2020b] Z. Yang, J. Dou, S. Kou, J. Dang, Y. Ji, G. Yang, W.-Q. Wu, D.-B. Kuang and M. Wang. 'Multifunctional Phosphorus-Containing Lewis Acid and Base Passivation Enabling Efficient and Moisture-Stable Perovskite Solar Cells'. *Advanced Functional Materials*, **vol. 30**, no. 15, p. 1910710 (2020) (cited p. 24)

[Yang *et al.* 2021] J. Yang, T. Yang, D. Liu, Y. Zhang, T. Luo, J. Lu, J. Fang, J. Wen, Z. Deng, S. F. Liu, L. Chen and K. Zhao. 'Stable 2D Alternating Cation Perovskite Solar Cells with Power Conversion Efficiency >19% via Solvent Engineering'. *Solar RRL*, **vol. 5**, no. 8, p. 2100286 (2021) (cited p. 32)

[Yin *et al.* 2014] W.-J. Yin, T. Shi and Y. Yan. 'Unusual defect physics in CH3NH3PbI3 perovskite solar cell absorber'. *Applied Physics Letters*, **vol. 104**, no. 6, p. 063903 (2014) (cited p. 17)

[Yong-Liang *et al.* 2020] C. Yong-Liang, T. Ya-Wen, C. Pei-Run, Z. Li, L. Qi, Z. Ying, H. Qian and Z. Xiao-Dan. 'Progress in perovskite solar cells based on different buffer layer materials'. *Acta Physica Sinica*, **vol. 69**, no. 13, pp. 138401–12 (2020) (cited p. ix, 20)

[Yoo *et al.* 2019] J. J. Yoo, S. Wieghold, M. C. Sponseller, M. R. Chua, S. N. Bertram, N. T. P. Hartono, J. S. Tresback, E. C. Hansen, J.-P. Correa-Baena, V. Bulović, T. Buonassisi, S. S. Shin and M. G. Bawendi. 'An interface stabilized perovskite solar cell with high stabilized efficiency and low voltage loss'. *Energy & Environmental Science*, **vol. 12**, no. 7, pp. 2192–2199 (2019) (cited p. 37, 83, 103)

[Yoon *et al.* 2016] S. J. Yoon, K. G. Stamplecoskie and P. V. Kamat. 'How Lead Halide Complex Chemistry Dictates the Composition of Mixed Halide Perovskites'. *The Journal of Physical Chemistry Letters*, **vol. 7**, no. 7, pp. 1368–1373 (2016) (cited p. 103)

[Yoshikawa *et al.* 2017] K. Yoshikawa, H. Kawasaki, W. Yoshida, T. Irie, K. Konishi, K. Nakano, T. Uto, D. Adachi, M. Kanematsu, H. Uzu and K. Yamamoto. 'Silicon heterojunction solar cell with interdigitated back contacts for a photoconversion efficiency over 26%'. *Nature Energy*, **vol. 2**, no. 5, pp. 1–8 (2017) (cited p. 13, 22)

[Zhang and Park 2022] Y. Zhang and N.-G. Park. 'Quasi-Two-Dimensional Perovskite Solar Cells with Efficiency Exceeding 22%'. *ACS Energy Letters*, **vol. 7**, no. 2, pp. 757–765 (2022) (cited p. 32)

[Zhang *et al.* 2009] S. Zhang, G. Lanty, J.-S. Lauret, E. Deleporte, P. Audebert and L. Galmiche. 'Synthesis and optical properties of novel organic–inorganic hybrid nanolayer structure semiconductors'. *Acta Materialia*, **vol. 57**, no. 11, pp. 3301–3309 (2009) (cited p. 26)

[Zhang *et al.* 2010] S. Zhang, P. Audebert, Y. Wei, A. Al Choueiry, G. Lanty, A. Bréhier, L. Galmiche, G. Clavier, C. Boissière, J.-S. Lauret and E. Deleporte. 'Preparations and Characterizations of Luminescent Two Dimensional Organic-inorganic Perovskite Semiconductors'. *Materials*, **vol. 3**, no. 5, pp. 3385–3406 (2010) (cited p. 46, 95)

[Zhang *et al.* 2018] P. Zhang, J. Wu, T. Zhang, Y. Wang, D. Liu, H. Chen, L. Ji, C. Liu, W. Ahmad, Z. D. Chen and S. Li. 'Perovskite Solar Cells with ZnO Electron-Transporting Materials'. *Advanced Materials*, **vol. 30**, no. 3, p. 1703737 (2018) (cited p. 20)

[Zhang *et al.* 2019] H.-y. Zhang, R. Li, W.-w. Liu, M. Zhang and M. Guo. 'Research progress in lead-less or lead-free three-dimensional perovskite absorber materials for solar cells'. *International Journal of Minerals, Metallurgy, and Materials*, **vol. 26**, no. 4, pp. 387–403 (2019) (cited p. 20)

[Zhao *et al.* 2016] T. Zhao, C.-C. Chueh, Q. Chen, A. Rajagopal and A. K.-Y. Jen. 'Defect Passivation of Organic–Inorganic Hybrid Perovskites by Diammonium Iodide toward High-Performance Photovoltaic Devices'. *ACS Energy Letters*, **vol. 1**, no. 4, pp. 757–763 (2016) (cited p. 77)

[Zhao *et al.* 2017] X. Zhao, H.-S. Kim, J.-Y. Seo and N.-G. Park. 'Effect of Selective Contacts on the Thermal Stability of Perovskite Solar Cells'. *ACS Applied Materials & Interfaces*, **vol. 9**, no. 8, pp. 7148–7153 (2017) (cited p. 47)

[Zhao *et al.* 2020] X. Zhao, T. Liu, A. B. Kaplan, C. Yao and Y.-L. Loo. 'Accessing Highly Oriented Two-Dimensional Perovskite Films via Solvent-Vapor Annealing for Efficient and Stable Solar Cells'. *Nano Letters*, **vol. 20**, no. 12, pp. 8880–8889 (2020) (cited p. 32)

[Zhao *et al.* 2022] X. Zhao, T. Liu and Y.-L. Loo. 'Advancing 2D Perovskites for Efficient and Stable Solar Cells: Challenges and Opportunities'. *Advanced Materials*, **vol. 34**, no. 3, p. 2105849 (2022) (cited p. 26)

[Zheng *et al.* 2018] H. Zheng, G. Liu, L. Zhu, J. Ye, X. Zhang, A. Alsaedi, T. Hayat, X. Pan and S. Dai. 'The Effect of Hydrophobicity of Ammonium Salts on Stability of Quasi-2D Perovskite Materials in Moist Condition'. *Advanced Energy Materials*, **vol. 8**, no. 21, p. 1800051 (2018) (cited p. 26)

[Zheng *et al.* 2019] Z.-H. Zheng, H.-B. Lan, Z.-H. Su, H.-X. Peng, J.-T. Luo, G.-X. Liang and P. Fan. 'Single Source Thermal Evaporation of Two-dimensional Perovskite Thin Films for Photovoltaic Applications'. *Scientific Reports*, **vol. 9**, no. 1, p. 17422 (2019) (cited p. 19)

[Zheng *et al.* 2020] X. Zheng, Y. Hou, C. Bao, J. Yin, F. Yuan, Z. Huang, K. Song, J. Liu, J. Troughton, N. Gasparini, C. Zhou, Y. Lin, D.-J. Xue, B. Chen, A. K. Johnston, N. Wei, M. N. Hedhili, M. Wei, A. Y. Alsalloum, P. Maity, B. Turedi, C. Yang, D. Baran, T. D. Anthopoulos, Y. Han, Z.-H. Lu, O. F. Mohammed, F. Gao, E. H. Sargent and O. M. Bakr. 'Managing grains and interfaces via ligand anchoring enables 22.3%-efficiency inverted perovskite solar cells'. *Nature Energy*, **vol. 5**, no. 2, pp. 131–140 (2020) (cited p. 35, 87)

[Zheng *et al.* 2022] Z. Zheng, S. Wang, Y. Hu, Y. Rong, A. Mei and H. Han. 'Development of formamidinium lead iodide-based perovskite solar cells: Efficiency and stability'. *Chemical Science*, **vol. 13**, no. 8, pp. 2167–2183 (2022) (cited p. 21)

[Zhong *et al.* 2019] M. Zhong, W. Zeng, H. Tang, L.-X. Wang, F.-S. Liu, B. Tang and Q.-J. Liu. 'Band structures, effective masses and exciton binding energies of perovskite polymorphs of CH3NH3PbI3'. *Solar Energy*, **vol. 190**, pp. 617–621 (2019) (cited p. 27)

[Zhou *et al.* 2014] H. Zhou, Q. Chen, G. Li, S. Luo, T.-b. Song, H.-S. Duan, Z. Hong, J. You, Y. Liu and Y. Yang. 'Interface engineering of highly efficient perovskite solar cells'. *Science*, **vol. 345**, no. 6196, pp. 542–546 (2014) (cited p. 16)

[Zhou *et al.* 2018] W. Zhou, Z. Wen and P. Gao. 'Less is More: Dopant-Free Hole Transporting Materials for High-Efficiency Perovskite Solar Cells'. *Advanced Energy Materials*, **vol. 8**, no. 9, p. 1702512 (2018) (cited p. 47)

[Zhou *et al.* 2019] Q. Zhou, L. Liang, J. Hu, B. Cao, L. Yang, T. Wu, X. Li, B. Zhang and P. Gao. 'High-Performance Perovskite Solar Cells with Enhanced Environmental Stability Based on a (p-FC6H4C2H4NH3)2[PbI4] Capping Layer'. *Advanced Energy Materials*, **vol. 9**, no. 12, p. 1802595 (2019) (cited p. 36, 63, 64, 95)

[Zhumekenov *et al.* 2016] A. A. Zhumekenov, M. I. Saidaminov, M. A. Haque, E. Alarousu, S. P. Sarmah, B. Murali, I. Dursun, X.-H. Miao, A. L. Abdelhady, T. Wu, O. F. Mohammed and O. M. Bakr. 'Formamidinium Lead Halide Perovskite Crystals with Unprecedented Long Carrier Dynamics and Diffusion Length'. *ACS Energy Letters*, **vol. 1**, no. 1, pp. 32–37 (2016) (cited p. 54)

[Zibouche and Islam 2020] N. Zibouche and M. S. Islam. 'Structure–Electronic Property Relationships of 2D Ruddlesden–Popper Tin- and Lead-based Iodide Perovskites'. *ACS Applied Materials & Interfaces*, **vol. 12**, no. 13, pp. 15328–15337 (2020) (cited p. x, 37)

université PARIS-SACLAY

ÉCOLE DOCTORALE
Ondes et matière
(EDOM)

Titre: Étude d'hétérostructures de pérovskites 2D/3D pour cellules photovoltaïques.
Mots clés: Pérovskites, photovoltaïque, matériau, interfaces.

Résumé: Dans le monde du photovoltaïque (PV), les cellules solaires à base de pérovskite ont connu un intérêt croissant au cours de la dernière décennie grâce à leurs propriétés idéales pour des applications PV et leur polyvalence. Cependant, certains défis restent à relever pour que cette technologie devienne un acteur majeur de l'industrie PV, notamment une amélioration de la stabilité des cellules. Dans ce but, ce travail se focalise sur le développement d'une hétérostructure de pérovskites 2D/3D, via l'ajout d'une couche de pérovskite 2D sur la couche de pérovskite 3D déjà utilisée, afin d'améliorer le rendement et la stabilité des cellules solaires. Cette thèse consiste à développer un procédé de synthèse d'hétérostructure 2D/3D et de l'intégrer dans des dispositifs de cellules solaires afin d'optimiser leurs performances. L'objectif est également une meilleure compréhension des mécanismes de formation de cette structure via la caractérisation de ses propriétés physico-chimiques, ce qui bénéficierait à l'optimisation de structures similaires déjà existantes et au développement de nouvelles structures analogues.

Title: Study of 2D/3D perovskites heterostructures for solar cells.
Keywords: Perovskites, photovoltaics, material, interfaces.

Abstract: In the world of photovoltaics (PV), perovskite solar cells have experienced increasing interest over the last decade thanks to their ideal properties for PV applications and their versatility. However, some challenges remain for this technology to become a major player in the PV industry, including improved cell stability. To this end, this work focuses on the development of a 2D/3D perovskite heterostructure, via the addition of a 2D perovskite layer on top of the 3D perovskite layer already used, in order to improve solar cells performance and stability. This thesis consists in developing a 2D/3D heterostructure synthesis process and integrating it into solar cell devices to optimize their performance. The objective is also a better understanding of the mechanisms of formation of this structure via the characterization of its physico-chemical properties, which would benefit the optimization of already existing similar structures and the development of new analogous structures.